Generation of Attosecond Pulses in Atoms and Molecules

Stefan Haessler

▶ **To cite this version:**

Stefan Haessler. Generation of Attosecond Pulses in Atoms and Molecules. Atomic Physics [physics.atom-ph]. Université Paris Sud - Paris XI, 2009. English. NNT : . tel-00440190v2

HAL Id: tel-00440190

https://theses.hal.science/tel-00440190v2

Submitted on 16 Jul 2012

HAL is a multi-disciplinary open access archive for the deposit and dissemination of scientific research documents, whether they are published or not. The documents may come from teaching and research institutions in France or abroad, or from public or private research centers.

L'archive ouverte pluridisciplinaire **HAL**, est destinée au dépôt et à la diffusion de documents scientifiques de niveau recherche, publiés ou non, émanant des établissements d'enseignement et de recherche français ou étrangers, des laboratoires publics ou privés.

THÈSE DE DOCTORAT DE L'UNIVERSITÉ PARIS-SUD XI

Effectuée au Service des Photons, Atomes et Molécules, IRAMIS, DSM
Commissariat à l'Energie Atomique, Saclay.

Spécialité: Lasers et Matière

GENERATION OF ATTOSECOND PULSES IN ATOMS AND MOLECULES

Présentée par

STEFAN HAESSLER

pour obtenir le grade de
DOCTEUR EN SCIENCES DE L'UNIVERSITÉ PARIS-SUD XI.

Soutenue le 03 décembre 2009
devant le jury composé de :

M.	MANFRED LEIN	Rapporteur
M.	JONATHAN MARANGOS	Rapporteur, non présent
Mme.	DANIELLE DOWEK	
Mme.	ANNE L'HUILLIER	
M.	ERIC MÉVEL	
M.	JOHN TISCH	
M.	PASCAL SALIÈRES	Directeur de thèse

GENERATION OF ATTOSECOND PULSES IN ATOMS AND MOLECULES

© 2009 Stefan Haessler
All rights reserved
Printed in Paris, 2009

Commissariat à l'Energie Atomique
Direction Science de la Matière
Institut Rayonnement Matière Saclay
Service des Photons, Atomes et Molécules
Bâtiment 522
F–91191 Gif-sur-Yvette
France

`http://iramis.cea.fr/spam/MEC/`

This thesis was typeset with the LaTeX-system and the memoir class, using a model developed by the smart people of the Atomfysik division at Lund University.

Abstract

When a low-frequency laser pulse is focused to a high intensity into a gas, the electric field of the laser light may become of comparable strength to that felt by the electrons bound in an atom or molecule. A valence electron can then be 'freed' by tunnel ionization, accelerated by the strong oscillating laser field and can eventually recollide and recombine with the ion. The gained kinetic energy is then released as a burst of coherent XUV light and the macroscopic gas medium then becomes a source of XUV light pulses of attosecond (1 as = 10^{-18} s) duration. This is the natural time-scale of electron dynamics in atoms and molecules.

The largest part of this thesis deals with experiments where molecules are the harmonic generation medium and the recolliding electron wave packet acts as a 'self-probe'. In several experiments, we demonstrate the potential of this scheme to observe or image ultra-fast intra-molecular electronic and nuclear dynamics. In particular, we have performed the first phase measurements of the high harmonic emission from aligned molecules. From measurements characterizing in amplitude and phase the high harmonic emission from CO_2 and N_2 molecules aligned in the laboratory frame, we extract the recombination dipole matrix element, i.e. the probability *amplitude* for the continuum electron to recombine into the bound state. This observable contains signatures of quantum interference between the continuum and bound parts of the total electronic wavefunction. It is shown how this quantum interference can be utilized to shape the attosecond light emission from the molecules. Furthermore, a set of recombination dipole matrix elements for electron-ion recollision directions from 0° to 360° may contain sufficient information to reconstruct the bound-state *wavefunction* using a tomographic algorithm. The theoretical basis of this method of molecular orbital tomography is examined, the technique's potential and limitations are presented and the experimental feasibility is demonstrated. This opens the perspective of imaging ultra-fast changes of, e.g., a frontier orbital during a chemical reaction.

In a second part of this thesis, we use the well characterized coherent XUV light emitted by rare gas atoms to photoionize molecules. Measuring the ejected photoelectron wave packet then allows to extract information on the photoionization process itself, and possibly about the initial bound and final continuum states of the electron. We measure how an auto-ionizing resonance in N_2 molecules modifies the spectral phase of the photoelectron wavepacket.

The last chapter of this manuscript describes studies of high harmonic and attosecond light pulse generation in a different medium: ablation plasmas. We perform the first temporal characterization of such a source, demonstrating the femtosecond and attosecond structure of the emitted XUV intensity profile.

SYNTHÈSE

Quand on focalise une impulsion laser dans un gaz, le champ électrique du laser peut atteindre des valeurs comparables à celle du champ ressenti par les électrons liés dans un atome ou une molécule. Un électron de valence peut donc être 'libéré' par ionisation tunnel, accéléré par le fort champ laser oscillant et peut finalement recollisionner et recombiner avec l'ion. L'énergie cinétique gagnée est alors restituée sous la forme d'un flash de lumière XUV cohérente, de sorte que le milieu gazeux macroscopique devient une source d'impulsions de lumière XUV de durée de l'ordre de 100 attoseconde (1 as = 10^{-18} s). Ceci est l'échelle de temps naturelle des dynamiques électroniques dans les atomes et les molécules.

La plus grande partie de cette thèse traite d'expériences où les molécules constituent le milieu de génération d'harmoniques et le paquet d'ondes électronique recollisionnant joue le rôle d'une 'auto-sonde'. Dans plusieurs expériences, nous démontrons le potentiel de ce schéma pour observer ou imager des dynamiques électroniques et nucléaires intra-moléculaires ultra-rapides. En particulier, nous avons effectué les premières mesures de phase de l'émission harmonique émise par des molécules alignées dans le référentiel du laboratoire. Ces mesures ainsi que celles de l'amplitude harmonique pour les molécules de CO_2 et N_2 nous permettent d'extraire l'élément de matrice du dipole de recombinaison, soit l'amplitude de probabilité pour la recombinaison de l'électron du continuum avec l'état lié. Cette observable contient la signature d'une interférence quantique entre les parties libre et liée de la fonction d'onde électronique totale. Il sera démontré que cette interférence quantique peut être utilisée pour mettre en forme l'émission attoseconde par les molécules. De plus, un jeu d'éléments de matrice du dipole de recombinaison pour des directions de recollision électron-ion de 0° à 360° peut contenir des informations suffisantes pour reconstruire la *fonction d'onde* de l'état lié par un algorithme tomographique. Les bases théoriques de cette méthode de tomographie d'orbitales moléculaires sont examinées, le potentiel de la technique et ses limitations sont présentés et la faisabilité expérimentale est démontrée. Ceci ouvre la perspective d'imager les distorsions ultra-rapides d'une orbitale frontière lors d'une réaction chimique.

Dans une deuxième partie de cette thèse, nous utilisons la lumière XUV cohérente bien caractérisée émise par des atomes de gaz rare pour photoioniser des molécules. La mesure du paquet d'ondes électronique émis permet ensuite d'extraire des informations sur le processus de photoionisation même, et potentiellement sur l'état initial lié et l'état final libre de l'électron. Nous avons mesuré comment une résonance auto-ionisante dans des molécules de N_2 modifie la phase spectrale du paquet d'ondes de photoélectrons.

Le dernier chapitre de ce manuscrit décrit des études de génération d'harmoniques et d'impulsions de lumière attosecondes dans un milieu différent: des plasmas d'ablation. Nous avons effectué la première caractérisation temporelle d'une telle source, démontrant la structure femtoseconde et attoseconde du profil d'intensité de l'émission XUV.

List of Publications

This thesis is based on the following papers, which will be referred to by their roman numerals in the text.

I **Coherent control of attosecond emission from aligned molecules**
W. Boutu, S. Haessler, H. Merdji, P. Breger, G. Waters, M. Stankiewicz, L. J. Frasinski, R. Taïeb, J. Caillat, A. Maquet, P. Monchicourt, B. Carré and P. Salières.
Nature Physics **4**, 545–549 (2008).

II **Attosecond imaging of molecular electronic wave-packets**
S. Haessler, J. Caillat, W. Boutu, C. Giovanetti-Teixeira, T. Ruchon, T. Auguste, Z. Diveki, P. Breger, A. Maquet, B Carré, R. Taïeb and P. Salières.
Nature Physics, accepted (2009).

III **Polarization-resolved pump-probe spectroscopy with high harmonics**
Y. Mairesse, S. Haessler, B. Fabre, J. Higuet, W. Boutu, P. Breger, E. Constant, D. Descamps, E. Mével, S. Petit and P. Salières.
New J. Phys. **10**, 025028 (2008).

IV **Attosecond chirp encoded dynamics of light nuclei**
S. Haessler, W. Boutu, M. Stankiewicz, L.J. Frasinski, S. Weber, J. Caillat, R. Taïeb, A. Maquet, P. Breger, P. Monchicourt, B Carré and P. Salières.
J. Phys. B **42**, 134002 (2009).

V **Phase-resolved attosecond near-threshold photoionization of molecular nitrogen**
S. Haessler, B. Fabre, J. Higuet, J. Caillat, T. Ruchon, P. Breger, B. Carré, E. Constant, A. Maquet, E. Mével, P. Salières, R. Taïeb and Y. Mairesse.
Phys. Rev. A **80**, 011404(R) (2009).

VI **Attosecond pulse generation in chromium ablation plasma**
L. B. Elouga Bom, S. Haessler, M. Perdrix, F. Lepetit, J.-F. Herrgot, B. Carré, T. Osaki and P. Salières.
in preparation, (2009).

Other related publications by the author:

Measuring the complex recombination dipole of aligned CO_2 molecules in high-order harmonic generation
S. Haessler, W. Boutu, H. Merdji, P. Breger, R. Taïeb, J. Caillat, A. Maquet, P. Monchicourt, B. Carré and P. Salières.
Proceedings of UVX 2008, 65–70 (2009), DOI: 10.1051/uvx/2009011.

High-contrast pump-probe spectroscopy with high-order harmonics
Y. Mairesse, W. Boutu, P. Breger, E. Constant, D. Descamps, N. Dudovich, B. Fabre, S. Haessler, J. Higuet, E. Mével, S. Petit, P. Salières, D.M. Villeneuve and P.B. Corkum.
Proceedings of UVX 2008, 107–111 (2009), DOI: 10.1051/uvx/2009017.

ABBREVIATIONS

APT	Attosecond Pulse Train
BO	Born-Oppenheimer
DME	Dipole Matrix Element
EWP	Electron Wave Packet
FFT	Fast Fourier Transform
FWHM	Full With at Half Maximum
HF	Hartree-Fock
IR	Infra Red
LCAO	Linear Combination of Atomic Orbitals
MO	Molecular Orbital
RABITT	Reconstruction of Attosecond harmonic Beating by Interference of Two-photon Transitions
SFA	Strong Field Approximation
TDSE	Time Dependent Schrödinger Equation
XUV	eXtreme Ultra Violet

CONTENTS

Introduction **1**

1 Theoretical Tools for Attosecond Physics **7**
1.1 Wave Packets . . . 8
1.1.1 Time-Frequency Properties . . . 10
1.1.2 Optical Wave Packets . . . 10
1.1.3 Electron Wave Packets . . . 11
1.2 Electrons in Atoms and Molecules . . . 11
1.2.1 Bound and Scattering States . . . 12
1.2.2 Atomic States . . . 12
1.2.3 Molecular States . . . 14
1.3 Electron Dynamics . . . 17
1.3.1 Tunnel ionization . . . 17
1.3.2 Semi-classical Description of High-order Harmonic Generation 19
1.3.3 Quantum Description of High-order Harmonic Generation . . . 21
1.3.4 XUV Photoionization . . . 26

2 Experimental Tools for Attosecond Physics **35**
2.1 The Attosecond Pulse Source . . . 37
2.2 Molecular Alignment . . . 38
2.3 Attosecond Pulse Measurement . . . 42
2.4 The Experimental Setup . . . 45

3 Self-probing of Electrons in Molecules **49**
3.1 Measuring the Recombination Dipole Matrix Element . . . 52
3.1.1 Sticking to the Plane-Wave Approximation . . . 54
3.1.2 Two-center Interference . . . 55
3.2 CO_2 Experiments . . . 55
3.2.1 Details on the Data Analysis . . . 57
3.2.2 Adding Ellipticity . . . 58
3.2.3 Question Marks . . . 60
3.2.4 Coherent Control of the Attosecond XUV Emission . . . 62
3.3 The difficult Case of N_2 . . . 62
3.3.1 XUV Polarization State . . . 63
3.3.2 Adding Ellipticity . . . 64
3.3.3 Phase Measurements . . . 65
3.4 Molecular Orbital Tomography . . . 68
3.4.1 Concept . . . 68
3.4.2 Symmetry Considerations . . . 69
3.4.3 Too Good to be True? . . . 71
3.4.4 Simulations . . . 74
3.4.5 Experimental Orbital Reconstructions . . . 75
3.4.6 Considerations on Dynamic Orbital Tomography . . . 77
3.5 Probing Nuclear Dynamics in Molecules with Attosecond Electron Wave Packets . . . 78
3.5.1 High-contrast Measurement of Rotational Revivals . . . 78
3.5.2 Sub-laser-cycle Vibrational Dynamics of Protons . . . 79
3.6 Conclusions . . . 83

4 Probing Molecules with Attosecond XUV Wavepackets **85**

4.1 Phase-resolved XUV Photo-ionization of N_2 Molecules 87
4.1.1 Deciphering the Spectra 87
4.1.2 Results 90
4.1.3 Verification of the Measured Phase Shift 91
4.1.4 Origin of the Phase Shift 93
4.1.5 What was Actually Observed? 93

5 Generating Ultrashort XUV Wavepackets in Ablation Plasmas 95
5.1 Specifics of the experimental setup 98
5.1.1 Experimental conditions 99
5.2 Non-resonant Harmonic Emission 100
5.2.1 Femtosecond XUV pulses 101
5.2.2 Attosecond Pulse Trains 103
5.3 Resonance-Enhanced Harmonic Emission 103
5.3.1 Femtosecond XUV pulses 104
5.3.2 RABITT measurements 105
5.4 Conclusions 106

General Conclusions and Outlook 107

A Atomic Units 111

B Exact scattering states for a 1D square well potential 113

C Symmetry properties of the Fourier transform: Oddness and Imaginarity 115

The author's contribution to the papers 117

Acknowledgments 119

References 121

Papers

I Coherent control of attosecond emission from aligned molecules 133

II Attosecond imaging of molecular electronic wave-packets 141

III Polarization-resolved pump-probe spectroscopy with high harmonics 161

IV Attosecond chirp encoded dynamics of light nuclei 175

V Phase-resolved attosecond near-threshold photoionization of molecular nitrogen 185

VI Attosecond pulse generation in chromium ablation plasma 191

Introduction

The title of this thesis announces that it will be concerned with the generation of attosecond pulses, i.e. pulses of light or matter that have a duration of about 100 attoseconds (as), 1 attosecond being 10^{-18} s, or one billionth of a billionth of a second.

Such pulses can play the role of a flash in photography, or that of a fast shutter. In a sense, the research presented here thus inscribes itself in the tradition of ultra-fast time-resolved observations started by british photographer Eadweard J. Muybridge and french physiologist and chrono-photographer Etienne-Jules Marey in the 1860s. Only in their days, 'ultra-fast' did not yet mean attoseconds, but anything the human eye could no longer resolve, i.e. milliseconds. One of the most famous examples of this work is Marey's falling cat (see figure 0.1), where the available precise knowledge about the cat's 'static structure' before and after the fall did not suffice to infer how the cat arrives to right itself and land on its feet, while preserving zero angular momentum. Only a time-resolved observation proved that the cat changes its shape by curling up and twisting, thereby changing its moment of inertia. Today, model cats are still studied by mathematicians and whole journal issues are devoted to them: (Enos [40]).

Figure 0.1. *A modern version of Marey's ultra-fast falling cat imaging. Photograph taken from (Stewart [189]).*

On the atomic-scale, where quantum mechanics govern the behavior of matter, often the same problem arises: we have precise knowledge about the static structure of systems (energy levels, equilibrium distances, initial and final states), but this knowledge is not always sufficient to infer how these systems actually 'work'. Again, time-resolved observation can shed light on this question. Dynamics or movement arises in quantum systems when two eigenstates, $|\phi_1\rangle$ and $|\phi_2\rangle$, with energies differing by ΔE are superposed (which is much like Schrödinger's cat, by the way). A beating term appears with a half-period of $\tau = \pi\hbar/\Delta E$, giving the fundamental time-scale of dynamics between the two states.

During the last 25 years, femtosecond laser pulses have been successfully used in femto-chemistry, i.e. the study of the movement of atoms and molecules involved in chemical reactions (Zewail [219]). The mass of the nuclei lead to typical energy distances between vibrational or rotational states of ~ 10 meV, and thus the time resolution necessary to observe such dynamics is $\tau \sim 100$ fs. Electronic bound states are much further apart on the energy axis, and the corresponding dynamics are consequently much faster. For $\Delta E > 2$ eV, the fundamental time-scale of dynamics becomes smaller than a femtosecond. Attosecond pulses thus allow to observe electron dynamics *inside* atoms or molecules, as demonstrated 7 years ago by (Drescher et al. [31]), shortly after the first measurement of attosecond light pulses by (Paul et al. [160]) in Saclay and by (Hentschel et al. [73]) in Vienna.

These studies can then again give input to femto-chemistry, because nuclei move in chemical reactions in a potential landscape set by the electrons – attosecond electron dynamics thus directly govern the nuclear dynamics. At-

tosecond physics is thus relevant not only to fundamental atomic and molecular physics, but also for chemistry and materials science. The US Department of Energy (Fleming et al. [44]) goes so far as to announce that the observation and understanding of electron dynamics on the quantum level can teach us how to control matter at this most fundamental level: "We need to go beyond the study of how quantum systems are put together and organized to the study of how they work. And we need to go still further, beyond how they work to how to make quantum-scale systems work for us." This ambitious perspective is the grand idea behind attophysics.

High Harmonic Generation

Creating the shortest events always relies on non-linear processes, so that an excitation $\sim f(t)$ provokes a response $\sim f(t)^n$, with $n > 1$, which will be shorter than the excitation. Attophysics, being concerned primarily with electrons, needs a tool to efficiently act on them causing the said non-linear response, and the electric field of ultra-short lasers proved to be such a tool. It is able to drive a variety of strong-field process. One of the most remarkable of these can be described in three steps (Corkum [22], Lewenstein et al. [117], Schafer et al. [176]), the first of which provides the very strong non-linearity. The strong laser pulse is focused into a cloud of atoms or molecules, where its electric field becomes of comparable strength as that binding the valence electrons to the nuclei. (i) It thus becomes possible for electrons to tunnel into the continuum. (ii) The freed electron is then accelerated by the strong laser field and (iii) eventually recollides with its parent-atom/molecule. One of the things that can happen then is recombination of the electron to its initial state and emission of a photon carrying away the energy gained by the electron in the laser field plus its binding energy.

This light emission, the spectrum of which can extend into the VUV or even the XUV and soft-X-ray region, has been discovered simultaneously in Saclay by (Ferray et al. [42]) and in Chicago by (Mcpherson et al. [142]), and was named 'High Harmonic Generation' (HHG). The whole process is directly laser driven and thus fully coherent, as shown by, e.g., (Salières et al. [173]), and for this reason alone it constitutes an extremely interesting source of XUV light for interferometry (Merdji et al. [144]) and imaging experiments (Ravasio et al. [165], Schwenke et al. [181]).

The most intriguing property of the HHG process, however, is its ultrashort, sub-laser-cycle time scale. The continuum electron is in fact a wave packet of attosecond duration. Since the above-described three-step process is repeated in each half-cycle of the driving laser field, the XUV pulses produced by HHG with femtosecond laser pulses consequently have features both on the femtosecond and the attosecond time-scales. On the femtosecond scale, they are conveniently described as high-order harmonics of the fundamental driving laser frequency, while on the attosecond scale, the picture of a recolliding electron wave-packet, emitting a short burst of XUV light every half-cycle of the driving field, is more appropriate.

Finally, the short duration of the XUV pulses is not only interesting for time-resolved studies, but it also concentrates the pulse energy in an extremely short time, allowing to combine high photon energies with high peak intensities, hardly available otherwise. Non-linear processes in the XUV domain become possible (Descamps et al. [26], Sekikawa et al. [183], Tzallas et al. [200]). Although short wavelength free-electron lasers such as FLASH in Hamburg and LCLS in Stanford are going online at this time, providing far superior photon numbers and intensities with (few) femtosecond pulsedurations, their billion-$ cost, stadium-size and limited availability leaves un-

challenged the status of HHG-based sources as relevant tools for ultra-fast physics in the XUV.

Studying Molecules with High Harmonic Generation

This thesis will mainly be concerned with how molecules and their dynamics can be studied using the process of HHG. Two basic experimental schemes for doing so with attosecond pulses can be discerned. They are illustrated in figure 0.2. In the first, the *XUV-ionization scheme*, the HHG process simply provides a source of ultra-short XUV pulses, used to pump or probe molecules by exciting or photo-ionizing them. One then detects the ejected photo-electrons, which carry information about the intra-atomic / molecular dynamics. In the *self-probing scheme*, the recolliding electron wave packet takes the role of an ultra-short probe pulse, while the emitted XUV light carries information about the atom or molecule. The excitation process launching dynamics could then directly be the tunnel-ionization or, more generally, a separate pump pulse.

While the XUV-ionization scheme is a logical extension of experiments like the time-resolved observation of the Auger process by (Drescher et al. [31]), it is much less obvious whether the self-probing scheme, based on the extremely simplified three-step model, could actually be realized experimentally.

The idea to use molecules as an HHG medium came up soon after the discovery of HHG itself and was first motivated by the greater de-localization of valence electrons in molecules and the corresponding greater polarizabilities, which promised larger conversion efficiencies. In 1994 (Liang et al. [119]) and two years later (Lyngå et al. [122]) compared small molecules with rare gas 'reference atoms' that have a similar ionization potential I_p. The hopes for more efficient HHG were disappointed and in the majority of cases, the molecules gave results for the shape of the spectrum and achievable cut-off positions reminiscent of those obtained with the reference atom, only with somewhat lower conversion efficiency. The comparison of O_2 with xenon, however, made an exception: the molecule lead to a higher signal and spectral cut-off position, although its I_p is very similar to that of xenon. This observation, eight years later explained by (Shan et al. [185]) as the result of ionization suppression in O_2 due to the symmetry of its highest occupied molecular orbital, constitutes the first observation of an effect of the bound state spatial structure with its Ångström features on the emission of high harmonics with ~ 10 nm wavelength.

After a four year period of silence around molecules and HHG – at least on the experimental side –, the group at Imperial College London relaunched research in this direction and (Hay et al. [69, 70]) reported in 2000 HHG in cyclic organic molecules, continuing to investigate the idea of using media with strongly de-localized valence electrons. Indeed, an enhancement compared to xenon was found, but only for a single harmonic order. This selectivity triggered a discussion about the role of VUV resonances in the molecules as well as about the applicability of the three-step 'wave packet recollision model' to molecular systems in order to study intra-molecular electron dynamics.

The perspective thus evolved from the XUV-source optimization towards studying molecular structure. It thus became necessary to align molecules in the laboratory frame relative to the electron recollision direction, which was first realized in the context of HHG in 2001 by (Hay et al. [71], Velotta et al. [204]) and later refined by (de Nalda et al. [24]). It was concluded that the symmetry of the molecular ground state gets imprinted on the outcome of strong-field phenomena such as HHG. An angle dependent phase of the molecular dipole was invoked and a possible origin of such a phase dependence was

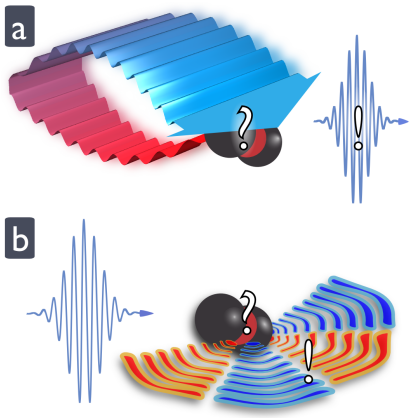

Figure 0.2. *Different experimental schemes: (a) The self-probing scheme, where the recolliding electron wave packet probes the parent atom or molecule. (b) The XUV-ionization scheme, where ultra-short XUV pulses interact with the atom or molecule and the ejected photo-electrons carry information.*

given shortly after by (Lein et al. [110, 111]). Although HHG in oriented molecules had been studied earlier numerically by (Kopold et al. [95], Lappas and Marangos [100], Yu and Bandrauk [217]), this work provided a major breakthrough since numerical results obtained for H_2^+ molecules could be explained by an analytical model. It proved that destructive interference between the recolliding electron wave and the electron bound-state *wavefunction* during the recombination step of HHG leaves a clear signature in the XUV emission.

At the same time, (Niikura et al. [153, 154]) clearly formulated the self-probing scheme and revealed its great potential for time-resolved measurements by characterizing the time structure of the recolliding electron wave packet itself and using it to trace the expansion of a D_2^+ ion immediately after ionization. The same dynamics were observed in greater detail in 2006 by (Baker et al. [5]) using a modified and experimentally more efficient (self-probing) scheme based on theory developed by (Lein [109]).

In 2004, a work pushing the idea of molecular imaging in the self-probing scheme to the extreme was published by (Itatani et al. [80]). It proposed a tomographic analysis of HHG spectra acquired for a range of molecule alignment directions to reconstruct the electron bound-state *wavefunction*, which certainly constituted a conceptual breakthrough, although based on many controversial assumptions. Although in this work a static wavefunction had been reconstructed, the potential of ultra-fast, possibly attosecond, time resolved imaging of electrons bound in molecules was evident. This paper launched enthusiastic activity in both experimental and theoretical groups and is also the main motivation behind most of the work in this thesis.

Almost simultaneously, intensity minima in HHG spectra generated in aligned CO_2 molecules were reported by (Kanai et al. [86], Vozzi et al. [206]) and interpreted as the first experimental observation of destructive quantum interference in the recombination step of HHG. Oddly enough though, the spectral position of the interference-features were not the same in both laboratories.

(Wabnitz et al. [210]) of our group at CEA Saclay published one year later a first measurement of spectral phases of the high harmonic emission from unaligned N_2 molecules, without, however, finding clear signatures of molecular structure. The attosecond temporal profile of the emission from the molecules and from the reference atom argon was almost the same, which was explained by the angular averaging in the isotropic molecular medium.

This work was continued in Saclay during the thesis of Willem (Boutu [12]), who developed a new phase measurement setup in order to do the experiment with aligned molecules. His work and this thesis overlapped by one year and a large part of the results presented here have been obtained conjointly.

The Aim and Outline of this Thesis

This work thus started in 2006 in an environment of great scientific perspectives and bright ideas that were already in the air, but rather little hard experimental evidence. The principle aim of this thesis was thus to do measurements that would help to assess and improve the existing models and to obtain truly experimental tomographic images of electrons bound in molecules based on a much reduced set of assumptions. The group in Saclay is one of the few that are able to measure the spectral phase of the high harmonic emission – an observable that had proved extremely valuable in the past and had so far barely been exploited in the experiments on HHG in molecules.

Chapters 1 and 2 give an overview of the theoretical and experimental tools, respectively, at the base of attophysics in general and used in this work in particular. The following chapters are essentially complements to the papers found at the end of the manuscript, describing in more detail the theoretical bases, experimental conditions and data analysis as well presenting more experimental data not discussed in the papers. We have tried to repeat as little as possible the content of these papers but only briefly summarize their main results. Their reading is thus highly recommended before reading the corresponding part of the chapter.

The third and largest chapter of this thesis will present experiments in the self-probing scheme. First, measurements of the recombination dipole matrix element for aligned CO_2 molecules will be discussed. This is a full account of the content of paper **I**, reporting the measurement of a spectral phase jump that provides new experimental evidence for destructive quantum interference in HHG. The control of this quantum interference for attosecond pulse shaping is demonstrated and possible applications of coherent control in the XUV and attosecond domain are discussed. Measurements of the same kind are then presented for N_2, where the interpretation of the dipole matrix elements turned out to be much more difficult. In paper **II**, we invoke a contribution of a lower lying orbital to HHG that is maximum when the molecules are aligned perpendicular to the driving laser field. Simultaneous ionization of two orbitals in fact corresponds to the creation of a hole in the molecular ion evolving with 1.5 fs period. The data analysis is then pushed further towards molecular orbital tomography, main subject of paper **II**.

In a second part of chapter 3, the self-probing scheme is applied to the probing of nuclear dynamics. Using a polarization-resolved detection scheme of high harmonics from aligned N_2 we detect with greatly enhanced contrast rotational wave packet dynamics, which are at the basis of the molecule alignment technique used in all our experiments. This work is the subject of paper **III**. Much faster dynamics are studied in paper **IV**, commented at the end of the third chapter. Here, we apply the PACER (probing attosecond dynamics by chirp encoded recollision) technique, developed by (Baker et al. [5], Lein [109]) to trace proton dynamics in molecular ions, and study the spectral phase of the high harmonic emission as observable. The theoretical studies, essential to the results discussed in this chapter have been done in close collaboration with the group of Richard Taïeb, Alfred Maquet and Jérémie Caillat at the Université Pierre et Marie Curie, Paris. The development of the 'self-probing' experimental setup as well as the measurements for paper **IV** have been done in collaboration with the group of Leszek Frasinski at the University of Reading (now at Imperial College London). The experiments for paper **III** have been obtained in collaboration with the group of Eric Constant at CELIA Bordeaux.

Chapter 4 then turns to experiments in the XUV-ionization scheme, subject of paper **V**. Ionizing N_2 molecules with ultrashort XUV pulses generated by HHG in argon, we measure the phase of the two-photon XUV-IR photoionization matrix element. An auto-ionizing excited state of N_2 resonant with harmonic 11 is shown to lead to a phase jump. The relation of this perturbative two-photon measurement to a direct measurement of the phase of the single-XUV-photon ionization dipole matrix element, which has yet to be rigorously studied, is discussed. Equivalence between the two would allow an interpretation in terms of a time-delay imposed by the resonant photoionization channel on the ejected photoelectrons. These experiments have again been done together with the CELIA Bordeaux and for the relevant theory, we worked with the Université Pierre et Marie Curie, Paris.

Chapter 5 presents experiments unrelated to molecules: the study of HHG

in lowly ionized ablation plasma plumes. This medium had been reported to yield intriguingly high XUV generation efficiencies and we teamed up with a leading group of this field, lead by Tsuneyuki Osaki at INRS Montréal, to do the first temporal characterization of this source. Part of the results, the measurement of an attosecond pulse train, are subject of paper **VI**. For all ablated target materials, we could show that the XUV emission is directly laser driven and thus presents an envelope of femtosecond duration. The conversion efficiency was, however, not as high as reported before. We attribute this to the lower available laser intensity for HHG in our experiments.

Finally, the manuscript ends with general conclusions drawn from the work done during the three years of this thesis, together with an outlook on future developments.

CHAPTER 1

THEORETICAL TOOLS FOR ATTOSECOND PHYSICS

Synthèse

We will make use of a number of theoretical tools essential to attophysics, elements of which will be described in this chapter. After a short introduction of the concept of a wave packet, essential to the physics describing small objects with rapid dynamics, we present the basics of the description of electrons in atoms and molecules – first in the static nuclear potential landscape only, and then in a time-dependent potential, created when a strong oscillating laser field is added to the binding potential. For infrared laser wavelengths, we focus on the process of high harmonic generation, which is at the heart of all the experiments discussed in the following chapters. Finally, we consider the presence of an high-frequency XUV field alone or in combination with an infrared laser field to discuss the principles of XUV photo-ionization. This process is used to characterize the attosecond light pulses generated via HHG in chapters 3 and 5 and is itself under study in chapter 4.

RÉSUMÉ DU CHAPITRE

Nous allons utiliser un certain nombre d'outils théoriques essentiels pour la physique attoseconde et dans ce chapitre nous allons en introduire quelques bases. Si on étudie des objets petits et rapides – comme les électrons dans des atomes ou des molécules ou bien des impulsions de lumière – il sera toujours avantageux de les décrire comme des paquets d'ondes, i.e. comme des superpositions de composantes spectrales. Nous décrivons les propriétés les plus importantes des paquets d'ondes au début de ce chapitre et détaillons les exemples de la lumière se propageant dans le vide ainsi que le cas d'un électron libre.

Si l'électron se trouve dans un potentiel formé par le(s) noyau(x) d'un atome / molécule, les états qu'il peut prendre et qui seront donc des éléments de base naturels pour construire des paquets d'ondes changent drastiquement. Nous introduirons donc les bases de la description des états électroniques stationnaires dans les atomes et les molécules, l'importante notion des orbitales ainsi que leurs symétries.

Pour 'faire' de la physique attoseconde, c'est-à-dire observer et contrôler les électrons dans les atomes et molécules, nous allons utiliser le champ électrique de la lumière laser. Nous allons donc ensuite étudier théoriquement

Synthèse

la dynamique électronique dans et autour d'un atome / molécule induite par un champ laser qui s'ajoute au potentiel atomique / moléculaire.

Pour des fréquences laser infrarouges, nous nous concentrerons d'abord sur le processus de la génération d'harmoniques et ses trois étapes: ionisation par effet tunnel, propagation d'un électron (quasi-)libre dans le continuum, et finalement recombinaison avec l'état fondamental. La description classique – où les première et dernière étapes n'apparaissent que comme des événements ponctuels libérant ou capturant l'électron, et la deuxième étape, comme la trajectoire classique d'un électron – donne déjà une assez bonne description du processus et des propriétés de la lumière émise. La description complètement quantique ajoute ensuite d'importantes notions comme l'élargissement latéral du paquet d'ondes électronique dans le continuum dû à la diffusion quantique ou l'image de la recombinaison comme une interférence entre le paquet d'ondes du continuum et l'état lié. Cette idée est au coeur du schéma d'auto-sondage qui donne le titre au chapitre 3. Finalement, en faisant l'approximation de phase stationnaire, on retrouve la notion des trajectoires électroniques qui sont maintenant des trajectoires quantiques dominantes.

Dans une dernière partie seront traités les électrons des atomes et molécules en présence d'un champ laser de fréquence élevée telle que l'énergie d'un photon est suffisante pour amener un électron de valence dans le continuum. C'est le cas des photons XUV produits par génération d'harmoniques. Nous allons voir que le paquet d'ondes électronique émis sera décrit en amplitude et phase spectrale comme une réplique du paquet d'ondes optique avec un filtre ajouté par l'élément de matrice dipolaire décrivant le processus de photoionisation. Si de plus un champ laser infrarouge est présent, il y a la possibilité de photoioniser par des processus à deux photons et deux couleurs – ce qui est à la base de nos techniques de caractérisation d'impulsions attosecondes. Les équations essentielles pour comprendre ces techniques seront donc dérivées et nous le ferons par deux approches différentes. L'une se base sur l'approximation du champ fort et nous allons considérer le champ infrarouge comme une porte de phase qui module la phase spectrale du paquet d'ondes électronique émis lors de l'ionisation par l'impulsion XUV. La deuxième approche utilise la théorie des perturbations de deuxième ordre pour calculer directement les éléments de matrice de la transition à deux photons. La phase de ces éléments de matrice à deux photons apparaîtra comme observable, ce qui n'était pas le cas dans le résultat de la première approche. Ce fait est pertinent pour les expériences discutées dans le chapître 4, où nous avons effectivement mesuré cette phase. L'interprétation physique de cette observable implique donc une compréhension théorique approfondie de son origine. La discussion de cette question marquera la fin de ce chapitre.

1.1 Wave Packets

Wave packets are an extremely useful concept to describe objects localized in space and time, arising from the superposition principle for the solutions of the linear differential equations describing these objects. If traveling waves are solutions then so is a superposition of them, which is called a wave packet. A wave packet has a non-negligible amplitude only during a short time/space span where all its components are in phase. It can be written as a complex

amplitude that is a function of time, t, and space, $\boldsymbol{r}$:

$$a(\boldsymbol{r},t) = \int \mathrm{d}\boldsymbol{k}\, a(\boldsymbol{k}) \mathrm{e}^{\mathrm{i}[\boldsymbol{k}\cdot\boldsymbol{r}-\omega(\boldsymbol{k})t]}\,, \tag{1.1}$$

where we have used traveling *plane* waves as components with the wave vector $\boldsymbol{k}$, complex spectral amplitudes $a(\boldsymbol{k})$ and angular frequencies $\omega(\boldsymbol{k})$. Obviously, at $t = 0$, this corresponds to a spatial Fourier transform and for purely real-valued $a(\boldsymbol{k})$, the wavepacket is Fourier limited, i.e. its spatial spread, Δx, is minimized for the bandwidth Δk given by the width of $a(\boldsymbol{k})$. The way ω depends on $\boldsymbol{k}$ is called the dispersion relation and is decisive for the temporal evolution of the wave packet.

Every component of the wave packet travels with a *phase velocity* $v_\mathrm{p} = \omega(\boldsymbol{k})/k$ into the direction pointed by $\boldsymbol{k}$, i.e. different components generally travel at different velocities except when $\omega(\boldsymbol{k})$ is linear in $\boldsymbol{k}$. In a small range around $\boldsymbol{k}_\mathrm{c}$, a linearization may approximate $\omega(\boldsymbol{k})$ [1]:

$$\omega(k) \approx \omega(k_\mathrm{c}) + \left(\frac{\partial\omega}{\partial k}\right)_{k_\mathrm{c}} (k - k_\mathrm{c}) \tag{1.2}$$

Inserting this into equation 1.1, yields

$$a(x,t) = \mathrm{e}^{\mathrm{i}[k_\mathrm{c}x-\omega(k_\mathrm{c})t]} \int \mathrm{d}k\, a(k) \mathrm{e}^{\mathrm{i}(k-k_\mathrm{c})[x-(\partial\omega/\partial k)_{k_\mathrm{c}}t]}\,. \tag{1.3}$$

One can then identify a carrier wave with angular frequency $\omega(k_\mathrm{c})$ traveling with the phase velocity $v_\mathrm{p} = \omega(k_\mathrm{c})/k_\mathrm{c}$, and an envelope $|a(x,t)|$, moving with the *group velocity* $v_\mathrm{g} = (\partial\omega/\partial k)_{k_\mathrm{c}}$. The shape of the envelope does not change during propagation.

Considering larger regions of wave vectors k, one can in general no longer neglect higher order terms in the dispersion relation. For different narrow k-slices, the group velocity will then be different and the wave packet will broaden during propagation. This effect is referred to as *group velocity dispersion*. To quantify it, consider an initially Fourier limited wave packet with a bandwidth Δk around k_c or correspondingly $\Delta\omega$ around ω_c. Two wave packet components on opposite edges of the bandwidth will take different times to propagate over a certain distance L due to their different group velocities. These times, $\tau_\mathrm{g} = L/v_\mathrm{g}$, are called *group delay* and are defined relative to the zero of the t-axis. The temporal duration of the wave packet during its propagation will increase by

$$\begin{aligned}\Delta\tau &\approx L \left| \left(\frac{\partial k}{\partial\omega}\right)_{\omega_\mathrm{c}-\Delta\omega/2} - \left(\frac{\partial k}{\partial\omega}\right)_{\omega_\mathrm{c}+\Delta\omega/2} \right| \\ &\approx L \left| \frac{\partial^2 k}{\partial\omega^2} \right|_{\omega_\mathrm{c}} \Delta\omega\,. \end{aligned} \tag{1.4}$$

The quantity relevant to the wave packet shape is the *variation* of group delay in its spectrum. This is quantified by the *group delay dispersion* (GDD), $L\left|\partial^2 k/\partial\omega^2\right|_{\omega_\mathrm{c}}$ with the unit $[s^2]$, or the GDD per unit propagation length, $\left|\partial^2 k/\partial\omega^2\right|_{\omega_\mathrm{c}}$, commonly referred to as *group velocity dispersion.*

[1] From here on, the equations are given for one dimension only for the sake of clarity of notation – to extend them to three dimensions, the derivatives $\partial/\partial k$ are simply to be replaced by ∇_k.

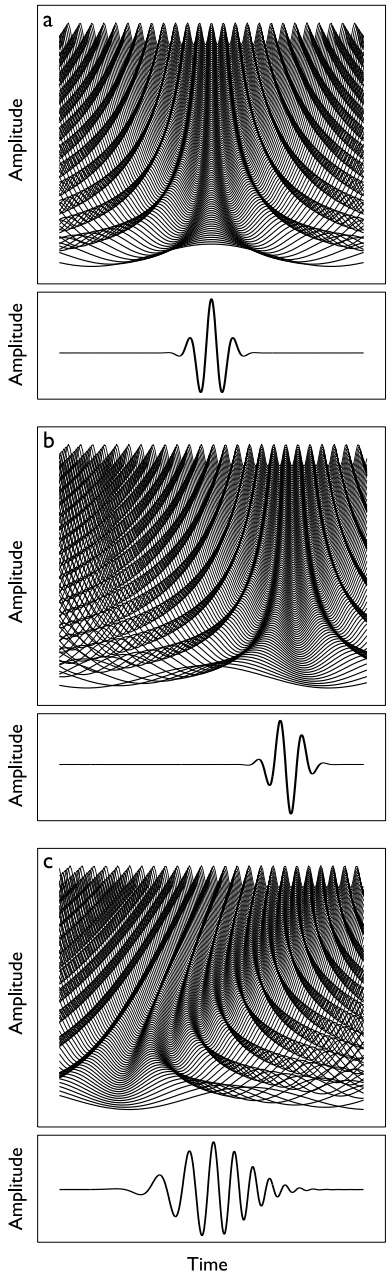

Figure 1.1. *Effect of different spectral phases on the wave packet.* $\varphi(\omega) = 0$ *(a),* $\varphi(\omega) \propto (\omega - \omega_c)$ *(b) and* $\varphi(\omega) \propto (\omega - \omega_c)^2$ *(c). Upper panels show the wave packet components,* $e^{-i\omega t + \varphi(\omega)}$ *with a small offset between them. Lower panels show the total amplitude,* $a(t)$ *of the wave packet formed by these components with Gaussian spectral amplitudes,* $a(\omega)$*.*

1.1.1 Time-Frequency Properties

The same can be re-formulated by writing the wave packet as a function of time, as seen from the perspective of an observer at the fixed position L:

$$\begin{aligned} a(t) &= \int \mathrm{d}k\, a(k) e^{i[kL - \omega(k)t]} \\ &= \int \mathrm{d}\omega\, a(\omega) e^{i\varphi(\omega)} e^{-i\omega t}\,, \end{aligned} \tag{1.5}$$

This is an $\omega \to t$ Fourier transform, and the term $k(\omega)L$ can be regarded as a phase $\varphi(\omega)$ added to the spectral amplitudes, i.e. as the *spectral phase* of the wave packet. A $\varphi(\omega)$ linear in ω, i.e. $\varphi(\omega) = \tau\omega$, corresponds simply to a shift in time of the wave packet $a(t)$ by τ. Now, the group delay and GDD can be defined as properties of the wave packet at a fixed point in space:

$$\tau_g(\omega) = \left.\frac{\partial \varphi(\omega')}{\partial \omega'}\right|_{\omega} \tag{1.6}$$

$$\mathrm{GDD}(\omega) = \left.\frac{\partial^2 \varphi(\omega')}{\partial \omega'^2}\right|_{\omega}\,. \tag{1.7}$$

Note, that these definitions are completely equivalent to the ones made above. This list can obviously be continued to include higher order terms in the spectral phase but looking at the effect of the first two orders on the temporal profile already captures the essential points. Figure 1.1 shows three prototypical cases: Starting from a Fourier-limited wave packet with $\varphi(\omega) = 0$, a linear spectral phase, $\varphi(\omega) = \tau_0(\omega - \omega_c)$, is added. This leads to a constant group delay, $\tau_g = \tau_0$ for all components and consequently the whole wave packet is shifted in time without broadening. The term $\tau_0\omega_c$ adds a total phase shift, so the so called carrier-envelope phase changes. For the case of a quadratic spectral phase, $\varphi(\omega) \propto (\omega - \omega_c)^2$, the group delay is frequency dependent: $\tau_g \propto 2(\omega - \omega_c)$. Different groups of modes are in phase at different times, leading to a time dependent instantaneous frequency of the total wave packet, $a(t)$, called a *chirp*. In the considered case, the group delay vanishes for $\omega = \omega_c$, so the wave packet envelope broadens but its peak is not shifted in time. Phase terms of higher order than 2 start inducing asymmetry to the temporal envelope of the wave packet.

1.1.2 Optical Wave Packets

Optical wave packets, i.e. light pulses, are built of traveling plane waves, which solve the electromagnetic wave equation for an isotropic, non-magnetic medium:

$$\frac{\varepsilon}{c^2}\frac{\partial^2}{\partial t^2}\boldsymbol{E}(\boldsymbol{r},t) = \nabla^2 \boldsymbol{E}(\boldsymbol{r},t)\,, \tag{1.8}$$

where ε is the dielectric constant and c is the speed of light in vacuum. These solutions have the dispersion relation

$$\omega(k) = \frac{ck}{n(k)}\,, \tag{1.9}$$

with the refractive index $n(k) = \sqrt{\varepsilon(k)}$. The wave packet amplitude given by equation 1.1 is one component of the complex electric field and $|a(\boldsymbol{r},t)|^2$ is proportional to the intensity. The phase and group velocities are then found to be:

$$v_p = \frac{c}{n(k)}\,, \qquad v_g = \frac{c}{n(k)}\left(1 - \frac{k}{n(k)}\frac{\partial n}{\partial k}\right). \tag{1.10}$$

When the refractive index is independent of k, which in particular is the case in vacuum with $n \equiv 1$, the two velocities are the same and the optical wave packet propagates without changing its shape. Group *velocity* dispersion is thus a medium property in the optical case and GDD is the distortion of a wave packet after traversing an optical element. In most transparent media in the visible spectral region, $\partial^2 k/\partial\omega^2 > 0$, i.e. the group velocity decreases with increasing angular frequency. This 'normal dispersion' thus leads to a positive chirp.

1.1.3 Electron Wave Packets

Free electron wave packets (free EWP) are put formed of traveling plane waves solving the Schrödinger equation for a *free* electron:

$$\mathrm{i}\hbar\frac{\partial}{\partial t}\psi(\boldsymbol{r},t) = \left(-\frac{\hbar^2}{2m_\mathrm{e}}\nabla^2 + V_0\right)\psi(\boldsymbol{r},t)\,, \tag{1.11}$$

with the reduced Planck constant $\hbar$, the electron mass m_e and some constant potential V_0. These waves, for $\omega > 0$, have the dispersion relation

$$\omega(k) = \frac{\hbar k^2}{2m_\mathrm{e}}\,. \tag{1.12}$$

This is a pleasing result as it recovers the classical relation between kinetic energy, E_kin, and mechanical momentum, p, with de Broglie's $E_\mathrm{kin} = \hbar\omega$ and $p = \hbar k$. The wave packet amplitude given by equation 1.1 is the electron wavefunction. The phase and group velocities are then given by:

$$v_\mathrm{p} = \frac{\hbar k}{2m_\mathrm{e}}\,, \qquad v_\mathrm{g} = \frac{\hbar k}{m_\mathrm{e}}\,. \tag{1.13}$$

An electron with the mechanical momentum p obviously moves with the group velocity v_g. The group velocity increases with k even in vacuum, i.e. group velocity dispersion is intrinsic to the physics of electrons and their wavefunctions broaden during propagation.

1.2 Electrons in Atoms and Molecules

As discussed in the introduction chapter, attophysics is concerned with electrons in atoms and molecules. The states these electrons can take are very different from those of the free electron. This is due to the presence of the spatially varying potential, $V(\boldsymbol{r})$, felt by the electron, replacing V_0 in the Schrödinger equation 1.11.

As long as the Hamiltonian, $\mathcal{H} = -\frac{1}{2}\nabla^2 + V(\boldsymbol{r})$, is time-independent, one can easily show that the solutions take the form $\psi(\boldsymbol{r},t) = \mathrm{e}^{-\mathrm{i}Et}\phi_E(\boldsymbol{r})$ and the Schrödinger equation for $\phi(\boldsymbol{r})$ writes

$$E\phi_E(\boldsymbol{r}) = \left(-\frac{1}{2}\nabla^2 + V(\boldsymbol{r})\right)\phi_E(\boldsymbol{r})\,. \tag{1.14}$$

Here and in all this thesis, atomic units ($\hbar = c = m_\mathrm{e} = 4\pi\varepsilon_0 = 1$) are used except stated otherwise – refer to Appendix A for the translation to the SI system. Equation 1.14 takes the form of an eigenvalue equation for the Hamiltonian $\mathcal{H}$ with eigenstates ϕ_E and eigenvalues E, identified with the total energy of the electron. Stationary electron wavefunctions are thus eigenstates of the Hamiltonian describing the system. Besides the mathematics of equation 1.14, a physical electron wavefunction has to be square integrable, i.e. $\int \mathrm{d}\boldsymbol{r}|\phi(\boldsymbol{r})|^2$ is finite.

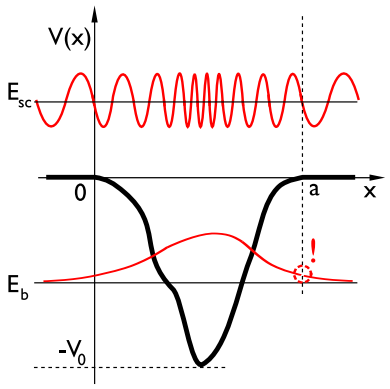

Figure 1.2. *Arbitrary one-dimensional potential with a bound state of energy E_b and a continuum state of energy E_{sc}. For bound states, the wavefunction has to be square integrable which allows states to exist only for discrete $E < 0$, whereas for continuum states ($E > 0$), all solutions for continuous E are allowed.*

1.2.1 Bound and Scattering States

Bound states are defined as *square integrable eigenstates of the Hamiltonian*. It is this physical requirement that allows only those discrete energy eigenvalues E that come with a square integrable eigenstate. (Cohen-Tannoudji et al. [20]) demonstrates that for any potential that approaches zero (or any constant value – which is a mere question of calibration) sufficiently fast for $r \to \pm\infty$, there can only be discrete bound states and their energy is negative. For a potential like the one shown in figure 1.2, in the region where $V(x) \approx 0$ one approaches the situation of a free particle as described by equation 1.11, where the solutions are plane waves, $e^{\pm ikx}$, with $k = \sqrt{2(E-V)}$.

For $\mathbf{E < 0}$, the wave vector k is imaginary, and one is easily convinced that for the solution to be square integrable, it has to drop exponentially to zero for $x \to \pm\infty$, i.e. go as $e^{\chi x}$ for $x < 0$ and $e^{-\chi x}$ for $x > a$, with $\chi = \sqrt{-2E}$. The solution within the potential well, governed by the precise shape of the potential $V(x)$, has to be continuously connected to these exponential functions, which is always possible on one side but on the other side only for the said discrete E.

For $\mathbf{E > 0}$, k is always real-valued, and thus the eigenstates approach plane waves as $x \to \infty$. It is hopeless to find square integrable eigenstates like this, but as seen in section 1.1.3, a superposition of such states, i.e. a wave packet, can be square-integrable and thus can represent an electron wavefunction. All eigenstates with continuously varying energies $E > 0$ are thus physically valid. These *eigenstates of the Hamiltonian with positive energy eigenvalues* are referred to as *continuum states* or *scattering states*. An electron cannot be in a pure scattering eigenstate but only in a superposition, which is *not* stationary. In appendix B, an analytic solution of the Schrödinger equation 1.14 for a finite square well potential is demonstrated for energies $E > 0$. It is found that the plane wave solutions for the free electrons are modified by E-dependent phases, i.e. the scattering states for different energies will have different phases. This is a general property of scattering states and plays a crucial role in papers **I** and **II**.

1.2.2 Atomic States

An electron in an atom interacting with the approximately point-shaped nucleus of charge Z at $\boldsymbol{r} = 0$ feels a Coulomb potential,

$$V(\boldsymbol{r}) = -Z/r\,. \tag{1.15}$$

Although the Coulomb potential nowhere strictly takes the value zero, the conclusions of the previous section remain valid. It is one of the few potentials, for which the Schrödinger equation 1.14 can be solved analytically and the procedure – at least for the bound states – is found in virtually any quantum physics text book (Cohen-Tannoudji et al. [20], Fick [43]).

Bound states ϕ_{lmn}, associated with energy eigenvalues $E_n = -Z^2/(2n^2)$, and characterized by three quantum numbers $n \in \mathbb{N}^+$, $l = 0, \ldots, n-1$ and $m = -l, \ldots, l$, can be written as a product of a radial and an angular part:

$$\phi_{nlm}(\boldsymbol{r}) = R_{nl}(r)Y_{lm}(\theta,\varphi)\,. \tag{1.16}$$

The radial part is of the form $R_{nl}(r) \propto e^{-r/n}(2r/n)^l L^{2l+1}_{n-l-1}(2r/n)$, where the $L^{2l+1}_{n-l-1}(2r/n)$ are the associated Laguerre polynomials. The angular part, $Y_{lm}(\theta,\varphi) \propto P^m_l(\cos\theta)e^{im\varphi}$, are the spherical harmonics, i.e. the eigenfunctions of the angular part of the Laplace operator, $\Delta = \nabla^2$, in spherical coordinates. Here, $P^m_l(\cos\theta)$ are the associated Legendre polynomials.

The precise functional form of all these elements combined into ϕ_{nlm} is not easy to see but the quantum numbers already tell about the important qualitative properties: $n-1$ gives the total number of nodes and l is the number of non-centrosymmetric nodes, i.e. planes or cone-shaped nodes, all crossing in $\boldsymbol{r} = 0$. The numbers $l = 0, 1, 2, 3, \ldots$ are also associated with the letters s, p, d, f,.... Non-centrosymmetric nodes can obviously have different possible orientations in three-dimensional space, $\boldsymbol{r}$. We, or some external field or close particle, can select a preferred direction and m denotes the orientation of the nodes relative to this direction. For example, a p-electron-state will have $n-2$ centrosymmetric nodes and one nodal plane, which can be perpendicular to the x,y or z-direction. There are thus three p-states: p_x, p_y and p_z. Figures 1.3 and 1.4 show some electron wavefunctions for the hydrogen atom, i.e. $Z = 1$, as given by equation 1.16 and including normalization.

These results are only exact for single electron atoms since in a multi-electron atom, the potential seen by the different electrons is no longer given by equation 1.15 – the spherical symmetry can be significantly perturbed and the strength of the interaction with the nucleus reduced due to the shielding by other electrons. Of course one could include the electron-electron-interaction in the Hamiltonian as $\sum_{i<j} 1/r_{ij}$, but then analytic solutions to equation 1.14 become impossible and even a numerical solution becomes extremely costly due to the high dimensionality.

For sufficiently simple systems one can model the shielding and find pseudo-potentials for a *single active electron*, which typically are l-dependent (Muller [150]). This is easy to comprehend: The higher l, the more nodes are crossing at $\boldsymbol{r} = 0$, i.e. the further away the electron density is from the nucleus and the stronger these electrons are thus shielded from the nucleus. An s-electron, on the other hand, has its $\phi_{n00}(\boldsymbol{r})$-maximum at $\boldsymbol{r} = 0$ and is less affected by the presence of its neighbors. This l-dependent shielding is also the reason why in multi-electron atoms, states of equal n and different l are no longer degenerate as in the one-electron case.

In the general case, one applies elaborate numerical techniques, which are at the core of the domain named *quantum chemistry*. One of the simplest of these is the **Hartree-Fock** (HF) method, sometimes also called self-consistent-field method. Here, the basic assumption is that the electron-electron-interaction $\sum_{i<j} 1/r_{ij}$ can be replaced by a sum of potentials, each for one electron i, exerted by the mean field created by the remaining ones: $\sum_i V_i^{\mathrm{el}}(\boldsymbol{r}_i)$. Then, the n-electron wavefunction, $\phi(\boldsymbol{r}_1, \ldots, \boldsymbol{r}_n)$, of the atom can be approximated by an antisymmetrized product of one-electron wavefunctions, $\phi(\boldsymbol{r}_i)$, referred to as *orbitals*. Starting from a basis of one-electron wavefunctions[2], linear combinations of the basis elements for each one-electron wavefunction are varied and at each step the orbital energy, i.e. expectation value of the single-electron Hamiltonian, is determined. The variation is then continued until the energy is minimal. This method, implemented in the GAMESS code package (Schmidt et al. [178]), has been used to calculate the theoretical electron wavefunctions for the reference atoms and for the molecules used in papers **I** and **II**.

Effectively, *orbitals* in a multi-electron atom have modified $R_{nl}(r)$ as compared to the solutions 1.16, whereas the $Y_{lm}(\theta, \varphi)$ are barely affected. This means that the main symmetry properties remain intact and the quantum numbers remain a valid concept.

Scattering states for the Coulomb potential 1.15 can again be written as a

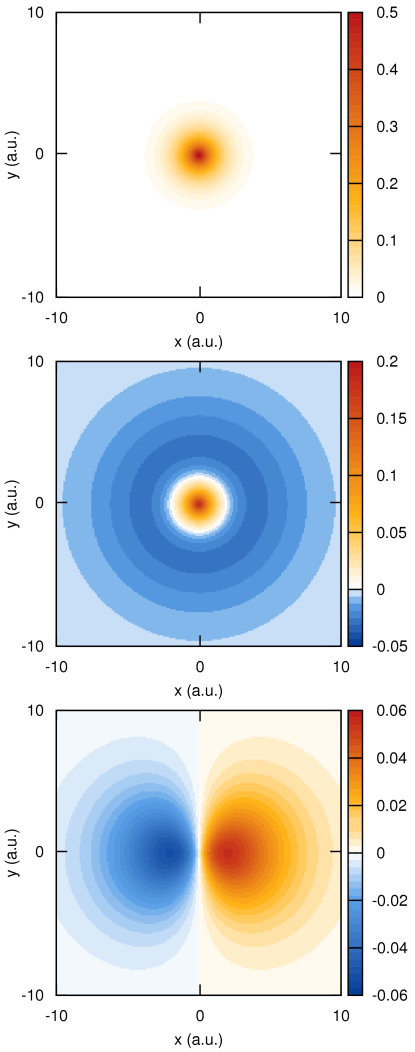

Figure 1.3. *Electron wavefunctions of the hydrogen atom.* ***Upper:*** *1s state, i.e.* $\phi_{100}(x, y, z = 0)$. ***Middle:*** *2s state, i.e.* $\phi_{200}(x, y, z = 0)$. ***Lower:*** *2p$_x$ state, i.e.* $\phi_{211}(x, y, z = 0)$.

[2]This could in principle be any complete basis set and the ϕ_{lmn} of the one-electron atom (equation 1.16) should be a good choice. In practice, often another more or less elaborate and at least approximately complete basis set is chosen, so as to make the iterations converge faster.

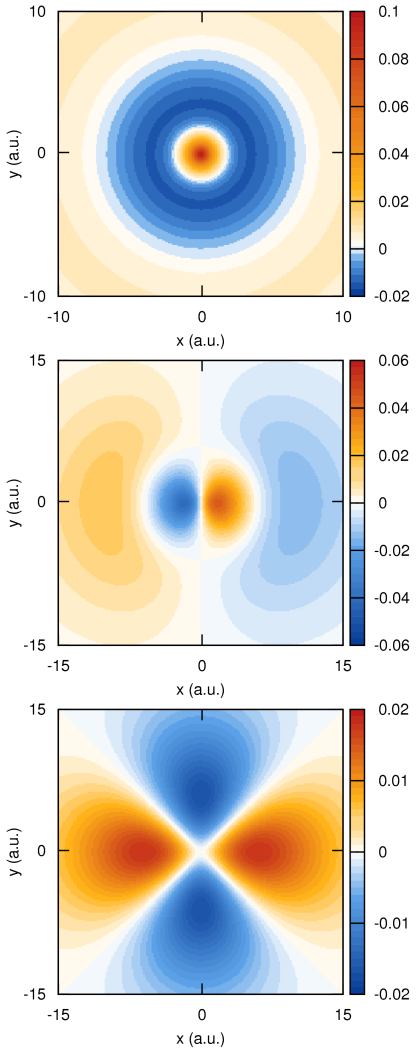

Figure 1.4. *Electron wavefunctions of the hydrogen atom.* ***Upper:*** *3s state, i.e.* $\phi_{300}(x, y, z = 0)$. ***Middle:*** *3p$_x$ state, i.e.* $\phi_{311}(x, y, z = 0)$. ***Lower:*** *3d$_{xy}$ state, i.e.* $\phi_{322}(x, y, z = 0)$. *Note, that the x and y-scales are changing.*

product of a radial and an angular part:

$$\phi_{klm}(\boldsymbol{r}) = R_{kl}(r)Y_{lm}(\theta, \varphi)\,, \tag{1.17}$$

where k is continuous and the associated energy eigenvalue is $E = k^2/2$. The quantum numbers $l \in \mathbb{N}^+$, and $m = -l \ldots, l$ remain discrete. $R_{kl}(r) \propto e^{ikr}(2kr)^l\, {}_1F_1(l + 1 + iZ/k; 2l + 2; 2ikr)$ takes a rather complicated form, with ${}_1F_1(a; b; c)$ being the confluent hypergeometric function. For large r, $R_{kl}(r) \xrightarrow{r\to\infty} \sin(kr - \frac{\pi}{2}l + \delta_l)/r$, i.e. k is identified as the asymptotic wave vector of a spherical wave, modulated by the spherical harmonics $Y_{lm}(\theta, \varphi)$. The functions ϕ_{klm} are referred to as *partial waves*, because they are a set of (infinitely many) degenerate eigenfunctions to the energy eigenvalue E. The phase $\delta_l = \arg[\Gamma(l + 1 + iZ/k)]$ is referred to as the partial wave (radial) phase shift and depends on k and hence on the energy E.

In practice, one is often concerned with an electron moving in the continuum in a certain direction with velocity $\boldsymbol{v} = \boldsymbol{k}$ (in atomic units, cp. equation 1.13), which is described by a superposition of (infinitely many) partial waves ϕ_{klm}:

$$\phi_{\boldsymbol{k}}(\boldsymbol{r}) \propto \sum_{l}^{\infty} \sum_{m=-l}^{l} i^l e^{-i\delta_l} Y^*_{lm}(\theta_{\boldsymbol{k}}, \varphi_{\boldsymbol{k}})\phi_{klm}(\boldsymbol{r})\,. \tag{1.18}$$

Here, $Y^*_{lm}(\theta_{\boldsymbol{k}}, \varphi_{\boldsymbol{k}})$ denotes the complex conjugate of the spherical harmonic and gives the probability amplitude for an electron in state ϕ_{klm} to move into the direction $\boldsymbol{k}/k$. The phase factor $e^{-i\delta_l}$ takes care that the boundary condition $\phi_{\boldsymbol{k}}(\boldsymbol{r}) \xrightarrow{r\to\infty} e^{i\boldsymbol{k}\cdot\boldsymbol{r}}$ be obeyed. The wavefunction then has a total energy dependent phase $\delta_{\boldsymbol{k}}$, given by the combined influence of the partial wave phase shifts δ_l.

These analytic equations are again only valid for a single electron in a Coulomb potential – computing scattering states for multi-electron atoms is possible only numerically. This still poses important problems today and most quantum chemistry codes are optimized for bound states in that they use basis sets of spatially very localized functions. If a pseudo-potential is available, finding scattering states is 'only' a matter of numerically integrating the Schrödinger equation, as was done for instance by (Wörner et al. [216]).

1.2.3 Molecular States

In molecules, the N nuclei can interact with each other and with each of the n electrons, and in general the Hamiltonian writes:

$$\mathcal{H} = \sum_{\alpha=1}^{N} -\frac{1}{2M_\alpha}\nabla^2_\alpha + \sum_{i=1}^{n} -\frac{1}{2}\nabla^2_i + \sum_{i<j}\frac{1}{r_{ij}} + \sum_{\alpha<\beta}\frac{Z_\alpha Z_\beta}{r_{\alpha\beta}} - \sum_{i,\alpha}\frac{Z_\alpha}{r_{i\alpha}}\,. \tag{1.19}$$

Here, the first two terms are the kinetic energy operators for the nuclei with masses M_α and for the electrons, respectively, whereas the remaining three terms describe the potential, $V(\boldsymbol{r}_\alpha, \boldsymbol{r}_i)$, felt by the nuclei at positions $\boldsymbol{r}_\alpha$ and the electrons at positions $\boldsymbol{r}_i$. Obviously, the number of degrees of freedom, and hence the dimensionality of the problem of solving the Schrödinger equation quickly becomes overwhelming. Yet, the quantum chemistry community has had impressive success in describing molecular properties (Hall [68], Lennard-Jones [113], Schneider and Merkel [179], Szabo and Ostlund [193]) by making smart approximations and great computational efforts.

The Born-Oppenheimer Approximation (BO) is one of the fundamental approximations made. The huge mass difference of nuclei and electrons allows in most cases to consider the positions of the nuclei to be fixed with respect to the electronic movement. The kinetic energy of the nuclei is thus

crossed out of the Hamiltonian 1.19 and the fourth term becomes just a constant depending on the fixed nuclear coordinates. The total wavefunction of the molecule can then be factorized into a nuclear and an electronic part: $\psi = \phi_{(\boldsymbol{r}_\alpha)}(\boldsymbol{r}_i)\chi(\boldsymbol{r}_\alpha)$. The subscript on the electronic part, ϕ, denotes that it obviously still parametrically depends on the – now fixed – nuclear coordinates in that the electrons move in the potential landscape given by the positions of the nuclei. For one such set of nuclear positions, suppose the Schrödinger equation (with the reduced Hamiltonian) can be solved to obtain the electronic wavefunction $\phi_{(\boldsymbol{r}_\alpha)}(\boldsymbol{r}_i)$ together with the corresponding energy eigenvalue $E_{(\boldsymbol{r}_\alpha)}$. Repeating this computation for a range of nuclear configurations, $(\boldsymbol{r}_\alpha)$, yields en electronic potential – referred to as the BO-potential $V_{\mathrm{BO}}(\boldsymbol{r}_\alpha) \equiv E_{(\boldsymbol{r}_\alpha)}(\boldsymbol{r}_\alpha)$ – and the electronic wavefunctions for each $(\boldsymbol{r}_\alpha)$. The nuclear part, $\chi(\boldsymbol{r}_\alpha)$, of the wavefunction now obeys the Schrödinger equation with the Hamiltonian (Fabre [41]):

$$\mathcal{H}_{\mathrm{nc}} = \sum_{\alpha=1}^{N} -\frac{1}{2M_\alpha}\nabla_\alpha^2 + V_{\mathrm{BO}}(\boldsymbol{r}_\alpha)\,. \tag{1.20}$$

We computed the eigenstates of this Hamiltonian and superposed them to describe the dynamics of H_2^+ and D_2^+ molecular ions in paper **IV**.

Having split off the nuclear degrees of freedom, one is still concerned with a multi-electronic wavefunction. The next level of approximation is thus again the HF approximation, i.e. replacing the third term in the Hamiltonian 1.19 by $\sum_i V_i^{\mathrm{el}}(\boldsymbol{r}_i)$, which allows factorization of the multi-electron wavefunction into single-electronic orbitals, $\phi(\boldsymbol{r}_i)$. The HF method, introduced in section 1.2.2, can then be applied to find molecular orbitals (MOs). Computing first the atomic orbitals and then combining these, each centered on their respective nucleus, the energy is minimized for varying combinations of atomic orbitals. Sometimes, the step of calculating atomic orbitals is omitted and functions out of another suitable basis set are directly combined on the different atoms to find the MOs. These other basis sets are chosen to be of a more 'computationally friendly' form – typically with Gaussian radial dependence, i.e. $\propto r^l \mathrm{e}^{-\alpha r^2}$ instead of the $\mathrm{e}^{-\alpha r}$-dependence of real atomic orbitals – which speeds up calculations significantly although one might need more basis elements. This is the method we applied in papers **I** and **II** and for the MOs shown in figures 1.5 and 1.6. The orbital of highest energy that is still occupied by an electron in the electronic ground state of the molecule (which is the one found by the HF algorithm), is called *lowest occupied molecular orbital* (HOMO). Counting down towards occupied orbitals with lower energies, one speaks of (HOMO-1), (HOMO-2), and so forth. The energetically *lowest unoccupied molecular orbital* is abbreviated (LUMO).

Linear Combination of Atomic Orbitals (LCAO) is the extremely useful and illustrative concept of constructing molecular orbitals by linearly combining atomic orbitals centered on the respective atoms. It was first proposed as early as 1929 by (Lennard-Jones [113]) and further generalized by (Roothaan [169]). It is applied in the HF method and, in principle, the basis set that should work best for the HF scheme is the set of all atomic orbitals of all atoms of the molecule. But even with a much reduced basis set, one can obtain at least qualitatively correct results.

Consider a molecule made up of two atoms of the same element – say **nitrogen, N_2**, the molecule relevant to papers **II**, **III** and **V** – and set the distance of the two nuclei to R with the inter-nuclear axis defining the x-direction. The reduced basis set to be used for the 'quick and dirty' LCAO are all occupied atomic orbitals, $\psi(\boldsymbol{r})$, but combining only $\psi(\boldsymbol{r})$ of the same kind to progressively build MOs: $\phi(\boldsymbol{r}) = c_{\mathrm{A}}\psi(\boldsymbol{r} + \hat{\boldsymbol{x}}R/2) + c_{\mathrm{B}}\psi(\boldsymbol{r} - \hat{\boldsymbol{x}}R/2)$. Since the molecule

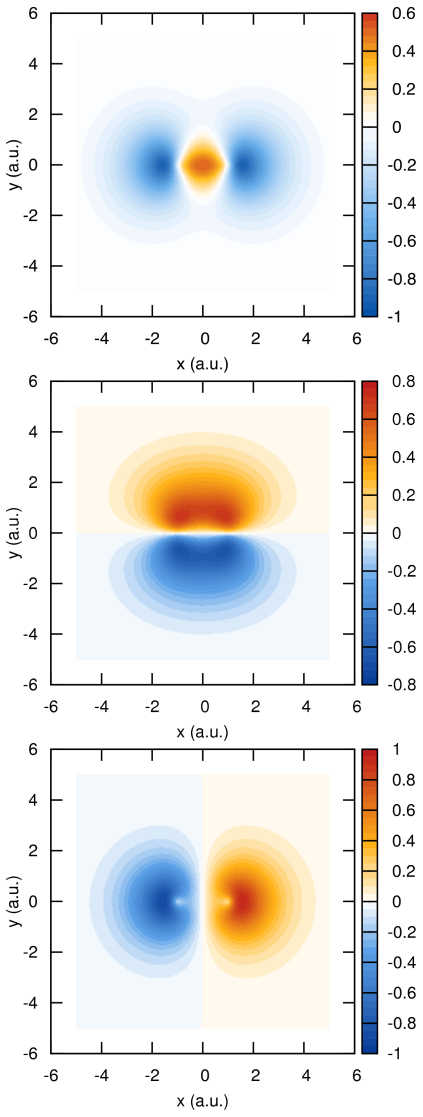

Figure 1.5. *Projection of N_2 orbitals onto the x-y-plane. The inter-nuclear axis is along the x-axis and the inter-nuclear distance is $R = 2$ a.u.. **Upper:** $\phi_{3\sigma_g}(\mathbf{r})$ – the HOMO of N_2. This MO is dominated by a $(\psi_{2p_x} - \psi_{2p_x})$ combination. **Middle:** One of the two degenerate $\phi_{1\pi_u}(\mathbf{r})$ – the HOMO-1 of N_2. This MO is dominated by a $(\psi_{2p_y} + \psi_{2p_y})$ combination. **Lower:** $\phi_{2\sigma_u}(\mathbf{r})$ – the HOMO-2 of N_2. This MO is dominated by a $(\psi_{2s} - \psi_{2s})$ combination.*

is symmetric, so must be the electron probability density, $\phi^*(\boldsymbol{r})\phi(\boldsymbol{r})$. It follows that $c_A = \pm c_B$. From every pair of atomic orbitals, an even and an odd molecular orbital can be formed. The modulus of the coefficients is then simply given by the normalization: $c_{A/B} = \pm 1/\sqrt{2(1+S)}$, with the overlap $S = \int \mathrm{d}\boldsymbol{r}\, \psi^*(\boldsymbol{r} + \hat{\boldsymbol{x}}R/2)\psi(\boldsymbol{r} - \hat{\boldsymbol{x}}R/2)$.

In the nitrogen atom with its seven electrons, following Pauli's principle[3], the occupied atomic orbitals are: $(1s)^2\ (2s)^2\ (2p)^3$, where, according to Hund's rule[4], the last three electrons occupy the $2p_x$, $2p_y$ and $2p_z$ orbitals, respectively. The simplest molecular orbitals resulting from these are thus[5]:

$$\phi_{1\sigma_g} = \psi_{1s} + \psi_{1s}\,, \tag{1.21}$$

$$\phi_{1\sigma_u} = \psi_{1s} - \psi_{1s}\,, \tag{1.22}$$

$$\phi_{2\sigma_g} = \psi_{2s} + \psi_{2s}\,, \tag{1.23}$$

$$\phi_{2\sigma_u} = \psi_{2s} - \psi_{2s}\,, \tag{1.24}$$

$$\phi_{1\pi_u} = \psi_{2p_{y/z}} + \psi_{2p_{y/z}}\,, \tag{1.25}$$

$$\phi_{3\sigma_g} = \psi_{2p_x} - \psi_{2p_x}\,. \tag{1.26}$$

Here, the greek letters σ and π denote the rotational symmetry about the inter-nuclear axis of the MO: σ-orbitals are completely invariant against rotation whereas π-orbitals are anti-symmetric against rotation by 180°. In other words: When viewed along the inter-nuclear axis, σ-orbitals look like an s-atomic-orbital, whereas π-orbitals look like a p-atomic-orbital. The subscripts g, for *gerade* (even), and u, for *ungerade* (odd), stand for the *parity* of the MO: If the MO is symmetric against $\boldsymbol{r} \to -\boldsymbol{r}$, with $\boldsymbol{r} = 0$ in the center of symmetry of the molecule, the MO is classified as even, if it is anti-symmetric, it is classified as odd. This obviously only makes sense for molecules for which a center of symmetry exists – for N_2, it is just half way between the two nuclei on the inter-nuclear axis. The different types of orbitals are then numbered according to increasing energy.

As a general rule, the energy of each type of MO (σ or π) constructed of orbitals of the same atomic shell, increases with the number of inter-nuclear nodes. The relative order of the σ and π-orbitals cannot be predicted readily – one has to calculate the expectation value of the single-electron Hamiltonian $\mathcal{H} = -\frac{1}{2}\nabla_i^2 + V_i^{\mathrm{el}}(\boldsymbol{r}_i) + V^{\mathrm{nc}}(\boldsymbol{r}_i)$, where $V^{\mathrm{nc}}(\boldsymbol{r}_i)$ denotes the last two terms of equation 1.19 for electron i and for a fixed nuclear configuration $(\boldsymbol{r}_\alpha)$. The MOs 1.21 to 1.26 are already ordered by increasing energies so obtained. The HOMO is obviously a linear combination of 2p-orbitals oriented along the inter-nuclear axis (i.e. their nodal planes are parallel to the y-z-plane), the HOMO-1 is built of two 2p-orbitals oriented perpendicular to the inter-nuclear axis, and so forth. The HOMO-1 is degenerate: it can be made up of two $2p_y$ or two $2p_z$ orbitals. The ground state electron configuration of the nitrogen molecule N_2 is thus: $(1\sigma_g)^2$, $(1\sigma_u)^2$, $(2\sigma_g)^2$, $(2\sigma_u)^2$, $(1\pi_u)^4$, $(3\sigma_g)^2$. A more precise calculation with the HF method shows that the overall shape of the orbitals is very well described by this construction, but for quantitatively satisfactory results, the basis set has to be enlarged: for σ/π-orbitals, one needs to include all atomic orbitals of σ/π symmetry with respect to the internuclear axis. Indeed, the N_2-HOMO, shown in figure 1.5, is found to be 'contaminated' by some 2s admixture, so the simple combination 1.26 should be replaced by

[3] No two electrons can occupy states with the same quantum numbers n,l,m and s in an atom, where $s = \pm 1/2$ is the spin of the electron. Each atomic orbital ψ_{nlm} can thus be occupied by a pair of electrons with opposite spins.

[4] To minimize the total energy, the *multiplicity* $2S + 1$, where S is the sum of all electron spins in the atom, has to be maximum.

[5] The normalization factors are ignored here for clarity.

$\phi_{3\sigma_g} = (\psi_{2p_x} - \psi_{2p_x}) - (\psi_{2s} + \psi_{2s})$. Such admixtures are much less important for the HOMO-1 and HOMO-2, also shown in figure 1.5. They agree very well with what is expected from the combinations 1.25 and 1.24, respectively.

For molecules with more than two atoms (possibly of different elements), the same principles apply but one has to use more atomic orbitals to construct MOs, which then spread over the entire molecule, not just two adjacent atoms. It is thus less simple to develop a "quick and dirty" picture for – say **carbon-dioxide**[6], **CO_2**, the molecule relevant to paper **I** – in the way just done for N_2. One can, however, interpret the results of a HF calculation for CO_2 with its 20 electrons in total, which yields the electron configuration $(1\sigma_g)^2$, $(1\sigma_u)^2$, $(2\sigma_g)^2$, $(3\sigma_g)^2$, $(2\sigma_u)^2$, $(4\sigma_g)^2$, $(3\sigma_u)^2$, $(1\pi_u)^4$, $(1\pi_g)^2$. The three energetically highest orbitals are shown in figure 1.6. The HOMO is the second π-orbital to occur and thus has one internuclear node. For this structure to appear, it must be dominated by a $\psi^O_{2p_{y/z}} - \psi^O_{2p_{y/z}}$ contribution, with oxygen atomic orbitals ψ^O – which is confirmed by the coefficients found by the HF algorithm. The HOMO-1, as the first π-orbital, has no internuclear nodes and is built approximately like $\psi^O_{2p_{y/z}} + \psi^C_{2p_{y/z}} + \psi^O_{2p_{y/z}}$. The HOMO-2 is the fourth σ-orbital made up from $n = 2$ atomic orbitals[7], hence the three inter-nuclear nodes. It turns out to be a fairly complicated combination[8] of $\psi^O_{2p_x} - \psi^O_{2s} - \psi^C_{2p_x} - \psi^O_{2s} + \psi^O_{2p_x}$.

Scattering states of electrons in molecules, are, for the same reason as for multi-electron atoms, extremely difficult to compute. The applied methods have been developed by the quantum chemistry community for a quite long time and are based on advanced scattering theory, as for instance described by (Gianturco and Lucchese [57], Lucchese et al. [121]). The knowledge of proper scattering states turns out to be of great importance for attosecond physics with molecules, as will become clear in the course of this thesis, and several groups bringing together specialists on laser-matter interaction and quantum chemistry are working on this subject. So far, only few authors have reported results (Le et al. [102, 103], Walters et al. [215]).

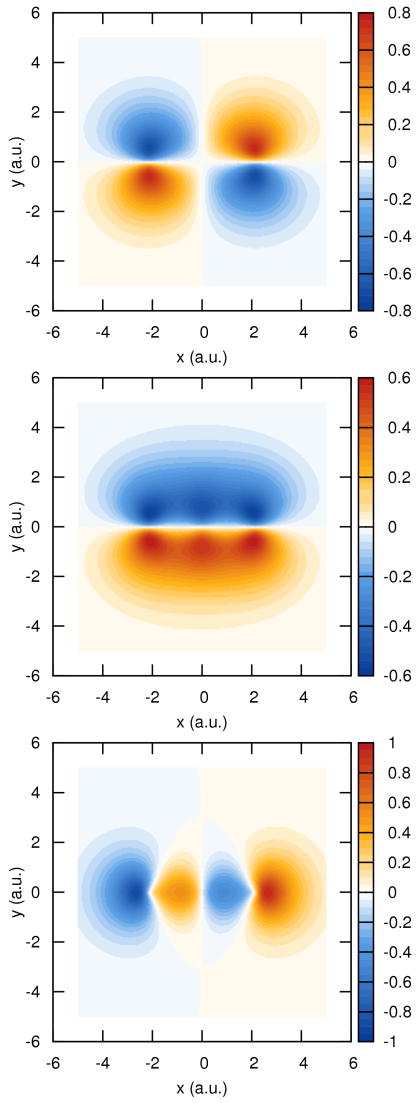

Figure 1.6. *Projection of CO_2 orbitals onto the x-y-plane. The inter-nuclear axis is along the x-axis and the inter-nuclear distance is $R = 4.3$ a.u.. **Upper:** One of the two degenerate $\phi_{1\pi_g}(\mathbf{r})$ – the HOMO of CO_2. This MO is dominated by a $(\psi^O_{2p_y} - \psi^O_{2p_y})$ combination. **Middle:** One of the two degenerate $\phi_{1\pi_u}(\mathbf{r})$ – the HOMO-1 of CO_2. This MO is dominated by a $(\psi^O_{2p_y} + \psi^C_{2p_y} + \psi^O_{2p_y})$ combination. **Lower:** $\phi_{3\sigma_u}(\mathbf{r})$ – the HOMO-2 of CO_2. This MO is dominated by a $(\psi^O_{2p_x} - \psi^O_{2s} - \psi^C_{2p_x} - \psi^O_{2s} + \psi^O_{2p_x})$ combination.*

1.3 Electron Dynamics

So far, the considered electrons have only felt a static potential. Speaking of *attosecond* physics, one of course thinks of extremely rapid dynamics, induced, and in the ideal case controlled, by a rapidly varying potential such as the one of a laser field. The theoretical tools most important for attophysics are thus the ones that help solve the time-dependent Schrödinger equation (TDSE):

$$i\frac{\partial}{\partial t}\psi(t) = \mathcal{H}(t)\psi(t) \tag{1.27}$$

In general, this is possible only numerically and in the waste majority of cases, the single-active-electron approximation is adopted. The laser field strengths typical in attosecond physics and the photon numbers per unit volume associated with them completely justify the classical treatment of the laser-electron interaction.

1.3.1 Tunnel ionization

Tunnel ionization is maybe the fundamental process of attophysics as it provides the extreme non-linearity required to push the limits of temporal reso-

[6] CO_2 is a linear molecule: O=C=O.

[7] The first three MO will most likely be combinations of the 1s orbitals of the three atoms.

[8] Note that we omit here the exact value of the coefficients found by the HF algorithm and simply list those orbitals of the basis that contribute significantly with the sign of their coefficient.

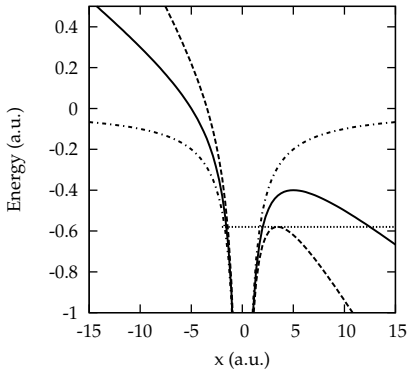

Figure 1.7. *Potential (1.28) with $Z_{\text{eff}} = 1$ and E=0 (dash-dotted line), E=-0.04 a.u. (solid line) and E=-0.084 a.u. (dashed line), corresponding to the barrier suppression limit for a single active electron in a bound state with energy -0.58 a.u., marked by the horizontal dotted line.*

lution into the attosecond regime. This section will not describe tunnel ionization in detail but merely define a parameter range where tunnel ionization occurs and plays an essential role in the electron dynamics.

When an atom is subjected to a strong electric field, $\boldsymbol{E} = \hat{\boldsymbol{x}}E$, the total potential felt by the single active electron writes (in length gauge):

$$V(x) = V_0(x) + xE\,, \tag{1.28}$$

where $V_0(x)$ is an effective binding potential resulting from the Coulomb potential and the shielding by the remaining electrons. For the following, assume that $V_0(x) = -Z_{\text{eff}}/|x|$, i.e. the remaining electrons shield the nucleus in a spherically symmetric way and the outermost electron sees an effective positive charge of Z_{eff}. As seen in figure 1.7, the electric field lowers the potential on one side and at some finite distance, $V(x)$ falls below the binding energy, $-I_{\text{p}}$, of the electron. There is thus a finite probability that the electron tunnels through the potential barrier into a continuum state. Precisely speaking, the wavefunction of the electron falls exponentially within the classically forbidden region where $V(x) > -I_{\text{p}}$, but as this region has a finite width, the wavefunction will have a finite amplitude after the barrier. How much of the wavefunction tunnels into the continuum obviously depends on the height and width of the barrier and on the time during which the barrier is lowered. The two extreme cases are $E = 0$ when the probability is zero, and a field strength E_{BS}, that completely suppresses the potential barrier, i.e. $V(x) \leq -I_{\text{p}}$ everywhere on one side, represented in figure 1.7 by the dashed line. One then speaks of *barrier suppression ionization* and the rate at which the electron wavefunction tunnels into the continuum increases drastically. This case is reached when the potential barrier maximum at distance $x_0 = \sqrt{Z_{\text{eff}}/E}$ is lowered to $V(x_0) = -I_{\text{p}}$. This directly leads to the field strength and corresponding intensity of

$$E_{\text{BS}} = \frac{I_{\text{p}}^2}{4Z}\,, \qquad I_{\text{BS}} = \frac{I_{\text{p}}^4}{16Z^2}\,, \qquad I_{\text{BS}}[\text{W/cm}^2] = 4\times10^9\,\frac{I_{\text{p}}^4[\text{eV}]}{Z^2}\,. \tag{1.29}$$

For the rare gases krypton and argon, where $Z_{\text{eff}} = 1$, this implies $I_{\text{BS}}^{\text{Kr}} = 1.5\times10^{14}\,\text{W/cm}^2$ and $I_{\text{BS}}^{\text{Ar}} = 2.5\times10^{14}\,\text{W/cm}^2$. The values in figure 1.7 correspond to those for argon.

As soon as these intensities are approached, the tunnel ionization rate becomes significant. Practically, this is possible by focusing a laser, the instantaneous electric field of which writes $\boldsymbol{E}(t) = \hat{\boldsymbol{x}}E_0\cos(\omega_0 t)$, into a gas of atoms. (Keldysh [91]) defined an adiabaticity parameter, γ, as the ratio of the time the electron would need to cross the barrier and the laser period $T_0 = 2\pi/\omega_0$ divided by[9] 4π. Approximating the barrier width as I_{p}/E and assuming a mean velocity of the electron of $\sqrt{2I_{\text{p}}}$, one finds

$$\gamma = \frac{\omega_0}{E}\sqrt{2I_{\text{p}}} = \sqrt{\frac{I_{\text{p}}}{2U_{\text{P}}}}\,, \tag{1.30}$$

where $U_{\text{P}} = E^2/4\omega_0^2$ is the ponderomotive potential, i.e. the mean quiver energy of a free electron in a laser field. For a laser field with strong amplitude and low frequency, the potential barrier is low during a long time and $\gamma \ll 1$. As long as the laser field remains below E_{BS}, one can thus speak of the *tunneling regime* of ionization. If, on the contrary, the laser field is rather weak and its frequency high, $\gamma \gg 1$ and tunnel ionization cannot be efficient. As long as

[9] This is an arbitrary choice that just simplifies the final formula for γ – but it is plausible as it defines a small fraction of T_0 around the laser field maximum, during which the potential barrier can be assumed to be suppressed sufficiently.

$\omega < I_p$, only the absorption of several laser photons can transfer the electron into the continuum and one speaks of the *multi-photon regime* of ionization. In the experiments presented in this thesis, a laser of 800 nm wavelength focused to $\sim 10^{14}\,\mathrm{W/cm^2}$ and atoms or molecules with $I_p \approx 15\,\mathrm{eV}$ are used. This yields $\gamma \lesssim 1$, corresponding to the tunneling regime with a low ionization rate.

The tunneling rate, Γ, depends on the probability density at the 'exit' of the tunnel. Since within the forbidden region, the wavefunction decreases exponentially, one can expect an $\exp[-I_p/E]$-dependence of the tunneling rate (with the above estimate of I_p/E for the barrier width). A proper calculation for the Coulomb potential, done by (Ammosov et al. [3], Gamow [48], Gurney and Condon [65]) leads to a very similar answer: $\Gamma \propto \exp[-2(2I_p)^{3/2}/(3E)]$.

1.3.2 Semi-classical Description of High-order Harmonic Generation

Virtually any attophysics experiment – the ones presented in this thesis make no exception – involves the process of high-order harmonic generation (HHG). Its theoretical description in three steps (Corkum [22], Schafer et al. [176]), introduced already in the introductory chapter, is probably the most often used theoretical tool. Even in its semi-classical formulation, it allows qualitative understanding of the relevant physics and does, in some aspects, even yield quantitative agreement with the experiment.

In the *first step*, at some time t_i, tunnel ionization leads to an electron being "born" in the continuum[10] with initially zero velocity. From this moment on, the electron is considered as a classical point charge, and during the *second step* one considers the driving laser field, $\boldsymbol{E}(t) = \hat{\boldsymbol{x}} E_0 \cos(\omega_0 t)$, to completely govern its evolution. The classical equation of motion is

$$\ddot{x}(t) = -E_0 \cos(\omega_0 t)\,. \tag{1.31}$$

The initial conditions are $\dot{x}(t_i) = 0$ and $x(t_i) = 0$. The second of these is a simplification neglecting the finite distance from the nucleus $x_0 \approx 10\,\mathrm{a.u.} = 0.5$ nm (cp. figure 1.7) at which the electron is "born". Although the electron will follow trajectories leading it only a few nm away from its parent ion, it is not worth worrying about this, since at this birth instant, the electron has so little kinetic energy (actually, in this model none at all), that its de Broglie wavelength is much larger than the 'problem' anyhow. Integration of equation 1.31 then leads to

$$\dot{x}(t) = -\frac{E_0}{\omega_0}\left[\sin(\omega_0 t) - \sin(\omega_0 t_i)\right]\,, \tag{1.32}$$

$$x(t) = \frac{E_0}{\omega_0^2}\left[\cos(\omega_0 t) - \cos(\omega_0 t_i)\right] + \frac{E_0}{\omega_0}\sin(\omega_0 t_i)(t - t_i)\,. \tag{1.33}$$

Equation 1.33 shows that not for every electron birth time, t_i, does the electron trajectory lead back to the parent ion at $x = 0$ – the slope of the second member could dominate the trajectory and the electron just drifts away. For $0 \le t_i \le \pi/2\omega_0$, however, the trajectory does reach $x = 0$ again and by numerically finding these roots, one determines pairs of ionizations times, t_i and recollision times t_r. Obviously, there may be several roots, i.e. recollisions, in the trajectory corresponding to one t_i. We will , however, only consider the first recollision, because the EWP will spread during propagation (cp. section

[10] The electrons we are concerned with – the ones that eventually recollide with the parent ion – are never really *ionized* because this would mean they remain in the continuum after the process is over. In fact, they must be considered *quasi-bound*. It is thus more precise to speak of "birth in the continuum" instead of ionization.

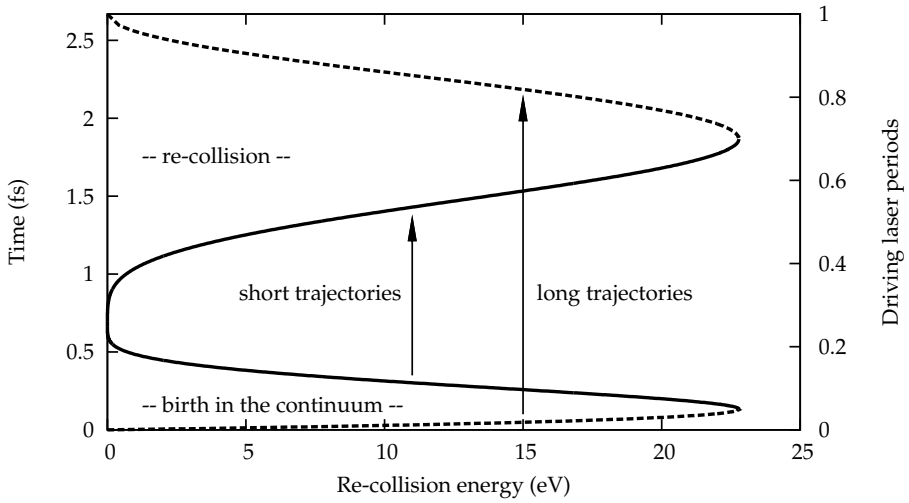

Figure 1.8. *Classical calculation of ionization and recollision times as a function of the electron recollision energy, for an 800 nm laser and an intensity of* $I = 1.2 \times 10^{14}$ *W/cm*^{2}*. The electric field of the driving laser has a cosine time-dependence, i.e. time zero marks the field maximum. Full and dashed lines mark the short and long trajectories, respectively.*

1.1.3), also in the direction perpendicular to its motion, thus reducing the importance of the subsequent recollisions. Phase matching effects further reduce the contribution of longer trajectories to the macroscopic signal measured in experiments (Antoine et al. [4]).

For every pair $(t_\mathrm{i}, t_\mathrm{r})$, the kinetic energy at recollision, $\dot{x}(t_\mathrm{r})^2/2$ can be determined. Figure 1.8 shows a plot of the ionization times, t_i, and recollision times, t_r, as a function of the associated electron energy at the instant of recollision. With every recollision energy, a long (dashed lines) and a short trajectory (solid lines) are associated, which join for the very highest recollision energy. Electrons are born in the continuum during the first quarter period of the driving laser. The short trajectories then lead to recollision mainly after the subsequent laser field minimum (i.e. after $T_0/2$) and electrons with the highest return energies recollide at $3T_0/4$, i.e. at a zero-crossing of the driving laser field. In the last quarter period, the long trajectories recollide.

At recollision, the electrons may recombine to the ground state, which is the *third step* of the three-step model. The emitted XUV photon has an energy of $\dot{x}(t_\mathrm{r})^2/2 + I_\mathrm{p}$. The highest of these energies turns out to be $q_\mathrm{max}\omega_0 = I_\mathrm{p} + 3.2U_\mathrm{P}$, which is the intensity and medium dependent cut-off law, found empirically by (Krause et al. [97]).

From figure 1.8, one can infer that recollision and thus XUV emission takes place only during a fraction of the driving laser cycle, i.e. in the form of extremely short XUV bursts. Furthermore, different spectral components are emitted at different instants, implying a chirp of the XUV emission, which is of different sign for the short and long trajectories. For now it is only plausible that the calculated recollision times correspond to the group delay of the XUV bursts, but in the following section, it will become clear that this is indeed the case.

It is also clear from these considerations that for efficient HHG, the driving laser must be linearly polarized. A small perpendicular component of the electric field that is π out of phase with the principle component, will lead to a perpendicular component of the electron trajectory, that drives the electron away from the parent ion. Only if there is a non-zero perpendicular compo-

nent in the initial electron velocity at birth in the continuum, the trajectory may be closed. We simulate this case in section 3.2.2. The probability for such a component is, however, very low, and the HHG signal will rapidly drop with increasing ellipticity.

The three-step process is repeated every half-cycle of the driving laser field, i.e. with a $T_0/2$ periodicity. The driving laser field obviously has a different sign in every other half-cycle, implying a sign change in the XUV emission. In a spectrometer, the contributions of the individual XUV bursts in the attosecond pulse train (APT) will interfere and one is easily convinced[11] that the resulting spectrum consists of peaks at the odd harmonic orders of the driving laser. The finite duration of the XUV emission imposes an envelope in the time domain and consequently a broadening of the peaks in the spectral domain.

1.3.3 Quantum Description of High-order Harmonic Generation

The semi-classical model sheds light on many experimental observations and provides an easily comprehensible framework. However, the use of classical physics is hardly justified and instead of a point-shaped electron flying along a trajectory and releasing a flash of light as it bounces back on its parent ion, the correct picture would be an electron wavefunction, bound in an atom or molecule, which is drastically deformed by a strong laser field. Part of the wavefunction is pulled away from the binding potential through the classically forbidden barrier and eventually interferes with the part left in the bound state.

With the constraints mentioned in relation to equation 1.27, the TDSE for the single active electron writes (in length gauge):

$$\mathrm{i}\frac{\partial}{\partial t}\psi(\boldsymbol{r},t) = \left[-\frac{1}{2}\nabla^2 + V_0(\boldsymbol{r}) + \boldsymbol{r}\cdot\boldsymbol{E}(t)\right]\psi(\boldsymbol{r},t)\,, \tag{1.34}$$

where $\boldsymbol{E}(t)$ is the electric field of the laser and $V_0(\boldsymbol{r})$ represents the interaction of the electron with the nucleus (or nuclei in the case of a molecule) shielded by the remaining bound electrons, which will in the following be referred to as *the core*. Initially, the atom/molecule is supposed to be in its ground state, i.e. $\psi(\boldsymbol{r}, t = 0)$ is given by the energetically highest orbital, $\psi_0(\boldsymbol{r})$, of this ground state.

The direct numerical solution of this equation is possible, using e.g. a pseudo-potential for $V_0(\boldsymbol{r})$. Suitable approximations can, however, make possible a fully analytical solution which will make it easier to shed light on the physics involved than an interpretation of a numerical solution could. Such an approximative solution has been demonstrated by (Lewenstein et al. [117]) shortly after the semi-classical model was proposed. The derivation is based on the strong-field approximation (SFA) of the TDSE (Keldysh [91]), which makes the following assumptions:

(i) Only the ground state of the atom/molecule is considered, all other bound states are neglected.

(ii) The influence of the core-potential $V_0(\boldsymbol{r})$ on the electron in the continuum is neglected, i.e. it is assumed to be small against the laser-electron interaction Hamiltonian $\boldsymbol{r}\cdot\boldsymbol{E}(t)$.

[11] Write, in the time domain, the pulse train as a convolution of one XUV burst with a variant of the dirac comb: $\Delta(t) = \sum_{n=-\infty}^{+\infty}(-1)^n\delta(t - nT_0/2)$. This comb-function is even in t and T_0-periodic (mind the sign change!). It can thus be expanded into a Fourier series $\sum_{m=1}^{\infty} a_m \cos[m(2\pi/T_0)t]$, with coefficients $a_m = 2/T_0 \int_{t_0}^{t_0+T_0} \Delta(t)\cos[m(2\pi/T_0)t]\mathrm{d}t = 2/T_0[1 - \cos(m\pi)]$, which turn out to be non-zero only for odd m.

The laser field has to be sufficiently strong for (ii) to hold, and of sufficiently low frequency for assumption (i). These conditions overlap with those defining the tunneling regime (cp. section 1.3.1). Assuming for simplicity the ground state depletion to be negligible, i.e. a laser intensity $I < I_{\mathrm{BS}}$, we can now make the ansatz

$$\psi(\boldsymbol{r},t) = \mathrm{e}^{\mathrm{i}I_{\mathrm{p}}t}\left[\psi_0(\boldsymbol{r}) + \int \frac{\mathrm{d}^3k}{(2\pi)^3} a(\boldsymbol{k},t)\mathrm{e}^{\mathrm{i}\boldsymbol{k}\cdot\boldsymbol{r}}\right], \tag{1.35}$$

i.e. the electron is in a superposition of states: mainly in its bound state $\psi_0(\boldsymbol{r})$ with energy $-I_{\mathrm{p}}$, but with a small time-dependent amplitude $a(\boldsymbol{k},t)$ also in continuum states $|\boldsymbol{k}\rangle$, which are written here as plane waves because the core-potential has been neglected for these continuum electrons. The amplitudes, $a(\boldsymbol{k},t)$, are complex valued and their phase is defined relative to that of the bound part, $\psi_0(\boldsymbol{r})$. Introducing this ansatz into the TDSE 1.34 and projecting onto the space spanned by $\psi_0(\boldsymbol{r})$ and the $|\boldsymbol{k}\rangle$ states, transforms the TDSE into an equation for $a(\boldsymbol{k},t)$, which can be solved analytically. This yields an expression for the time-dependent electron wavefunction $\psi(\boldsymbol{r},t)$ containing the complete information about the system.

Extracting the XUV spectrum – different forms for the dipole operator

The complex XUV spectrum $\boldsymbol{\epsilon}_{\mathrm{XUV}}(\omega)$ radiated by a single atom or molecule is given by the Fourier transform $\mathcal{F}_{t\to\omega}$ of the dipole acceleration. The latter should be obtained as the expectation value of the dipole acceleration operator $\hat{\mathbf{a}} = -\nabla_{\boldsymbol{r}}V(\boldsymbol{r})$ ('acceleration form'):

$$\boldsymbol{\epsilon}_{\mathrm{XUV}}(\omega) = \mathcal{F}_{t\to\omega}\left[\langle\psi(\boldsymbol{r},t)\,|\hat{\mathbf{a}}|\,\psi(\boldsymbol{r},t)\rangle\right]. \tag{1.36}$$

Via the Ehrenfest theorem, one can replace $\langle\hat{\mathbf{a}}\rangle$ in equation 1.36 by $\mathrm{d}/\mathrm{d}t\langle\hat{\mathbf{p}}\rangle$ ('velocity form'), where $\hat{\mathbf{p}} = -\mathrm{i}\nabla_{\boldsymbol{r}}$ is the dipole momentum operator. Alternatively, $\langle\hat{\mathbf{a}}\rangle$ may be replaced by $\mathrm{d}^2/\mathrm{d}t^2\langle\hat{\boldsymbol{r}}\rangle$, where $\hat{\boldsymbol{r}} = \boldsymbol{r}$ is the dipole moment operator ('length form'). Depending on the choice of form for the dipole operator, $\hat{\mathbf{d}}$, equation 1.36 thus transforms to[12]

$$\boldsymbol{\epsilon}_{\mathrm{XUV}}(\omega) = \mathcal{F}_{t\to\omega}\left[\frac{\mathrm{d}}{\mathrm{d}t}\langle\psi(\boldsymbol{r},t)\,|\hat{\mathbf{p}}|\,\psi(\boldsymbol{r},t)\rangle\right] = \mathrm{i}\omega\mathcal{F}_{t\to\omega}\left[\langle\psi(\boldsymbol{r},t)\,|\hat{\mathbf{p}}|\,\psi(\boldsymbol{r},t)\rangle\right] \tag{1.37}$$

$$\boldsymbol{\epsilon}_{\mathrm{XUV}}(\omega) = \mathcal{F}_{t\to\omega}\left[\frac{\mathrm{d}^2}{\mathrm{d}t^2}\langle\psi(\boldsymbol{r},t)\,|\hat{\mathbf{r}}|\,\psi(\boldsymbol{r},t)\rangle\right] = -\omega^2\mathcal{F}_{t\to\omega}\left[\langle\psi(\boldsymbol{r},t)\,|\hat{\mathbf{r}}|\,\psi(\boldsymbol{r},t)\rangle\right] \tag{1.38}$$

The equivalence of these forms only holds if the continuum wave packet in equation 1.35 is composed of exact scattering wavefunctions, i.e. eigenfunctions of the same Hamiltonian as the bound state wavefunction $\psi_0(\boldsymbol{r})$. Within the plane wave approximation for the continuum, however, these three forms are *not* equivalent any more and one cannot say which of the three is *a priori* the best choice. Until recently, it was the length form, i.e. equation 1.38, that was used almost exclusively, including Lewenstein's original paper. In connection to HHG in molecules, this matter is now being debated: (Gordon and Kärtner [61]) claim that the acceleration form should be preferred whereas (Chirilă and Lein [16]) showed that the velocity form yields very reliable results, while being easier and faster to evaluate than the acceleration form.

[12] $$\frac{\mathrm{d}}{\mathrm{d}t}f(t) = \frac{\mathrm{d}}{\mathrm{d}t}\int f(\omega)\mathrm{e}^{\mathrm{i}\omega t}\mathrm{d}\omega = \int(\mathrm{i}\omega)f(\omega)\mathrm{e}^{\mathrm{i}\omega t}\mathrm{d}\omega = \mathcal{F}_{\omega\to t}[\mathrm{i}\omega f(\omega)].$$

Whatever the choice of form for the dipole operator, $\hat{\mathbf{d}}$, the time dependent dipole moment / momentum / acceleration $\boldsymbol{d}(t) = \langle\psi(\boldsymbol{r},t)|\hat{\mathbf{d}}|\psi(\boldsymbol{r},t)\rangle$, writes:

$$\boldsymbol{d}(t) = -\mathrm{i}\int_0^t \mathrm{d}t_\mathrm{i}\int \mathrm{d}^3\boldsymbol{p}\,\boldsymbol{d}^*_{\boldsymbol{p}+\boldsymbol{A}(t)}\,\mathrm{e}^{\mathrm{i}S(\boldsymbol{p},t_\mathrm{i},t)}\,\boldsymbol{E}(t_\mathrm{i})\cdot\boldsymbol{d}^\mathrm{L}_{\boldsymbol{p}+\boldsymbol{A}(t_\mathrm{i})}\,. \tag{1.39}$$

Note that in this expression, only bound-continuum cross-terms are considered. Continuum-continuum transitions, which do not contribute to HHG, are omitted, as is the time-independent $\langle\psi_0(\boldsymbol{r})|\hat{\mathbf{d}}|\psi_0(\boldsymbol{r})\rangle$, which anyway vanishes for bound states with defined parity, which is the case for atoms and symmetric molecules.

$$S(\boldsymbol{p},t_\mathrm{i},t) = -\int_{t_\mathrm{i}}^t \mathrm{d}t''\left[\frac{[\boldsymbol{p}+\boldsymbol{A}(t'')]^2}{2}+I_\mathrm{p}\right] \tag{1.40}$$

is the action of the continuum electron, $\boldsymbol{p} = \boldsymbol{k} - \boldsymbol{A}(t_\mathrm{i})$ is its canonical momentum and $\boldsymbol{A}(t) = -\int_{-\infty}^t \boldsymbol{E}(t')\mathrm{d}t'$ is the vector potential of the laser field. In equation 1.39, the three steps of the semi-classical approach (section 1.3.2) are recovered as three factors in the integrand as follows: (i) At time t_i, part of the electron wavefunction makes a transition to a continuum state with canonical momentum $\boldsymbol{p}$, the transition amplitude for which is given by $\boldsymbol{E}(t_\mathrm{i})\cdot\boldsymbol{d}^\mathrm{L}_{\boldsymbol{p}+\boldsymbol{A}(t_\mathrm{i})}$. Here, $\boldsymbol{d}^\mathrm{L}_{\boldsymbol{p}+\boldsymbol{A}(t_\mathrm{i})} = \langle\boldsymbol{p}+\boldsymbol{A}(t_\mathrm{i})|\hat{\boldsymbol{r}}|\psi_0(\boldsymbol{r})\rangle$ is a dipole matrix element (DME) in *length form* since the operator is not selected by our choice of $\hat{\mathbf{d}}$, but comes from the length gauge interaction Hamiltonian $\boldsymbol{r}\cdot\boldsymbol{E}(t)$ in the TDSE 1.34. (ii) In the continuum, the electron propagates under the influence of the laser field only, acquiring a phase relative to the ground state of $S(\boldsymbol{p},t_\mathrm{i},t)$. (iii) At time t, the electron has a mechanical momentum $\boldsymbol{k} = \boldsymbol{p}+\boldsymbol{A}(t)$ and recombines with the core, the amplitude of which is given by the matrix element $\boldsymbol{d}^*_{\boldsymbol{p}+\boldsymbol{A}(t)} = \langle\psi_0(\boldsymbol{r})|\hat{\mathbf{d}}|\boldsymbol{p}+\boldsymbol{A}(t)\rangle$, which is the only term in equation 1.39, that depends on the choice for $\hat{\mathbf{d}}$.

According to equations 1.36 to 1.38, the complex XUV spectrum, $\boldsymbol{E}_\mathrm{XUV}(\omega)$, is proportional to the Fourier transform of equation 1.39:

$$\boldsymbol{\epsilon}_\mathrm{XUV}(\omega) \propto \int \boldsymbol{d}(t)\,\mathrm{e}^{\mathrm{i}\omega t}\mathrm{d}t = \int \mathrm{d}t\int_0^t \mathrm{d}t_\mathrm{i}\int \mathrm{d}^3\boldsymbol{p}\,\boldsymbol{b}(t,t_\mathrm{i},\boldsymbol{p})\,\mathrm{e}^{\mathrm{i}\varphi_\mathrm{XUV}(t,t_\mathrm{i},\boldsymbol{p})}\,, \tag{1.41}$$

with

$$\varphi_\mathrm{XUV}(t,t_\mathrm{i},\boldsymbol{p}) = \omega t + S(\boldsymbol{p},t_\mathrm{i},t)\,, \tag{1.42}$$

where $\boldsymbol{b}(t,t_\mathrm{i},\boldsymbol{p}) = \boldsymbol{d}^*_{\boldsymbol{p}+\boldsymbol{A}(t)}\,\boldsymbol{E}(t_\mathrm{i})\cdot\boldsymbol{d}^\mathrm{L}_{\boldsymbol{p}+\boldsymbol{A}(t_\mathrm{i})}$ is the amplitude of each contribution. Equation 1.41 is an integral over infinitely many quantum paths, i.e. triplets of canonical momentum, $\boldsymbol{p}$, ionization times, t_i and recombination times, t, which makes its evaluation in general very costly.

Saddle-point approximation

The quintuple integral in equation 1.41 can be drastically simplified, and the analogy to the semi-classical model can at the same time be driven further, by realizing that those contributions for which the phase φ_XUV is stationary with respect to the variables $(t,t_\mathrm{i},\boldsymbol{p})$ will largely dominate, whereas a rapidly varying phase will make the contributions of most quantum paths vanish. In analogy to the classical principle of stationary action, one can thus find three equations, corresponding to the derivative of φ_XUV with respect to the

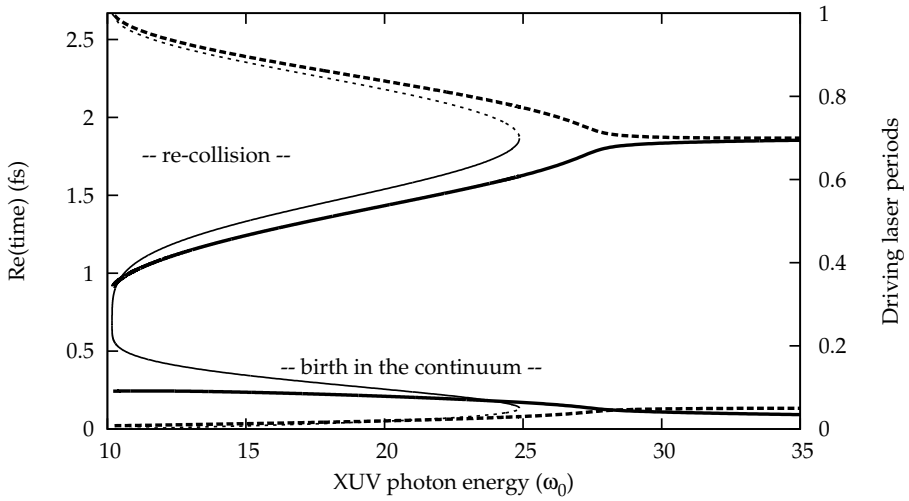

Figure 1.9. *Real part of ionization and recombination times as a function of the harmonic order, i.e. the emitted XUV photon energy in units of the driving laser photon energy, obtained by solving the coupled equations 1.43 to 1.45 for HHG in argon, $I_p = 15.7$ eV, with an 800 nm laser and an intensity of $I = 1.2 \times 10^{14}$ W/cm^2. The electric field of the driving laser has a cosine time-dependence, i.e. time zero marks the field maximum. Full and dashed lines correspond to the short and long trajectories, respectively. The thin lines shown again the results of the classical calculation from figure 1.8.*

variables t_i, $\boldsymbol{p}$ and $t = t_r$:

$$\frac{[\boldsymbol{p} + \boldsymbol{A}(t_i)]^2}{2} + I_p = 0 \tag{1.43}$$

$$\int_{t_i}^{t_r} [\boldsymbol{p} + \boldsymbol{A}(t')]\, dt' = 0 \tag{1.44}$$

$$\frac{[\boldsymbol{p} + \boldsymbol{A}(t_r)]^2}{2} + I_p = \omega \tag{1.45}$$

Each of these three equation reflects one of the three steps of the semi-classical model: (1.43) implies that the kinetic energy of the electron at the time of birth in the continuum is negative, which is classically impossible, but can be reached mathematically by a complex valued ionization time, t_i. Its imaginary part can be seen as a trace of the tunnel ionization process. (1.44) means simply that the dominating quantum paths correspond to closed trajectories. Finally, (1.45) states that the energy of the emitted XUV photon is given by the sum of the ionization potential and the kinetic energy of the continuum electron at the (complex valued) recombination instant, t_r. Solving these three coupled equations yields triplets, $(t_i, t_r, \boldsymbol{p})$, allowing e.g. to plot the real part of ionization and recombination times as a function of the XUV photon energy, shown in figure 1.9. This calculation was done by Armelle de Bohan and Thierry Auguste.

The saddle-point equations 1.43 to 1.45 select a finite number of quantum paths contributing to each frequency component of the atomic/molecular dipole and thus of the XUV emission. The different quantum paths are ordered according to the continuum electron excursion time, $\tau_n = t_r^n - t_i^n$, and the first two of these, τ_1 and τ_2, shown in figure 1.9, can be identified as the short and long trajectory found in the classical treatment. The simple semi-classical model turns out to be in reasonable agreement but, obviously, the more rigorous quantum-mechanical calculation yields a more precise description – notably in the cut-off region, i.e. the classically forbidden region of the

highest photon energies. The major difference must come from the tunneling step which can obviously not be treated classically. With the finite number of saddle-point trajectories, equation 1.41 can be re-written as a sum

$$\boldsymbol{\epsilon}_{\mathrm{XUV}}(\omega, I) = \sum_n \boldsymbol{b}^n(\omega, I)\, \exp[\mathrm{i}\varphi^n_{\mathrm{XUV}}(\omega, I)]\,, \tag{1.46}$$

where I is the driving laser intensity, for which the saddle point equations have been solved. The amplitude b is largest for the first two trajectory classes, $n = 1, 2$, i.e. the short and long trajectory already mentioned above.

Macroscopic XUV emission

The XUV light that is measured and used in experiments is obviously not radiated by a single atom or molecule but by an HHG medium consisting of many emitters with a certain density profile $n(\boldsymbol{r})$. This medium interacts with a focused laser beam with a transverse and longitudinal intensity distribution $I(\boldsymbol{r})$. All emitters radiate according to the local laser intensity and phase and propagate in a dispersive medium. The *macroscopic* XUV spectrum $\boldsymbol{E}_{\mathrm{XUV}}(\omega)$ in the far field is obtained as a solution of Maxwell's wave equation with a source term $\propto n(\boldsymbol{r})\boldsymbol{\epsilon}_{\mathrm{XUV}}(\omega, I(\boldsymbol{r}))$. This calculation corresponds essentially to coherently summing up the contributions of all single-emitters in the medium, and the macroscopic field can be obtained as (L'Huillier et al. [118]):

$$\boldsymbol{E}_{\mathrm{XUV}}(\omega, \boldsymbol{r}') \propto \sum_n \int \frac{\mathrm{e}^{\mathrm{i}k(\omega)|\boldsymbol{r}'-\boldsymbol{r}|}}{|\boldsymbol{r}'-\boldsymbol{r}|} n(\boldsymbol{r})\boldsymbol{b}^n[\omega, I(\boldsymbol{r})]\, \exp\left[\mathrm{i}\varphi^n_{\mathrm{XUV}}[\omega, I(\boldsymbol{r})]\right] \mathrm{d}^3\boldsymbol{r}\,. \tag{1.47}$$

Interference is constructive mostly in the forward (i.e. driving laser propagation) direction and significant amplitude in the far field is obtained when the wave front mismatch between the newly generated field $\boldsymbol{\epsilon}_{\mathrm{XUV}}$ and the phase front of the propagating field $\boldsymbol{E}_{\mathrm{XUV}}$ is minimized at each point in the medium. Much theoretical and experimental effort has been invested into approaching this condition and studying the effects caused by deviations from it, see e.g. (Balcou et al. [7], Constant et al. [21], Durfee et al. [36], Gaarde et al. [47], L'Huillier et al. [118], Ruchon et al. [171], Salières et al. [172]). In particular several thesis works in Saclay (Hergott [74], Kovacev [96], Le Déroff [107]) have focused on this subject.

Since for increasing n, the phase $\varphi^n_{\mathrm{XUV}}(\omega, I)$ varies more and more rapidly with I, phase matching is increasingly hard to achieve. A number of studies have shown that, consequently, the contribution of only a *single* trajectory class can be retained in the macroscopic emission if phase matching is optimized for this class (see, e.g., (Salières et al. [172])). Then, one term of the sum in equation 1.47 will completely dominate.

This thesis will mainly deal with HHG on the single-emitter level and we will in section 2.1 briefly motivate a few experimental strategies to ensure good phase matching such that the macroscopic XUV field can be considered an 'amplified true replica' of the single-atom/molecule emission, *restricted to the shortest trajectory*. This is strictly the case only for perfect phase matching throughout the medium and it may appear to be a crude over-simplification for realistic conditions. At least for the phase of the macroscopic XUV field, however, it turns out to be a valid description. (Ruchon et al. [171]) theoretically finds only very small modifications of the phase due to macroscopic effects. Furthermore, the XUV spectral phases measured by different groups, including us, are generally in very good agreement with single-emitter theory, restricted to the shortest trajectory and done for some effective intensity close to the peak intensity of the driving laser pulse (Doumy et al. [30], Dudovich et al. [33], Goulielmakis et al. [64], Mairesse et al. [127], Varjú et al. [203]) .

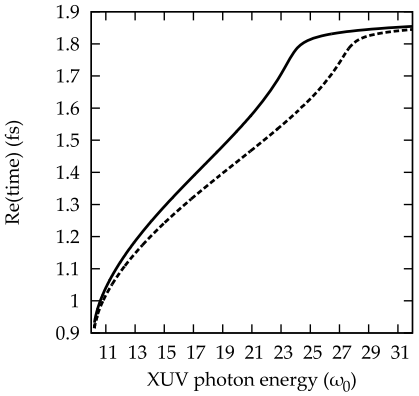

Figure 1.10. *Real part of the recombination times for the short trajectories as function of harmonic order, obtained from the saddle-point equations for HHG in argon, I_p = 15.7 eV, with an 800 nm laser and an intensity of 9×10^{13} W/cm^2 (solid line) and 1.2×10^{14} W/cm^2 (dashed line).*

Time profile of the XUV emission

If only one class, n, of trajectories dominates the macroscopic XUV emission, which is usually ensured by phase-matching, equation 1.46 simplifies to $\boldsymbol{\epsilon}_{\mathrm{XUV}}(\omega, I) = \boldsymbol{b}(\omega, I)\, \exp[\mathrm{i}\varphi_{\mathrm{XUV}}(\omega, I)]$. When the phase of $\boldsymbol{b}(\omega, I)$ varies slowly, which is the case for atoms but in general not for molecules, $\varphi_{\mathrm{XUV}}(\omega, I)$ imposes the most important spectral phase variation of the emitted XUV wave packet. As shown by (Mairesse et al. [127]), using equations 1.42 - 1.45, the XUV group delay can then be calculated as:

$$\frac{\mathrm{d}\varphi_{\mathrm{XUV}}}{\mathrm{d}\omega} = \underbrace{\frac{\partial \varphi_{\mathrm{XUV}}}{\partial \omega}}_{=t_\mathrm{r}} + \underbrace{\frac{\partial \varphi_{\mathrm{XUV}}}{\partial t_\mathrm{i}}}_{=0} \frac{\partial t_\mathrm{i}}{\partial \omega} + \underbrace{\nabla_{\boldsymbol{p}} \varphi_{\mathrm{XUV}}}_{=0} \frac{\partial \boldsymbol{p}}{\partial \omega} + \underbrace{\frac{\partial \varphi_{\mathrm{XUV}}}{\partial t_\mathrm{r}}}_{=0} \frac{\partial t_\mathrm{r}}{\partial \omega} = t_\mathrm{r}\,. \tag{1.48}$$

The XUV group delay is thus equal to the recombination time. The intuitive picture of different spectral components being emitted at different times, corresponding to a non-zero GDD and thus a chirped XUV emission, holds even in the quantum mechanical model and contains the essential physics on the attosecond time scale. The group delay has thus also been called *emission time* in (Mairesse et al. [127]).

The dependence of the recombination times on experimental parameters, like the ionization potential of the generating medium or the laser intensity, thus directly translates to the group delay of the XUV wave packets, which governs their attosecond structure. An example for this is shown in figure 1.10: The GDD of the XUV emission, i.e. the slope of the group delay in the region before the cut-off, is inversely proportional to the laser intensity. At the same time, the cut-off position increases – two effects, that may help shorten the attosecond XUV bursts[13].

In the above considerations, a temporally constant laser intensity has always been assumed. The fact that the generating laser pulses are not infinitely long but have a temporal envelope on the femtosecond time scale leads to features of the XUV emission on the femtosecond scale. Roughly, the attosecond XUV bursts, produced in each laser half-cycle, will vary according to the varying intensity envelope. (Varjú et al. [203]) give a review of the rich physics connected to the time profile of the XUV emission on different time scales. This thesis, however, will, with an exception in chapter 5, exclusively be concerned with the sub-laser-cycle structure of the XUV emission. We will study attosecond pulses which represent an average over the train of varying pulses.

1.3.4 XUV Photoionization

Many attosecond physics experiments eventually use the generated XUV wave packets to ionize atoms or molecules – either to characterize the XUV pulses or the study the ionized species. The probability of finding the ejected electron in a continuum state with momentum $\boldsymbol{k}$, is $|a(\boldsymbol{k})|^2$, where $a(\boldsymbol{k})$ is the transition amplitude. According to first-order perturbation theory, under the single-active electron approximation, and at times large enough for the XUV pulse to have passed, this is given by

$$a(\boldsymbol{k}) = -\mathrm{i} \int_{-\infty}^{+\infty} \mathrm{d}t\, \boldsymbol{d}(\boldsymbol{k}) \cdot \boldsymbol{E}_{\mathrm{XUV}}(t) \mathrm{e}^{\mathrm{i}\left(I_\mathrm{p} + k^2/2\right)t}\,, \tag{1.49}$$

where I_p is the ionization potential of the target atom/molecule and $\boldsymbol{d}(\boldsymbol{k})$ the DME $\langle \boldsymbol{k}|\hat{\mathbf{d}}|0\rangle$ between the bound state $|0\rangle$ and the continuum state $|\boldsymbol{k}\rangle$. If $\boldsymbol{d}(\boldsymbol{k})$

[13] As long as the GDD is large, increasing the spectrum will, however, not necessarily shorten the wave packet. The opposite might actually happen if the synchronization of the new spectral components with the others is bad.

were simply unity, equation 1.49 would be a Fourier transform and the EWP would be an exact replica of the XUV pulse in amplitude and phase, only shifted in energy by I_p. However, since $\boldsymbol{d}(\boldsymbol{k})$ is a complex vector,

$$\boldsymbol{d}(\boldsymbol{k}) = \boldsymbol{\mu}(\boldsymbol{k})\, \mathrm{e}^{\mathrm{i}\phi^\mathrm{d}(k)}\,, \tag{1.50}$$

with amplitude vector $\boldsymbol{\mu}$ and a phase ϕ^d, it leaves an imprint of the ionization process on the electron 'replica' of the XUV pulse. A dependence of $\boldsymbol{\mu}$ on $\boldsymbol{k}$ can easily be corrected for by known ionization cross-sections. If the phase dependence $\phi^\mathrm{d}(\boldsymbol{k})$ is known from either theory or experiment, it can be corrected for as well. The task of measuring the XUV-field can thus be accomplished by measuring the spectral amplitude and phase of the EWP.

Conversely, when ionizing with a known XUV pulse, the characterization of the EWP amplitude and phase can in principle yield a measurement of the matrix element $\boldsymbol{d}(\boldsymbol{k})$. In the absence of resonances in the continuum, the phase ϕ^d has its origin in the energy dependent phases of exact scattering wave functions $|\boldsymbol{k}\rangle$ (see end of section 1.2.2). Near resonances, another important contribution comes into play, which is the subject of paper **V**.

Two-color ionization

When additionally an IR laser field, $\boldsymbol{E}_\mathrm{L}(t) = -\partial\boldsymbol{A}/\partial t$, is present, the created EWP may also exchange energy with the laser field [14]. Using the SFA, i.e. neglecting the influence of the core-potential on the continuum electron, is justified even for weak IR fields if the XUV photon energy is much larger than I_p. With this additional approximation, once both the XUV and the IR laser fields have vanished, the transition amplitude $a(\boldsymbol{k},\tau)$ to the final continuum state $|\boldsymbol{k}\rangle$, for a delay τ between the two fields, is given by (Quéré et al. [162]):

$$a(\boldsymbol{k},\tau) = -\mathrm{i}\int_{-\infty}^{+\infty} \mathrm{d}t\, \mathrm{e}^{\mathrm{i}\phi_\mathrm{IR}(t)}\boldsymbol{d}[\boldsymbol{k}+\boldsymbol{A}(t)]\cdot\boldsymbol{E}_\mathrm{XUV}(t-\tau)\mathrm{e}^{\mathrm{i}\left(I_\mathrm{p}+k^2/2\right)t}\,, \tag{1.51}$$

$$\phi_\mathrm{IR}(t) = -\int_{t}^{+\infty} \mathrm{d}t'[\boldsymbol{k}\cdot\boldsymbol{A}(t') + \boldsymbol{A}^2(t')/2]\,. \tag{1.52}$$

The main effect of the laser field is obviously to induce a temporal phase modulation $\phi_\mathrm{IR}(t)$ upon the continuum EWP.

To see what this modulation looks like, consider a linearly polarized IR pulse, $\boldsymbol{E}_\mathrm{L}(t) = \hat{\boldsymbol{e}}E_0(t)\cos(\omega_0 t)$, the envelope $E_0(t)$ of which is sufficiently long for the slowly-varying envelope approximation to be valid, so that $\boldsymbol{A}(t) = -\hat{\boldsymbol{e}}\frac{E_0(t)}{\omega_0}\sin(\omega_0 t)$. Equation 1.52 then writes

$$\begin{aligned}
\phi_\mathrm{IR}(t) &= \phi_\mathrm{P}(t) + \phi_\mathrm{SB}(\boldsymbol{k},\hat{\boldsymbol{e}},t)\,, \qquad \text{with}\\
\phi_\mathrm{P}(t) &= -\int_{t}^{+\infty} \mathrm{d}t\, U_\mathrm{P}(t)\,, \qquad (1.53)\\
\phi_\mathrm{SB}(\boldsymbol{k},\hat{\boldsymbol{e}},t) &= \frac{1}{2\omega_0}\left[4\sqrt{U_\mathrm{P}(t)}\boldsymbol{k}\cdot\hat{\boldsymbol{e}}\cos(\omega_0 t) - U_\mathrm{P}(t)\sin(2\omega_0 t)\right]. \qquad (1.54)
\end{aligned}$$

For a constant $U_\mathrm{P} = E_0^2/4\omega_0^2$, i.e. in the limit of an IR pulse much longer than the XUV pulse, ϕ_P is linear in time, inducing an energy shift of $-U_\mathrm{P}$ of the photoelectrons, according to the Fourier transform shift-theorem (cp. also section 1.1.1). This is called the ponderomotive shift and can be seen as an increase of the effective ionization potential.

In most cases, $k^2/2 \gg U_\mathrm{P}$: for an IR intensity of $5\times10^{12}\,\mathrm{W/cm^2}$, $U_\mathrm{P} = 0.3\,\mathrm{eV}$ at a wavelength of 800 nm, whereas the photoelectron energies one typically looks at are $\sim 10\,\mathrm{eV}$. The term $\propto \cos(\omega_0 t)$ in equation 1.54 then dominates the phase modulation. Note that the scalar product $\boldsymbol{k}\cdot\hat{\boldsymbol{e}}$ implies that

[14] This is only possible as long as the EWP is in close proximity to the core – a free electron (spin 1/2) cannot absorb photons (spin 1) as angular momentum would not be conserved.

the phase modulation depends on the observation direction, $\boldsymbol{k}/k$, but varies slowly around the laser polarization direction $\hat{\boldsymbol{e}}$.

The effect of this oscillating phase variation can be very complex and depends on the duration of the XUV pulse. As just discussed, a linear phase variation in time causes an energy shift, ΔW, of the photoelectrons:

$$\Delta W(t) = -\frac{\partial \phi_{\mathrm{IR}}}{\partial t} \approx \Delta W_0 \sin(\omega_0 t) \propto A(t)\,, \tag{1.55}$$

where the approximative expression is valid for $\boldsymbol{k}^2/2 \gg U_{\mathrm{P}}$.

When photoionizing with an isolated XUV pulse much shorter than an IR half-cycle, the phase modulation imposed on the very short EWP can be considered as linear in time. The EWP is then shifted by ΔW according to the XUV-IR delay, i.e. the EWP samples small temporal slices of the IR wave. The spectrogram, i.e. a set of photoelectron spectra for different XUV-IR delays, then maps the shape of the vector potential $A(t)$ of the IR field, leading to the famous 'direct image of a light wave' of (Goulielmakis et al. [62]). For a somewhat longer XUV pulse (yet shorter than an IR half cycle), one has to consider that at the extrema of $\boldsymbol{E}_{\mathrm{L}}(t)$, the phase modulation is approximately quadratic with different signs for maxima and minima. A quadratic modulation of the temporal phase modifies the spectral width of the EWP (cp. section 1.1.1): different temporal slices of the EWP experience different energy shifts. From the evolution of the EWP spectral width with the XUV-IR delays, the quadratic component of the XUV spectral phase can be extracted, which is the essence of the 'attosecond streak camera' technique, proposed by (Itatani et al. [79]). The method applied by (Hentschel et al. [73]) for the first measurement of an isolated attosecond XUV pulse is closely related to this effect.

An XUV wave packet with a total duration on the order of an IR field cycle or longer will create an EWP, different temporal parts of which experience different phase modulations and thus energy shifts. Electrons, ionized at different times during the interaction with the XUV pulse may end up at the same final energy and thus interfere in the spectral domain. These interferences lead to complex modulations of the photoelectron spectrum, which are hard to interpret intuitively.

Nonetheless, (Mairesse and Quéré [126]) have developed a method to extract both the complete, arbitrarily complex XUV and IR light *fields* from such a measurement, by recognizing the spectrogram as a FROG (Frequency Resolved Optical Gating) trace, with the IR field taking the role of an ultrafast phase gate. Existing iterative phase-retrieval algorithms for this problem, pioneered by (Trebino [199]), could thus be transferred to the attosecond domain. The 'FROG for Complete Reconstruction of Attosecond Bursts' method (FROG-CRAB) has been applied successfully by different groups to measure both isolated attosecond pulses (Goulielmakis et al. [63], Sansone et al. [174], Thomann et al. [195]) and APTs (Kim et al. [92]).

Sidebands

For APTs, the photoelectron spectrogram simplifies again due to the discretization of the photoelectron spectrum. (Quéré et al. [162]) describe the transition into this regime in terms of the difference of phase modulations $\phi_{\mathrm{IR}}(t)$ experienced by successive XUV bursts in an APT.

A more intuitive multi-photon picture can be obtained by recognizing the exponential $\exp[\mathrm{i}\phi_{\mathrm{SB}}(t)]$ as an infinite sum over generalized Bessel functions (Kitzler et al. [93], Madsen [124]):

$$\mathrm{e}^{\mathrm{i}\phi_{\mathrm{IR}}(t)} = \sum_{n=-\infty}^{+\infty} \mathrm{J}'_n\left[2\boldsymbol{k}\cdot\hat{\boldsymbol{e}}\sqrt{U_{\mathrm{P}}(t)}/\omega_0\,,\, U_{\mathrm{P}}(t)/(2\omega_0)\right]\mathrm{e}^{\mathrm{i}n\omega_0 t}\,. \tag{1.56}$$

Each term in the sum contributes a linear phase with slope $n\omega_0$, corresponding to an energy shift of $-n\omega_0$, i.e. the stimulated emission ($n > 0$) or the absorption ($n < 0$) of $|n|$ IR photons.

The expansion 1.56 transforms equation 1.51 into an infinite sum:

$$a(\boldsymbol{k},\tau) = -\mathrm{i}\sum_{n=-\infty}^{+\infty}\int_{-\infty}^{+\infty}\mathrm{d}t\,\boldsymbol{d}[\boldsymbol{k}+\boldsymbol{A}(t)]\cdot\boldsymbol{E}_{\mathrm{XUV}}(t-\tau)\mathrm{e}^{\mathrm{i}\left(I_\mathrm{p}+k^2/2\right)t+\mathrm{i}\phi_\mathrm{P}(t)} \times \mathrm{J}'_n\left[2\boldsymbol{k}\cdot\hat{\boldsymbol{e}}\sqrt{U_\mathrm{P}(t)}/\omega_0\,,\,U_\mathrm{P}(t)/(2\omega_0)\right]\mathrm{e}^{\mathrm{i}n\omega_0 t}\,. \quad (1.57)$$

This expansion is exact and independent of the particular shape of the XUV field, but is particularly valuable for APTs, because their spectra consist of discrete peaks, spaced by $2\omega_0$. Then, $\phi_\mathrm{IR}(t)$ causes clearly distinguishable sidebands to appear in the photoelectron spectra at energies corresponding to even multiples of ω_0. Figure 1.11 shows how the main harmonic peaks get depleted with increasing IR intensity (given by $|\mathrm{J}'_0|^2$). Higher-order sidebands then appear one after the other.

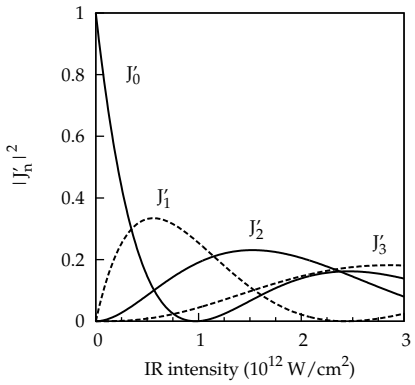

Figure 1.11. *Square of the generalized Bessel functions $n = 0, 1, 2, 3$ with arguments as in equation 1.56. The photoelectron final energy is $\mathbf{k}^2/2 = 30$ eV and $\mathbf{k} \parallel \hat{\mathbf{e}}$. The IR laser has a wavelength of 800 nm.*

RABITT

For a rather long APT, such that the individual attosecond bursts vary slowly within the train, it is useful to consider the harmonics as a comb of discrete, i.e. monochromatic, modes, with amplitude vectors $\boldsymbol{A}_q$ and a phases φ_q. Neglecting the finite spectral width and the phase variation within the harmonic peaks amounts to neglecting the femtosecond structure of the APT, i.e. the temporal envelope and variations between successive IR half-cycles (Varjú et al. [203]). The attosecond structure, i.e. the shape of an average attosecond pulse in the train, is entirely described by the $(\boldsymbol{A}_q, \varphi_q)$, to which the XUV field is related by a Fourier transform:

$$\boldsymbol{E}_\mathrm{XUV}(t) = \sum_{q=q_1}^{q_N}\boldsymbol{A}_q\,\exp[-\mathrm{i}q\omega_0 t+\mathrm{i}\varphi_q]\,, \quad (1.58)$$

where harmonic orders q_1 to q_N of the fundamental IR laser frequency ω_0 have been taken into account [15].

If the IR laser intensity is kept low enough so that the $|\mathrm{J}'_n|^2$ are negligible for $|n| \geq 2$, i.e. in the example shown in figure 1.11, $I \lesssim 2.5\times10^{11}$ W/cm^2, a very intuitive two-photon picture, illustrated in figure 1.12, can be devised: at each sideband energy $q\omega_0 - I_\mathrm{p}$, a spectrally shifted replica [16] of the harmonic peaks at $(q-1)\omega_0 - I_\mathrm{p}$ and $(q+1)\omega_0 - I_\mathrm{p}$ overlap and interfere [17]. Assuming the spectral phase of the XUV pulses to vary in a very similar way within the widths of two neighboring harmonic peaks, '$(q-1)$' and '$(q+1)$', one can define a relative phase, $\Delta\varphi_q$, of two neighboring harmonics, which governs

[15] Experimentally, the spectral range can be limited in such a way by a high-pass filter, such as aluminum foils of some 100 nm thickness. It is in fact necessary to do so in order to obtain a 'clean' APT on target, as otherwise the low order harmonics, generated in the 'usual perturbative' process, strongly dominate the XUV temporal structure. Such filters can also have negative dispersion, therefore counteracting the intrinsic GDD of the short-trajectory contributions (Martens et al. [135]). One can, of course, also simulate such filters by artificially considering only some limited spectral range-of-interest in equation 1.58.

[16] Again, the term 'replica' is to be taken with some care: The J'_n are real valued and their variation within the width of one harmonic peak is negligible. The term $\mathrm{e}^{\mathrm{i}n\omega_0 t}$ induces only an energy-shift and no other phase modulation. However, the transition amplitude to the sideband contains the single-XUV-photon matrix element $\boldsymbol{d}(\boldsymbol{k})$ for the *final* state of the *two*-photon transition, i.e. for the sideband-energy and *not* for the energy of the harmonic peak. The difference of the $\boldsymbol{d}(\boldsymbol{k})$ for these two slightly different continuum states, separated by ω_0 in energy, causes a deviation from the idea of a perfect 'replica'.

[17] The RABITT-method thus bears a strong resemblance to SPIDER, as pointed out by (Muller [151]).

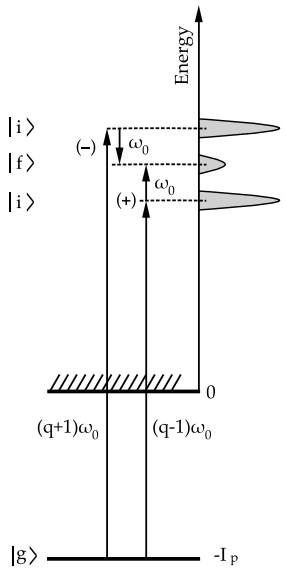

Figure 1.12. *Schematic of the two quantum paths, (+) and (-), leading to one sideband.*

the interference in the sidebands. Attributing one (absolute) phase φ_q to a harmonic order is thus valid.

A very low IR intensity also implies that $\boldsymbol{k}_{q\mp1}^2 \gg \boldsymbol{A}^2 \sim U_\mathrm{P}$ and we can thus simplify equation 1.57 by omitting $\boldsymbol{A}(t)$ in the argument of the (single-XUV-photon) matrix element $\boldsymbol{d}$ and by neglecting ϕ_P. If we are only interested in the transition amplitudes to a sideband 'q', it will be sufficient to consider only the two quantum paths depicted in figure 1.12. The path (+), involving absorption of an IR photon, is described by the $n = -1$ term of 1.57 and the spectral component $(q-1)\omega_0$ of $\boldsymbol{E}_\mathrm{XUV}$. With equation 1.58, we can thus use $\boldsymbol{E}_\mathrm{XUV}(t-\tau) = \boldsymbol{A}_{q-1}\exp[-\mathrm{i}(q-1)\omega_0(t-\tau)+\mathrm{i}\varphi_{q-1}]$. Analogously, for the path (-), it is sufficient to consider the $n = +1$ term of 1.57 and the spectral component $(q+1)\omega_0$ of the XUV field, i.e. $\boldsymbol{E}_\mathrm{XUV}(t-\tau) = \boldsymbol{A}_{q+1}\exp[-\mathrm{i}(q+1)\omega_0(t-\tau)+\mathrm{i}\varphi_{q+1}]$. The IR field can be taken with a constant value, i.e. U_P =const.. Equation 1.57 for the (+) path now writes:

$$\begin{aligned} a^+(\boldsymbol{k},\tau) &= -\mathrm{i}\int_{-\infty}^{+\infty} \mathrm{d}t\, \boldsymbol{d}(\boldsymbol{k})\boldsymbol{A}_{q-1}\,\mathrm{e}^{-\mathrm{i}(q-1)\omega_0(t-\tau)+\mathrm{i}\varphi_{q-1}}\,\mathrm{e}^{\mathrm{i}\left(I_\mathrm{P}+k^2/2\right)t}\,\mathrm{J}'_{-1}(\boldsymbol{k})\mathrm{e}^{-\mathrm{i}\omega_0 t} \\ &= -\mathrm{i}2\pi\,\mathrm{J}'_{-1}(\boldsymbol{k})\,\boldsymbol{\mu}(\boldsymbol{k})\boldsymbol{A}_{q-1}\,\mathrm{e}^{\mathrm{i}(q-1)\omega_0\tau+\mathrm{i}\varphi_{q-1}+\mathrm{i}\phi^d(\boldsymbol{k})}\,\delta_\mathrm{D}\left[q\omega_0-\left(I_\mathrm{P}+\frac{k^2}{2}\right)\right], \end{aligned} \tag{1.59}$$

where the generalized Bessel function is taken with arguments as in equation 1.56, $\boldsymbol{\mu}$ and ϕ^d are the amplitude vector and phase of the DME $\boldsymbol{d}(\boldsymbol{k})$ (cp. equation 1.50), and δ_D is a Dirac-delta function. Analogously, for the (-) path, one has:

$$a^-(\boldsymbol{k},\tau) = -\mathrm{i}2\pi\,\mathrm{J}'_{+1}(\boldsymbol{k})\,\boldsymbol{\mu}(\boldsymbol{k})\boldsymbol{A}_{q+1}\,\mathrm{e}^{\mathrm{i}(q+1)\omega_0\tau+\mathrm{i}\varphi_{q+1}+\mathrm{i}\phi^d(\boldsymbol{k})}\,\delta_\mathrm{D}\left[q\omega_0-\left(I_\mathrm{P}+\frac{k^2}{2}\right)\right]. \tag{1.60}$$

The Dirac-delta functions are obviously an artefact due to the infinite duration of IR and XUV fields in this model. Here, they simply confirm that the ±1 terms in the development 1.56 lead to peaks in the EWP spectrum at an energy decreased or increased by one IR photon energy. The contributions of the (+) and (-) paths thus overlap at $\Omega_q = \boldsymbol{k}_q^2/2 = q\omega_0 - I_\mathrm{P}$. The measurable signal will be:

$$\begin{aligned} S(\Omega_q,\tau) &= |a^+(\boldsymbol{k}_q,\tau)+a^-(\boldsymbol{k}_q,\tau)|^2 \\ &\propto S_0 + S_1\cos(2\omega_0\tau+\varphi_{q+1}-\varphi_{q-1})\,. \end{aligned} \tag{1.61}$$

The sideband oscillates with frequency $2\omega_0$ and by extracting its phase, one can obtain the relative phase of two neighboring harmonics. This leads to a method allowing direct reconstruction of an average XUV pulse in the train, which has been called 'Reconstruction of Attosecond Beating by Interference of Two-photon Transitions' (RABITT) (Muller [151]), and served for the first measurement of an APT (Paul et al. [160]). This is the technique applied for the attosecond measurements presented in this thesis. Its experimental implementation is discussed in section 2.3.

Note that the J'_n in equation 1.56 are real valued. This implies that only the sideband *amplitude* varies with the observation direction relative to the IR laser polarization due to the scalar product $\boldsymbol{k}\cdot\hat{\boldsymbol{e}}$, whereas the phase modulation $\exp[in\omega_0 t]$ is angle-independent. One can thus use an angle-integrating detector for RABITT measurements, which greatly increases the signal-to-noise ratio and decreases acquisition time.

It is somewhat counter-intuitive that the phase ϕ^d acquired by the EWP during the absorption of the XUV photon does not seem to play a role here. This is because in the above SFA formulation, the DME is taken for the *final* energy of the continuum electron, which is obviously the same for both quantum paths, (+) and (-). The two-photon picture is apparently not adequately

described by the SFA model – there is no notion of an intermediate state of the two-photon process and thus no phase difference due to different intermediate states for the (+) and (-) paths appears.

The atomic/molecular phase

It turns out that our intuition is not mistaken in this case and a more rigorous two-photon calculation resolves this problem. The second-order perturbative matrix elements [18] of the two quantum paths (+) and (-) write (Toma and Muller [196], Véniard et al. [205]):

$$M^{+}_{gf} = \tilde{M}^{gf}_{q-1}\,\exp[\mathrm{i}\,\phi^{gf}_{q-1}] = \sum\!\!\!\!\!\!\int_i \frac{\langle f|\boldsymbol{r}\cdot\hat{\boldsymbol{e}}|i\rangle\,\langle i|\boldsymbol{r}\cdot\hat{\boldsymbol{e}}|g\rangle}{(q-1)\omega_0 - I_\mathrm{p} - \epsilon_i}\,, \tag{1.62}$$

$$M^{-}_{gf} = \tilde{M}^{gf}_{q+1}\,\exp[\mathrm{i}\,\phi^{gf}_{q+1}] = \sum\!\!\!\!\!\!\int_i \frac{\langle f|\boldsymbol{r}\cdot\hat{\boldsymbol{e}}|i\rangle\,\langle i|\boldsymbol{r}\cdot\hat{\boldsymbol{e}}|g\rangle}{(q+1)\omega_0 - I_\mathrm{p} - \epsilon_i}\,, \tag{1.63}$$

where g, i, and f denote ground, intermediate and final state, respectively (cp. figure 1.12), ϵ_i is the energy of the intermediate state, and $\hat{\boldsymbol{e}}$ is a unit vector in the common polarization direction of the IR and XUV fields. The $\phi^{gf}_{q\pm1}$ are the phases of these matrix elements, usually referred to as atomic/molecular phases.

The integral runs over the complete set of eigenstates $|i\rangle$ of the atomic/molecular Hamiltonian. Since in our case $(q \pm 1)\omega_0 - I_\mathrm{p} > 0$, there is always a (continuum) state for which the integrand has a $1/x$-singularity. The integration can nonetheless be done via the Cauchy principle value, as e.g. described by (Toma and Muller [196]).

These matrix elements 1.62 and 1.63 have to be calculated for all possible ground states of energy $-I_\mathrm{p}$ (e.g. in argon, 3p electrons are ionized, and separate calculations for $m = 0$ and ±1 have to be done) and all possible final states with the same energy. For each of these possible processes (the number of which remains small due to the severe selection rules of dipole transitions), transition amplitudes to the final states with energy Ω are found as:

$$\begin{aligned} a^{+}_{gf}(\Omega,\tau) &= \int_{-\infty}^{+\infty} \mathrm{d}t\,\mathrm{e}^{-\mathrm{i}(\Omega+I_\mathrm{p})t}\,M^{+}_{gf}\,E^0_\mathrm{IR}\,\mathrm{e}^{-\mathrm{i}\omega_0 t}\,A_{q-1}\,\mathrm{e}^{-\mathrm{i}(q-1)\omega_0(t-\tau)+\mathrm{i}\varphi_{q-1}} \\ &= 2\pi\tilde{M}^{gf}_{q-1}\,E^0_\mathrm{IR}A_{q-1}\mathrm{e}^{\mathrm{i}(q-1)\omega_0\tau+\mathrm{i}\varphi_{q-1}+\mathrm{i}\phi^{gf}_{q-1}}\,\delta_\mathrm{D}[q\omega_0-(\Omega+I_\mathrm{p})]\,, \end{aligned} \tag{1.64}$$

$$\begin{aligned} a^{-}_{gf}(\Omega,\tau) &= \int_{-\infty}^{+\infty} \mathrm{d}t\,\mathrm{e}^{-\mathrm{i}(\Omega+I_\mathrm{p})t}\,M^{-}_{gf}\,E^0_\mathrm{IR}\,\mathrm{e}^{\mathrm{i}\omega_0 t}\,A_{q+1}\,\mathrm{e}^{-\mathrm{i}(q+1)\omega_0(t-\tau)+\mathrm{i}\varphi_{q+1}} \\ &= 2\pi\tilde{M}^{gf}_{q+1}\,E^0_\mathrm{IR}A_{q+1}\mathrm{e}^{\mathrm{i}(q+1)\omega_0\tau+\mathrm{i}\varphi_{q+1}+\mathrm{i}\phi^{gf}_{q+1}}\,\delta_\mathrm{D}[q\omega_0-(\Omega+I_\mathrm{p})]\,, \end{aligned} \tag{1.65}$$

where we used the IR and XUV fields as discussed in the above paragraph. The structure of these amplitudes is the same as in equations 1.59 and 1.60 and the contributions of (+) and (-) path interfere at $\Omega_q = q\omega_0 - I_\mathrm{p}$. The difference is that here, a transition matrix element appears, which is different for the two quantum paths and thus induces an additional phase shift of the RABITT signal. Again, the measurable signal, associated to one process $g \to f$, is

$$\begin{aligned} S(\Omega_q,\tau) &= |a^{+}_{gf}(\Omega,\tau) + a^{-}_{gf}(\Omega,\tau)|^2 \\ &\propto\; S_0 + S_1\cos(2\omega_0\tau + \varphi_{q+1} - \varphi_{q-1} + \phi^{gf}_{q+1} - \phi^{gf}_{q-1})\,. \end{aligned} \tag{1.66}$$

[18] Only those where the XUV photon is absorbed before the IR photon are considered (Toma and Muller [196], Véniard et al. [205]).

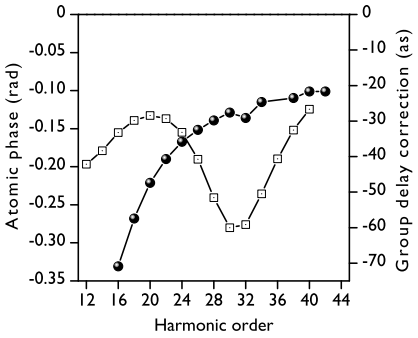

Figure 1.13. *Atomic phase correction $\Delta\phi_q^{\mathrm{at}}$ for argon (empty squares) and neon (full circles) as a function of the harmonic, or rather sideband order. On the right ordinate, the same quantity is converted to a group delay correction $\Delta\phi_q^{\mathrm{at}}/(2\omega_0)$ (cp. section 2.3).*

For the total, angle-integrated sideband, all participating processes have to be added up:

$$\boxed{\begin{aligned} T(\Omega_q,\tau) &= \sum_{(g,f)} |a_{gf}^{+}(\Omega,\tau) + a_{gf}^{-}(\Omega,\tau)|^2 \\ &\propto T_0 + T_1\cos(2\omega_0\tau + \varphi_{q+1} - \varphi_{q-1} - \Delta\phi_q^{\mathrm{at}})\,, \end{aligned}} \tag{1.67}$$

where

$$\Delta\phi_q^{\mathrm{at}} = \arg\left(\sum_{(g,f)} \tilde{M}_{gf}^{+}\tilde{M}_{gf}^{-}\exp[\mathrm{i}(\phi_{q-1}^{gf} - \phi_{q+1}^{gf})]\right). \tag{1.68}$$

Equation 1.67 gives the correct expression for the sideband signal observed in experiments. In the experiments presented in papers **I**, **II**, **IV**, and **VI**, where the aim was to characterize the attosecond XUV emission, i.e. to measure $\varphi_{q+1} - \varphi_{q-1}$ over a range of harmonic orders, the atomic phase $\Delta\phi_q^{\mathrm{at}}$, characteristic of the detection gas, should be corrected for. We used argon or neon as detection gases, the atomic phases for which are shown in figure 1.13, as calculated by Richard Taïeb with the method described above. They agree very well with those extracted from TDSE simulations (Mauritsson et al. [138]), using the same pseudo-potentials, confirming the validity of a perturbative treatment.

Physical meaning of the atomic/molecular phase

This phase correction, $\Delta\phi_q^{\mathrm{at}}$, due to the ionization process is a non-trivial quantity, rigorously defined via equation 1.68 for the IR-XUV *two*-photon-ionization process. This process is actually used only to probe the EWP released upon *single*-XUV-photon ionization. Yet, the relation between $\Delta\phi_q^{\mathrm{at}}$ and the single-photon matrix element phase as defined in equations 1.49 and 1.50 is not well understood. This leaves us in the awkward situation of having an experimental observable, that is both well defined as well as directly measurable (see paper **V** and section 4.1), but the meaning of which relative to photoionization dynamics remains somewhat unclear.

In the literature, most authors argue in the picture invoked above to describe the attosecond pulse measurement techniques based on two-color photoionization: XUV photoionization creates a continuum EWP that is a replica of the XUV pulse, except for the imprint left by the amplitude and phase of the single-photon DME. The IR probe field then acts as a pure phase gate, creating again replicas of the EWP, shifted in energy by $\pm\omega_0$, without, this time, adding another phase. It is thus sometimes accepted that the atomic/molecular phase is equal (or at least very close to) the phase difference of the XUV single-photon DMEs, as defined in equation 1.50, for two neighboring harmonics. Measuring the $\Delta\phi_q^{\mathrm{at}}$ would thus mean measuring the group delay, characteristic of the ionized system, added by the *single-XUV-photon* photoionization process. This idea is further discussed in section 4.1.5, in connection to a measurement of $\Delta\phi_q^{\mathrm{at}}$ for nitrogen molecules.

(Mauritsson et al. [138, 139]) do indeed use the phase difference of *single-photon* matrix elements synonymous with the atomic/molecular phase, without, however, formally justifying it. Also, no direct comparison of the 'proper' atomic phases, as defined by equation 1.68, and the much easier to calculate phase difference of single-XUV-photon matrix elements has been published so far. (Mauritsson et al. [138]) do, however, report several interesting observations on TDSE solutions: (i) The atomic phases extracted from TDSE calculations have been found to be very similar for processes $g \to f$ with *different* degenerate final states $|f\rangle$ as long as the intermediate state, $|i\rangle$, is the same. This has been verified for different rare gas atoms, for which pseudo-potentials are

available. (ii) Prominent features in the single-XUV-photon matrix element, such as the phase jump due to the Cooper minimum in argon, appear in the atomic phase as soon as the two harmonics and thus the intermediate states, $|i\rangle$, are on opposite sides of the resonance (see (Mauritsson et al. [138]) and figure 1 in paper **V**). (iii) Studying the transition towards vanishing IR intensity, the atomic phase first decreased until it saturates at some low value > 0. For IR intensities typically used in RABITT measurements, the value has already saturated and does not decrease further when the IR intensity is further decreased. These results combined provide strong support that the major contribution to the phase ϕ^{gf}, as defined in equations 1.62 and 1.63, comes from the absorption of the XUV photon, i.e. from the process that takes the system from the initial to the intermediate state. Claiming equality of the difference of single-XUV-photon DME phases ϕ^{d}, defined in equation 1.50, and the atomic/molecular phase is, however, admittedly still arguable.

To recover this simple picture, allowing to identify the atomic/molecular phase as the phase shift imposed onto the outgoing EWP by the single-XUV-photon DME, one had to modify equations 1.59 and 1.60 'by hand', and evaluate the matrix elements $\boldsymbol{\mu}(\boldsymbol{k})\exp[\mathrm{i}\phi^{d}(\boldsymbol{k})]$ for the *intermediate* instead of the final states, i.e. at $k' = \sqrt{k^2 - 2\omega_0}$ in equation 1.59 and $k' = \sqrt{k^2 + 2\omega_0}$ in equation 1.60. This would make the phase difference of the single-photon DME appear in the argument of the cosine in equation 1.61, just as it does in the equations used by (Mauritsson et al. [139]). Such tinkering is obviously utterly unsatisfactory and a rigorous way of simplifying the second-order perturbative matrix elements 1.62 and 1.63 is desirable.

The 'soft-photon' approximation (Kroll and Watson [98], Maquet and Taïeb [133]), where the probe laser photon energy is small against the energy of the outgoing electrons ($\omega_0 \ll k^2/2$), simplifies the two-photon matrix elements, $M^{\pm}_{gf}$, but does not directly help on, as it recovers the SFA-based result of equations 1.59 and 1.60, valid under the same condition as the soft-photon approximation. In this limit, the energies of the intermediate and the final state of the two-photon transition coincide and, as in the SFA-based model, no explicit atomic/molecular phases appear.

The question raised in this paragraph leads to a formidable theoretical problem, which is beyond the scope of this thesis. It is, however, a challenge most worthwhile to tackle, as a clear understanding of the information content of the atomic/molecular phases would put interpretations of experiments measuring them on a sound basis and possibly allow to infer detailed attosecond time-resolved dynamics of the interaction of matter with ultrashort XUV pulses. This question is also relevant to streaking experiments like that of (Cavalieri et al. [15]).

CHAPTER 2

EXPERIMENTAL TOOLS FOR ATTOSECOND PHYSICS

The experiments of attosecond physics are based upon the interaction of a wave packet of attosecond duration with the studied system. An experiment including HHG intrinsically contains a source of sub-femtosecond EWP on the single-atom/molecule level and the XUV emission may take the role of the signal carrying information about the core, which corresponds to the self-probing scheme in figure 0.2a. Other types of experiments use HHG purely as a source of XUV wave packets, which are potentially further shaped and finally used in an XUV-ionization scheme as depicted in figure 0.2b. Both types of experiments are realized with essentially the same experimental setup and in this chapter, the principle components will be introduced.

All experiments in this thesis – with the exception of some of the measurements presented in paper **III** – have been done with the *Laser Ultra-Court Accordable* (LUCA) at the Saclay Laser-matter Interaction Center (SLIC). It has a spectrum centered around 795 nm and delivers to our experiment pulses of 55 fs duration at 20 Hz repetition rate with up to 30mJ per pulse. It is run as a server, being entirely taken care of by a dedicated laser-development group. The laser drives HHG and the emitted XUV wave packets are subsequently characterized by measuring their spectral amplitude and phase. Since XUV light is strongly absorbed at atmospheric pressures, all experiments have to be done in vacuum.

The HHG stage, described in section 2.1, obviously does not consist of a single driven atom or molecule, as was the case in the theoretical discussion of the previous chapter, but of a macroscopic number of such emitters, the radiated XUV fields of all of which coherently add up to a detectable macroscopic signal. For the self-probing scheme, it is crucial that this macroscopic signal be a true representation of the single-atom/molecule emission, which is possible only if all emitters radiate *in phase*. Similarly, for the XUV-ionization scheme, one requires a sufficiently large number of photons and ideally temporally well confined XUV wave packets. This, again, requires good phase matching within the HHG medium.

The experiments described in papers **III**, **I** and **II** have used molecules *aligned* relative to the driving laser polarization. The preparation of this generating medium is described in section 2.2.

For full characterization of the XUV wave packets, a rather elaborate detection stage follows, based on photo-ionization of a suitable detection gas and described in section 2.3.

Synthèse

RÉSUMÉ DU CHAPITRE

Les expériences de physique attoseconde se basent sur l'interaction d'un paquet d'ondes de durée attoseconde avec le système étudié. Une expérience qui comporte une étape de génération d'harmoniques contient intrinsèquement une source de paquet d'ondes électronique sub-femtoseconde au niveau de l'atome / molécule unique et l'émission XUV peut jouer le rôle du signal encodant l'information sur l'atome / molécule, ce qui correspond au schéma d'auto-sondage illustré dans la figure 0.2a. D'autres types d'expériences utilisent la génération d'harmoniques uniquement comme source de paquets d'ondes XUV, qui peuvent encore être mis en forme et finalement être utilisés dans un schéma d'ionisation XUV, montré en figure 0.2b. Ces deux types d'expériences sont réalisés avec essentiellement le même dispositif et nous allons introduire ses composants principaux dans ce chapitre.

*Toutes les expériences dans cette thèse – à l'exception de certaines mesures présentées dans l'article **III** – ont été faites avec le* Laser Ultra-Court Accordable *(LUCA) du Saclay Laser-matter Interaction Center (SLIC). Son spectre est centré autour de 795 nm et les impulsions fournies avec un cadence de 20 Hz à notre dispositif ont une durée de 55 fs et une énergie allant jusqu'à 30 mJ. Il est exploité comme un serveur entièrement géré par un groupe de développement laser. Le laser génère des harmoniques d'ordre élevé et les paquets d'ondes XUV ainsi formés sont ensuite caractérisés en mesurant leur amplitude et phase spectrale. Toutes les expériences sont faites sous vide car la lumière XUV est absorbée très fortement dans l'air.*

La partie génération d'harmoniques du dispositif, décrite dans le paragraphe 2.1, ne contient évidemment pas seulement un atome ou une molécule unique – comme c'était le cas dans la discussion théorique du chapitre précédent – mais un nombre macroscopique de tels émetteurs. Les champs XUV rayonnés s'ajoutent de façon cohérente pour donner un signal détectable. Pour le schéma d'auto-sondage, il est très important que ce signal macroscopique soit une représentation fidèle de l'émission de l'atome / molécule unique, ce qui est possible uniquement si tous les emetteurs rayonnent en phase. *De façon similaire, pour le schéma d'ionisation XUV, nous avons besoin d'un nombre suffisant de photons et idéalement de paquets d'ondes XUV bien confinés temporellement. Encore une fois, cela nécessite un bon accord de phase dans le milieu de génération d'harmoniques. Travaillant dans des conditions avec une très faible ionisation et des longueurs de milieu très faibles, il est raisonnable de supposer un accord de phase (presque) parfait dans nos expériences.*

*Dans les expériences présentées dans les articles **III**, **I** et **II**, nous avons utilisé des molécules* alignées *par rapport à la direction de polarisation du laser. La préparation de ce milieu de génération sera décrite dans le paragraphe 2.2. Bien que ce chapitre soit principalement dédié aux outils expérimentaux, nous détaillerons les aspects théoriques de l'alignement. Nous utilisons la technique d'alignement impulsionel où une impulsion laser crée par effet Raman stimulé un paquet d'ondes rotationel dans la molécule qui va ensuite évoluer librement. Comme tous les niveaux rotationnels J ont des énergies de valeur harmonique de l'énergie de $J = 0$, ce paquet d'ondes va régulièrement reproduire la distribution partiellement alignée atteinte peu après que l'impulsion laser soit passée. Pour prendre en compte la distribution thermique des niveaux rotationnels dans l'ensemble des molécules de notre milieu de génération, nous devrons ensuite faire une moyenne incohérente. La compréhension de la dynamique moléculaire à la base de cette technique d'alignment nous permet ensuite de l'optimiser et d'estimer la qualité d'alignement obtenue dans nos expériences.*

Pour la caractérisation complète des paquets d'ondes XUV, un dispositif de détection assez sophistiqué est nécessaire, basé sur l'ionisation d'un gaz cible adapté. Les bases théoriques des méthodes de caractérisation sont décrites dans le paragraphe 1.3.4 du chapitre pécédent. Ici sera décrit comment une impulsion moyenne du train d'impulsions attosecondes peut être reconstruite à partir d'une série de spectres de photoélectrons obtenus par photoionisation à deux couleurs en fonction du délai entre les deux champs (XUV et IR), contrôlé avec une précision supérieure à la demi-période du laser IR. Nous discutons les différentes étapes de l'analyse des données.

Finalement, les dispositifs expérimentaux utilisés pour les travaux de cette thèse sont présentés.

2.1 The Attosecond Pulse Source

Apart, of course, from the needed driving laser, HHG is experimentally fairly simple: It comes down to focusing a laser pulse, sufficiently energetic and short to reach the required intensity, into a gas cloud being provided either by a cell with static pressure or, as was the case for all experiments presented in this thesis, by a pulsed gas jet. This has the advantage of providing the HHG medium with relatively high density while keeping the amount of gas injected low.

A cold HHG medium As explained in section 2.2, we need rotationally cold molecules to achieve a high degree of molecular alignment. This is achieved by forcing gas with high pressure (a few bars backing pressure) through a small orifice (a few hundred microns) into vacuum, forming a so called supersonic jet. This is because the molecules are accelerated to become faster than the local speed of sound, which in turn decreases rapidly as the gas density drops during the expansion. In this adiabatic process, the heat energy of the gas (i.e. random translation, vibration, rotation) is converted into directed translational energy through numerous collisions. Very rapidly, the gas plume has expanded so far that the individual particles do no longer collide. Full thermodynamic equilibrium is lost during the expansion and the different degrees of freedom must be represented by different temperatures. Important to us is the rotational temperature, T_{rot}, which typically decreases to a few tens of kelvin. To minimize T_{rot}, the backing pressure can be increased (we typically use 2-3 bars), the orifice diameter decreased (we used between 100 and 1000 microns) and the distance to the orifice increased (we use about 500 microns). Obviously, there is a trade-off to be made between high gas density (and thus high XUV signal), low rotational temperature (which decreases while the gas expands and thus always comes at the price of rather low gas density), and sufficient pumping power (we have a 1300 l turbo-molecular pump directly under the gas jet) balancing the gas injection in order to maintain a low residual pressure in the experimental chambers.

Phase matching As mentioned on page 25 in the theory chapter, it is necessary to ensure good phase matching in the experiment in order to obtain a strong macroscopic signal and to be able to infer single-atom / molecule information from it. This means that one has to arrange conditions that minimize the phase difference between the propagating XUV field and the driving polarization over the medium length.

Essentially three contributions cause a phase mismatch between along the medium length (Haessler and Swoboda [67]): (i) The *Gouy phase shift* of π

of the driving laser as is goes through its focus (Svelto [192]). (ii) The *dipole phase*, i.e. the phase of the radiating atomic/molecular dipole, φ_{XUV}, given by equation 1.42, which varies approximately linearly with intensity (Varjú et al. [203]). (iii) *Dispersion*, i.e. the difference of phase velocity between the driving laser and the XUV radiation, dominated by the free electrons created by ionization[1], the density of which obviously strongly depends on the local intensity.

Loose focusing can slow down the first two of these variations. In addition, one can arrange that the phase mismatch due to the intensity dependent dipole phase of the short trajectory contribution cancels out that caused by the Gouy phase shift at a short distance after the laser focus (Haessler and Swoboda [67], Salières et al. [172]). Placing a rather short generation medium at this distance thus allows to approach perfect on-axis phase matching. Significant ionization does, however, cause strong dispersion that rapidly ruins any phase matching. Moreover, it depletes the ground state of the emitters. The pulsed gas jet, used in all experiments in this thesis, except the ones of chapter 5, provided a medium with an effective length of < 1 mm. Ionization was kept at very low level and no important dependence on the longitudinal medium position was observed, other than that due to the intensity variation. This confirms that phase matching was excellent and that the measured signal was a true amplification of the single-atom/molecule emission. Moreover, the emission times measured for atomic gases was in very good agreement with the single-atom theory described in section 1.3.3.

The dipole phase, $\varphi^n_{\mathrm{XUV}}(\omega, I)$ (cp. equation 1.46) changes about ten times faster for the long trajectories ($n = 2$) than for the short ones ($n = 1$). This implies that the radial intensity profile of the driving laser beam translates to an XUV phase front curvature that is larger for the long trajectory contribution. The different divergences thus cause the contributions of short and long trajectories to spatially separate in the far field. In our experiments, we always select the on-axis emission, and thus the short-trajectory contribution.

2.2 Molecular Alignment

The experiments in papers **I**, **II** and **III** have used as generation medium molecules *aligned* relative to the driving laser polarization. Alignment and anti-alignment conventionally refer to head-on versus broadside localization of some particular axis of a molecule, whereas *orientation* refers to control of the up and down directions of an aligned molecule. Within this thesis, only linear symmetric molecules have been used so that alignment is completely sufficient. We will use a non-adiabatic alignment scheme, first proposed by (Seideman [182]) and later demonstrated by (Rosca-Pruna and Vrakking [170]), where a relatively strong laser pulse 'kicks' the molecules and creates a wave-packet of rotational states, which evolves freely after the pulse has passed. It will regularly re-phase and lead to an effectively aligned angular distribution in field-free conditions.

When injecting the molecules into the experiment chamber, their axes are of course randomly aligned. To get them to align along a certain direction in space, a torque has to be applied and strong electric fields are a good tool to do so. The oscillating electric field, $\mathbf{E}$, of an IR laser induces a molecular dipole, $\boldsymbol{\alpha}\cdot\mathbf{E}$, due to the oscillating electrons, where $\boldsymbol{\alpha}$ is the polarizability tensor. The molecule then has a potential energy, $U = -(\boldsymbol{\alpha}\cdot\mathbf{E})\cdot\mathbf{E}$, and it will only feel a torque, $-\mathrm{d}U/\mathrm{d}\theta$, if its polarizability tensor $\boldsymbol{\alpha}$ is anisotropic, i.e. there is a most-

[1] Note that these are not the quasi-bound continuum electrons of the three step model, but those permanently detached from the core forming a free electron gas in the HHG medium.

polarizable axis, along which the polarizability component is $\alpha_\parallel$. Along the second-most-polarizable axis, perpendicular to the first one, we have $\alpha_\perp < \alpha_\parallel$, and it can be shown that the potential, time-averaged over one laser cycle [2], writes (Friedrich and Herschbach [46]):

$$U(\theta,t) = -\frac{1}{4}\Delta\alpha E_0^2 f^2(t)\cos^2\theta = -U_0(t)\cos^2\theta\,, \tag{2.1}$$

where E_0 is the maximum field strength of the laser pulse with envelope $f(t)$, varying much slower than the field oscillations, $\Delta\alpha = \alpha_\parallel - \alpha_\perp$, and θ is the angle between the laser polarization direction and the molecule's most-polarizable axis, which, for the linear molecules dealt with in this thesis, is always the internuclear axis. The molecules will thus see an angular potential well with minima for parallel alignment of their internuclear axis to the laser polarization. This potential is also known as the angular AC Stark shift.

Quantum evolution The angular part, $\psi(\theta,\phi,t)$ of the nuclear wavefunction of molecules (cp. section 1.2.3) is conveniently expressed on the basis of eigenfunctions of the rotational energy operator, $B\mathbf{J}^2 = B_0 J(J+1)$, where B_0 has the unit of a frequency and is referred to as the rotation constant. These are the spherical harmonics $Y_{JM}(\theta,\varphi)$, with the orbital momentum quantum number $J = 0,1,2,\ldots$ and its projection, $M = -J,-(J-1),\ldots,(J-1),J$, onto a particular direction of space, which in our case is the laser polarization direction. The evolution of $\psi(\theta,\phi,t)$, including interaction with a linearly polarized laser pulse as described above, follows the TDSE

$$\mathrm{i}\frac{\partial}{\partial t}\psi(\theta,\phi,t) = \left[B\mathbf{J}^2 - U_0(t)\cos^2\theta\right]\psi(\theta,\phi,t)\,. \tag{2.2}$$

Molecules are no rigid rotors, i.e. in high orbital momentum states J, their bonds stretch and thus their moment of inertia increases. This is taken into account by a correction to the rotational energy operator [3]: $B\mathbf{J}^2 = B_0 J(J+1) - D_0[J(J+1)]^2$ (Svanberg [191]). Since typically $D_0 \sim 10^{-6}B_0$, this only becomes significant for rather high J.

To solve equation 2.2, the initial condition has to be fixed. Rotational levels of small molecules are only about 1 meV apart (Svanberg [191]), so that even at the low rotational temperatures reached through supersonic expansion, the thermal ensemble will correspond to a statistical mixture – or an incoherent superposition – of rotational eigenstates $Y_{JM}(\theta,\varphi)$. The weights are given by the Boltzmann distribution

$$P_J = g_J(2J+1)\mathrm{e}^{-E_J/k_\mathrm{B}T_\mathrm{rot}}\,, \tag{2.3}$$

where $E_J = B_0 J(J+1) - D_0[J(J+1)]^2$ is the rotational energy of the state $Y_{JM}(\theta,\varphi)$, the (2J+1) term accounts for the degeneracy of a given J level due to the different M sub-levels, and g_J is a factor controlling the relative weight between even and odd J states, arising from nuclear spin statistics (Dooley et al. [29]). Figure 2.1 shows some of these initial distributions for CO_2, N_2 and H_2 for rotational temperatures typical in our experiments. The used molecular properties are compiled in table 2.1.

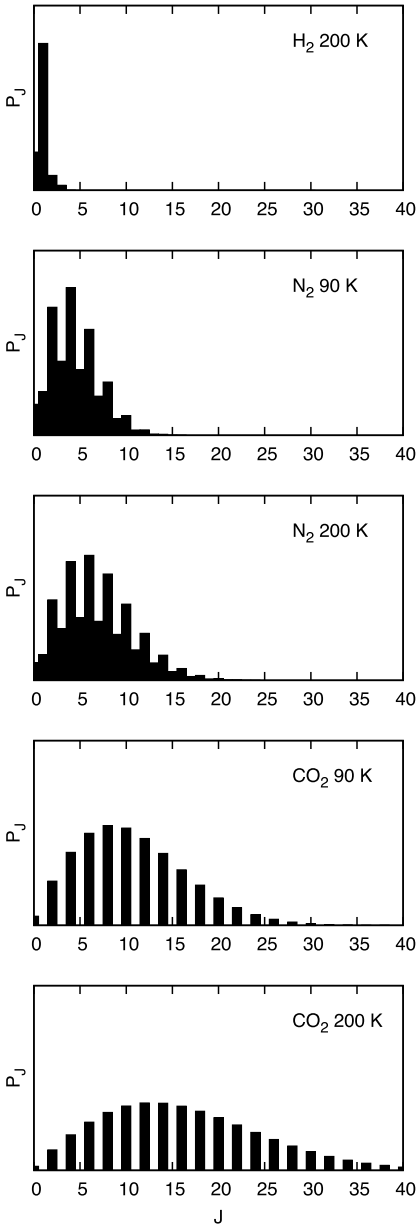

Figure 2.1. *Boltzmann distributions of rotational levels J, populated in the initial thermal ensemble for different molecules and rotational temperatures.*

[2] The IR laser field we use is far off resonance with rotational transitions and oscillates too fast for the nuclei to follow directly.

[3] Further corrections arising from vibrational excitation can be neglected as (i) low-lying vibrational energy levels are ~ 100 meV apart, such that even at room temperature ($k_\mathrm{B}T$ = 25 meV) essentially no thermal excitation exists, (ii) the spectra of the laser pulses used in our experiments are too narrow to excite vibrations via a stimulated Raman-process, and (iii) the linear symmetric molecules we use have no permanent electric dipole moment and can thus not be excited by direct absorption of an IR photon, i.e. they are IR inactive (Svanberg [191]).

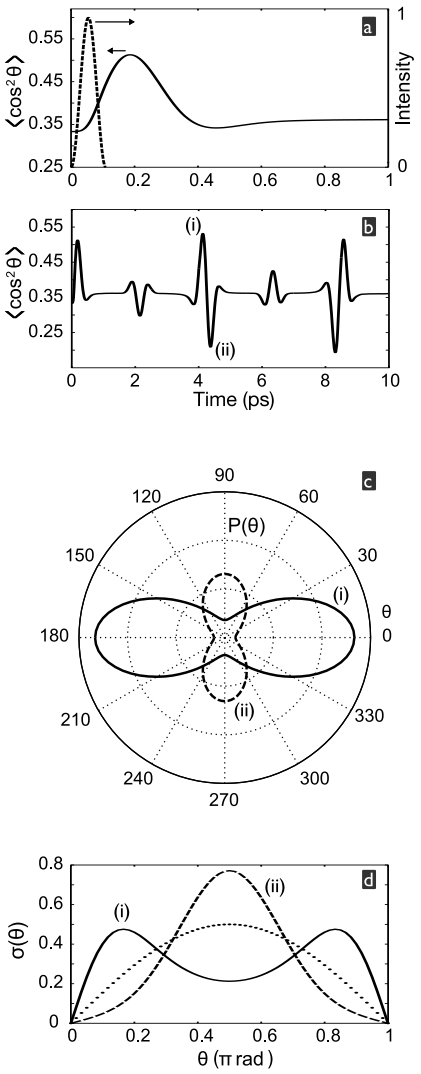

Figure 2.2. *Results of a calculation for N_2 molecules with rotational temperature $T_{rot} = 90$ K, interacting with a laser pulse of duration $\tau = 55$ fs and peak-intensity of 5×10^{13} W/cm^2. In panel **(a)**, the full line shows the $\cos^2\theta$-measure during the first picosecond as well as the laser pulse intensity envelope $f^2(t)$. In panel **(b)**, the evolution of the $\cos^2\theta$-measure is traced over more than one rotational period of N_2. The first recurrence of alignment at the so-called half-revival at $t = 4.135$ ps as well as the immediately following anti-alignment at $t = 4.38$ ps are marked as (i) and (ii), respectively. Panel **(c)** then shows the angular distributions $P(\theta)$ of the molecules at these times (i) and (ii). Panel **(d)** contains the same information, but integrated over the azimuthal angle ϕ: $\sigma(\theta) = 2\pi P(\theta)\sin\theta$, which is proportional to the probability of finding the molecule found with an angle between θ and $\theta + d\theta$. The dotted line shows an isotropic distribution for comparison.*

Molecule	B_0 (cm^{-1})	D_0 (cm^{-1})	$\Delta\alpha$ (Å^3)	g_{even}	g_{odd}
N_2	1.9896	5.67×10^{-6}	1.0	2	1
CO_2	0.3902	0.135×10^{-6}	2.0	1	0
H_2	59.322	0.0471	0.2	1	3
D_2	29.90	0.01141	0.2	2	1

Table 2.1: Properties of the different molecules considered in this thesis (Huber and Herzberg [78], Miller [145, 146]).

Equation 2.2 is solved for each rotational state $Y_{JM}(\theta,\varphi)$ with a significant relative weight as the initial condition $\psi(\theta,\phi,t=0)$. For example for N_2 molecules with $T_{rot} = 200$ K, this has to be done for $J = 0,\ldots,21$, which amounts in total to $\sum_0^{21}(J+1) = 253$ times [4] of solving equation 2.2. The laser pulse envelope, with full width at half maximum τ, is taken as $f^2(t) = \sin^2[(\pi t)/(2\tau)]$ for $0 \le t \le 2\tau$ and $f^2(t) = 0$ otherwise. Sébastien Weber wrote the program that numerically calculates the evolution of $\psi(\theta,\phi,t)$ using the fourth-order Runge-Kutta method (Press et al. [161]) over the duration of the laser pulse.

During the solution of equation 2.2, it turns out that the laser couples only $J \leftrightarrow J+2$ and $J \leftrightarrow J-2$ via a stimulated Raman process, while different M states are not coupled (Dooley et al. [29]). Gradually, more rotational levels J are populated and a *coherent* rotational wave packet is formed. For a laser pulse duration on the order of the rotational period of the molecules, this will lead to the molecules becoming trapped in the potential well $\propto \cos^2\theta$ (cp. figure 2.3e). One then speaks of adiabatic alignment. This scheme has the disadvantage that molecular alignment disappears again when the aligning pulse is gone. However, during laser pulse durations of $\lesssim 200$ fs, as typically used in our experiments, molecules like N_2 or CO_2 barely move: the aligning pulse rather gives them a strong 'kick' towards alignment. This is followed by free propagation of the rotational wave packet according to $\psi(\theta,\phi,t) = \sum_J A_{J,M}\exp[iE_J t]\,|Y_{JM}\rangle$, with $A_{J,M} = \langle Y_{JM}|\psi(\theta,\phi,t=2\tau)\rangle$. As we will see in the next paragraph, the molecules will align after the laser pulse has passed, and since the rotational energies E_J are all even integer multiples of the fundamental frequency B_0 (neglecting the small correction $\propto D_0$), the wave packet will re-phase with a period $T_{\mathbf{rot}} = \pi/B_0$ (or, with B_0 in [cm^{-1}], $T_{rot} = (2B_0c)^{-1}$)), which is equal to the rotational period of the molecules. Such behavior is called a *wave packet revival* [5].

Angular distribution The angular distribution of the molecular ensemble at any instant is now given by a statistical average – i.e. an incoherent sum with weights given by the initial Boltzmann distribution (equation 2.3) – over the different $\langle\psi_{J,M}|\psi_{J,M}\rangle$, obtained for the different initial conditions:

$$P(\theta,t) = \langle\langle\psi|\psi\rangle\rangle_{stat} = \frac{\sum_{J,M} g_J e^{-E_J/k_B T_{rot}}\,\langle\psi_{J,M}|\psi_{J,M}\rangle\,(\theta,\phi,t)}{\sum_J P_J}. \qquad (2.4)$$

Note that we always have all M sub-levels present with equal weights, because the initial angular distribution was isotropic and the Hamiltonian in equation 2.2 is ϕ-independent and thus does not couple different M-states. The angular distribution is thus at every instant ϕ-independent: $P = P(\theta,t)$.

[4] Note that it is sufficient to do the calculation for $M = 0,\ldots,J$, since the result for M is the same as that for $-M$.

[5] In this sense, the recurrence of XUV light pulses in an attosecond pulse train is also a wave packet revival.

While looking at the angular distribution at different instants is very clear and graphic, a rigorous quantification of the degree of alignment is desirable. Many possible ways could be found to do so, but the standard measure of alignment is defined as the statistical average over the expectation value $\langle\psi|\cos^2\theta|\psi\rangle$. This measure approaches unity for an angular distribution perfectly peaked along $\theta = 0$ and π, $\langle\cos^2\theta\rangle = 0$ for a disk-shaped distribution peaked along $\theta = \pi/2$, and $\langle\cos^2\theta\rangle = 1/3$ for an isotropic distribution.

The time-dependent $\cos^2$-measure is plotted for an exemplary case in figure 2.2. This calculation was done for parameters typical for our experiments. During the pulse duration, which is much shorter than the rotational period of N_2 molecules, $\tau_{\text{rot}} = 8.38\,\text{ps}$, the molecules start rotating towards alignment, but is it is really only the onset of the wave packet evolution. After $\tau_0 = 190\,\text{fs}$, $\langle\cos^2\theta\rangle$ goes through a maximum, i.e. a situation of (imperfect) alignment occurs, referred to as 'prompt' alignment. One rotational period later, i.e. at the wave packet revival at $t = \tau_0 + T_{\text{rot}} = 8.57\,\text{ps}$, this situation is reproduced. Interestingly, the alignment also recurs in between: $\langle\cos^2\theta\rangle\,(t_{(\text{i})} = 4.135\,\text{ps}) = 0.53$, shortly before $t_{(\text{ii})} = \tau_0 + T_{\text{rot}}/2 = 4.38\,\text{ps}$, where the opposite situation, an anti-alignment, occurs. At the instant (i), the angular distribution $P(\theta)$ is strongly peaked at $\theta = 0$, albeit having a certain width $\Delta\theta \approx 30°$. To calculate the fraction of all molecules within a certain θ-range, P has to be integrated over the azimuthal angle ϕ, which leads to the distributions $\sigma(\theta, t) = 2\pi P(\theta, t)\sin\theta$. At the instant of alignment, (i), this distribution is peaked at $\theta = \pi/6 = 30°$.

Optimizing alignment Sébastien Weber's code allows to extensively study theoretically the dependence of the achievable alignment quality on experimental parameters. In figure 2.3, for instance, we show the evolution of $\langle\cos^2\theta\rangle$ for different pulse durations. We found the best alignment to be achievable with $\tau \approx 120\,\text{fs}$. Longer pulses start distorting the rotational wave packet during the prompt alignment and in figure 2.3e a situation corresponding to adiabatic alignment is reached. Experimentally, we could stretch LUCA's pulses to 120 fs by propagating them through a glass block, while increasing the pulse energy to keep the intensity constant. For the experiments in this thesis, the alignment pulse had a duration of $\tau \approx 55\,\text{fs}$.

The simulations also show that, of course, a more intense aligning pulse also improves the maximum $\langle\cos^2\theta\rangle$ achievable. This is easy to understand, since a longer and more intense pulse enhances the coupling and leaves more time to gradually populate a spectrally broad rotational wave packet, leading to sharper revivals with higher degree of alignment. Experimentally, there are of course certain boundaries. The laser intensity we can use is not only limited by the onset of ionization of the molecules, but already by HHG. We want to generate APTs in aligned molecules, i.e. with a second laser pulse, delayed such that it interacts with the molecular medium at the *half-revival*, i.e. the instant marked as (i) in figure 2.2. Any harmonic signal already produced by the collinearly propagating alignment pulse would thus be a nuisance. This effectively limits us to $I = 5\times10^{13}\,\text{W/cm}^2$. Using a small angle between between alignment and HHG beam would allow higher intensities to be used, but complicates the optical setup.

The rotational temperature of the molecules is another very important parameter. Only the wave packets created starting from one particular $Y_{J,M}$ eigenstate are coherent. A high T_{rot} causes a wide J-distribution over which is averaged *incoherently*. This significantly decreases the achievable degree of alignment, as shown in figure 2.4a. This dependence can be observed experimentally. Although we did not directly measure $\langle\cos^2\theta\rangle$, as is possible using Coulomb explosion (Dooley et al. [29]), the dependence of the harmonic intensity is closely related to it (Ramakrishna and Seideman [163]). Indeed,

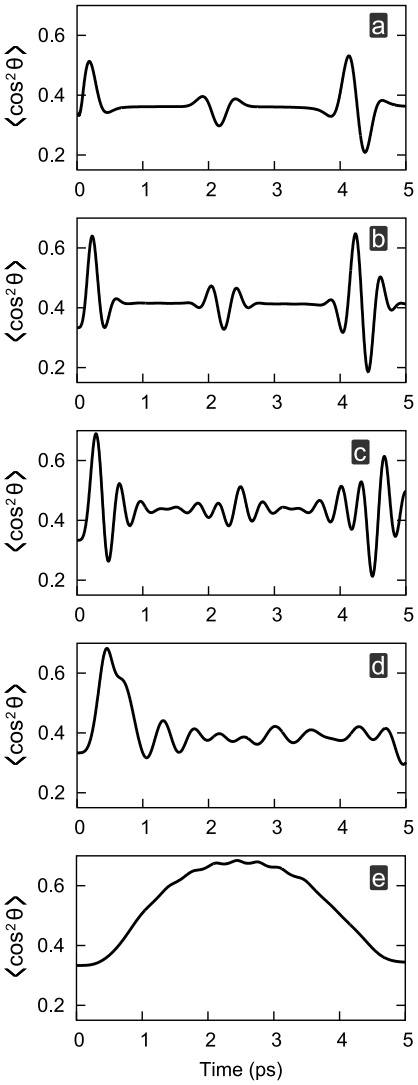

Figure 2.3. *Calculated dependence of the alignment quality on the laser pulse duration. The parameters are the same as in figure 2.2, except for the pulse duration, which is 55 fs (a), 120 fs (b), 200 fs (c), 500 fs (d) and 2500 fs (e).*

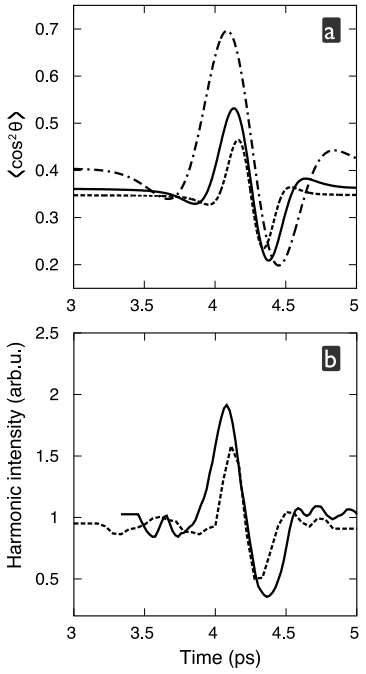

Figure 2.4. *Dependence of the degree of alignment on the rotational temperature. Panel* ***(a)*** *shows calculations for the same parameters as in figure 2.2, except for the temperature: T_{rot} = 20 K (dash-dotted line), T_{rot} = 90 K (solid line), T_{rot} = 200 K (dashed line). Panel* ***(b)*** *shows measurements of the intensity of harmonic 21 as a function of the delay between aligning and HHG-pulse for two gas jet orifice diameters: 300 microns (solid line) and 1 mm (dashed line). The rotational temperatures reached with these were estimated as 90 K and 200 K, respectively.*

in N_2 molecules, the intensity of harmonics, generated at varying delays after the aligning pulse, follows closely the $\langle\cos^2\theta\rangle$-measure. In figure 2.4, we compare calculations for different rotational temperatures with such measurements. The rotational temperature of our gas jet was discussed in section 2.1. The trade-off between medium density, temperature and pumping power led us to use an orifice of 300 microns and a backing pressure of 3 bar in most experiments. The temperature then was estimated to be T_{rot} = 90 K. This estimate is based on the Fourier transform of measured revival curves, which show peaks corresponding to the beating between the different J-levels. These are compared to Fourier transformed theoretical $\langle\cos^2\theta\rangle$-curves for different initial T_{rot}. This allows a determination of the experimental temperature up to ±10 K, but the precise value might fluctuate between different measurement runs due to possible variations of the distance between orifice and HHG source as well as the proper functioning of the jet.

2.3 Attosecond Pulse Measurement

Ultra-short light pulses are, almost by definition, shorter than the response time of any electronic instrument. Additionally, photodetectors are intrinsically *intensity*-detectors, i.e. insensitive to the phase of incident electric field. Numerous methods overcoming these limitations exist today for light pulses in the IR and visible domain, all consisting of at least one time-nonstationary and one time-stationary filter (Walmsley and Wong [214]). See (Walmsley and Dorrer [213]) for an extensive tutorial on these techniques. Their direct application to the XUV and attosecond domain is, however, not straightforward because of the extraordinarily large bandwidth of typically tens of eV and the mean wavelength of the pulses being in a spectral region where there are no standard linear or nonlinear materials. Therefore there are only limited options for optics that can be used to manipulate these pulses.

Nonetheless, 'classical' all-optical methods like intensity auto-correlation (Sekikawa et al. [183], Tzallas et al. [200]) and interferometric auto-correlation (Nabekawa et al. [152]) have been demonstrated on APTs using XUV multi-photon-ionization of a target gas as non-linear element, i.e. time-gate and thus non-stationary filter. 'Spectral phase interferometry for direct electric field reconstruction' (SPIDER) has been demonstrated to measure the femtosecond profile of one harmonic peak (Mairesse et al. [128]), and (Cormier et al. [23]) have proposed a scheme to transfer the 'spatially encoded arrangement for SPIDER' (SEA-SPIDER) to the attosecond domain.

RABITT

The most successful techniques thus far, one of which is the RABITT method applied in the experiments presented in this thesis, are based on converting the optical wave packet $\boldsymbol{E}_{XUV}(t)$ to an EWP, by ionizing a target gas. The relevant physics have been discussed in section 1.3.4.

The formulae relevant to the measurement of an average pulse in an APT with RABITT are equations 1.58 and 1.67. The electric field of the XUV pulse is obtained from

$$\boldsymbol{E}_{XUV}(t) = \sum_{q=q_1}^{q_N} \hat{\boldsymbol{n}}_q A_q \exp[-\mathrm{i}q\omega_0 t + \mathrm{i}\varphi_q], \tag{2.5}$$

with the scalar amplitudes A_q and phases φ_q of the discrete harmonics and the unit-vectors $\hat{\boldsymbol{n}}_q$ describing their polarization state. The latter is linear and parallel to the driving laser for atoms due to their spherical symmetry, whereas

for molecules this is in general not the case. In paper **III**, we measure the polarization of the high-order harmonics emitted by aligned nitrogen molecules. The amplitudes A_q are easily accessible via an intensity spectrum, obtained for example with a grating and an XUV-sensitive detector.

For the phase measurement, one extracts by a fast Fourier transform the phase of the oscillating part of the sidebands at energies $q\omega_0 - I_p$, given as

$$S_q(\tau) = \cos(2\omega_0\tau + \varphi_{q+1} - \varphi_{q-1} - \Delta\phi_q^{at}), \tag{2.6}$$

and corrects for the atomic phase $\Delta\phi_q^{at}$. In this measurement of the relative phases $\varphi_{q+1} - \varphi_{q-1}$, the IR *probe* beam is the phase reference.

In many experiments, however, the IR HHG *driving* laser would be an even more interesting phase reference. In other words, one wants to shift the origin of the time-axis by τ_0, such that the HHG driving laser field is maximum at $t' = t - \tau_0 = 0$. One easily verifies[6] that such a change of the time-origin adds an additional phase term $2\phi_{tot} = +2\omega_0\tau_0$ to the argument of the cosine in equation 2.6.

The delay τ_0 between the two IR fields can be measured by making the IR driving beam, $\propto \cos[\omega_0(t - \tau_0 - \tau)]$, interfere with the IR probe beam, $\propto \cos(\omega_0 t)$, in the HHG medium. With typically three orders of magnitude lower intensity, the IR probe beam cannot generate harmonics on its own, but will very weakly modulate the total intensity according to $\cos[\omega_0(\tau + \tau_0)]$. Due to the high non-linearity of the HHG process, this weak modulation will become perceptible as a small modulation of the total (i.e. spectrally integrated) XUV intensity. From this oscillation, superposed on the complete RABITT scan, one can extract $\phi_{tot} = \omega_0\tau_0$ and finally subtract $2\phi_{tot}$ from the measured sideband oscillation phases.

From the so-obtained relative phases of neighboring harmonics $\varphi_{q+1} - \varphi_{q-1}$, one can calculate the XUV group delay, also called emission time, t_e, as:

$$t_e(q\omega_0) := \left.\frac{\partial\varphi}{\partial\omega}\right|_{q\omega_0} \approx \frac{\varphi_{q+1} - \varphi_{q-1}}{2\omega_0}, \tag{2.7}$$

As the phase reference is the IR driving laser field, $t_e = 0$ coincides with a driving laser field maximum. The slope of these emission times correspond to the intrinsic chirp of the XUV emission on an attosecond time-scale, which is thus referred to it as the *attochirp*. The absolute values of the emission times correspond to the delay between the attosecond XUV burst and a preceding IR driving field maximum. It is determined by the measurement of ϕ_{tot} and referred to as the *absolute timing*.

The XUV spectral phase $\varphi(\omega)$ can finally be obtained at the discrete harmonic frequencies q_n by integration of the group delay. This implies that the spectral phase is measured up to an integration constant φ_0, which takes the role of an absolute phase of the XUV field given by equation 2.5, and has no influence on the temporal intensity profile. In the experiments presented in papers **I** and **II**, however, this absolute phase becomes of importance.

Since the sidebands have to be kept very weak so as to avoid distortions due to higher-order processes (i.e. sidebands of second order and higher), the harmonic peaks in the spectra are very weakly affected. We can thus extract the spectral intensity from a RABITT scan by integrating over τ and obtain the same spectrum as we would have by taking a separate spectrum with no IR probe beam present.

Data analysis Concretely, an example of a RABITT scan is shown in figure 2.5. This scan was taken with a generation intensity of $I = 1.2 \times 10^{14}$ W/cm^2 in

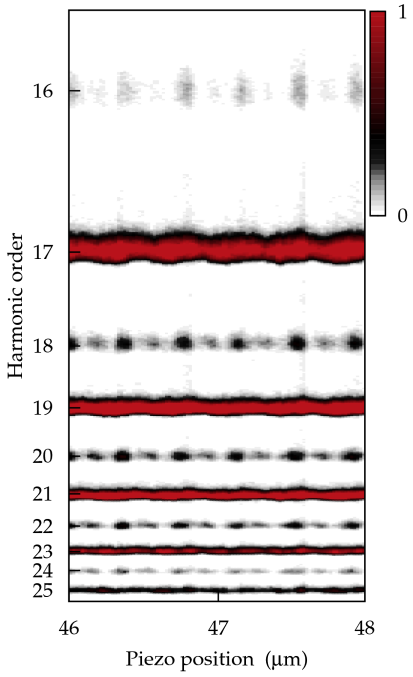

Figure 2.5. *Raw data of a RABITT scan, taken with an HHG intensity of $I = 1.2 \times 10^{14}$ W/cm^2 in nitrogen molecules aligned parallel to the driving laser polarization and detecting in neon. The piezo step size is 20 nm and 100 laser shots are averaged per spectrum. The acquisition of this scan thus took about 10 minutes. The ordinate is scaled according to the time-of-flight of the detected photoelectrons, but the corresponding harmonic orders are marked.*

[6] Just replace $t \to t' = t - \tau_0$ in the derivation of equation 1.67.

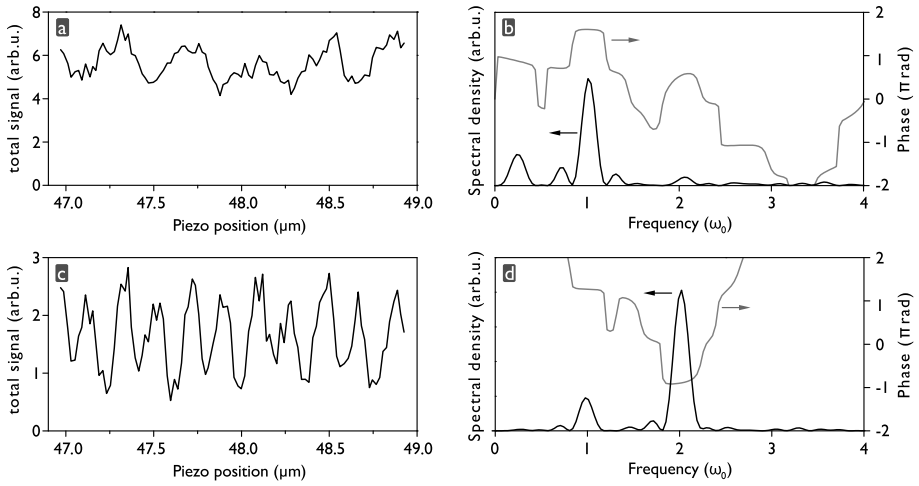

Figure 2.6. *Analysis of the RABITT scan shown in figure 2.5. The total, i.e. spectrally integrated, signal (a) is modulated with frequency ω_0. From its FFT (b), we obtain ϕ_{tot}. Sideband 22 (c), normalized by the total signal, oscillates at $2\omega_0$ with strong contrast. The phase of its FFT (d) at $2\omega_0$ equals $\varphi_{23} - \varphi_{21} - \Delta\phi_{22}^{\mathrm{at}} + 2\phi_{\mathrm{tot}}$. Before doing the FFT, the dc-component of the signal has been subtracted in both cases.*

nitrogen molecules aligned parallel to the driving laser polarization and using neon, $I_{\mathrm{p}} = 21.57\,\mathrm{eV} = 13.9\omega_0$, as the detection gas. The lowest order harmonic detected is thus $q_1 = 15$. Integrating the whole scan over the photoelectron energies leads to the total signal as shown in figure 2.6a. A clear peak is seen at frequency ω_0 in the squared modulus of the fast Fourier transform (FFT) (i.e. the spectral density) of this total signal and ϕ_{tot} can now be obtained by averaging the phase over the full width at half maximum (FWHM) of the ω_0-peak.

In order to remove the ω_0-modulation of the total signal as well as fluctuations, the RABITT trace is now normalized by the total signal. Then, for each sideband, integrating over its spectral width yields the sideband-signal, shown for sideband 22 in figure 2.6c. The spectral density peaks at frequency $2\omega_0$ and the phase – again averaged over the FWHM of the $2\omega_0$-peak – yields the sideband phase $\varphi_{23} - \varphi_{21} - \Delta\phi_{22}^{\mathrm{at}} + 2\phi_{\mathrm{tot}}$. It remains to subtract $2\phi_{\mathrm{tot}}$ and to correct for the atomic phases[7] to finally obtain the relative phase of harmonics 23 and 21.

The error bar to each point is given by the standard deviation of the sideband FFT phase within the FWHM of the $2\omega_0$-peak plus twice the standard deviation of the FFT phase of the total signal, within the FWHM of the ω_0-peak.

The spectral density of the sideband still shows a small peak at ω_0 despite the normalization by the total signal. This is due to some IR radiation of the HHG driving laser being diffracted in the HHG medium and thus not being blocked completely before focusing harmonics and IR probe beam into the MBES. This diffracted radiation then interferes with the probe beam, adding an additional dc and ω_0-component to the sideband signal. These do, however, not perturb the modulation at $2\omega_0$ and thus the measurement of relative phases (Dinu et al. [27]).

[7] Actually, we usually omit correcting for them, since they are very small and mainly contained within the error bars.

Magnetic Bottle Electron Spectrometer The EWPs, the characterization of which most of our experiments are based on, are generated in the small source volume of the magnetic bottle electron spectrometer (MBES). This apparatus was developed by (Kruit and Read [99]), and consists of a 'normal' time-of-flight electron spectrometer with the addition of a strong magnetic field (≈ 1 T) in the source region, which gradually reduces to $\sim 10^{-3}$ T towards the flight tube, where it remains constant. The field lines are parallel to the flight tube direction. The electrons spiral around these field lines and convert their initial velocity to longitudinal velocity, i.e. along the flight-tube direction, without, however, changing their kinetic energy. All electrons emitted in the source point which initially have a velocity component along the flight-tube direction will thus eventually reach the detector. Thus, electrons ejected with the same kinetic energy into a solid angle of 2π all arrive at the same time at the end of the flight tube. A microchannel plate detector converts the impinging electrons into a time-dependent voltage proportional to the time-dependent electron current, $\mathrm{d}N/\mathrm{d}t$, integrated over the detector area. This signal is read out with an oscilloscope.

The time-of-flight, t_{TOF}, of the electrons can be converted to kinetic energy, E_{kin}, by a suitable calibration. For our purposes, where the central energies of the electron spectral peaks are known to be given by the odd harmonic orders of the driving laser and the ionization potential, I_{p}, of the target gas, a rough calibration based on the distance, $L = 1.5$ m, between the source point and the detector, proved to be sufficient:

$$E_{\mathrm{kin}} = \hbar\omega - I_{\mathrm{p}} = \frac{m_{\mathrm{e}}}{2}\left(\frac{L}{t_{\mathrm{TOF}}}\right)^2 . \tag{2.8}$$

Here, SI units are used and m_{e} is the electron mass.

Since we detect the signal in equally spaced time-bins, it is clear that the spectral resolution of the MBES decreases rapidly with increasing kinetic energy. On the other hand, the signal-to-noise ratio increases with kinetic energy. For RABITT measurements, one usually only requires sufficient spectral resolution to discern harmonics and sidebands. In the experiment discussed in paper **V**, these constraints do, however, play a role.

The detection gas is injected directly into the MBES source volume by an effusive jet, providing a static pressure in the source region of $\sim 10^{-4}$ mbar. This ensures sufficient density for good XUV detection efficiency while avoiding space charge effects which would deteriorate the spectral resolution. The detection gas is chosen according to its ionization potential and cross section. The total, i.e. angle-integrated, ionization cross-sections of argon and neon are shown in figure 2.7. Argon detects lower harmonic orders more efficiently but from harmonic 23 on, neon is the better choice.

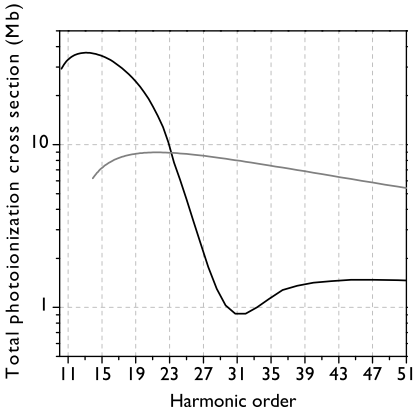

Figure 2.7. *Total photo-ionization cross sections for argon (black line) and neon (gray line) as function of the harmonic order of an 800 nm laser.*

2.4 The Experimental Setup

The setup used for the experiments presented in papers **I**, **II**, **IV**, and **V** is shown in figure 2.8. The original scheme was developed by Willem Boutu during his thesis (Boutu [12]). The work of paper **III** was partly carried out in Saclay on almost the same setup, except for the necessary additions to perform polarimetry measurements.

The heart of this setup is the Mach-Zehnder type interferometer for the RABITT measurement. Drilled mirrors separate the annular generating beam (outer diameter cut to 17 mm by an iris), which contains most of the energy (~ 1 mJ), and the weak central part ($\sim 50\,\mu$J, diameter $\approx$4 mm). The latter can be delayed by a piezoeletric translation stage with interferometric stability,

i.e. the stability of the optical path difference between the two interferometer arms has to be ~ 50 nm. In both arms, combinations of half-wave plate and polarizer allow to finely control the pulse energy. The two beams are then collinearly focused by the same lens of 1 m focal length ≈5 mm before the HHG gas jet ($F_{\#} \approx 60$ for the generating beam and $F_{\#} \approx 250$ for the probe beam). An iris then blocks the annular generating beam in the far field and the high harmonic beam together with the on-axis probe beam are focused by a broad-band toroidal gold mirror into the MBES. In its detection volume, the target gas neon, injected by a permanent leak, is photoionized by the high harmonics. With the HHG and detection gas jet running, the pressure is ~ 10^{-3} – 10^{-2} mbar in the HHG chamber, ~ 10^{-5} mbar in the toroidal mirror chamber, ~ 10^{-4} mbar in the MBES interaction volume and ~ 10^{-6} mbar in the MBES flight tube.

The stability of this interferometer is one crucial and delicate part of the experiment, the correct alignment of the toroidal mirror is the other. The optical table the RABITT interferometer is mounted on is apart from the one carrying the vacuum chambers and thus decoupled from the vibrations induced by the vacuum pumps. As for the alignment of the toroidal mirror, we image the focal spot in the MBES detection volume on a camera after the MBES. This allows to verify that (i) the focal spot of the annular generating beam (passing when the motorized iris before the toroidal mirror is opened somewhat more) is free of aberrations and (ii) this focal spot overlaps well in space and time with the central IR probe beam. This makes sure that wavefront distortions are minimized and the wavefronts of the XUV and IR probe beams are parallel.

The toroidal mirror together with the following flat mirror cause two grazing-incidence (11.5°) reflections of the HHG radiation on Au-surfaces, preferentially transmitting the s-polarized component into the MBES (with a 2:1 contrast). The generating laser is kept s-polarized while the molecular alignment axis is rotated in order to predominantly detect the HHG polariza-

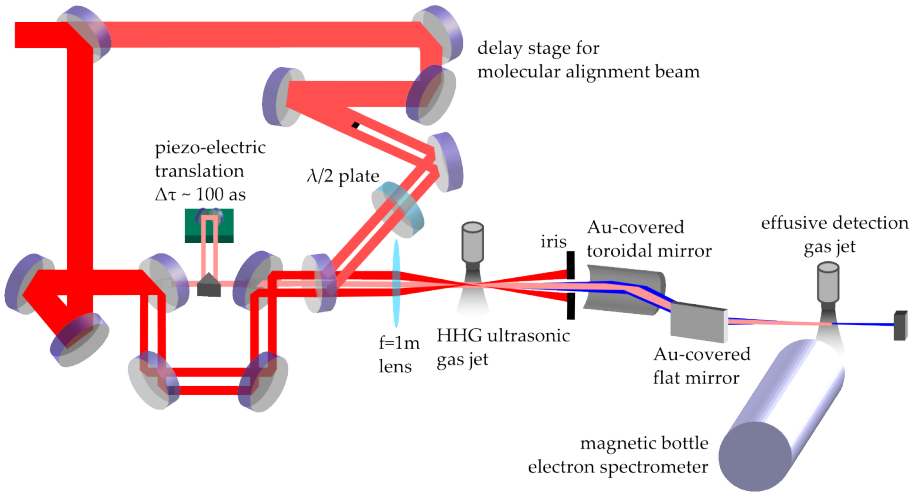

Figure 2.8. ***Setup used for the experiments discussed in chapters 3, 3.5 and 4, and papers papers I to V.*** *The laser beam enters at the upper left of the scheme. The part transmitted through the first beam splitter is the alignment beam. In the lower left part of the figure, the drilled mirror based interferometer for the RABITT measurement is depicted. Here, the large annular beam is the harmonic generating beam, whereas the small central part is the probe beam for RABITT. From the focusing lens on, the setup is placed under vacuum.*

tion component parallel to the driving laser.

To align molecules in the HHG gas jet, a third laser pulse with controllable delay, polarization and intensity is needed. To this end, a larger interferometer, based on amplitude beam splitters, is set up around the compact RABITT interferometer. One fifth of the incoming pulse energy is transmitted into the arm for the aligning beam and passes a motorized delay stage. Here, the stability requirements are much less severe than for the RABITT interferometer, since the angular distribution of the molecules varies on a $\sim 10\,\mathrm{fs}$ timescale (cp. section 2.2). The central part (≈ 4 mm diameter) of this beam is blocked so as to limit the amount of its energy passing into the MBES and thus prevent above-threshold ionization. The polarization direction of the aligning beam is set by a motorized half-wave plate, thus controlling directly the aligning angle of the molecular ensemble with respect to the generating laser polarization direction at the half-revival delay. The pulse energy in the aligning beam is limited by an iris (cutting the beam to typically 12 mm diameter), thereby limiting the aligning beam intensity to $\approx 5 \times 10^{13}\,\mathrm{W/cm^2}$ in the HHG gas jet. This also ensures that the aligning beam focal spot is larger than that of the HHG beam.

For the experiments presented in chapter 5 and paper **VI**, we generated high-order harmonics in a laser ablation plasma plume. To this end, part of the uncompressed laser output (300 ps) was split off and focused onto a a solid metal target with a lens of focal length $f = 20\,\mathrm{cm}$ ($F_\# \approx 40$). The remaining part is delayed by $\approx 80\,\mathrm{ns}$, thus requiring a $\approx 20\,\mathrm{m}$ long delay line, before being compressed to the usual 55 fs. The so modified setup is shown in figure 2.9. The major experimental difficulty was the deterioration of spatial beam quality in this long delay line, leading to a reduced attainable peak intensity in the HHG medium as well as worsened phase matching conditions. More details are given in chapter 5.

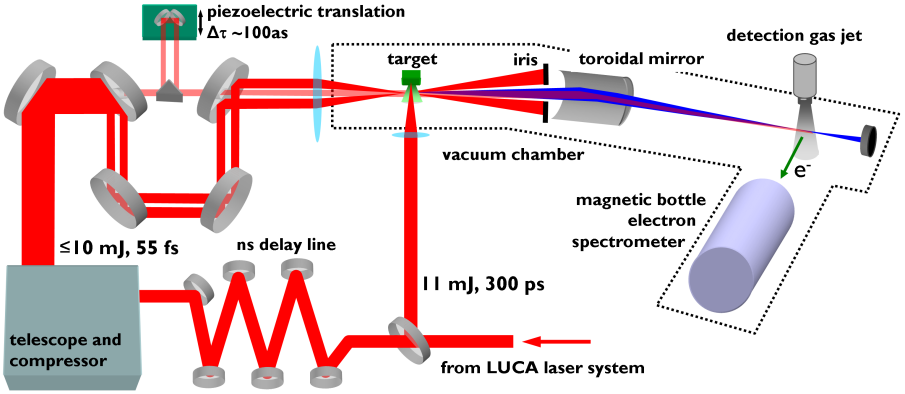

Figure 2.9. ***Setup used for the experiments discussed in chapter 5 and paper VI.*** *The RABITT-part is the same as in the standard setup shown in figure 2.8. Here, the HHG medium is an ablation plasma plume, generated by focusing part of the uncompressed laser output onto a a solid metal target. HHG and probe pulse are delayed by ≈ 80 ns.*

CHAPTER 3

SELF-PROBING OF ELECTRONS IN MOLECULES

This chapter – the most extensive of this thesis – will deal with experiments making use of the self-probing scheme, illustrated in figure 3.1. The electron-core recollision (third step of the three-step model) is considered as a probe process, where the attosecond EWP interrogates the molecule[1]. The quantity of interest in these experiments is the recombination dipole matrix element (DME) d_r. The latter is not directly measurable but extracted from a more readily accessible observable – in our case the XUV field emitted when the recollision leads to a radiative transition to the neutral ground state.

The DME, d_r, is a very interesting and rich observable because it is a complex valued vector quantity, i.e. one can in principle measure intensity and phase of its three components as a function of the recolliding electron energy and its recollision angle θ. This is plenty of information to test theoretical models. From a conceptual point of view, d_r is interesting because, if one has sufficient knowledge of the recolliding electron, one can extract information about the molecule and its dynamics.

After demonstrating how the DME can be extracted from measured XUV spectral intensities and phases, we will discuss experiments with CO_2 and N_2 molecules, also subject of papers **I** and **II**, essentially testing the methods for extracting the DME and imaging the active electronic orbital(s). In the case of N_2, we develop an interpretation revealing electron dynamics in the molecular ion on a sub-femtosecond time-scale.

In the last section of this chapter, measurements of nuclear dynamics are presented – first on a picosecond timescale for rotating N_2 molecules and finally on attosecond time scale for vibrating H_2^+ ions.

RÉSUMÉ DU CHAPITRE

Ce chapitre – le plus gros de cette thèse – traitera des expériences utilisant le schéma d'auto-sondage, illustré par la figure 3.1. La recollision électron-coeur (troisième étape du modèle en trois étapes) est considérée comme un processus de sondage, où le paquet d'ondes électronique attoseconde interroge la molécule. La quantité intéressante dans ces expériences est l'élément de matrice dipolaire de la recombinaison d_r. Ce dernier n'est pas directement

[1]Note that one can neither say that the molecular ion would be probed, nor the neutral ground state. As shown in section 3.4.3, one has to think of a somewhat more complicated object: the Dyson-orbital, which is, illustratively speaking, the result of projecting out the difference between the neutral multi-electron ground state and the multi-electron ionic state.

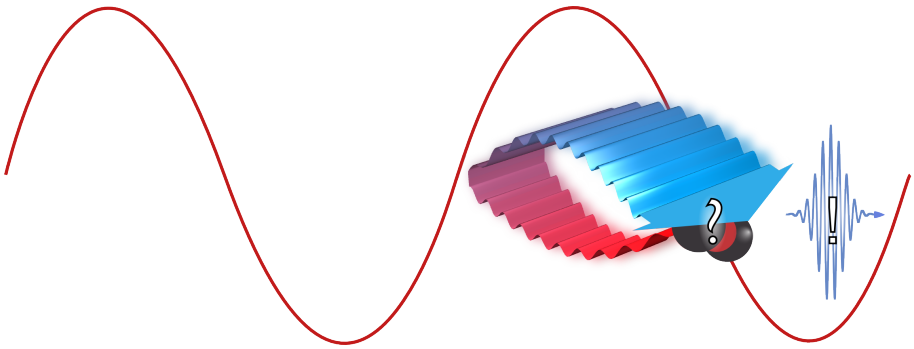

Figure 3.1. *Illustration of the Self-probing scheme.*

mesurable mais sera extrait d'une observable plus directement accessible – dans notre cas le champ XUV émis si la recollision mène à une transition radiative vers l'état fondamental neutre.

L'élément de matrice dipolaire, d_r, est particulièrement intéressant car il s'agit d'une quantité vectorielle complexe et on peut, en principe, mesurer les intensités et phases des trois composantes en fonction de l'énergie et de l'angle de recollision θ de l'électron. Cela donne des informations abondantes pour tester des modèles théoriques. D'un point de vue conceptuel, d_r est intéressant parce qu'une connaissance suffisante de l'électron recollisionnant permet d'extraire des informations sur la molécule et sa dynamique.

Dans le cadre du modèle de Lewenstein, le champ XUV émis par une molécule peut être écrit comme le produit de l'élément de matrice dipolaire de recombinaison et de l'amplitude spectrale complexe, $a(k)$, du paquet d'ondes électronique recollisionnant. L'idée centrale pour accéder à l'élément de matrice dipolaire recherché est de calibrer les amplitudes $a(k)$ avec une deuxième mesure effectuée avec un atome de référence, ayant un potentiel d'ionisation très similaire à la molécule étudiée. On se base donc sur l'hypothèse que l'amplitude $a(k)$ ne depend que très peu de la structure spatiale de l'orbitale active et est surtout déterminée par le potentiel d'ionisation: le processus d'ionisation tunnel agit comme un filtre spatial très efficace. Nous déterminons donc l'amplitude et la phase de d_r par le rapport des amplitudes et la difference des phases spectrales mesurés pour la molécule et l'atome de référence. La direction du vecteur d_r est la même que la direction de polarisation de l'émission XUV de la molécule considérée.

Résultats principaux

Nous avons mesuré les amplitudes et phases spectrales pour des molécules de CO_2 alignées, en variant θ de 0° à 90° par pas de 10°, ainsi que l'amplitude et la phase spectrale de référence dans le krypton. Ces mesures nous permettent d'extraire d_r. Nous observons un minimum d'amplitude et un saut de phase de $\lesssim 2.7$ rad autour de $\theta = 0°$, correspondant à un changement de signe de la partie réelle de d_r. Le même changement de signe est obtenu par un calul théorique pour $d_r = \langle\psi_0(\mathbf{r})|\hat{\mathbf{d}}|e^{i\mathbf{k}\cdot\mathbf{r}}\rangle$, où $\hat{\mathbf{d}}$ est l'opérateur dipolaire et ψ_0 est l'orbitale moléculaire occupée la plus élevée (HOMO) de CO_2. C'est une interférence quantique destructive entre ψ_0 et la fonction d'onde de l'électron recollisionnant qui provoque ce changement de signe. Ce resultat vient conforter la possiblité de sonder des molécules – et dans ce cas une orbitale électronique dans une molécule – par le schéma d'auto-sondage. De plus, nous démontrons comment l'interférence quantique peut être utilisée pour mettre en forme le profil temporel attoseconde de l'émission XUV.

Les mêmes données mesurées pour des molécules de N_2 (et l'atome de référence argon) s'avèrent beaucoup plus difficiles à interpréter. Nous avons développé une interprétation faisant appel à une contribution supplémentaire ajoutée à celle de la HOMO: celle de l'orbitale énergétiquement directement dessous (HOMO-1).

L'analyse des données peut être poussée plus loin en lisant $d_r = \langle\psi_0(\mathbf{r})|\hat{\mathbf{d}}|e^{i\mathbf{k}\cdot\mathbf{r}}\rangle$ comme une transformée de Fourier de l'orbitale 'active' $\psi_0(\mathbf{r})$. Une mesure de d_r pour une gamme spectrale et angulaire suffisante permet donc en principe de recontruire la fonction d'onde $\psi_0(\mathbf{r})$ par une méthode tomographique. Cette méthode et les approximations faites dans le traitement théorique seront discutées en détail, basé sur des simulations et sur des reconstructions d'orbitales à partir de nos données expérimentales. Il est important de garder en vue que nos mesures sont toujours incomplètes et que nous sommes pour le moment obligés d'imposer la symétrie des orbitale reconstruites. Pour une comparaison entre les orbitales théoriques et expérimentales, nous avons donc besoin de propriétés structurales caractéristiques autres que la symétrie qui domine l'aspect visuel.

Cela n'est pas vraiment possible pour la HOMO de CO_2 et la reconstruction expérimentale ne peut donc pas strictement être considérée comme une imagerie réussie. Pour N_2, la symétrie différente des deux orbitales actives permet de séparer leurs contributions à l'élément de matrice dipolaire total mesuré, et nous pouvons en extraire des images des deux orbitales. C'est la HOMO de N_2 qui se prête particulairement bien à une comparaison avec des simulations et nous en concluons que la reconstruction est réussie. Cela constitue une démonstration convaincante du potentiel du schéma d'auto-sondage et de la faisabilité de la tomographie d'orbitales moléculaires. Combinée à l'image de la HOMO-1, également extraite de nos mesures, nous avons en fait accès à un paquet d'ondes dépendant du temps créé lors de l'ionisation tunnel, interprété comme le trou laissé dans l'ion. Ce trou évolue sur un échelle de temps sub-femtoseconde: nous avons donc démontré la possibilité d'imager des dynamiques électroniques intra-moléculaires.

Dans la dernière partie de ce chapitre, une autre variante du schéma d'auto-sondage est appliquée à l'obervation des dynamiques nucléaires dans des molécules. L'evolution des paquets d'ondes rotationnels dans N_2 et CO_2 – au coeur de la technique d'alignment non-adiabatique utilisée dans nos expériences – peut être suivie facilement car elle se passe sur une échelle de temps picoseconde. Nous démontrons une technique capable d'augmenter le contraste de la détection d'un facteur 8 en ne détectant que la composante de polarisation des harmoniques perpendiculaire au champ laser de génération. La dynamique vibrationelle dans les molécules les plus legères, H_2 et D_2, peut être très rapide et nous utilisons la technique PACER ('Probing Attosecond dynamics by Chirp-Encoded Recollision') pour la suivre avec une résolution attoseconde. Nous avons verifié expérimentalement le lien entre la fréquence de la lumière XUV détectée et le délai attoseconde après lequel l'évolution du paquet nucléaire dans l'ion moléculaire est sondée. Théoriquement, nous démontrons comment la phase de l'émission XUV encode la dynamique nucléaire et nous comparons à nos mesures de phase.

Conclusions

Dans plusieurs exemples, le potentiel du schéma d'auto-sondage pour l'imagerie de dynamiques électroniques et nucléaires intra-moléculaires ultrarapides a pu être démontré expérimentalement. En particulier, nous avons fait les premières mesures de phase de l'émission harmonique émise par des molécules alignées. Celles-ci ont permis de confirmer sans ambiguïté

l'interprétation en termes d'interférences quantiques des mesures d'intensité spectrale faites auparavant par d'autres groupes. La tomographie d'orbitales était – et reste– un sujet vivement débattu dans la communauté. Nous avons fait des progrès majeurs du côté experimental ainsi que sur la compréhension théorique, ce qui nous amène à la conclusion que cette imagerie est bien réalisable expérimentalement. Les distortions spatiales de l'orbitale reconstruite resteront vraisemblablement importantes – comme dans nos reconstructions expérimentales – mais ne devraient pas empêcher qu'un changement ultra-rapide puisse être imagé. La perpective la plus intéressante est donc la tomographie dynamique *plutôt que l'imagerie d'orbitales statiques à haute résolution spatiale.*

3.1 Measuring the Recombination Dipole Matrix Element

In the framework of the Lewenstein model, discussed in section 1.3.3, the high-order harmonic field, $\boldsymbol{\epsilon}_{\mathrm{XUV}}(\omega)$, emitted by a single atom or a molecule is given by equations 1.37 or 1.38 in velocity or length form, respectively. We omit here the acceleration form because in general the corresponding operator is unknown. Assuming the driving laser field to be linearly polarized along the x axis, we expand the total electron wavefunction similar to the SFA ansatz 1.35 into a sum of a bound part:

$$\psi_0(\boldsymbol{r},t) = \psi_0(\boldsymbol{r})\mathrm{e}^{\mathrm{i}I_\mathrm{p}t}\,, \tag{3.1}$$

and a continuum plane-wave packet:

$$\psi_\mathrm{c}(\boldsymbol{r},t) = \int \mathrm{d}k\, a(k)\mathrm{e}^{\mathrm{i}[k\cdot r-(k^2/2)t]}\,, \tag{3.2}$$

with complex-valued amplitudes $a(k)$, including e.g. the intrinsic chirp. The electron wave vector $\boldsymbol{k} = (k,0,0)$ is parallel to the driving laser polarization direction. Neglecting, as discussed in connection with equation 1.39, bound-bound and continuum-continuum matrix elements, one finds a complex harmonic spectrum

$$\begin{aligned}
\boldsymbol{\epsilon}_{\mathrm{XUV}}(\omega) &\propto \mathcal{F}_{t\to\omega}\,\langle\psi_0(\boldsymbol{r},t)|\hat{\mathbf{d}}|\psi_\mathrm{c}(\boldsymbol{r},t)\rangle + \mathrm{c.c.}\\
&= \int \mathrm{d}t\,\mathrm{e}^{\mathrm{i}\omega t}\int \mathrm{d}k\, a(k)\,\mathrm{e}^{-\mathrm{i}(k^2/2+I_\mathrm{p})t}\,\langle\psi_0(\boldsymbol{r})|\hat{\mathbf{d}}|\mathrm{e}^{\mathrm{i}kx}\rangle + \mathrm{c.c.}\\
&= 2\pi\int \mathrm{d}k\, a(k)\,\langle\psi_0(\boldsymbol{r})|\hat{\mathbf{d}}|\mathrm{e}^{\mathrm{i}kx}\rangle\,\delta_\mathrm{D}(k^2/2+I_\mathrm{p}-\omega)\\
&= 2\pi\, a(k)\,\langle\psi_0(\boldsymbol{r})|\hat{\mathbf{d}}|\mathrm{e}^{\mathrm{i}kx}\rangle \qquad \text{for } \omega = k^2/2+I_\mathrm{p}\,,
\end{aligned} \tag{3.3}$$

where only positive XUV frequencies ω have been considered and the dipole operator is $\hat{\mathbf{d}} = \boldsymbol{r}$ in length form and $\hat{\mathbf{d}} = -\mathrm{i}\nabla_{\boldsymbol{r}}$ in velocity form. Note that the above laser-field-free derivation is only 'intuitive' – for a more rigorous analysis, see (**?**]). The single-emitter XUV field $\boldsymbol{\epsilon}_{\mathrm{XUV}}$ is thus proportional to the product of the recombination DME and the complex valued continuum EWP amplitude. The latter contains both the result of the tunnel-ionization and the continuum acceleration step. This remarkably simple result has first been noted by (Itatani et al. [80]) and has later been more firmly established by (Le et al. [102, 103]) for rare gas atoms and the simplest of all molecules, H_2^+. For good agreement between exact [2] TDSE simulations and the result of equation 3.3, however, the plane-wave DME, appearing in the Lewenstein model, has

[2] For the rare gases, well established single-active-electron pseudo-potentials have been used.

to be replaced by a more accurate version, including exact scattering waves. Equation 3.3 should thus be re-written as

$$\boldsymbol{\epsilon}_{\mathrm{XUV}}(\omega) = \eta\, a(k)\, \langle \psi_0(\boldsymbol{r}) | \hat{\mathbf{d}} | k \rangle\,, \qquad \omega = k^2/2 + I_\mathrm{p}\,, \tag{3.4}$$

where η is a proportionality constant, essentially describing an overall tunneling probability, and the scattering state $|k\rangle$ is labeled by the asymptotic momentum (in the driving laser polarization direction, x) of the continuum electron. The wave packet amplitudes, $a(k)$, can still be calculated with the SFA.

In the theoretical study of (Le et al. [102, 103]) it was found that these amplitudes, $a(k)$, essentially depend on the driving laser field but *not* on the precise structure of the ground state, except for a constant scaling factor, which is included in η. The tunnel ionization step thus acts as a strong spatial filter.

This directly leads to a scheme, proposed by (Itatani et al. [80]), where the recombination DME for a system under study – in our case a molecule – can be measured by calibrating the continuum EWP amplitudes in a measurement with a suitable known reference system. 'Known' means that the DME can be calculated accurately, as is the case for rare gas atoms. This is based on using the expressions 3.3 and 3.4 for the *macroscopic* XUV field $\boldsymbol{E}_{\mathrm{XUV}}$ – an experimental observable. The validity of doing so has very recently been studied theoretically by (Jin et al. [82]), concluding that in reasonably good phase matching conditions, one can just replace the EWP amplitude $a(k)$ by a 'macroscopic' EWP amplitude $\tilde{a}(k)$ that is largely independent of the medium. 'Reasonably good' means that the free electron density and absorption should negligible, which is the case in out experiments (cp. section 2.1). Experiments by (Levesque et al. [116]) with rare gas atoms confirm this result.

Thus, using a reference with the same ionization potential as the studied molecule (so that one harmonic order is associated with the same continuum electron momentum k) in the same experimental conditions (so that phase matching is the same) the macroscopic EWP can indeed be calibrated. Taking then the ratio of the measured complex XUV spectra of the studied molecule and the reference, the electron wavepacket amplitudes $\tilde{a}(k)$ will cancel out:

$$\frac{\boldsymbol{E}^{\mathrm{mol}}_{\mathrm{XUV}}(\omega)}{E^{\mathrm{ref}}_{\mathrm{XUV}}(\omega)} = \frac{\eta_{\mathrm{mol}}\, \langle \psi_{\mathrm{mol}}(\boldsymbol{r}) | \hat{\mathbf{d}} | k \rangle}{\eta_{\mathrm{ref}}\, \langle \psi_{\mathrm{ref}}(\boldsymbol{r}) | \hat{\mathrm{d}}_x | k \rangle}\,. \tag{3.5}$$

Note that we divide here by a scalar: the XUV field emitted by an atom is polarized parallel to the driving laser and thus to the electron re-collision direction $\boldsymbol{k}/k \parallel x$, and we normalize by this component. The orbitals $\psi_{\mathrm{mol}}(\boldsymbol{r})$ and $\psi_{\mathrm{ref}}(\boldsymbol{r})$ are of course oriented in some way in the laboratory frame. As for the reference atom, the laser polarization direction, x, also fixes the quantization direction. The reference atoms used in the experiments presented in this thesis are argon and krypton, for which the relevant orbital is 3p or 4p, respectively. For symmetry reasons, only the p_x-orbitals will contribute to HHG[3], so these are used for the calculation of the matrix element. For the (linear) molecule, the internuclear axis imposes the quantization direction and this axis can be aligned with respect to the laser field at an angle θ. The matrix element is thus θ-dependent and so is η. Writing the complex XUV spectra as in equation 2.5, i.e. splitting them into spectral amplitudes $A(\omega)$ and phases $\varphi(\omega)$, one can write the sought-for molecular DME as

$$\langle \psi_{\mathrm{mol}}(\theta) | \hat{\mathbf{d}} | k \rangle = \hat{\boldsymbol{n}}_{\mathrm{mol}}(\omega,\theta) \frac{\eta_{\mathrm{ref}}}{\eta_{\mathrm{mol}}(\theta)} \frac{A_{\mathrm{mol}}(\omega,\theta)}{A_{\mathrm{ref}}(\omega)} \mathrm{e}^{\mathrm{i}[\varphi_{\mathrm{mol}}(\omega,\theta) - \varphi_{\mathrm{ref}}(\omega)]} \times \langle \psi_{\mathrm{ref}}(\boldsymbol{r}) | \hat{\mathrm{d}}_x | k \rangle\,. \tag{3.6}$$

[3] This was experimentally demonstrated by (Shafir et al. [184]) for neon and its 2p orbitals

The spectral amplitudes, $A_{\mathrm{mol}}(\omega,\theta)$ and $A_{\mathrm{ref}}(\omega)$, and phases, $\varphi_{\mathrm{mol}}(\omega,\theta)$ and $\varphi_{\mathrm{ref}}(\omega)$, for the molecule at some alignment angle θ and the reference atom, respectively, can be measured in two separate RABITT scans, keeping the same experimental conditions. The measurement of the polarization state, $\hat{\boldsymbol{n}}_{\mathrm{mol}}(\omega,\theta)$, of the harmonics emitted by the aligned molecule requires a separate experiment, as demonstrated e.g. in paper **III** for nitrogen. As mentioned in section 2.4, in our setup, the component of the XUV light parallel to the driving laser is transmitted preferentially to the detector. We make the approximation that the polarizing elements are perfect and assume to measure *only* this component and thus access in our measurements the molecular recombination DME projected onto the driving laser polarization direction. The ionization probabilities could be measured in a separate experiment as well [4], or calculated with ADK theory.

3.1.1 Sticking to the Plane-Wave Approximation

The computation of exact scattering states $|k\rangle$ is much harder than for bound states but it is becoming possible today. The 'exact' photo-*ionization* DME used by (Le et al. [102, 103]) contain characteristic features, notably intensity spikes and phase jumps at resonances (shape resonances and auto-ionizing resonances like that discussed in section 4.1) induced by the precise shape of the potential landscape seen by a continuum electron. Many of these features are, however, spectrally very sharp and it would be worth studying whether such features would not disappear in photo-*recombination* DME relevant to HHG. This is because for the (short) quantum paths relevant to a macroscopic HHG signal (see page 25), the electron spends less than a laser cycle in the continuum. One would expect that sharp features, often associated with multiple-scattering, can simply not develop during so short times. The result would then be that in HHG, one is sensitive to a strongly smoothed DME as compared to photo-ionization. Note that this does not violate the detailed-balance principle stating that photo-ionization is nothing else but reversed photo-recombination and that the corresponding DMEs are simply the complex conjugate of one another. It is the difference in the involved timescales (in photo-ionization, one considers the ejected electron long after the interaction is over whereas in HHG the electron spends only ≈ 1.5 fs in the continuum) that would lead to differences in the relevant DME. Note also that shape resonances are strongly aligned along the molecular axis and may be smoothed out by the angular distributions provided by non-adiabatic alignment in our conditions.

Thus, for the sake of simplicity as well as due to lack of more appropriate description, we will in the theoretical treatment stick to plane waves: $|k\rangle = \exp[\mathrm{i}kx]$. This will also have the great advantage, that the matrix elements will take the form of a Fourier transform with all its handy symmetry properties.

As we argue in paper **II**, a first correction for the error introduced by coming back to plane waves is a heuristic adjustment of the relation between the frequency ω of the high order harmonic emission and the electron energy $k^2/2$. Equation 3.4 states $\omega = k^2/2 + I_{\mathrm{p}}$, which is true for the *asymptotic* value of k, i.e. far from the potential of the core. Close to the core, where the interference between the re-colliding continuum electron and its bound state generates the XUV radiation, $k^2/2$ will have increased due to the acceleration into the core

[4] In such an experiment, it is, however, not immediately clear how to separate multi-photon absorption (i.e. above-threshold ionization) from tunnel ionization, which is the process relevant to HHG.

potential, which has a depth of approximately I_p. Thus, the heuristic relation $\omega = k^2/2$ is often used.

3.1.2 Two-center Interference

Which obvious features can be expected to appear in those molecular DMEs and how can they be easily related to the molecular structure? Consider a simple, diatomic, mono-nuclear molecule whose HOMO can be written as an antisymmetric combination of two atomic orbitals: $\psi_\mathrm{mol}(\theta) = \phi_0(\boldsymbol{r} - \boldsymbol{R}/2) - \phi_0(\boldsymbol{r} + \boldsymbol{R}/2)$, where $\boldsymbol{R}$ is the internuclear distance vector, making an angle θ with the driving laser polarization direction and thus with the re-colliding electron wave vector $\boldsymbol{k} = (k, 0, 0)$. The recombination DME in velocity form then reads:

$$\langle \psi_\mathrm{mol}(\theta) | \hat{\mathbf{d}} | \mathrm{e}^{\mathrm{i}\boldsymbol{k}\cdot\boldsymbol{r}} \rangle = 2\mathrm{i}\boldsymbol{k} \sin\left(\frac{kR}{2}\cos\theta\right) \langle \phi_0(\mathbf{r}) | \mathrm{e}^{\mathrm{i}\boldsymbol{k}\cdot\boldsymbol{r}} \rangle \,. \tag{3.7}$$

This result is simply a consequence of the Fourier shift theorem. Obviously, destructive quantum interference, i.e. a sign change of the recombination DME, occurs for

$$R\cos\theta = n\lambda_e, \tag{3.8}$$

where n is an integer and $\lambda_e = 2\pi/k$ is the electron de Broglie wavelength. Destructive interference thus occurs if the re-collinding electron wavelength is equal to the internuclear distance projected on the recollision direction. The molecule thus behaves like a two-point emitter whose emissions are dephased due to i) the path difference between the centers, ii) the symmetry of the orbital.

If, instead, one considers an symmetric combination of atomic orbitals, $\psi_\mathrm{mol}(\theta) = \phi_0(\boldsymbol{r} - \boldsymbol{R}/2) + \phi_0(\boldsymbol{r} + \boldsymbol{R}/2)$, one finds along the same lines destructive interference for:

$$R\cos\theta = \left(n - \frac{1}{2}\right)\lambda_e \,, \tag{3.9}$$

i.e. if *half* the re-collinding electron wavelength is equal to the internuclear distance projected on the recollision direction. The latter relation together with the heuristic dispersion relation $\omega = k^2/2$ predicts an interference position in the harmonic spectrum that agrees well with that obtained from TDSE simulations (Ciappina et al. [19], Kamta and Bandrauk [84]) for H_2^+.

Such destructive interference, i.e. a recombination DME going through zero and changing phase by π, should leave a clear trace in the high harmonic spectrum of aligned molecules. This was first observed in numerical experiments by (Lein et al. [110, 111]), who solved the TDSE for H_2^+ and indeed observed minima in the spectral intensity and phase jumps of $\approx \pi$ value at the positions predicted by equation 3.9.

Note that the recombination DME in length form can be expressed in a similar, yet more complicated form as equation 3.7. It also presents a sign change, but not necessarily at the same position as in velocity form, which is due to the error introduced by using plane waves in the model (cp. the discussion of different forms of the DME in section 1.3.3).

3.2 CO_2 Experiments

For an experimental observation of this interference effect, a 'candidate' molecule has to be found, which can be well aligned and has a combination of I_p and internuclear distance R, allowing the interference position to fall within the observable range of harmonic orders.

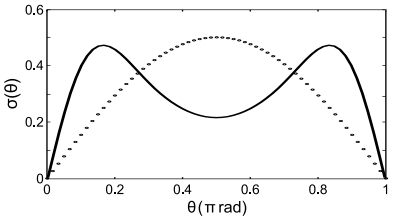

Figure 3.2. *Angular distribution of CO_2 molecules (full line) at the half-revival, τ = 21.1 ps, calculated for the conditions of our experiments, i.e. are the same parameters as in figure 2.2. The distribution peaks at $\theta = 30°$. For comparison, an isotropic distribution is shown (dotted line).*

The CO_2 molecule, although triatomic, is a good prototype for the simple two-center model as its HOMO is a Π orbital essentially formed by an antisymmetric combination of two p orbitals centered on the oxygen atoms (cf. figure 1.6). It thus comes as no surprise that the plane-wave recombination DME calculated with the CO_2 HOMO, shown in figure 1 of paper **I**, presents a sign change that agrees very well with the prediction of equation 3.8, except for a small shift. This deviation is ascribed to the admixture to the HOMO of the d_{xy} (x along the internuclear axis) carbon orbital (7%), and also to a lesser extent of the d_{xy} oxygen orbitals (2%). The dipole contribution of the d_{xy} carbon orbital obviously does not present any interference. As for the d_{xy} oxygen orbitals, they contribute to the total HOMO as a symmetric combination and thus give rise to a destructive interference following equation 3.9.

For $\theta = 0$, the predicted interference position is harmonic 23 if $\omega = k^2/2$ is used, falling into an easily observable spectral range. Moreover, with krypton, a suitable reference atom exists: $I_p^{Kr} = 14.00\,\text{eV} \approx I_p^{CO_2} = 13.77\,\text{eV}$.

In measured harmonic intensities, alignment-dependent minima have been observed by (Kanai et al. [86], Vozzi et al. [206]), but as pointed out by (Le et al. [101]), these could be explained by the interplay between the angular distributions of the partially aligned molecules and the angle-dependence of the harmonic yield. For a more convincing observation of two-center quantum interference, it is thus required to also observe the spectral phase of the high harmonic emission.

We have measured, using the setup shown in figure 2.8, the spectral intensity and phase for CO_2 molecules aligned at angles from $\theta = 0$ to $\theta = 90°$, in steps of 10°, as well as for krypton under the same experimental conditions. The angular distribution of the CO_2 molecules in this experiment (i.e. at the half-revival, τ = 21.1 ps), shown in figure 3.2, peaks at $\theta = 30°$.

Applying equation 3.6, we can extract the recombination DME for CO_2 as a function of the alignment angle. Since the ratio of overall ionization probabilities $\eta_{ref}/\eta_{mol}(\theta)$ is real-valued and varies smoothly with angle, and the Kr dipole, $\langle\psi_{ref}(\theta)|\hat{\mathbf{d}}|e^{i\boldsymbol{k}\cdot\boldsymbol{r}}\rangle$, presents a smooth behaviour with k, the essential features of the CO_2 dipole, $\langle\psi_{mol}(\theta)|\hat{\mathbf{d}}|e^{i\boldsymbol{k}\cdot\boldsymbol{r}}\rangle$, should directly show up in the experimental data. Note that the normalization of the CO_2 measurements by a krypton measurement under the same experimental conditions also corrects for any possible influence of the experimental apparatus possibly not corrected for during the usual data analysis procedure.

The observation of a phase jump at the same spectral position as the intensity minimum (harmonic 23) is one of the major results we present in paper **I**. This position also agrees with that of the sign change in the theoretical plane-wave DME for the CO_2 HOMO if the dispersion relation $\omega = k^2/2$ is used. We find that the emission times for CO_2 molecules aligned perpendicular to the driving laser polarization are in perfect agreement with those measured with krypton, thus verifying that the continuum dynamics of the EWP are the same for the reference atom and the molecule. When aligning the molecules parallel to the driving laser polarization, the phase jumps by 2.0 ± 0.6 rad. This value is averaged over 8 independent RABITT scans for $\theta = 0$ and the measurement shown in figure 2 in paper **I** is the extreme case. When the molecules are rotated away from parallel alignment, the phase jump decreases and finally disappears completely from $\theta = 30°$ on (cp.figure 3 in paper **I**).

The observed phase jump is not sudden but rather stretched out over two harmonic orders, as opposed to the theoretical plane wave dipole which is purely real-valued and changes its sign, corresponding to a sudden π phase jump. A convolution with the real-valued alignment distribution cannot explain the decreased and stretched phase jump, corresponding to a complex-valued DME. As we argue in paper **I**, this deviation may be due to the dis-

tortion of the re-colliding EWP by the core potential, i.e. due to the exact scattering states which are not included in the model. Indeed, (Ciappina et al. [19])observed such smoothed and reduced phase jumps when using Coulomb waves in SFA simulations for H_2^+.

Very recently, (Chirilă and Lein [18]) reported an additional explanation of the smoothness of the structural phase jump. An SFA calculation for H_2^+ *without* stationary phase approximation for the momentum integration in equation 1.41 yielded a smoothed $\approx \pi$ phase jump. The uncertainty in the recombination momentum due to non-saddle-point dynamics in the full SFA stretches the phase jump further than is expected from Coulomb distortion effects, without, however, significantly reducing its size. This effect, which remained unseen in HHG with atoms and is now detected for the first time in molecules, thus complements the conclusions reported in paper **I**.

3.2.1 Details on the Data Analysis

These results are obtained from a series of RABITT measurement with CO_2 molecules aligned at different angles as well as one RABITT scan with krypton under the same experimental conditions. From these scans, harmonic intensities, i.e. the square of the amplitudes $A_{\mathrm{mol}}(\omega,\theta)$ and $A_{\mathrm{ref}}(\omega)$ are extracted, as well as emission times, $\partial\varphi/\partial\omega$ (cp. equation 2.7). Already in the measured emission times, shown in figure 3.3a,b and figure 2 of paper **I**, a phase jump is clearly apparent as a 'hump' of the emission times superposed on the linear increase of emission times with harmonic order typical for the short trajectory contribution to HHG and studied in detail by (Mairesse et al. [127]). In order to apply equation 3.6, we need to integrate these emission times to obtain the spectral phases $\varphi_{\mathrm{mol}}(\omega,\theta)$ and $\varphi_{\mathrm{ref}}(\omega)$.

Fluctuations of the absolute timing At this step, special care needs to be taken: Small fluctuations within the error bars of the emission times accumulate to large errors on the obtained phase. The most important source of such errors is the absolute timing, i.e. the absolute position of the emission time curve on the time-axis. It is determined by the measurement of ϕ_{tot} (cp. section 2.3) and is found to be rather sensitive to fluctuations of experimental conditions. It systematically shifts, in every generation gas, molecular or atomic, as soon as significant free electron densities occur in the HHG medium. Increasing the HHG intensity or increasing the medium density have the same effect. The attochirp, i.e. the slope of the emission time vs. harmonic order curve, remains unaffected while its absolute position moves. These shifts can become quite important (several hundreds of attoseconds) when ionization in the HHG medium is strong. In a series of RABITT scans, however, the absolute timing fluctuations remain fairly small (typically ±50 as), see figure 3.3a. Since we have never observed a systematic shift of the absolute timing with the molecule alignment angle, we are sure that the observed shifts are a measurement error rather than a real single-molecule effect. Albeit being small, these fluctuations induce rather large errors in the integration to obtain the spectral phases, which is why we usually remove them. To this end, we choose a sideband order where the fluctuation of the emission time is small – in general the lowest order – and add a constant value to every curve of the series such that the emission time for the chosen sideband agrees for all curves and is equal to the average value over the fluctuating values. A result is shown in figure 3.3b.

We assume, that these fluctuations are no single-emitter effect but rather a macroscopic one as indicated by their dependence on the medium ionization. (Dinu et al. [27]) have analyzed the issue of phase drifts between the

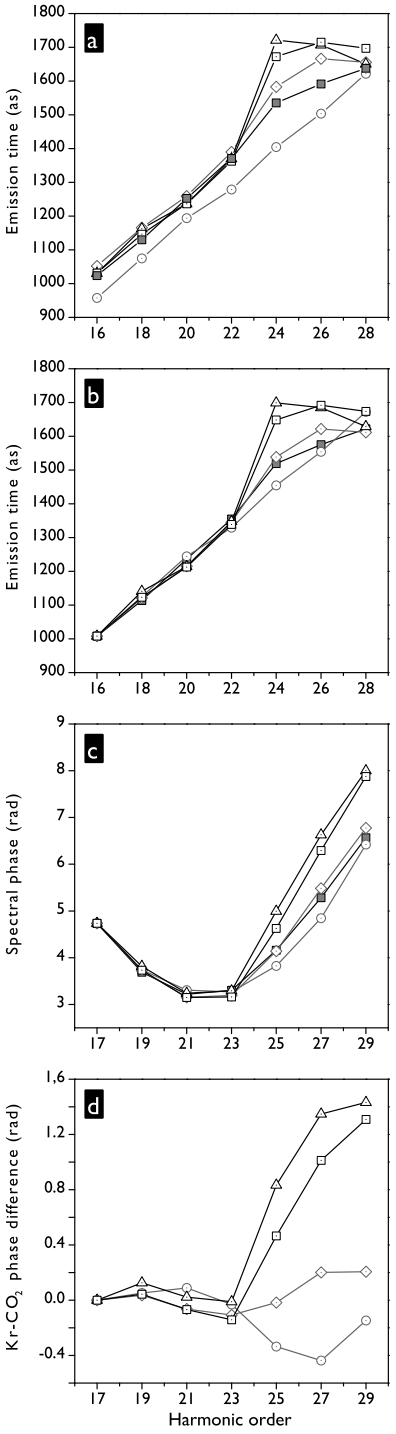

Figure 3.3. *The steps of data analysis: from the measured emission times to the DME phase. These data are some of those plotted in figure 3 in paper **I**: Krypton (■), CO_2 aligned at θ = 0° (⊡), 10° (△), 30° (◇) and 90° (⊙). Emission times as measured (a), Emission times with normalized absolute timing (b), phase obtained by integrating the emission times (c), CO_2-phases normalized by the krypton phase (d). Error bars are omitted for clarity; they have about the size of the symbols.*

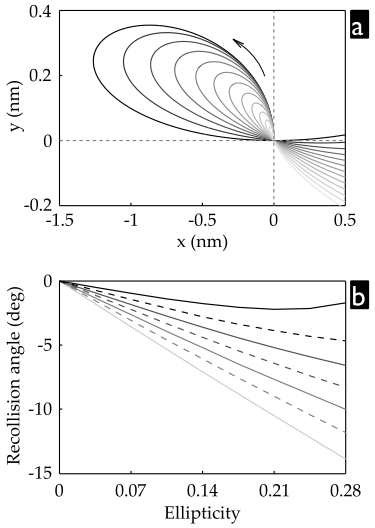

Figure 3.4. *Classical electron trajectories (a) in a driving laser field with ellipticity $\epsilon = 0.28$ and an intensity of 1.8×10^{14} W/cm^2. Only some of the short trajectories are shown here, and the longer and darker the line, the higher the re-collision energy, i.e. the higher the associated harmonic order. The longest of the trajectories shown here corresponds to the cut-off harmonic 29. The arrow indicates the direction of propagation. Panel (b) shows the re-collision angles α as a function of ellipticity for a constant intensity, where the lines from brighter to darker gray and larger to smaller $|\alpha|$ are for harmonics 17 to 29.*

IR driving and probe fields on the way between HHG medium (where the interference serving for the measurement of absolute timing occurs) and the detector (where the interference serving for the measurement of the attochirp takes place) and concluded that these will be negligible. Additional terms in the argument of the 'RABITT-cosine' in equation 2.6, owing to the different intensity depedence of the phase of different harmonic orders (and thus different 'harmonic chirps' in the language used by (Varjú et al. [203])) are expected to be too small to account for the observed shift. The same conclusion can be drawn for the influence of phase matching in the HHG medium, simulated with the model described by (Ruchon et al. [171]).

We assume that this shift is a distortion induced by the influence of the free electron dispersion in the HHG medium on the IR probe beam. Another possibility could be the perturbation of the IR probe beam in the detection region by part of the IR driving beam, diffracted due to a free electron density gradient in the HHG medium and thus passing the iris that is supposed to block it.

The integration constant A second point to discuss in connection to the calculation of the spectral phases $\varphi_{\mathrm{mol}}(\omega, \theta)$ and $\varphi_{\mathrm{ref}}(\omega)$, is the integration constant. As mentioned in section 2.3, RABITT measures the derivative of the spectral phase with respect to the XUV frequency, not the spectral phase itself. Methods exist to measure the θ-dependence of the phase at a particular harmonic order, which would give the complementary information to the RABITT result. One of these is based on far field interference of the XUV emission from aligned molecules with that of a reference, such as an unaligned sample of the same molecules (Mairesse et al. [129], Smirnova et al. [186], Zhou et al. [220]). Another one is based on HHG in a gas mixture (Kanai et al. [88, 90], Wagner et al. [211]), where the contributions of both species interfere in the macroscopic signal and their relative phase can be extracted if those contributions are known from a measurement in the pure gases. With both these techniques, no significant variations of the spectral phase of low harmonics, such as $q = 15$ with the alignment angle θ has been observed (Mairesse et al. [129], Wagner et al. [211]). We thus set the integration constant to zero for every angle when calculating the spectral phases from the measured emission times. Figure 3.3c shows the phases obtained by integration of the emission times in figure 3.3b. The integration is performed as a simple summation of the sideband phases, equal to $t_e 2\omega_0$, where the phase of harmonic 15 is set to zero for all angles and for the krypton scan. According to equation 3.6, subtracting the phase for krypton from the phase for CO_2 at the different angles θ finally yields the phase of the DME, shown in figure 3.3d and figure 3 of paper **I**.

3.2.2 Adding Ellipticity

A second way to observe the dependence on the re-collision direction of the quantum interference in the recombination DME is to use a driving laser with elliptical polarization, i.e. with a field $\boldsymbol{E}_{\mathrm{IR}} = (E^{\mathrm{x}}, E^{\mathrm{y}}) = (E_0 \cos(\omega_0 t), \epsilon E_0 \sin(\omega_0 t))$, where ϵ is the ellipticity. Classsical electron trajectories in such a field can be calculated in the way discussed in section 1.3.2, only that here, the calculation has to be done in two dimensions, x and y. The initial condition $x(t_{\mathrm{i}}) = y(t_{\mathrm{i}}) = 0$ obviously remains unchanged, as does $\dot{x}(t_{\mathrm{i}}) = 0$. Additionally, we demand that the trajectory be closed, $x(t_{\mathrm{r}}) = y(t_{\mathrm{r}}) = 0$, which is possible only if the electron has a non-zero initial velocity component in the y-direction, $\dot{y}(t_{\mathrm{i}})$. The pair $(t_{\mathrm{i}}, t_{\mathrm{r}})$ is fixed by the x-component of the trajectory, as in section 1.3.2, and $\dot{y}(t_{\mathrm{i}})$ is then fixed by the

condition $y(t_r) = 0$. For a laser intensity of 1.8×10^{14} W/cm^2 and an ellipticity $\epsilon = 0.28$, this leads to the trajectories shown in figure 3.4a. The direction of the velocity vector at the re-collision instant, $(\dot{x}(t_r), \dot{y}(t_r))$, corresponds to the re-collision angle, α, shown in figure 3.4b. Obviously, for the cut-off harmonics, the y-component of the velocity at re-collision vanishes and the re-collision angle approaches $\alpha = 0°$. In the plateau, lower harmonics are associated with a larger (modulus of the) re-collision angle α, where the sign of α is different for short and long (not shown in figure 3.4) trajectories. Varying the ellipticity thus corresponds to a control of the continuum electron trajectories and is a means to vary the re-collision angle.

Experimentally, we added a a half-wave plate followed by a quarter-wave plate to the setup shown in figure 2.8, between the drilled mirror recombining HHG and probe beam and the beam splitter recombining the two with the aligning beam. If the laser polarization direction is along the x-direction (corresponding to s-polarization in our setup), orienting the fast axis of the half-wave plate at an angle δ from the x direction, laser polarization is rotated by 2δ. With the fast axis of quarter-wave plate along the x-direction, it imposes an ellipticity $\epsilon = \tan(2\delta)$ upon the laser beam, with the major axis of the ellipse along the x-direction.

The measured spectral intensity of harmonics 21 to 31, generated in CO_2 aligned at $\theta = 0°$ and $\theta = 90°$, is shown in figure 3.5 as function of the ellipticity. Each curve was normalized to the average value of the intensities measured with the three lowest ellipticity values, i.e. $\epsilon = 0$ and $\epsilon = \pm 0.035$. The HHG intensity in this experiment was $I = 1.25 \times 10^{14}$ W/cm^2. For harmonics 21 and 23, the ellipticity dependence is the same at both parallel and perpendicular alignment. The harmonic orders 25 and 27, in contrast, show a strong difference: For parallel alignment, the signal of H25 is barely affected up to $\epsilon = 0.014$, for H27 even up to $\epsilon = 0.21$, whereas for perpendicular alignment, the harmonic yield shows the same dependence as the lower orders. Similar results have been reported by (Vozzi et al. [206]).

A possible interpretation is that at these orders, 25 and 27, destructive quantum interference occurs for molecules aligned parallel to the recollision direction for $\epsilon = 0$. As the ellipticity is increased, the re-collision angle, initially zero, increases and the destructive interference gets weaker. This seems to compensate for the drop of signal due to the decreasing probability of a non-zero y-component of the initial electron velocity, which dominates the curves for $\theta = 90°$ and the low harmonics. From a certain ellipticity value on, the re-collision angle has increased to a value that shifts the respective harmonic order out of 'resonance' with the interference condition. This obviously happens at higher ϵ for the higher harmonic, 27, and one would expect a signal suppression due to destructive interference to appear at harmonic 29. Due to the low signal-to-noise ratio for the H29 signal, this is, however, not clearly visible. A quantitative comparison between the experiment and the classical calculation [5] is probably not justified, as classical trajectories are not precise enough (cp. figure 1.9), all the more so close to the cut-off region. The classical calculation in figure 3.4 had to be done with a higher intensity than that actually estimated in the experiment, because otherwise the classical cut-off would have limited the calculation to orders 23 and below. The qualitative trend, however, should be valid.

RABITT measurements in these conditions were only possible up to $\epsilon = 0.175$ and the low signal posed serious signal-to-noise problems. Figure 3.6 shows for increasing ellipticity the ratio of spectra obtained with CO_2 aligned

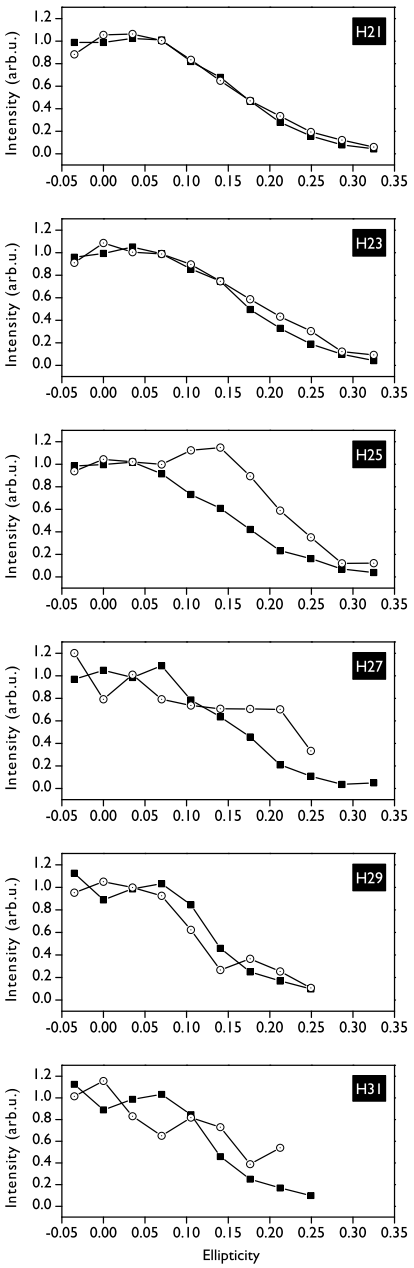

Figure 3.5. *Dependence of the normalized intensity of harmonics 21 to 31 generated in CO_2 aligned at $\theta = 0°$ (⊙) and $\theta = 90°$ (■) on the driving laser ellipticity. These results are obtained in the same experimental conditions as the data shown in figure 2 of paper* ***I****, i.e. with an intensity of $I = 1.25 \times 10^{14}$ W/cm^2. This reproduces the result reported by (Vozzi et al. [206]), but with a lower interference position at harmonic 25.*

[5] One could compare the re-collision angle found for H25 at $\epsilon = 0.175$ with the angular width of the alignment distribution, shown in figure 3.2, and conclude that interference should still be dominating.

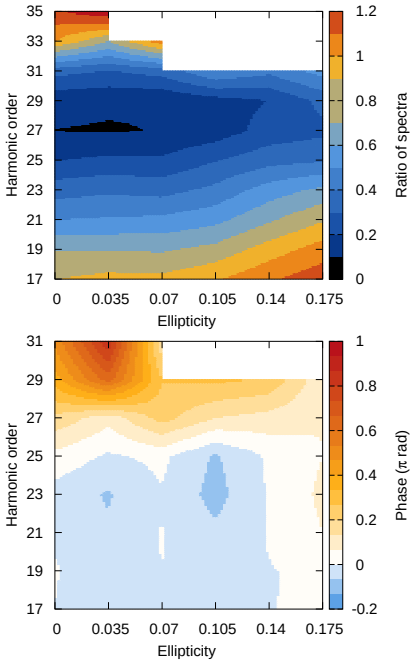

Figure 3.6. *Harmonic spectra measured with CO_2 aligned at $\theta = 0$, normalized by those measured with $\theta = 90°$ (upper panel), and difference of spectral phase $\varphi_{CO_2}(\omega, \theta = 0°) - \varphi_{CO_2}(\omega, \theta = 90°)$ (lower panel), as function of the driving laser ellipticity. The white area in the upper right of both plots notes missing data – at higher ellipticities, the highest harmonic orders can no longer be detected reliably. Note that the phase is plotted up to harmonic 31 only, whereas the spectral ratio is plotted up to H35.*

at $\theta = 0°$ and $\theta = 90°$ and the difference of harmonic spectral phases between those two cases. This corresponds to using the perpendicular-aligned CO_2 as a reference system in equation 3.6, which is not unreasonable since at this alignment, CO_2 gives very similar results to krypton (cp. figure 3.3 and paper **I**). The expected spectral minimum and phase jump are detected at harmonic 25–27. Similar to the data shown in figure 3 of paper **I**, it is not very clear whether one can say that a shift of the interference features to higher orders with increasing ellipticity is observed, or rather a vanishing without a shift. On the other hand, these ellipticity values are quite low and since the interference position is rather close to the spectral cut-off, one would not expect an important increase of the re-collision angle with ellipticity.

3.2.3 Question Marks

So far, the observations presented here and in paper **I** could be successfully explained by quantum interference in the recombination step. With our experimental conditions, the spectral minimum and phase jump are in the cut-off region and we cannot clearly observe their shift to higher harmonic orders as the alignment (or re-collision) angle increases, which is predicted by equation 3.8. We do, however, observe the disappearance of these traces of quantum interference with increasing angle. (Mairesse et al. [130]) have used shorter driving laser pulses and only measured the harmonic intensity, which allowed them to increase to intensity further than in our case before being hampered by strong ionization in the HHG medium. They were able to clearly see the interference minimum shift with angle, shown in figure 5 in (Mairesse et al. [130]).

Missing sign change? A second problematic point is the fact that the theoretical DME in figure 1 of paper **I** changes sign from one quadrant to another, i.e. when crossing $\theta = 0°$ and $\theta = 90°$. This sign change is due to the π-symmetry of the CO_2 HOMO (see section 3.4.2). There are two reasons why such a sign change does not appear in our data: We measure the frequency-derivative of the spectral phase, not the spectral phase itself, i.e. we measure the change of the dipole phase only along the radial direction in figure 1 of paper **I**. A sign change, and thus π phase jump, of the dipole for all electron energies from one angle to another, i.e. in the polar direction of figure 1 of paper **I**, is simply not detectable with RABITT. Actually, this sign change of the plane-wave dipole is probably not detectable in the high harmonic emission at all; or at least not without special arrangements. This is because we apply a *self*-probing scheme: in the recombination step of HHG, the orbital is not probed by an external plane wave, but by part of the *same* electron wavefunction that has been teared away by the strong laser field. This part stems from outermost 'tail' of the bound state orbital in the laser field direction at the tunneling instant, i.e. if the orbital changes sign from one angle to another, so does the EWP. In the recombination dipole, formed by interference of the bound state orbital and the EWP, the sign will thus always be the same. In brief: As long as the continuum EWP is driven by a linearly polarized laser field, the π-symmetry of the HOMO will not show up in the HHG recombination dipole. Finding ways to experimentally detect this fundamental symmetry of the active orbital is an interesting problem. The work of (Shafir et al. [184]) opens this perspective, based the control of the continuum electron trajectory by the addition of a weak, perpendicularly polarized second harmonic laser field. Illustratively, thinking in terms of classical trajectories, one can imagine to make the electron exit from one orbital lobe and steer it to recombine on another. This technique is currently being explored by Dror Shafir and

Nirit Dudovich at Weizmann Institute in Isreal as well as Hiromichi Niikura at NRC Canada.

Intensity dependent interference position? There is nonetheless one point that remains unsettling with regard to the quantum interference interpretation. The position of the spectral minimum and the phase jump found in our experiments shift towards higher XUV frequencies with higher HHG intensity. We could not explore a large intensity range since at low intensity ($I \lesssim 7 \times 10^{13}\,\mathrm{W/cm^2}$), the signal quickly gets too weak to perform RABITT scans. Note that, in contrast to N_2, the harmonic signal actually decreases for parallel aligned CO_2 as compared to the unaligned molecules and that the RABITT signal is observed on the sidebands, which are a about a factor 3 weaker than the harmonic peaks in the photoelectron spectra. If, on the other hand, the HHG intensity is increased above $I \approx 1.3 \times 10^{14}\,\mathrm{W/cm^2}$, the free electron dispersion generated by ionization in the HHG medium starts to seriously perturb the IR beams and RABITT measurements start to give unreliable results. In the remaining intensity range, though, we observed the spectral minimum and phase jump at harmonic 23 for $I = 9.5 \times 10^{13}\,\mathrm{W/cm^2}$ (this data is shown in figure 3.3 as well as figure 3 in paper **I**), whereas for $I = 1.25 \times 10^{14}\,\mathrm{W/cm^2}$, the interference position was found to be at harmonic 25 (shown in figure 3.6 and figure 2 in paper **I**). (Mairesse [125]), who observed the harmonic intensity minimum with aligned CO_2 molecules in experiments at the NRC Canada, found this trend to continue when further increasing the intensity, which is possible with shorter driving pulses.

This may in fact explain the different interference positions reported by (Kanai et al. [86]) (harmonic 25) and (Vozzi et al. [206]) (harmonic 33), although both claim a generating intensity of $2 \times 10^{14}\,\mathrm{W/cm^2}$. We observe rather strong ionization already well below this intensity (setting in at $\approx 1.3 \times 10^{14}\,\mathrm{W/cm^2}$), which could mean that in those two experiments, HHG was actually happening at lower effective intensities, which are rather difficult to estimate from harmonic intensities only. The shorter pulse duration in the experiment of (Vozzi et al. [206]) may well allow a significantly higher effective generating intensity and lead to the observation of the interference features at higher harmonic orders.

Such an intensity dependence does, however, come as a surprise as the quantum interference in the DME should depend solely on the spatial structure of the HOMO and not at all on the laser field. (Smirnova et al. [186]) thus propose an alternative explication of both the intensity minimum and the phase jump, based on the contribution of the HOMO-2 (cp. figure 1.6) to HHG. This contribution may become significant at $\theta = 0°$ since at this angle, tunnel-ionization of the HOMO-2 is favored over that of the HOMO due to its σ symmetry. The ionization of the HOMO, having π-symmetry, might be so strongly suppressed at $\theta = 0°$ (and $\theta = 90°$), that even though the HOMO-2 has a higher ionization potential, it may contribute significantly to the XUV emission. The different contributions would then interfere and lead to the observed effects on the spectral intensity and phase. The observed intensity dependence may then be explained by the relative weight of the two contributions, depending strongly on the driving laser intensity.

On the other hand, the theoretical results reported by (Le et al. [104, 105]) reproduce well the data in figure 2 of paper **I**. They are based on equation 3.4 with accurate (yet laser field-free) DMEs for the HOMO, including scattering states from advanced quantum-chemistry calculations but do not take other orbital contributions into account. This agreement is again much in favor of an interpretation in terms of structural interference and it shows that exact scattering states still allow a 'clean' observation of the interference features.

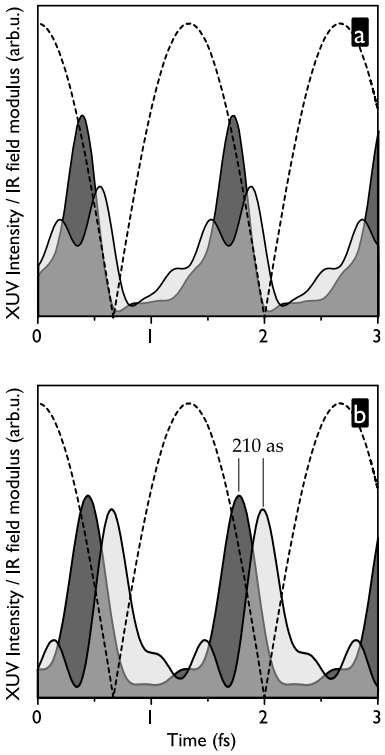

Figure 3.7. *Attosecond pulse trains reconstructed using the data shown in figure 2a of paper* **I**, *taking into account harmonics 23 to 31 (a), or harmonics 25 to 31 (b). The intensity profile of the APT produced by CO_2 at perpendicular alignment is shaded dark gray, that for parallel alignment light gray. The driving IR laser field modulus is shown by the dashed line.*

Following (Marangos et al. [134]), we assume both effects, structural interference as well as multi-orbital contributions, to play a role and the challenge is to disentangle them.

3.2.4 Coherent Control of the Attosecond XUV Emission

Generating attosecond pulse trains in aligned molecules does not only provide a signal that encodes information about the molecular structure, but it also provides a means to coherently control the attosecond time profile of the XUV emission. We discuss the pulse-shaping potential offered by this new means of control in paper **I**. Figure 3.7 shows reconstructions of the APT intensity profile, i.e. the square of equation 2.5, emitted by CO_2 molecules aligned at $\theta = 0°$ and 90° for two slightly different spectral ranges. For these, the data shown in figure 2a of paper **I** with the corresponding spectra (not shown) have been used. Due to the spreading of the phase jump over 3 harmonic orders, the corresponding emission times are shifted to larger values, resulting in a delayed attosecond emission. Including only the harmonic orders undergoing the phase jump in the APT reconstruction, the obtained intensity profile for $\theta = 0°$ is delayed by 210 as with respect to the case of $\theta = 90°$, as compared to 150 as in the measurement shown in figure 4b of paper **I**. Including one more harmonic order before the phase jump position, as done in figure 3.7a, causes a strong distortion of the pulse profile, with destructive interference causing a dip just at the temporal position where constructive interference of all spectral components builds up the pulse peak in the case of $\theta = 90°$. We are approaching the double-pulse profile simulated in figure 4c in paper **I**.

What are the possible applications of this pulse shaping method? XUV pulse shaping can be achieved, of course, partly by amplitude shaping using filters or specifically designed mirrors. Including only certain harmonic orders in the APT reconstruction is already a 'virtual' amplitude shaping. The most interesting feature of aligned molecules as an APT source is the phase jump that can be 'switched' on and off and placed at a chosen spectral position according to the molecule and its alignment. The capability of adding a phase jump, close to π, at some spectral position is a central element in any pulse shaping scheme, like the one presented by (Monmayrant and Chatel [149]), which has until recently not been available in the XUV. Such a phase jump, placed at the transition energy, can serve to transiently enhance a resonant transition (Dudovich et al. [32]), which is one of the simplest coherent control schemes. Below- and above-resonance contributions to the excited state population then interfere constructively and result in so called coherent transients. The phase jump in the XUV emission from aligned molecules can thus be used to drive a transient enhancement of the population of a spectrally large resonance in the XUV region.

3.3 The difficult Case of N_2

The nitrogen molecule has many properties making it favourable for experiments (it is inert and non-toxic, can be well aligned, yields a good HHG efficiency, argon is a suitable reference atom) but the interpretation of the obtained results has caused a lot of headaches in Saclay and around the world. It is clear that the nitrogen molecule, with its HOMO that is neither a purely symmetric nor purely antisymmetric combination of atomic orbitals, will lead to a sign change in the corresponding DME, which cannot be described as easily as that for CO_2. The principle is the same, only the analytic equations to describe the sign change position become much more complex, as shown by (Odžak and Milošević [156]). Nonetheless, one can calculate the DME for

the HOMO and plane waves, and see what structures to look for in the data. One should, however, keep in mind that such a plane-wave calculation can give qualitative predictions at best, since the result will depend on the chosen dipole operator (i.e. the choice of length or velocity form) and the relation between harmonic order and electron wave number is no longer clearly defined (see section 3.1.1).

Theoretical DMEs, calculated with the N_2 HOMO, ψ_{HOMO} (shown in figure 1.5), and plane waves are shown in figure 3.8. There, the component parallel to $\boldsymbol{k}$, and thus parallel to the driving laser polarization direction, is plotted for electron recollision energies $k^2/2$ from 0.4 a.u. (corresponding to harmonic 17 with $\omega = k^2/2 + I_\mathrm{p}$) to 1.9 a.u. (corresponding to harmonic 33 with $\omega = k^2/2$). This means that the plotted electron energy range covers approximately the range of XUV photon energies that we can expect to detect. Length and velocity form of the matrix element clearly give different predictions, notably on the position of the sign change. Neither of the two forms is *a priori* superior to the other, though, which leaves quite some uncertainty. The sign change does, however, qualitatively still follow the two-center interference model in that it appears at higher energies for higher recollision angles $|\theta|$.

Our experiments with aligned N_2 molecules (the angular distribution at the half-revival calculated for our experimental conditions is shown in figure 2.2) have been done in the same way as those with CO_2 discussed in section 3.2. The reference atom is now argon ($I_\mathrm{p}^{\mathrm{Ar}} = 15.76\,\mathrm{eV} \approx I_\mathrm{p}^{\mathrm{N_2}} = 15.58\,\mathrm{eV}$) and the analysis of the RABITT data follows the scheme outlined in section 3.2.1. The effective intensity of the generating laser was $1.2 \times 10^{14}\,\mathrm{W/cm^2}$ in all experiments presented in this section, unless otherwise stated.

A number of results on HHG with aligned N_2 molecules have been published. All groups (see e.g. (Itatani et al. [80], Mairesse et al. [130])) report a spectral intensity minimum at harmonic 25, corresponding to $k^2/2 = 1.4$ a.u. with $\omega = k^2/2$, or $k^2/2 = 0.8$ a.u. with $\omega = k^2/2 + I_\mathrm{p}$, appearing independently of the alignment angle θ. We have observed the same, as shown in figure 1b of paper **II**. Given the uncertainty in the theoretical model using plane waves, it is not problematic to find a minimum at a different spectral position than predicted, but a minimum due to structural interference should really move to higher harmonic orders when the molecules are rotated towards perpendicular alignment. Even a convolution with a rather large angular distribution of the molecules in the experiment cannot explain the fact that the minimum always appears at the same angle. So far, no explanation has been proposed for this peculiar minimum.

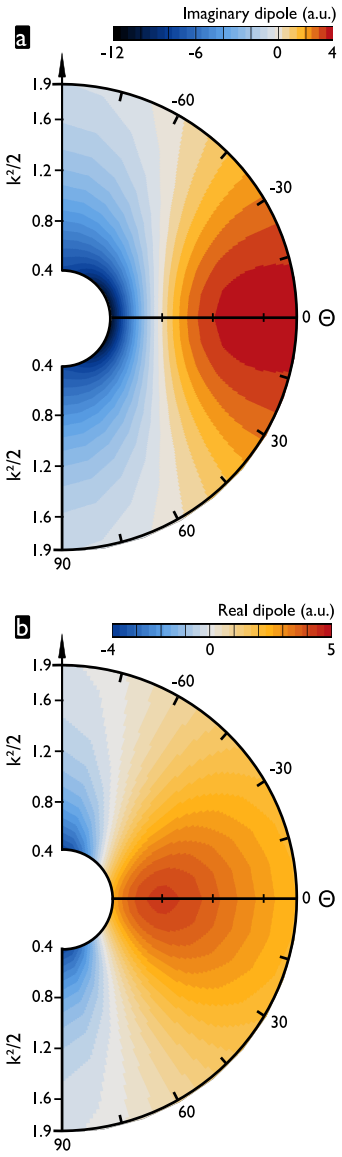

Figure 3.8. *Dipole transition matrix elements $\langle\psi_{\mathrm{HOMO}}|\hat{\mathbf{d}}|e^{i\mathbf{k}\cdot\mathbf{r}}\rangle$, calculated with the N_2 HOMO, ψ_{HOMO} (shown in figure 1.5a), and plane waves. Plotted is the component parallel to $\mathbf{k}$ as a function of the electron recollision angle θ (i.e. the angle between $\mathbf{k}$ and the internuclear axis) and the electron recollision energy $k^2/2$. The energy range corresponds to typical electron recollision energies in HHG. Due to the HOMO symmetry, these matrix elements are even in k_x and k_y. One could thus extend these plots to the third and fourth quandrant by mirroring horizontally. (a) Length form, i.e. $\hat{\mathbf{d}} = \mathbf{r}$. (b) Velocity form, i.e. $\hat{\mathbf{d}} = -i\nabla_{\mathbf{r}}$. Note that here, the DME is always parallel to $\mathbf{k}$.*

3.3.1 XUV Polarization State

When high harmonics are produced in an isotropic medium, the polarization of the XUV field is parallel to that of the driving laser field. As soon as there is an anisotropy in the generating medium, the polarization of the harmonics will in general be different from the laser polarization, leading to the appearance of an orthogonal component of the XUV field. In figure 3.8a, only the component parallel to $\boldsymbol{k}$ is plotted. In fact, there is a non-zero perpendicular component, thus leading for the harmonic emission to the prediction of linear polarization with a finite angle between the XUV field and $\boldsymbol{k}$, and thus the driving laser polarization direction. Note that the velocity form DME in figure 3.8b cannot account for this perpendicular component since for plane waves, it is always parallel to $\boldsymbol{k}$.

With the setup shown in figure 2 of paper **III**, polarimetry measurements of the high-order harmonic emission from aligned N_2 molecules have been done. The result, shown in figure 4 of paper **III**, is in qualitative agreement

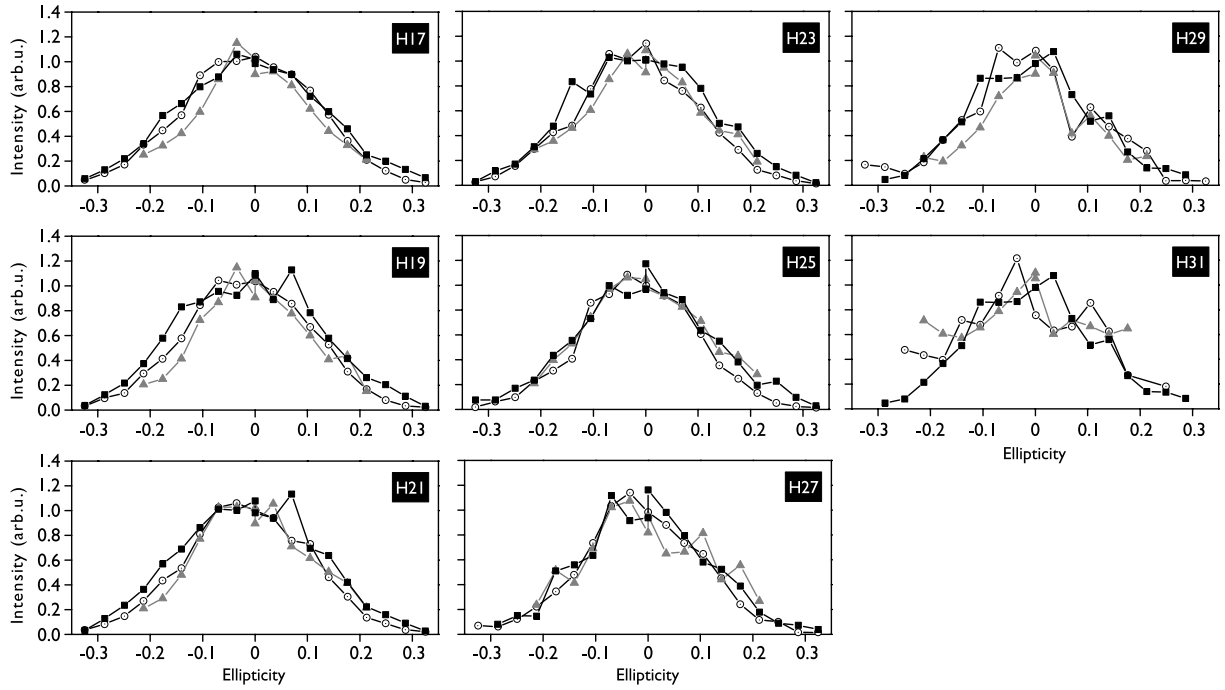

Figure 3.9. *Dependence of the intensity of harmonics 17 to 31 generated in argon (⊙) and N_2 aligned at $\theta = 0°$ (■) and $\theta = 90°$ (▲) on the driving laser ellipticity. All curves have been normalized such that the average value for $\epsilon = 0, \pm 0.035$ be unity. These results are obtained in the same experimental conditions as the data shown in paper **II**, i.e. with an intensity of $I = 1.2 \times 10^{14}$ W/cm^2.*

with that of (Levesque et al. [115]), who have first reported such measurements. Quantitative differences probably originate from a lower alignment quality in our case.

(Levesque et al. [115]) found qualitative agreement between the measured polarization angle for different alignment directions and the plane-wave, length-form DME, using $\omega = k^2/2 + I_p$. However, to obtain this agreement, they had to add exchange terms to their model, shown by (Patchkovskii et al. [158, 159], Santra and Gordon [175]) to occur when the recombination DME is written in its full, multi-electronic form. This formulation will be discussed in section 3.4.3, where it will also be explained why it is questionable whether such exchange terms calculated with *plane waves* lead to an improvement of the theoretical description, or whether they rather worsen the error introduced by plane waves.

(Zhou et al. [221]) have reported the observation of an ellipticity of high-order harmonics generated in aligned N_2 molecules with a linearly polarized driving laser, which is confirmed by recent measurements of (Mairesse [125]). This means that there is a phase lag of the orthogonal XUV field component, not predicted by the plane-wave DME, whether exchange terms are included or not. Exact scattering states could already introduce such a phase difference, as could contributions of other orbitals but the HOMO. At this time, no theoretical study has been published.

3.3.2 Adding Ellipticity

First experiments on the driving laser ellipticity dependence of harmonic intensity spectra generated in unaligned N_2 and argon have been reported by (Flettner et al. [45]). Aligning the N_2 molecules at $\theta = 0°$, (Kanai et al. [87]),

report a behavior of the 31st harmonic intensity very similar to the one we have observed for harmonic 25 emitted by CO_2 aligned at $\theta = 0°$ (see figure 3.5), with a maximum of the 31st harmonic signal for $\epsilon = \pm 0.05$ and a local minimum for $\epsilon = 0$. They interpret this result as a signature of structural interference but give no indication about the behavior of other harmonic orders.

We have done the same measurements, analogous to those already discussed for CO_2 (see figure 3.5), aligning N_2 at $\theta = 0°$ or 90° and tracing the intensity of harmonics as a function of the driving laser ellipticity. Results are shown in figure 3.9. Up to harmonic 25, we consistently observe a slower drop of signal for N_2 at $\theta = 0°$ as compared to N_2 at $\theta = 90°$, as also measured by (Mairesse et al. [130]). For harmonic orders close to the cut-off (27–31), the data become rather noisy.

The argon curve, shown as a reference in figure 3.9, is located in between the two N_2-curves and consistently drops slightly faster than that for N_2 at $\theta = 0°$. Our data thus show the same trend as those of (Kanai et al. [87]) (who normalized differently, namely such that all curves coincide in the wings, i.e. for large ϵ) already at lower harmonic orders (clearly from harmonic 19 on). Comparing to CO_2 (see figure 3.5), the effect is much more subtle here, though, and we tend to reject for the lower orders the interpretation by means of structural interference. Whether structural interference occurs at harmonic 31 cannot be concluded from these data. The main limitation in these experiments was the precision and reproducibility of the ellipticity values (see e.g. in some curves with two data points for $\epsilon = 0$) due to setting the wave plate orientations by hand instead of a step motor.

Another interpretation was proposed by (Mairesse et al. [130]). The different widths of the harmonic intensity vs. ellipticity curves could be a signature of the different continuum EWP spreads due to a narrower/larger width of the 'tunnel' through which the initial continuum EWP is created at $\theta = 0°$ and 90°, respectively. The same difference of EWP lateral spreads has also been assumed by (Itatani et al. [80]).

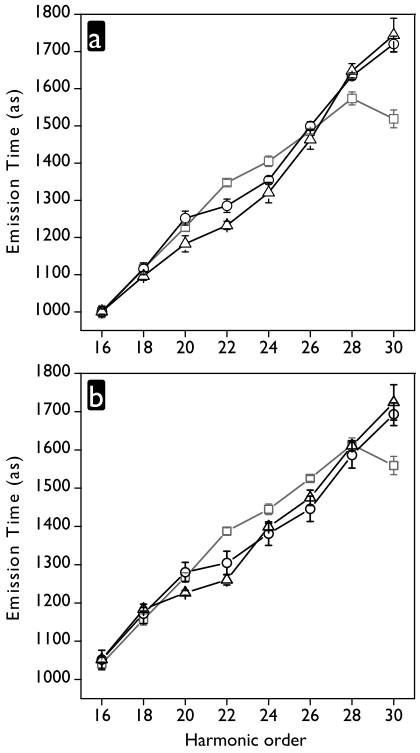

Figure 3.10. *Emission times measured for N_2, aligned at $\theta = 0°$ (○) and $\theta = 90°$ (△), and the reference atom argon (□). The data in (a) and (b) are taken from two independent series of RABITT scans, both done with the experimental parameters given in paper **II**, such as a laser intensity of $I = 1.2 \times 10^{14}$ W/cm^2.*

3.3.3 Phase Measurements

Up to now, there is not much agreement between the experiments and the predictions of the plane-wave DME for the HOMO – but there are also no clear hints as to where the simple model, introduced in section 3.1 and justifying this comparison, fails. New information from phase measurements will definitely be interesting in this regard.

We thus made series of RABITT scans, analogous to those done for CO_2, leading to emission times as shown in figure 3.10. At first sight, one concludes that the difference with the emission times measured for the reference atom argon varies with harmonic order, but it does so quite smoothly over the whole spectral range and no clear jump – like that seen with CO_2 – is observed. Additionally, this phase variation seems to be similar at all angles θ. The latter conclusions is, however, not confirmed when the spectral phase is calculated. Rather small differences in the emission times, when integrated, become significant. As shown in figure 1c of paper **II**, there is a quite regular variation of the spectral phase with the alignment angle. This behavior is reproducible: emission times for $\theta = 0°$ and 90°, taken from a second, independent series of RABITT scans, are shown in figure 3.10b.

A set of RABITT scans done with increasing ellipticity of the driving laser, analogous to the study with CO_2 summarized in figure 3.6, has been done with N_2 molecules aligned at $\theta = 0°$. Apart from the intensity decrease visible in figure 3.9, no significant modification of the emission times was found.

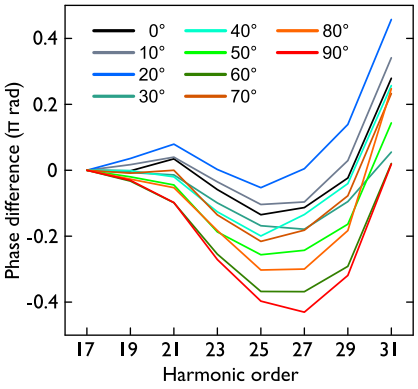

Figure 3.11. *Phase of the DME for N_2 molecules, obtained from the experiment according to equation 3.6 as described in section 3.2.1. This data is the same as that shown in figure 1c of paper **II**.*

Interplay between HOMO and HOMO-1 contributions

In the first part of paper **II** we describe how our measured phases can be understood when a contribution of the HOMO-1 of N_2 (shown in figure 1.5) is brought into play. Due to the greater size of molecules as compared to atoms, valence orbitals are energetically closer. One thus can no longer safely assume that only the energetically highest occupied orbital is ionized in the tunnel-ionization step, as was always done for rare-gas atoms. (McFarland et al. [141]) have reported first indications in intensity measurements around the half-revival for a significant HOMO-1-contribution for N_2 close to perpendicular alignment, $\theta = 90°$. This is due to the greater extent of the HOMO-1 probability density in the direction perpendicular to the internuclear axis, favoring it in tunnel ionization over the HOMO, despite its $\Delta\epsilon = 1.4\,\text{eV}$ larger binding energy (see the vertical distance of the potential curves for the X and A states of N_2^+ shown in figure 4.2). Additionally, the plane-wave recombination DME turns out to be larger for the HOMO-1 than for the HOMO close to $\theta = 90°$.

We thus invoke a transition from a dominating HOMO contribution to a dominating HOMO-1 contribution to the emitted XUV field when the N_2 molecules are rotated from $\theta = 0°$ towards $\theta = 90°$. The key idea in this interpretation is the fact that the recombination DME, calculated with plane waves for the N_2 HOMO is purely imaginary valued, whereas that for the HOMO-1 is purely real-valued. This separation in the complex plane is due to the different symmetries of the two relevant orbitals and the symmetry properties of the Fourier transform, as will be demonstrated in section 3.4.2.

Paper **II** explains that the value of the relative phase $\Delta\phi = \phi_{\text{HOMO}-1} - \phi_{\text{HOMO}}$ of the two orbital contributions is not simply given by that of the recombination DME. Rather, it is a sum, $\Delta\phi = \Delta\phi_i + \Delta\phi_c + \Delta\phi_r$, of the phase differences $\Delta\phi_i$ acquired during tunnel ionization, $\Delta\phi_c$ accumulated during the continuum acceleration, and $\Delta\phi_r$ due to the recombination DMEs. As for ionization, we assume $\Delta\phi_i = 0$, relying on the result of (Smirnova et al. [186]) for CO_2, who claim that this value is 'expected in the tunnelling regime'. For $\Delta\phi_c$, we derive $\Delta\phi_c = -\Delta\epsilon\tau$, where τ is the continuum electron excursion time, and we find $\Delta\phi_c \approx -\pi$ for our experimental spectral range. Finally, $\Delta\phi_r = \pm\pi/2$ for the plane-wave DMEs, which we assume to still hold for DMEs including proper scattering states. In paper **II**, we support this by a calculation using Coulomb waves. More precisely, one should ask how similar are the scattering states of equal energy in the continua of the ions in the X and A state? We assume, that they are almost equal. It is at this time unclear to us how to decide on the sign of $\Delta\phi_r$ – it depends on the signs of the two DMEs, which we feel cannot be determined reliably in a plane-wave calculation. In total, we find $\Delta\phi \approx \pm\pi/2$ in the spectral region accessible to our experiments. $\Delta\phi_c$ decreases with the electron recollision energy (see figure 2a of paper **II**), but it is uncertain whether the total phase difference, $\Delta\phi$, then evolves towards 0 or $-\pi$ with increasing harmonic order, i.e. towards constructive or destructive interference.

The measured DME phase, shown in figure 3.11 as well as figure 1c of paper **II**, decreases between harmonic 17 and 25/27 – very little around parallel alignment ($\theta = 0°$), and by $\approx \pi/2$ close to perpendicular alignment ($\theta = 90°$). This phase shift may indicate a regular transition between two contributions with $\approx \pi/2$ relative phase – as is the case for the HOMO-1 and HOMO contributions. At the end of the spectrum, from harmonic 27 on, the phase increases rather rapidly, by $\approx \pi/2$ at all angles. For close to parallel alignment, this could be a signature of structural interference associated with the HOMO, if one reads this phase increase as a beginning phase jump.

For larger angles θ, where the HOMO-1 contribution is supposed to be dominant, this rapid phase increase should then not occur. The phase should deviate from $-\pi/2$ due to the decreasing $\Delta\phi_c$, but the direction of this deviation is unclear due to the uncertainty on the the sign of $\Delta\phi_c$. In any case, this drift is expected to be fairly slow (cp. figure 2a in paper **II**) and cannot explain the rather rapid increase observed at the end of the spectrum for large θ. There might thus be an additional effect, such as the HOMO contribution becoming dominant again at all angles, thus reversing the initial phase decrease. Such a 'transient' dominance of the HOMO-1 contribution might be induced by IR laser driven dynamics in the molecular ion during the electron excursion, i.e. the second step of the HHG process. Laser coupling of the X and A ion states is very likely in N_2 since they are only separated by about one laser photon. The model of (Smirnova et al. [186]) is able to treat such dynamics. We do, however, not include it in our analysis in paper **II**.

While the analysis of the different phase terms adding up to the total $\Delta\phi$ has a firm theoretical basis, the interpretation of the specific features of the measured DME phase, shown in figure 3.11, is fairly complicated and certainly not bullet-proof. One should keep in mind that the relative amplitudes of the HOMO and HOMO-1 contributions are expected to vary with harmonic order and alignment angle. This will lead to a complicated behavior of the total recombination DME, **D**, defined in equation 1 of paper **II** as a coherent sum of the two recombination DMEs associated with the HOMO and HOMO-1.

The presented phase measurements suffer from a limitation that was already mentioned in section 3.2.1: our measured phases are determined only up to an integration constant, which we *arbitrarily* set to zero for all angles θ. This means that we suppose that the phase of harmonic 17, and thus the phase of the associated DME, is equal for all θ. Measuring this missing element is highly desirable, as it would provide us with true *ab inito* data and provide a more sound basis for the above interpretation. In different generation conditions, the variation of the phase of harmonic 17 as a function of θ was indeed found to be small (≈ 0.5 rad), as measured at the NRC Canada by (Mairesse [125]) with the two-source method, also used for the results of (Smirnova et al. [186]).

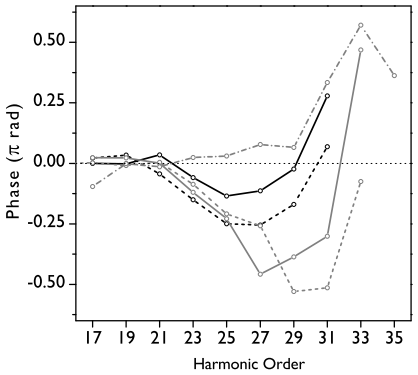

Figure 3.12. *Phase of the recombination DME measured with different laser intensities for N_2 aligned at $\theta = 0°$. These data are obtained according to equation 3.6, i.e. as a difference of the spectral phases measured for high-order harmonics generated in N_2 and argon under the same conditions. The intensities (estimated from the slope of the emission times obtained with argon) are 1.2×10^{14} W/cm^2 (full and dashed black line), 1.6×10^{14} W/cm^2 (full gray line), 1.7×10^{14} W/cm^2 (dashed gray line), and 2.0×10^{14} W/cm^2 (dash-dotted gray line). The data represented by the full black line is taken from the series shown in figure 1 of paper **II**.*

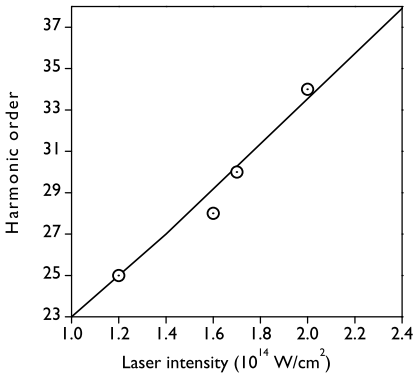

Figure 3.13. *Spectral position where the relative phase, $\Delta\phi$, between the HOMO and HOMO-1 contribution takes the value $-\pi/2$ (full line), corresponding to an electron excursion time $\tau \approx 1.5$ fs, compared to the spectral position of the negative-phase feature in the measured phase of the DME (⊙).*

Intensity dependence

Not mentioned in paper **II** but relevant to the interpretation are phase measurements with different driving laser intensities. If the phase decrease from harmonic 17 to 27 in figure 3.11 is due to a transition to a dominating HOMO-1 contribution, it may occur at different spectral positions for different laser intensities. The $\exp[-2(2I_p)^{3/2}/(3E_L)]$-dependence of the tunneling rate on the peak laser field E_L (see section 1.3.1), will cause the difference in binding energies of the HOMO-1 and HOMO to be less and less important. Thus, the HOMO-1 contribution should show up more prominently when the laser intensity is increased.

DME phases, extracted from measurements with N_2 aligned at $\theta = 0°$ and argon at four different laser intensities are shown in figure 3.12. It cannot be guaranteed that the alignment quality is the same for all curves in this figure since they have not been measured in one series, but are compiled from various data acquisition runs. The alignment may thus be rather mediocre in some of these measurements, which may be considered an advantage, though, since this leads to more molecules being aligned at large angles with the laser polarization direction and thus increases the HOMO-1 contribution. It is clear from the curves in figure 3.12 that the decreasing-phase-feature in the data shifts towards higher harmonic orders when the laser intensity, I, is increased.

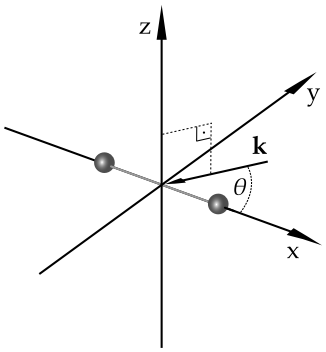

Figure 3.14. *Coordinates in the description of molecular orbital tomography. The two spheres mark the nuclei of a simple linear molecule – the internuclear axis is along the x-axis. The electron wave vector* **k***, confined to the (x,y)-plane, makes an angle* θ *with the internuclear axis. The angle* θ *is known and can be varied because we can align the molecule in the lab frame.*

Eventually, for $I = 2.0 \times 10^{14}\,\mathrm{W/cm^2}$, it appears to have moved to the very end of the accessible spectral range.

As shown in figure 3.13, the harmonic order where the minimum of the decreasing-phase-feature occurs, is in very good agreement with the harmonic order where the relative phase of the two orbital contributions takes the value $\Delta\phi \approx \pm\pi/2$ (calculated as described in paper **II**). This spectral position increases with laser intensity because it includes a term proportional to the continuum electron excursion time ($\Delta\phi_c$ in paper **II**). This also means that the measured phase minimum always occurs at the same electron excursion time $\tau \approx 1.5$ fs. The phase increase at the highest harmonic orders, interpreted as the beginning of a structural phase jump in the HOMO contribution, does not seem to move with intensity except where it fully overlaps with the decreasing-phase-feature. Both these observations support our interpretation.

3.4 Molecular Orbital Tomography

It has been mentioned that one of the motivations to stick to plane waves for the description of the recolliding EWP in the self-probing scheme is that the recombination DME, $\langle\psi_{\mathrm{mol}}(\boldsymbol{r})|\hat{\mathbf{d}}|e^{i\boldsymbol{k}\cdot\boldsymbol{r}}\rangle$, takes the form of a Fourier transform, $\mathcal{F}_{\boldsymbol{r}\to\boldsymbol{k}}$. (Itatani et al. [80]) recognized that this formulation implies a potential for imaging electrons in molecules. We can thus push the analysis of the measured DMEs one step further and extract an image of the bound electron.

3.4.1 Concept

The recombination DME, $\boldsymbol{d}$, measurable as described in section 3.1, is in general a complex-valued vector. Let (x,y,z) be the coordinates of the molecular reference frame, with the internuclear axis (or any other distinct axis on a more complicated molecule) along x. Being able to align molecules means that (x,y,z) can also be used for the laboratory frame, and the (x,y,z)-coordinates of the laser polarization direction and thus $\boldsymbol{k}$ are known[6]. We can arrange that z is the light propagation direction, such that $k_z \equiv 0$ (the electron is driven by the laser field which has no component in its propagation direction). The situation is depicted in figure 3.14. Furthermore, although d may have non-zero z-component, we cannot measure it since the XUV light polarized along this direction cannot propagate to the detector. We will thus only consider the x and y-components of $\boldsymbol{d}$.

The q-component ($q = x, y$) of the matrix element in length form then writes

$$d_q(\boldsymbol{k}) = \langle\psi_{\mathrm{mol}}(\boldsymbol{r})|q|e^{i\boldsymbol{k}\cdot\boldsymbol{r}}\rangle = \iint \left[q \int \psi^*_{\mathrm{mol}}(x,y,z)\mathrm{d}z\right] e^{i(k_x x + k_y y)}\,\mathrm{d}x\mathrm{d}y. \quad (3.10)$$

Each component of $\boldsymbol{d}$ thus contains the Fourier transform of $q\tilde{\psi}_{\mathrm{mol}}(x,y) = q\int\psi^*_{\mathrm{mol}}(x,y,z)\mathrm{d}z$, i.e. q times the bound state orbital[7] projected onto the plane perpendicular to the laser propagation direction. This implies that an orbital odd in z will not contribute and e.g. only one of two degenerate π-orbitals need be considered (the driving laser should impose the quantization axis). For orbitals that are even in z, this projection contains the complete information and is in fact the quantity shown in all 2D-plots of orbitals in this thesis.

[6] Note that in section 3.1 we considered the laser polarization and thus $\boldsymbol{k}$ to be fixed rotated the orbitals. Here, we will rather think of fixed-in-space orbitals and rotate the laser polarization direction.

[7] The star denotes complex conjugation, but the orbital can be chosen to be real-valued and the star might as well be omitted.

Measuring d_q for one alignment angle θ thus yields data points in Fourier space of the object $q\tilde{\psi}_{\text{mol}}(x,y)$ – points at the coordinates (k_x, k_y) that all lie on a line, given by the recollision angle, θ, and the length of the electron wave vectors, k, of the recolliding EWP components. These are associated with the harmonic photon energy, ω, via energy conservation: $k^2/2 = \omega$. For aligned molecules, such that the molecular frame is fixed in some orientation in the laboratory frame, each harmonic order is thus associated with one point (k_x, k_y). A whole spectrum consequently yields a slice through one quadrant of Fourier space, as illustrated in figure 3.15. Repeating the measurement for more θ-values, slice per slice of Fourier space is collected until it is sufficiently well sampled[8].

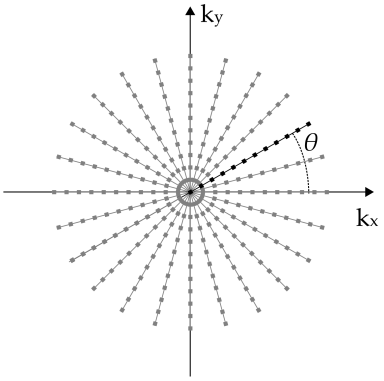

Figure 3.15. *Fourier space of the object $q\tilde{\psi}_{\text{mol}}(x,y)$. A measurement for one molecule alignment angle θ yields a line of data points (shown in black). Repeating the measurement for more θ-values, slice per slice of Fourier space is collected. If the symmetry of $q\tilde{\psi}_{\text{mol}}(x,y)$ is known, one can limit the θ-range to one quadrant and complete the Fourier space data according to this symmetry (see section 3.4.2).*

The inverse 2D Fourier transform, $\mathcal{F}_{\boldsymbol{k}\to\boldsymbol{r}}$, applied to the so obtained data, thus yields $q\tilde{\psi}_{\text{mol}}(x,y)$ in real space, and the sought-for molecular orbital (projection) can be reconstructed as

$$\tilde{\psi}^q_{\text{mol}}(x,y) = \frac{\mathcal{F}_{\boldsymbol{k}\to\boldsymbol{r}}[d_q(k_x,k_y)]}{q}. \tag{3.11}$$

The explicit, discretized version of this equation is given as equation 2 in paper **II** (using a different notation, though).

From both DME components, x and y, i.e. parallel and perpendicular to the internuclear axis, the *same* orbital can be reconstructed. Due to the limited discrete sampling in Fourier space, they will, however, not give the same result and in general

$$\tilde{\psi}_{\text{mol}}(x,y) = \frac{1}{2}\left(\tilde{\psi}^x_{\text{mol}}(x,y) + \tilde{\psi}^y_{\text{mol}}(x,y)\right) \tag{3.12}$$

is used as the definition of the *reconstructed molecular orbital* (projection). The three dimensional orbital can be obtained if it is even in z.

Velocity form

The same scheme can be written based on the velocity form of the recombination DME, i.e. with $\hat{\mathbf{d}} = -\mathrm{i}\nabla_{\boldsymbol{r}}$. Equation 3.10 is then replaced by

$$d_q(\boldsymbol{k}) = -\mathrm{i}\,\langle\psi^*_{\text{mol}}(\boldsymbol{r})|\frac{\partial}{\partial q}|\mathrm{e}^{\mathrm{i}\boldsymbol{k}\cdot\boldsymbol{r}}\rangle = k_q \iint\left[\int \psi_{\text{mol}}(x,y,z)\mathrm{d}z\right]\mathrm{e}^{\mathrm{i}(k_x x + k_y y)}\,\mathrm{d}x\mathrm{d}y. \tag{3.13}$$

It follows that the orbital can be obtained via equation 3.12 using

$$\tilde{\psi}^q_{\text{mol}}(x,y) = \mathcal{F}_{\boldsymbol{k}\to\boldsymbol{r}}\left[\frac{d_q(k_x,k_y)}{k_q}\right]. \tag{3.14}$$

Again, neither this nor equation 3.11 is *a priori* superior to the other and they may give different results.

3.4.2 Symmetry Considerations

It will be helpful to consider the connection between the symmetry of $\tilde{\psi}_{\text{mol}}(x,y)$ in real space and properties of the corresponding plane-wave DME $\boldsymbol{d}$. The symmetry properties of the Fourier transform[9] are summarized in appendix C.

With these, for the HOMO of N_2 (see figure 1.5) which is chosen to be real-valued and even in x and y, we find for the length form:

[8] What 'sufficiently' means has yet to be figured out in simulations, discussed in section 3.4.4.

[9] In appendix C, the much more common 'minus i'-transform is considered, i.e. there is a minus in the argument of the exponential in $\mathcal{F}_{r\to k}$. As in a plane wave, there is no such minus, our matrix elements are a 'plus i'-transform. This difference in conventions has no influence on the symmetry properties to be used here – it merely swaps $F(\boldsymbol{k})$ for $F(-\boldsymbol{k})$.

- $x\tilde{\psi}_{\mathrm{mol}}(x,y)$ is real-valued, odd in x, even in y
  $\rightarrow d_x$ is imaginary valued, odd in k_x, even in k_y.
- Analogously: $y\tilde{\psi}_{\mathrm{mol}}(x,y)$ is real-valued, even in x, odd in y
  $\rightarrow d_y$ is imaginary valued, even in k_x, odd in k_y.
- The two components of $\boldsymbol{d}$ thus do not have the same symmetries. For the component parallel to $\boldsymbol{k}$, $d_\parallel = d_x \cos\theta + d_y \sin\theta$, we find that it is imaginary valued and even in k_x as well as in k_y.

For the velocity form, these results are to be multiplied by an imaginary unit, i.e. in the end, $d_\parallel$ is real-valued and even in k_x as well as in k_y. The harmonic emission nonetheless has the same phase, whatever formulation is used, because the dipole *momentum* (i.e. the velocity form DME) has to be differentiated only once to obtain the dipole acceleration, whereas the dipole *moment* (i.e. the length form DME) has to be differentiated twice. For the following argumentation based on the symmetry-induced phase of the recombination DME to make sense, we have to take care to *compare* matrix elements using the *same* dipole operator. Whether one matrix element may be imaginary or real-valued is thus not very important, but it is relevant whether there is a $\pi/2$ or zero phase difference between two matrix elements.

Repeating this consideration for the length form and the HOMO-1 of N_2 (see figure 1.5) which is real-valued, even in x and odd in y, leads to:

- $x\tilde{\psi}_{\mathrm{mol}}(x,y)$ is real-valued, odd in x, odd in y
  $\rightarrow d_x$ is real valued, odd in k_x, odd in k_y.
- Analogously: $y\tilde{\psi}_{\mathrm{mol}}(x,y)$ is real-valued, even in x, even in y
  $\rightarrow d_y$ is real valued, even in k_x, even in k_y.
- $d_\parallel$ is thus real valued and even in k_x and odd in k_y.

For the same reason, the length form DMEs for our reference atoms argon/krypton are real-valued[10]. One considers the 3p/4p orbitals aligned parallel to the laser polarization direction and thus to $\boldsymbol{k}$ (the laser field aligns the orbitals and HHG is largely dominated by the one parallel to the field, as demonstrated by (Shafir et al. [184]) for neon and its 2p orbitals).

In conclusion, one could give the following simple rules, valid for the length as well as the velocity form: *The DME component parallel to the driving laser polarization, $d_\parallel$, has the same symmetries in k_x and k_y as the orbital in x and y. 'Oddness' in real space creates an imaginary unit in Fourier space – so if one orbital is odd in n more dimensions than the other, there will be an $n\pi/2$ phase difference (modulo π) between the DMEs for the two.*

Completing the data for tomography

These symmetry considerations are of course also relevant for the inverse Fourier transform and thus for the tomographic reconstruction via equations 3.11 and 3.14. If the real-space symmetry of the 'active' orbital is known, one can limit the measurement of $\boldsymbol{d}(k_x,k_y)$ to the first quadrant of real space, i.e. scan only $\theta = 0° \ldots 90°$, and then complete the Fourier space data according to the symmetry. In this way, a certain symmetry is *imposed* to the reconstructed orbital and one should be careful not to confuse this perfect symmetry in the result with a proof for the successful reconstruction of a molecular orbital.

What if one had an outstandingly long-term-stable experimental setup and just rotates the laser polarization all the way around 360°? Unfortunately, this

[10] Consequently, the velocity form matrix elements are imaginary-valued, contrary to what is written in paper **I**.

would *not* immediately render superfluous the above symmetry considerations. The reason is discussed in section 3.2.3 under the point "Missing sign change": a purely θ-dependent sign change in the DME is not easily detectable – neither with RABITT nor one of the other techniques measuring the phase as a function of θ. Special arrangements, such as the control of the continuum electron trajectory demonstrated by (Shafir et al. [184]), would be necessary to obtain an *ab inito* measurement of $\boldsymbol{d}(k_x, k_y)$ by means of a self-probing scheme.

3.4.3 Too Good to be True?

This scheme for reconstructing molecular orbitals from measured data is based on a strongly simplified physical picture invoking a whole range of approximations. It would thus be pretentious to speak of *measuring* orbitals, as pointed out by (Schwarz [180]) in his essay on the question "Measuring Orbitals: Provocation or Reality?". Purists and enthusiasts of proper quantum theory thus need not be alarmed as no-one is going to claim that with the extraction of a (Hartree-Fock type) orbital from a set of measured data, all further measurements become redundant since now, the wave function is known and every observable can be calculated. Even if the models at the basis of the orbital tomography scheme were to be more and more refined and thus approach further and further something that is commonly considered 'exact'[11], the measurement necessarily remains incomplete. Whether one day a wave function can be reconstructed that is more precise than a theoretical one – which would be a great reward for going through the trouble of doing the experiment – remains unclear. Certainly, for static bound states, this is close to impossible – the true motivation, however, are *dynamic* systems, for which computations are orders of magnitude harder.

Other than the impossibility of a ψ-meter, i.e. an apparatus that would *directly measure* the wave function of a system, there is no law ruling out the possibility of inferring a wave function from a set of measured data. In fact, this is done by many physicists with great success – see e.g. (Raymer [166]) for a review or the 'Special Issue on Quantum State Preparation and Measurement' of the Journal of Modern Optics, edited by (Schleich and Raymer [177]).

Besides these fundamental questions, there are obviously many technical points that raise doubt about whether or not this scheme can work. The article of (Itatani et al. [80]) launched a lively discussion and a multitude of papers – mainly based on numerical experiments – have since been published, for example by (Gibson and Biegert [58], Jordan and Scrinzi [83], Le et al. [106], Patchkovskii et al. [158, 159], Torres and Marangos [197], van der Zwan et al. [202], Walters et al. [215]). On can easily write down a list of issues that could potentially destroy all hope for experimental orbital tomography but it is much harder to actually estimate the importance of each of these issues. Three major simplifications made for the orbital imaging scheme lined out in section 3.4.1, shall be discussed here.

The plane wave approximation is responsible for the surprisingly simple direct reconstruction by means of an inverse Fourier transform. It is also the approximation that is most under attack while unfortunately being extremely hard to improve on. If one measures a DME between two states – bound and continuum – one cannot avoid making an educated guess about one of the two if one wants to *directly* extract the other. This could only be avoided

[11] There is no such thing as a properly *exact* description of reality. What we call exact, is typically a mathematically exact solution of the TDSE, which itself has a limited region of validity, and, most of all, contains a Hamiltonian which always describes no more than an idealized *model* of reality.

by developing algorithms that iteratively improve this guess, such as the one sketched by (Patchkovskii et al. [159]).

Numerical experiments that use 'exact' scattering states and then apply the tomographic reconstruction procedure based on plane waves give rather mixed results. (van der Zwan et al. [202]), who have calculated harmonic spectra by solving the TDSE, tend to be optimistic and obtain very good reconstructions. (Walters et al. [215]), on the other hand, who calculate DMEs using scattering states obtained from a specialized quantum chemistry code, reports significant distortions of the orbitals reconstructed using electron recollision energies as low as those in typical HHG experiments (i.e. below, say, 100 eV). This is the same method as that used by (Le et al. [102, 103]). Note the comment made in section 3.1.1 concerning these 'exact' photo-*ionization* DMEs and the fact that DMEs relevant to HHG may be expected to be significantly less 'distorted'. Calculating these seems, however, even harder than for photoionization.

Our answer is based on a less sophisticated calculation but it gives very interesting insight. In figures 2b,c of paper **II**, we compare the DME for the N_2 HOMO calculated using plane waves and Coulomb waves, i.e. scattering states of the Coulomb potential (see section 1.2.2). This can be seen as a first order improvement on plane waves since, from far away, the N_2^+ ion seen by the recolliding electron looks just like a proton. The result is that the distortions of the Coulomb-wave completely ruin the features of the plane-wave DME at very low electron energies $\lesssim 10\,\mathrm{eV}$ (these energies are defined asymptotically, i.e. far away from the ion). For very high electron energies ($\gtrsim 300\,\mathrm{eV}$), plane waves do yield a very good description. At intermediate energies, one can say that all features of the plane wave DME containing the information needed for orbital tomography are conserved, only translated by $\approx I_\mathrm{p}$ to lower electron energies. This nicely corresponds to the idea that the recolliding electrons are accelerated by the ionic potential gaining $\approx I_\mathrm{p}$ in energy before recombining. For relatively narrow spectral windows like those considered in our experiments, one can define an absolute phase shift added to the Coulomb-wave-DME (the Coulomb phase shift), which can be factored out and thus translates into an absolute phase shift of the final reconstructed orbital.

The next improvement would be the use of two-center Coulomb waves as done by (Ciappina et al. [19]). Here, again, the main structures of the plane wave DME are well recovered, only with smoothed and slightly reduced phase jumps.

A single active electron is assumed in the SFA upon which all our data analysis including the orbital tomography scheme is based. From the start, i.e. already in the ansatz 1.35, only one-electron wavefunctions are considered. (Patchkovskii et al. [158, 159], Santra and Gordon [175]) have shown that in a multi-electron system, i.e. in all the HHG media we use, the recombination DME should be written using (properly anti-symmetrized) multi-electron wavefunctions: $\Psi_0(\boldsymbol{r}_1,\ldots,\boldsymbol{r}_f)$ for the neutral with f electrons and $\Psi^+(\boldsymbol{r}_1,\ldots,\boldsymbol{r}_{f-1})\chi(\boldsymbol{r}_f)$ for the ionized system, where Ψ^+ describes the (f-1) electrons of the ionic core and χ the correlated continuum electron. The length-form recombination DME can then be transformed to

$$\boldsymbol{d} = \langle\Psi_0|\sum_{m=1}^{f}\boldsymbol{r}_m|\Psi^+\chi\rangle = \langle\psi^\mathrm{D}|\boldsymbol{r}_f|\chi\rangle + \boldsymbol{d}^\mathrm{ex}, \tag{3.15}$$

where $\boldsymbol{d}^\mathrm{ex}$ is an exchange correction term and $\psi^\mathrm{D}(\boldsymbol{r}_f) = \sqrt{f}\,\langle\Psi_0|\Psi^+\rangle$ is the Dyson-orbital – the scalar product of the multi-electron wavefunctions of the

neutral and the ionic core. Calculating the Dyson orbital can be interpreted as projecting out the difference between the neutral and the ionic core, which could be seen as a 'hole in the ion'.

These terms become transparent within the Hartree-Fock framework (i.e. the multi-electron wavefunctions are expressed as products of single-electron-orbitals, ϕ_m, see section 1.2.2) and using Koopmans' approximation (Bransden and Joachain [13], Koopmans [94]), i.e. any relaxation of the one-electron orbitals in the ion upon ionization is neglected and the ionic wavefunction, Ψ^+, is built with the same single-electron orbitals as the neutral – taking out only the the 'active orbital', i.e. the one-electron orbital from which electron f has been ionized. Then,

$$\psi^{\mathrm{D}}(\boldsymbol{r}_f) = \phi_f(\boldsymbol{r}_f), \tag{3.16}$$

i.e. the Dyson-orbital is identical to the orbital from which electron f has been ionized (i.e. in most cases the HOMO). Furthermore,

$$\boldsymbol{d}^{\mathrm{ex}} = \sum_m \left(\boldsymbol{d}_{mm} \langle \phi_f | \chi \rangle - \boldsymbol{d}_{fm} \langle \phi_m | \chi \rangle \right), \tag{3.17}$$

where the $\boldsymbol{d}_{mm}$ are permanent dipole moments, which vanish for centrosymmetric molecules, and the $\boldsymbol{d}_{fm}$ are transition dipole moments between the occupied one-electron orbitals and the 'active orbital' f. The crucial terms to consider are, however, the scalar products of the bound state orbitals ϕ_m with the scattering state χ. Since χ is a one-electron eigenstate of the neutral and the ϕ_m are one-electron eigenstates of the ion, they are orthogonal as long as Koopmans' approximation is valid. The scalar products $\langle \phi_m | \chi \rangle$ thus rigorously vanish in Koopmans' approximation. It is the amount of relaxation in the ion that decides about the relevance of exchange terms.

We think that calculating exchange terms using plane waves for χ, as done by (Levesque et al. [115], Patchkovskii et al. [158, 159]) due to lack of a more precise description of the continuum, artificially blows up their importance and introduces spurious contributions. Thus, we will rather neglect exchange terms in the following, since we expect them to be very small anyhow. In this case, orbital tomography yields an image of the Dyson orbital, which resembles very closely the active Hartree-Fock orbital ϕ_f.

A single active orbital has so far been assumed, i.e. in the above multi-electron description, ϕ_f is the HOMO. Both for CO_2 and N_2, it has already been mentioned, though, that several orbitals may be ionized. In this case, Ψ^+ is a superposition of ionic states[12], with an electron 'missing' in different orbitals. This situation still involves a single active electron only, which is delocalized within the neutral molecule due to its indistiguishability from the others and thus the anti-symmetry of Ψ. Illustratively speaking, the continuum electron cannot be sure from which orbital is has been ionized and neither can the ion. There are however weights for the different possibilities given by the tunneling rate for each orbital. The corresponding Dyson orbital – the object that is imaged by orbital tomography (as long as exchange terms are negligible) – is then time dependent due to the energy difference of the contributing active orbitals. If this energy difference is larger than ~ 1 eV, which is the case for the small molecules considered here, this dynamics happens on an attosecond timescale. It was proposed by (Smirnova et al. [186]) to consider this object as a time-dependent hole in the ion, which is the interpretation we adopted in paper **II**.

[12] It is actually a touchy question whether this statement is correct and whether one can speak of a 'wave packet in the ion'. The answer is *yes*, if the different continuum wavefunctions, χ, correlated to each ion state are equal or at least have a large overlap. (Smirnova et al. [187]) recently showed for CO_2 that this is indeed the case.

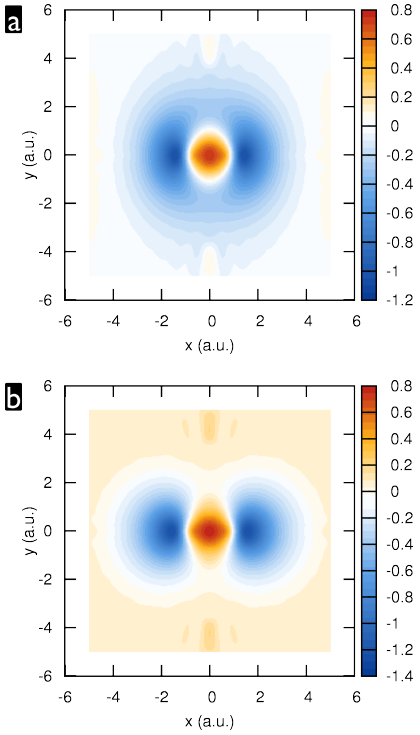

Figure 3.16. *Simulation of a tomographic reconstruction, sampling k-points corresponding to harmonics 1 to 999 and an angular step of $\Delta\theta = 10°$, (a) with and (b) without restricting the DME to its parallel component, $d_\parallel$, only.*

3.4.4 Simulations

These simulations do not aim at testing the above approximations used to derive the orbital tomography scheme itself but rather suppose that we are able to measure accurate DME and address the question of how precise the discrete sampling has to be. This issue will be studied on the example of the N_2 HOMO, which is a good candidate as it has very distinct features besides its σ_g symmetry that can serve as a reference, such as the nodes at the nuclei positions (at $x = \pm 1$ a.u.) and the diamond-shaped central lobe. We thus start from the Hartree-Fock HOMO (see figure 1.5), which will be considered 'exact', and calculate the plane-wave DME vector, $\boldsymbol{d}$, at $\boldsymbol{k}$-points given by a range of harmonic orders of an 800 nm laser ($\omega_0 = 0.057$ a.u.) with $\omega = k^2/2$, and an angular step $\Delta\theta$. All simulations will consider the length form only, i.e. the DME will be calculated in length form and the reconstruction will be based on equations 3.11 and 3.12.

The first question to be addressed is whether it will be necessary to measure the DME *vector* or whether it can be sufficient to suppose it to be parallel to $\boldsymbol{k}$. In order to stay close to the experiment, we project the calculated DME vector on the laser polarization direction, obtaining $d_\parallel$. We then re-calculate the x- and y-component of the DME as $d_x = \cos\theta d_\parallel$ and $d_y = \sin\theta d_\parallel$. This means that in these simulations, we neglect the DME component perpendicular to $\boldsymbol{k}$. This is done because in the experiment, only the XUV polarization component parallel to the driving laser is measured and then, the DME, $\boldsymbol{d}$, is supposed to have no perpendicular component. This is obviously a simplification, but with the limited k-ranges explored in the experiment, we have not found any visible differences between orbitals reconstructed from the 'full' $\boldsymbol{d}$ and orbitals reconstructed from $d_\parallel$ only. The distortions introduced by the limited sampling are much more important.

Concerning the sampling, there are essentially two questions to be answered: Which k-range in the recombination DME has to be taken into account for a reasonably good reproduction of the orbital and with which density does this range have to be sampled? A very large spectral range (harmonic 1 to 991) is considered in figure 3.16. With this gigantic spectral width, the reconstruction is close to perfect if the full vector DME is considered, whereas the approximation of using only $d_\parallel$ causes the outer part of the orbital in figure 3.16a to be more spherical than the exact N_2 HOMO. For strongly restricted spectral widths, this distortion appears as well but the one caused by limited sampling is largely dominant.

In figure 3.17, only $d_\parallel$ is used for the reconstructions and $\Delta\theta$ is varied, considering only the experimentally accessible spectral range (harmonics 17 to 31). Between $\Delta\theta = 5°$ (figure 3.17a) and $\Delta\theta = 10°$ (figure 3.17b and, larger, in figure 3.19c), not difference is visible. Zooming out from the orbitals, another effect of the discrete sampling becomes apparent. If the sampling of the DME were done with an equidistant grid in $\boldsymbol{k}$-space, the result would be a periodic repetition of the reconstructed orbital in real space, thus imposing a certain minimal sampling density. In the experiment, we sample points equidistant on a k^2-scaling, along lines with an angular step $\Delta\theta$. This leads to the effect shown in figure 3.17b,c, were the reconstructed orbital is repeated on the x and y axes, with a period inversely proportional to the sampling steps in $\boldsymbol{k}$-space. Due to the non-equidistant sampling, the repetitions become smeared out more and more as the distance from the origin increases. With $\Delta\theta = 20°$, the first repetition gets dangerously close to the actual reconstructed orbital, whereas $\Delta\theta = 10°$ again turns out to be sufficiently small.

We have seen above that the narrow experimental spectral range allows to recover the principle structure of the N_2 HOMO. How sensitive is this on

the exact position of the narrow spectral window and how fast does the reconstruction improve if the spectrum is enlarged? Looking at the N_2 HOMO, one can already guess that there is some characteristic spatial frequency that should be included in the k-range if the essential shape of the orbital should be reproduced. This frequency is $k = 2\pi/L = 1.75$ a.u., and corresponds to the distance $L \approx 3.6$ a.u. of the two negative lobes (see figure 1.5). What other frequencies are important?

Figure 3.18 shows reconstructions using $\Delta\theta = 10°$ and different large spectral ranges. The reconstruction is still fairly close to the exact HOMO using harmonics 3 to 99, which, in comparison with figure 3.16, shows that the improvement by including 900 more harmonic orders is rather marginal. Cutting the highest orders further and including only harmonics 3 to 53 completely ruins the reconstruction, though. It is due to the dominant low frequency components, that the characteristic shape of the HOMO is hidden. Cutting these, as done in figures 3.18c,d, very quickly allows to recover the characteristic shape of the N_2 HOMO. If one is constrained to limit the used spectral range, it should thus be cut on the low frequency side as well as on the high frequency side around the characteristic spatial frequency.

Still, these simulations involve rather large spectra and high harmonic orders that we have not been able to generate. In the difficult phase measurements, we have been limited to 8 harmonic orders, from H17 to H31 – and we have already seen in figure 3.17, that these may contain sufficient information. Figure 3.19 shows reconstructions using only 8 harmonic orders. Clearly, when the considered spatial frequencies are too low and the above mentioned characteristic spatial frequency is not contained in the range, the orbital structure is not reproduced. Around the characteristic frequency, the exact position of the narrow spectral window is crucial – in the experiment one thus really has to hit the 'sweet spot' of the DME. Using harmonics 17 to 31 indeed seems to be very close to this optimal situation[13]. With only too high frequencies, the reconstructions turn out less satisfactory again.

These simulations show that it is realistic to acquire experimental data that contain sufficient information to recover the shape of the active orbital beyond its essential symmetry. When using spectra as narrow as those in our experiments, though, tomographic reconstruction becomes a game of chance about just hitting the essential part of the DME. For a reliable extraction of an a priori unknown orbital, the used experimental spectra clearly have to be rather large, which could be achieved using mid-IR lasers[14]. However, even if the spectral width is driven to extreme values, the reconstructions of static orbitals will probably never be precise enough to be considered a benchmark for calculations. On the other hand, for the observation of dynamics, the attainable spatial resolution should be sufficient for most cases and it will be the *temporal resolution* that makes molecular orbital tomography relevant to scientific applications. This perspective will be further discussed in section 3.4.6.

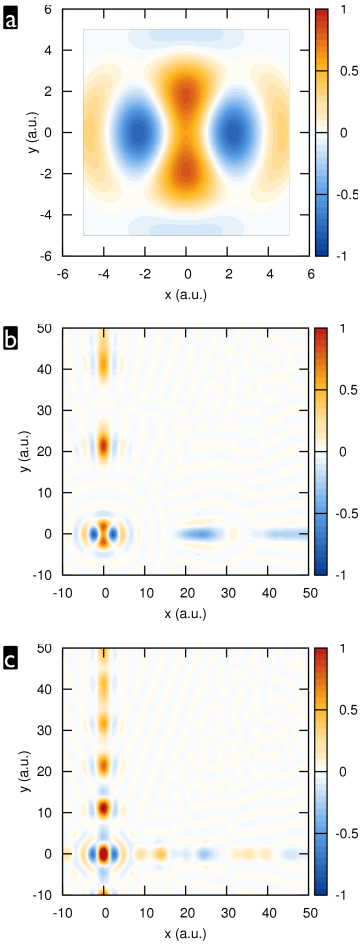

Figure 3.17. *Simulation of a tomographic reconstruction, based on the parallel component, $d_\parallel$, of the DME only, sampling k-points corresponding to harmonics 17 to 31 and an angular step of (a) $\Delta\theta = 5°$, (b) $\Delta\theta = 10°$ and (c) $\Delta\theta = 20°$.*

3.4.5 Experimental Orbital Reconstructions

Molecular orbital tomographic using our N_2 data is treated in detail in paper **II**. It turns out that with these data, we indeed reconstruct an experimental image of the N_2 HOMO with distortions very similar to those obtained in

[13] It should again be noted that these simulations are based on length-form DME and $\omega = k^2/2$ is used. The conclusions drawn here can thus only be qualitative and there is significant uncertainty in the link of the harmonic orders considered here to those observed in the experiment.

[14] The ponderomotive potential as $U_p \propto I\lambda^2$ (with I . . .intensity), such with longer laser wavelengths, λ, at constant intensity, much higher cut-off positions are possible.

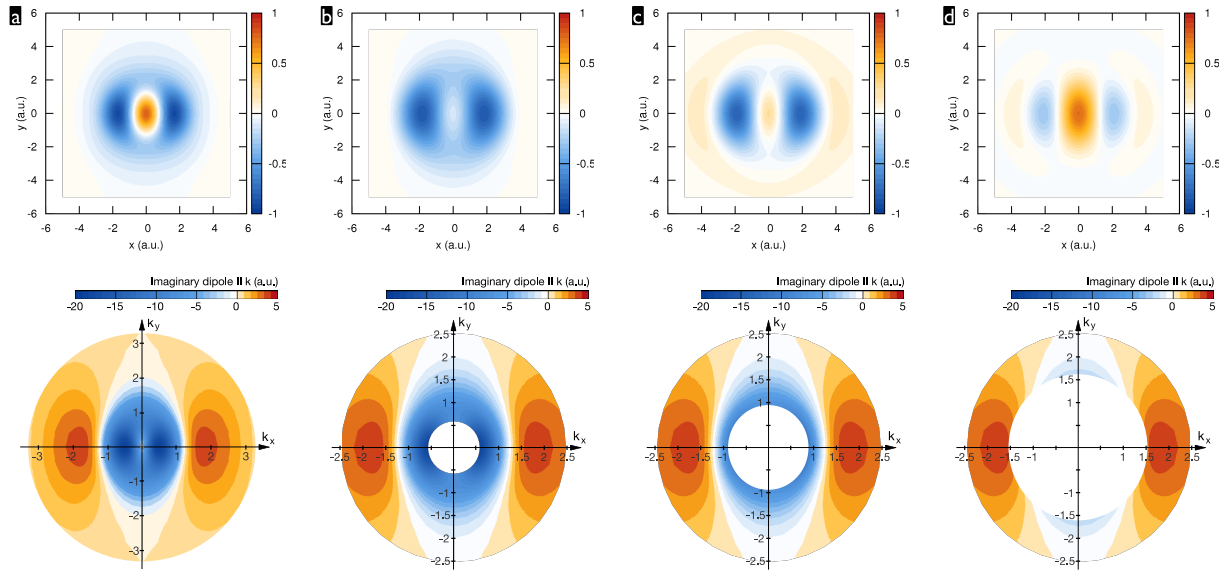

Figure 3.18. *Tomographic reconstructions and the slice of the DME that have been used. These slices are sampled at points corresponding to harmonic orders of an 800 nm laser and an angular step of $\Delta\theta = 10°$. The considered harmonic range is (a) H3–H99, (b) H3–H53, (c) H7–H53 and (d) H21–H53.*

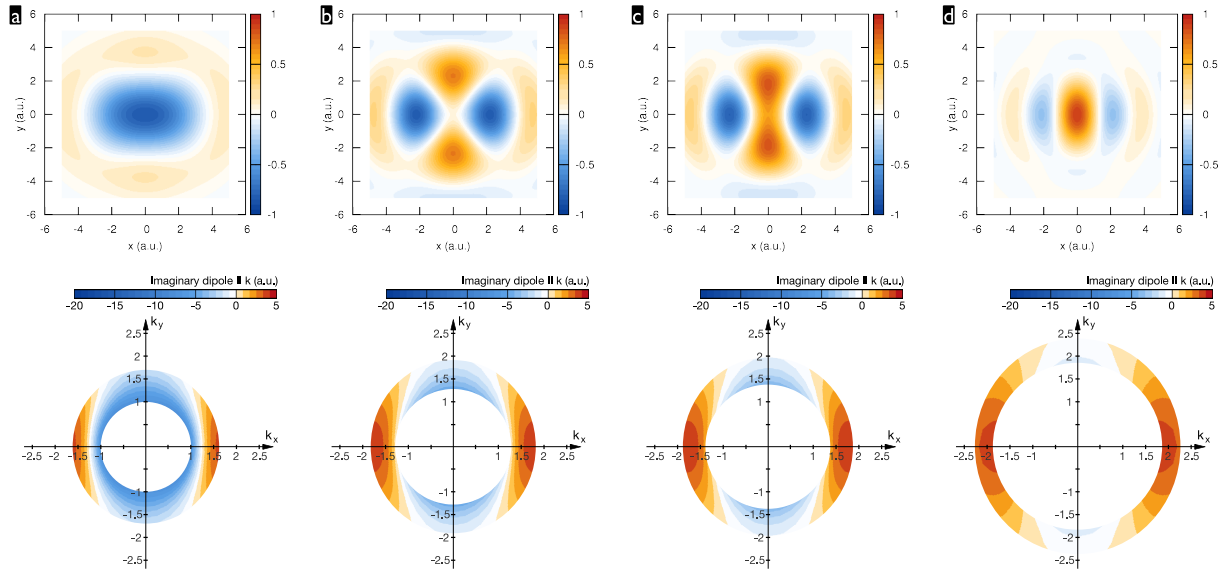

Figure 3.19. *Tomographic reconstructions and the slice of the DME that have been used. These slices are sampled at points corresponding to harmonic orders of an 800 nm laser and an angular step of $\Delta\theta = 10°$. The considered harmonic range is (a) H9–H23, (b) H15–H29, (c) H17–H31 and (d) H31–H45.*

the above simulations (figure 3.19c). According to our analysis, this image is contained in the imaginary part of the measured DME, further completed with the corresponding symmetry (i.e. $\mathrm{Im}(d_\parallel)$ is completed such that it is even in both k_x and k_y). The real part contains the contribution of the HOMO-1 and when imposing the corresponding symmetry ($\mathrm{Re}(d_\parallel)$ is completed such that it is even in k_x and odd in k_y), we can extract an experimental image of the HOMO-1.

It should also be noted that the separation of both contributions in real and imaginary part of the DME is not perfect and there is an approximately

linear variation of their relative phase over the spectral range. Furthermore, the relative weight of both contributions is not constant but varies both with frequency and angle, which introduces an additional filter-function in Fourier space and thus distortions in real space.

While the image of the HOMO contains clear spatial structure that is not simply imposed by the symmetric extrapolation of the DME, this is not the case for the image of the HOMO-1. It is essentially a result of the considered spectral range and the imposed symmetry: when setting the DME amplitudes to unity and the phases to zero for all angles and frequencies, the obtained image is almost the same as that extracted from the real part of the measured DME. Although this is expected for the HOMO-1, the DME of which does not have any particular structure in the considered spectral range, the absence of structure in both simulation and experimental result does not allow to claim a reconstruction of the HOMO-1. It is rather an indication of the consistency of our experimental observations and their interpretation.

This issue is also raised in the case of CO_2, where the data shown in figure 3 of paper **I** can be used to perform a tomographic reconstruction as well. Imposing the corresponding symmetry (odd in both k_x and k_y, which implies that the DME is set $\equiv 0$ at $\theta = 0°, 90°$) we obtain the results shown in figure 3.20b. It is not possible to say whether the experimental result is closer to the simulation based on a calculated DME for the CO_2 HOMO, or whether it is simply a consequence of the spectral range and the imposed symmetry, simulated in figure 3.20c. Nonetheless, the comparison of the measured DME phases with the plane wave simulation, done in paper **I**, leads to very satisfactory agreement such that we can safely say that the spatial structure of the CO_2 HOMO is encoded in the measured data.

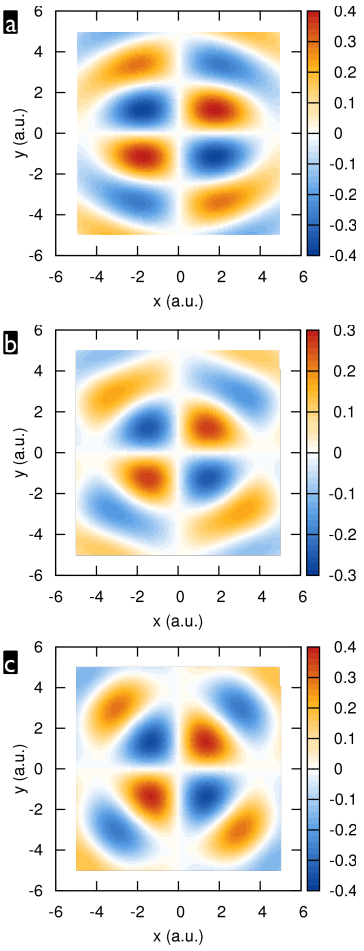

Figure 3.20. *Tomography with the CO_2 data, based on the velocity form. (a) Simulation using the experimental sampling ($\Delta\theta = 10°$, harmonics 17–29). (b) Using the experimental DME, the phase and squared amplitude of which are shown in figure 3 of paper **I**. (c) Using a DME with unity amplitude and zero phase, i.e. without any information content.*

3.4.6 Considerations on Dynamic Orbital Tomography

We have seen that the attainable precision of the reconstructed orbitals will probably be insufficient to be a relevant benchmark to calculated static orbitals. This is due to the necessarily limited spectral range sampled in experiments but also due to the simplifications made in the model the tomography-scheme itself is based on. It is nonetheless worthwhile to continue research on molecular orbital tomography because it contains the potential of time resolved imaging of intra-molecular electron dynamics – with temporal resolution essentially limited by the attochirp that spreads the recollision instants associated with different spectral components over typically a few hundred attoseconds.

Therefore, as we argue in paper **II**, the images we reconstruct from the N_2-data have been made with an 'exposure time' of ≈600 as at ≈ 1.5 fs after the ionization instant. Furthermore, if our interpretation is accurate, we can sum the two orbitals we extract from the real and imaginary part of the experimental DME to obtain a snapshot of the time-dependent Dyson orbital, interpreted as a hole in the ion by (Smirnova et al. [186]). This certainly qualifies as imaging of intra-molecular electron dynamics – the simplest possible kind of such dynamics, namely a beating of two pure quantum states. It is not obvious, though, how to interpret this dynamics: it is not immediately clear that one can speak of electron re-arrangement upon ionization as does (Vrakking [208]). Also, the connection of this 'hole', or more precisely Dyson orbital, to the concept of an exchange-correlation hole and its dynamics, treated e.g. by (Breidbach and Cederbaum [14], Remacle and Levine [167]), is not clear to us at this point.

The snapshot of the 'hole' shown in figure 3e,f of paper **II** is based on a number of assumptions and one should refrain from pushing the analysis

further based on this image. Some of the most important assumptions could be lifted by measuring the full phase of the DME, i.e. its spectral and angular dependence, without having to impose its value at some spectral component (as we did at harmonic 17) and without having to complete three quadrants of $\boldsymbol{k}$-space according to an assumed symmetry. In section 3.2.3, it was discussed how these improvements could be made. Then, one could really speak of an *ab initio* imaging method. This would also fulfill one necessary condition for the reconstruction of asymmetric (Dyson-) orbitals. These would lead to a DME that is asymmetric in $\boldsymbol{k}$-space as well.

A second necessary condition is that one has to be able to discern between θ, $-\theta$ and $\theta + 180°$ – i.e. one has to *orient* molecules instead of only aligning them. Techniques for doing this are being developed, e.g. by (Dion et al. [28], Goban et al. [60], Kanai and Sakai [85], Machholm and Henriksen [123], Vrakking and Stolte [209]). Furthermore, the electron recollision has to be limited to one side of the molecule only, as pointed out by (van der Zwan et al. [202]), which requires either half-cycle laser pulses or some means of control over the continuum electron trajectory, such as a driving laser field with the second harmonics added (see e.g. (Mauritsson et al. [140])).

Dynamics that are not launched by the ionization-step but by an ultrashort pump-pulse will pose a contrast problem: the pump pulse will always only excite a more or less important fraction of all molecules contributing to the XUV signal. It is thus going to be necessary to arrange for a preferential detection of the XUV light generated in the excited species. This is, however, a 'classic' problem in experimental physics and numerous approaches exist to solve it. In the case of HHG in molecules, two techniques have been developed: polarization resolved detection, which is the subject of section 3.5.1 and paper **III**, and transient grating spectroscopy, demonstrated by (Mairesse et al. [131]).

3.5 Probing Nuclear Dynamics in Molecules with Attosecond Electron Wave Packets

In the preceding sections, the probed or imaged objects were electrons, bound in molecules. The self-probing scheme can, however, also provide information about nuclear dynamics in the molecule. These can happen on quite different time scales, depending on the degree of freedom and, obviously, the mass of the nuclei. In the vast majority of cases, the nuclear dynamics take very long compared to the sub-IR-cycle dynamics of the EWP probing the molecule at re-collision. In this case, the whole 3-step process of HHG can be used as a probe process[15] of dynamics initiated by a preceding pump pulse and temporal resolution is limited by the total duration of the HHG driving pulse. This is the kind of experiments discussed in section 3.5.1. The lightest nuclei, the extreme case of which is the hydrogen nucleus, i.e. a single proton, may move significantly during an IR field cycle. Then, the three steps of HHG may be used as a pump, delay stage, and probe, which is the essence of the experiment presented in section 3.5.2.

3.5.1 High-contrast Measurement of Rotational Revivals

A measurement of rotational dynamics has actually been part of the data acquisition runs in all the experiments where aligned molecules have been used. As mentioned in connection to figure 2.4, the XUV yield from N_2 molecules

[15] This constitutes a special variant of the self-probing scheme, differing from the one introduced so far.

as a function of the delay between aligning and HHG pulse bears a strong resemblance to the calculated $\langle\cos^2\theta\rangle$-measure of molecular alignment. So does the CO_2-signal, expect that it always evolves in the opposite sense, i.e. it decreases for increasing $\langle\cos^2\theta\rangle$ and vice versa. Calculated $\langle\cos^2\theta\rangle$-curves and measured XUV signals as a function of the aligning pulse - HHG pulse delay are shown in figure 3.21.

In paper **III**, we discuss in detail the technique of polarization resolved spectroscopy with high-order harmonics to strongly enhance the contrast of this kind of measurement. It is based on the detection of a selected component of the field that vanishes if the effect to be observed is absent, thus detecting with a vanishing background signal.

As discussed in section 3.3.1, aligning a molecular sample produces an anisotropy and a selective detection of the orthogonal XUV field component thus allows to observe with high contrast the re-phasing of the rotational wave packet created by the aligning pulse. To this end, we added a pair of uncoated silver mirrors at 60° incidence between the toroidal mirror and the detection (cp. figure 2.8). These act as a polarizer with a 30 times higher reflectivity for s-polarization than for p-polarization at harmonic order 21 (see figure 3.22). Since the HHG beam was p-polarized, the harmonic signal detected with unaligned molecules was strongly reduced and represents the background signal. In these experiments, we measured only harmonic intensities and since the transmission of the polarizer was quite low, we detected with a photon multiplier instead of the MBES, which offers very high gain with high signal-to-noise ratio. Using this technique, we reached an enhancement of the contrast from ~ 2 with the conventional detection scheme (see figure 3.21b), to 8 (see figure 3.23 and figure 6 in paper **III**) when aligning the molecules at $\theta = 40°$ from the HHG beam polarization, which provided the strongest perpendicular XUV field component.

In a second series of experiments at CELIA Bordeaux using the setup shown in figure 2 of paper **III**, providing very similar conditions as the setup in Saclay, we could show that with polarization resolved spectroscopy, one can easily detect the alignment of N_2 molecules in a 1:1 mixture with argon gas. This is hardly possible without the polarization resolution since argon generates harmonics with about a factor of 3 higher efficiency than N_2 and thus strongly dominates the XUV emission of the gas mixture. This result shows that with suitable contrast enhancing techniques, another example of which is transient grating spectroscopy (Mairesse et al. [131]), even weak contributions to a signal can be detected efficiently. The problem of such weak contributions is posed for example if a carrier gas has to be used, which is what we mimic with the N_2-argon mixture, or if the studied system is in a weakly populated excited state.

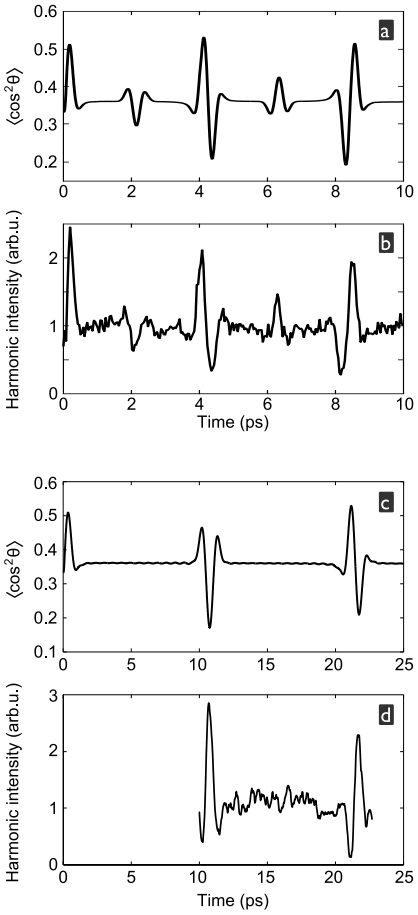

Figure 3.21. *Calculated $\langle\cos^2\theta\rangle$ for N_2 (a) and CO_2 (c) with rotational temperature T_{rot} = 90 K, 'kicked' by a 55 fs laser pulse with an intensity of 5×10^{13} W/cm^2 (cp. section 2.2). Measured dependence of the intensity of harmonic 21 generated in N_2 (b) on the delay between HHG pulse and aligning pulse. Same dependence, for harmonic 25 generated in CO_2 (d).*

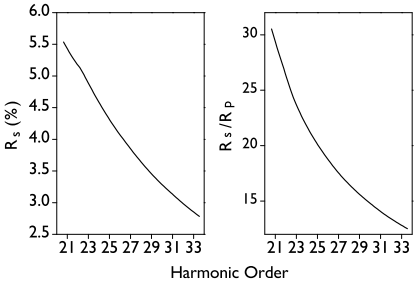

Figure 3.22. *Reflectivity of a pair of silver mirrors with 60° incidence (defined with respect to the surface normal) for s-polarized light (left). Reflectivity ratio for s- and p-polarized light (right), i.e. the extinction ratio of the polarizer. These data are based on (Henke et al. [72]).*

3.5.2 Sub-laser-cycle Vibrational Dynamics of Protons

In the vibrational degrees of freedom, nuclear dynamics are usually much faster than the rotation considered above. In particular in the molecule with the lightest nuclei, molecular hydrogen, the protons may indeed move on an attosecond timescale. This movement is understood most easily within the Born-Oppenheimer approximation, introduced in section 1.2.3. The nuclei, described by a nuclear part, $\chi(R)$, of the total molecular wavefunction, then move in a potential of electron energy. The ground state BO potentials for H_2 and H_2^+ are shown in figure 3.24. Since the equilibrium internuclear distance of the ion is larger than that of the neutral molecule, the nuclei will move apart as soon as the molecule is ionized. As the H_2^+ ground state is a bound state, the molecular ion will, however, not dissociate but rather vibrate

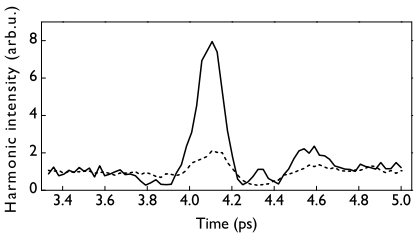

Figure 3.23. *Intensity of harmonic 21 generated in N_2 as function of the aligning pulse - HHG pulse delay. The dashed line shows the results recorded with the conventional setup (figure 2.8), equivalent to the data shown in figure 3.21b. The solid line is the result of polarization resolved spectroscopy, detecting preferentially the XUV field component orthogonal to the driving laser. Both data sets are normalized to the level of signal detected with unaligned molecules.*

– the H-H bond will be stretched and compressed with an oscillation period of $2\pi\hbar/\Delta E_\nu \approx 17$ fs, where $\Delta E_\nu \approx 0.25$ eV is the energy separation of the two lowest vibrational states of H_2^+.

PACER

(Lein [109]) first studied the role played by this expansion in the HHG process by analyzing results of non-BO TDSE simulations. He normalized the HHG spectrum generated in H_2 by that generated in D_2, having nuclei twice as heavy as those of H_2. Within the BO approximation, the sole difference between these two molecules lies in the nuclear part of their wavefunctions, so any difference in the high harmonic spectra must come from there. A Lewenstein (SFA) theory with nuclear motion incorporated within the BO approximation, developed by (Lein [109]) and discussed in paper **IV**, gives results that compare very well to the exact TDSE calculations – at least for an 800 nm laser and an intensity of $\sim 1 \times 10^{14}$ W/cm^2. Besides the computational simplification, the SFA theory reveals a beautifully simple scheme, illustrated in figure 3.24, to explain the influence of nuclear motion on HHG. Based on this scheme, the nuclear dynamics can be retrieved by means of a genetic algorithm (Lein [109]).

This was experimentally demonstrated by (Baker et al. [5]), who measured intensities of high harmonics generated in H_2 and D_2 and analyzed their ratio just as (Lein [109]) did with his TDSE results. They termed the technique PACER: 'Probing Attosecond dynamics by Chirp-Encoded Recollision'. The three steps, commonly used to describe HHG, are considered as a pump, a delay-stage, and a probe process: (i) A strong laser field ionizes the molecule, launching simultaneously an electron wavepacket of attosecond duration into the continuum and a time dependent nuclear wavepacket onto the electronic ground state potential surface of the molecular ion. (ii) The continuum EWP is subsequently accelerated and driven back to the ion by the laser field, while the nuclear wavepacket evolves in parallel. (iii) At recollision, there is a certain probability for recombination to the ground state, releasing the accumulated kinetic energy of the electron in the form of an attosecond burst of XUV light. For *coherent* emission, recombination has to lead back to the initial state [16], the nuclear part of which is the vibrational ground state of the neutral molecule. The probability of this transition depends on the overlap of this ground state nuclear wavefunction with the evolved nuclear wavepacket of the molecular ion at the recombination time, i.e. recombination will be all the less likely the further the ion has evolved. In his SFA theory, reviewed in

[16] The coherence of the whole HHG process is crucial so that many molecules in a macroscopic medium emit high harmonic radiation coherently, their contributions adding up to a macroscopic signal. Of course, the HHG process could, for instance, start with the molecule in the ground state and end with a vibration excited molecule. This excited state would, however, have an arbitrary phase relative to the continuum electron, which is 'phase locked' to the ground state and the light emission would consequently be incoherent and not participate to the high harmonic spectrum detected in experiments. Obviously, the initial state of the molecule can already be a coherent superposition of vibrational states. In the experiment, before the IR laser pulse, all molecules are in the vibrational ground state: We are using a supersonic jet, i.e. our molecules are cold. But even at room temperature, $k_B T = 0.025$ eV is much smaller than the energy difference of two vibrational states of H_2 / D_2: $\Delta E_\nu = 0.5$ eV /0.35 eV. The IR laser may then vibrationally excite the neutral molecules, e.g. via a Raman process. The laser bandwidth, however, is by far insufficient to drive a stimulated Raman process (one would need 250 nm laser bandwidth to couple vibrational states in H_2 with an 800 nm laser) so only spontaneous Raman scattering could populate higher vibrational states. This process is not only very inefficient but it would also *not* create a coherent vibrational wavepacket in the molecules. (Lein et al. [112]) have done TDSE calculations without adopting the BO or single-active-electron approximation for a 1D H_2 model molecule in laser fields of $0.75 - 2 \times 10^{14}$ W/cm^2. The results showed that the nuclei of the neutral molecules remain very close to their equilibrium distance which means that high harmonic generation starts from a situation that is very close to the field-free ground state of H_2.

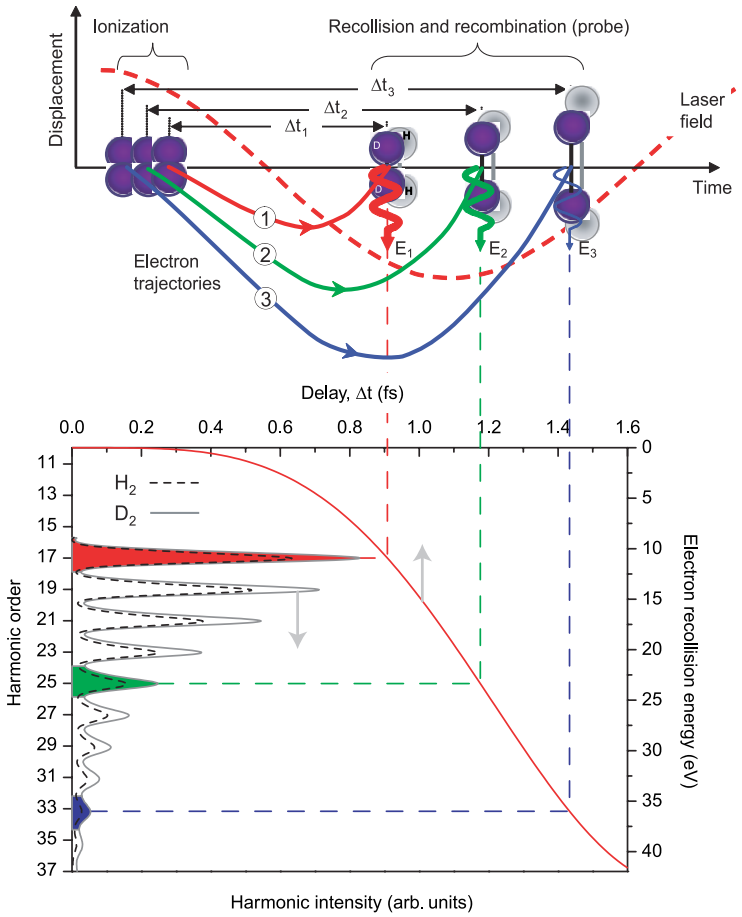

Figure 3.25. *Encoding of the nuclear dynamics within harmonic spectra. Upper panel: The trajectory of the ionized electron differs depending on the exact time of ionization. Three possible electron trajectories labeled 1, 2, and 3 are shown, which re-collide with the molecular ion after delays Δt_1, Δt_2, and Δt_3, with increasing kinetic energy E_1, E_2, and E_3, resulting in the emission of increasingly higher frequency photons after re-combination (shown as the 17th, 25th, and 33rd harmonics for the purpose of this illustration). Note: Although the E vs. Δt-curve in the lower panel is a physically accurate result of a classical calculation (cp. section 1.3.2), the electron trajectories shown in the upper panel have been slightly altered to improve clarity. [Figure taken from (Baker et al. [5])]*

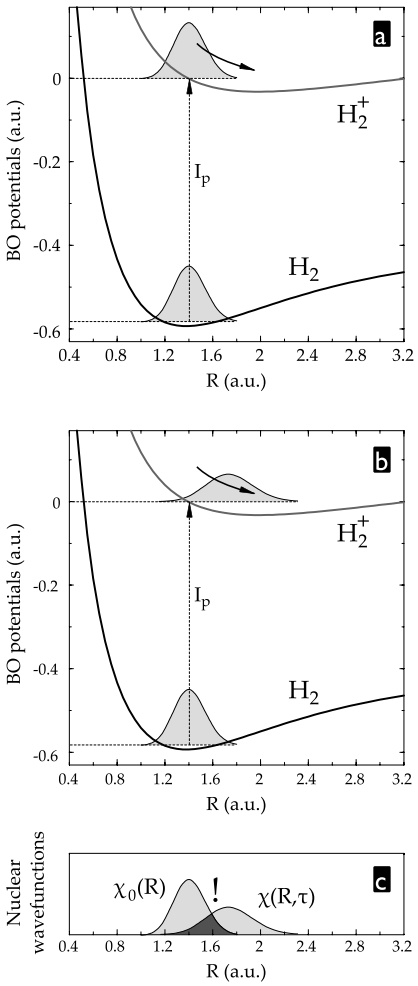

Figure 3.24. *Nuclear dynamics during the three steps of HHG in H_2, according to the model described in paper **IV**: (a) The ionization step takes the ion into the electronic ground state via a Franck-Condon transition, i.e. the initial vibrational wave packet of the ion resembles the vibrational ground state of the neutral molecule. (b) During the continuum excursion of the active electron, the nuclei of the ion evolve on the BO potential curve, which is repulsive in the beginning. The wavepacket thus moves to higher R and spreads. (c) Recombination has to lead back to the neutral ground state and only the overlap of the nuclear wavefunction parts of the ground state and the evolved ion can contribute to HHG. The BO potentials here are shown with the energy calibration used in paper **IV**.*

paper **IV**, (Lein [109]) reduces the effect of nuclear dynamics on the emitted harmonic radiation to an overlap integral

$$C(\tau) = \int \chi_0(R)\chi(R,\tau)\mathrm{d}R, \tag{3.18}$$

where τ is the pump-probe delay, i.e. the electron excursion time, $\chi_0(R)$ and $\chi(R,\tau)$ are the nuclear parts of the neutral ground state and the time dependent wavefunction of the molecular ion, respectively, and R is the internuclear distance. The emitted XUV field is proportional to this overlap integral. As long as the ion expands, the XUV emission thus gets weaker with τ (cp. figure 3.24).

Scanning the pump-probe delay is achieved by the inherent chirp of the re-colliding EWP: for the short electron trajectories, higher harmonics are associated with larger electron excursion times, τ, and thus larger recollision times. Knowing the EWP chirp thus allows to map the easily measurable harmonic frequency to a pump-probe delay in the PACER scheme as illustrated in figure 3.25. (Baker et al. [5]) assumed this chirp to be the same as for rare-gas

atoms, as measured by (Mairesse et al. [127]). In this thesis, we have shown that the atomic and molecular emission times – i.e. the group delay of the XUV emission – may be equal provided that (i) the nuclear movement can be neglected on a sub-laser-cycle timescale (which is true for heavier molecules such as N_2 and CO_2), (ii) the sample is aligned in such a way that two-center interference (cf. section 3.1.2) does not occur, and (iii) the two species have the same ionization potential.

In paper **IV**, we study the case when (i) is not realized. We measure the emission times for both H_2 and D_2 with RABITT and compare to those measured with argon, whose ionization potential is very similar. Figure 4a of paper **IV** shows that the emission times are indeed very close. This is experimental evidence that the effect of the nuclear dynamics on the XUV spectral phase is small and that the *excursion* time, and thus the frequency-time mapping at the heart of the PACER scheme, is essentially the same for the two isotopes as well as the atom.

Nuclear dynamics and the XUV spectral phase

(Baker et al. [5]) have measured intensity spectra with H_2 and D_2 and used their ratio to extract the nuclear dynamics. Such an intensity measurement is technically fairly easy to make but the measured spectra are extremely sensitive to macroscopic effects and experimental conditions. In paper **IV**, we show for example that the rather high residual pressures due to the low pumping efficiencies of turbo-molecular pumps for H_2 as compared to D_2 can completely ruin the PACER measurement.

As the XUV spectral phase is generally less sensitive than the intensity to fluctuations of experimental conditions and macroscopic effects, we study it in paper **IV** as a possible observable for PACER. We thus analyze in detail the SFA model of (Lein [109]) in terms of a possible imprint of the nuclear dynamics on the spectral phase of the high harmonic emission. We find that (i) the electron continuum dynamics remain unaffected, justifying the use of excursion times known from atoms for the time-frequency mapping a done by (Baker et al. [5]). (ii) In the recombination step, the nuclear overlap integral $C(\tau)$ (equation 3.18) comes into play, which is in general complex valued. Its phase is thus transferred to the XUV emission. The spectral phase difference of high harmonics emitted by H_2 and D_2 molecules thus contains information about the nuclear dynamics in the ion just in the same way as the intensity ratio measured by (Baker et al. [5]) does. The difference is that the intensity ratio is proportional to the ratio of the squared moduli of $C(\tau)$, whereas the harmonic phase difference is directly given by the phase difference of the $C(\tau)$ for the two isotopes. In paper **IV**, we calculate this phase difference and compare it to measured data. The theoretical values fall within the experimental error bars, and in order to extract nuclear dynamics from phase measurements, higher precision would be needed.

Our measurements as well as those of (Kanai et al. [89]) do, however, indicate a larger D_2-H_2 phase difference than expected from the SFA and BO approximation based theory. Phase measurements with higher precision, such as RABITT scans over a longer delay range and more precise control over experimental parameters, or the analysis of interferences from long and short trajectory, as demonstrated by (Zaïr et al. [218]), will increase the precision of experimental observations.

Further theoretical studies will then allow to elucidate the origin of the phase effect. Focusing on harmonic intensities as observable, (Chirilă and Lein [17]) have found the IR laser induced coupling of the ion ground state with (dissociative) excited states to be negligible within the pump-probe delay

range covered by PACER with an 800 nm driving laser. When R increases, the BO potential curves of these excited ion states get closer to the ground state and coupling becomes more efficient. In H_2^+ this effect should thus play a stronger role than in D_2^+, leading to differences not included in the SFA model that forced the ions to remain in their ground state. Non-BO effects are another candidate for explaining the (possibly) observed deviation and it would be exciting to observe their influence in the harmonic phase.

Let us note finally that (Baker et al. [6]) observed transient two-center interference in PACER experiments with H_2 and D_2 molecules, partially aligned by a sufficiently long generating laser pulse. This effect still remains to be seen in phase measurements.

3.6 Conclusions

In several examples, we have experimentally demonstrated the potential of the self-probing scheme to observe or image ultra-fast intra-molecular electronic and nuclear dynamics. In particular, we have done the first phase measurements of the high harmonic emission from aligned molecules. These provide unambiguous evidence for quantum interference at the origin of the intensity minima observed by other groups. Orbital tomography has been intensely discussed and we have made major progress both on the experimental and on the theoretical side, which takes us to conclude that this imaging is indeed experimentally realizable. Distortions of the reconstructed orbitals are unavoidable, due to both the plane-wave approximation and the limited experimental spectral range – as in our experimental reconstructions – but this should not prevent imaging of ultra-fast changes of, e.g., a frontier orbital. The most interesting perspective is thus *dynamic* orbital tomography instead of high-spatial-resolution imaging of static orbitals.

Chapter 4

Probing Molecules with Attosecond XUV Wavepackets

In this chapter, an experiment will be presented that makes use of XUV wavepackets to probe molecules as schematized in figure 4.1. The XUV pulse almost always ionizes the molecule (see section 1.3.4 for the theoretical description of this process) and by analyzing the ejected photoelectron wave packet, details about the photoionization process and its dynamics can be extracted. Examples for this kind of measurement are the time-resolved observation of Auger- and shake-up processes in atoms by (Drescher et al. [31]) and (Uiberacker et al. [201]), and of photoelectron emission from solid surfaces by (Cavalieri et al. [15]).

Information about bound and scattering states of the ionized atom or molecule can also be accessed as demonstrated for example by (Remetter et al. [168]), who measured the symmetry of the 3p orbital of argon via the interference of photoelectron wave packets.

The experimental techniques for the XUV-probing scheme are very much the same as those used in the self-probing scheme, discussed in the previous chapter. There, photoionization was the experimental tool to characterize the attosecond XUV pulses encoding the sought-for information, whereas here, the XUV pulses are the tool and the ionized system is the studied object.

Photoionization of atoms and molecules with XUV radiation is of course not an invention of the attophysics community but has been applied in experiments with synchrotron radiation since the 1970s. The fully coherent and, most importantly, ultra-short (femto- or even attosecond vs. picosecond for synchtrotrons) XUV radiation generated by HHG, however, opens new possibilities for such experiments, shifting the focus from extreme spectral to extreme temporal resolution. A useful compromise of both can be obtained by using APTs, the spectrum of which is a comb of narrow harmonics and the temporal envelope is typically ~ 10 fs large.

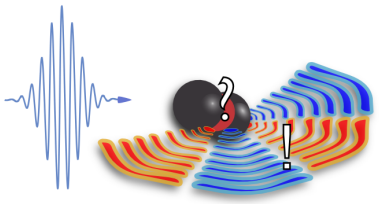

Figure 4.1. *XUV-probing scheme: Ionizing a molecule with ultrashort XUV pulses and analyzing the ejected continuum electron wave packet can give access to the dynamics of the photoionization process, the structure of the continuum etc.*

Résumé du Chapitre

Dans ce chapitre, une expérience sera présentée, dans laquelle des paquets d'ondes XUV sont utilisés pour sonder des molécules suivant le schéma montré dans la figure 4.1. Dans la plupart des cas, l'impulsion XUV ionise la molécule (cf. la section 1.3.4 pour une description théorique de ce proces-

sus) et l'analyse du paquet d'ondes électronique émis permet d'extraire des détails sur le processus de photoionisation et sa dynamique.

Les outils expérimentaux pour le schéma d'ionisation XUV sont essentiellement les mêmes que ceux utilisés pour le schéma d'auto-sondage, discuté dans le chapitre précédent. Dans ce dernier, la photoionisation XUV était l'outil expérimental pour caractériser les impulsions XUV attosecondes encodant l'information recherchée, alors qu'ici, les impulsions XUV sont l'outil et c'est le système ionisé qui est l'objet étudié.

Résultats principaux

Nous avons mesuré par la méthode RABITT la 'phase moléculaire': la phase de l'élément de matrice dipolaire pour la photoionisation à deux photons et deux couleurs. En supposant que cette phase soit égale à celle de l'élément de matrice dipolaire à un *photon, cette mesure répond donc à la question: comment le processus d'ionisation par absorption d'un photon XUV modifie-t-il le paquet d'ondes électronique éjecté par rapport au paquet d'ondes XUV incident? Nous avons fait les expériences avec des molécules de N_2 (non-alignées), qui sont ionisées par un train d'impulsions attosecondes généré dans l'argon. En fonction de l'état électronique et vibrationel final de l'ion – discernable dans nos spectres de photoélectrons grâce à la résolution spectrale permise par le train d'impulsions attosecondes par rapport à une impulsion isolée – nous observons l'influence d'une résonance complexe auto-ionisante dans le continuum des états ioniques. Il s'agit d'un état de la molécule neutre fortement excité électroniquement qui est quasiment résonnant avec l'ordre harmonique 11 de notre laser. Le canal d'ionisation passant via cet état résonnant impose un saut de phase sur le paquet d'ondes électronique à l'énergie résonnante et change donc sa forme temporelle. Nous mesurons un saut de phase de $\geq 0.9\pi$ rad, correspondant à un délai de groupe imposé sur la composante spectrale résonnante du paquet d'ondes électronique de ≥ 600 as.*

Conclusions

Ces résultats sont déjà plus que simplement une démonstration de principe car l'état résonnant en question n'est pas encore très bien connu et la dynamique de photoionisation via cet état intermédiaire est très probablement complexe et inclut une couplage avec une autre série d'états. Cependant, plusieurs questions importantes restent ouvertes. Théoriquement, il est nécessaire d'avoir une meilleure compréhension de la 'phase moléculaire' et de son lien avec la phase de l'élément de matrice de photoionisation à un photon. Cela permettrait d'en déduire des durées effectives de photoionisation (ou d'auto-ionisation) et des informations quantitatives sur des états résonnants ou des états de diffusion. Expérimentalement, une série d'extensions seraient très intéressantes comme, evidemment, le balayage de la fréquence laser pour faire glisser la fréquence de l'harmonique 11 sur la largeur de la résonance et par exemple échantillonner le saut de phase entier et déterminer sa valeur et sa largeur. La détection des photoélectrons avec une résolution angulaire permettrait de discerner les differentes ondes partielles du continuum. Nous avons prévu de tenter ces expériences bientôt.

Plusieurs autres groupes sont maintenant en train de faire des mesures similaires pour observer des dynamiques dans le processus de photoionisation XUV, soit avec la méthode RABITT soit avec une impulsion attoseconde unique et la 'caméra électronique à balayage de fente attoseconde'.

4.1 Phase-resolved XUV Photo-ionization of N_2 Molecules

The original idea to this experiment was to measure the XUV photoionization matrix elements for N_2 molecules and compare them to the recombination matrix elements discussed in the previous chapter. At first glance, according to the detailed balance principle, the two should be precisely equal. According to the arguments raised in section 3.1.1, this is, however, probably not the case. The different measurements methods would thus be able to access quite different effects.

The amplitude of the photoionization matrix element has of course been known for a long time from synchrotron experiments and can for example be found in (Itikawa et al. [81]). The phase, however, is harder to access and, as we argue in paper **V**, experiments using quasi-monochromatic synchrotron light are not able to measure the *spectral* phase of the photoionization matrix element, i.e. its energy dependence. They can, from fits of measured angular distributions in the molecular frame (Lebech et al. [108]), access the *relative* phases of photoionization matrix elements for different partial waves, i.e. degenerate scattering states of different angular momentum, at a *given energy*.

Measuring the energy dependence of the photoionization matrix element phase should be possible with ultra-short XUV pulses, because, according to equation 1.49, the photoelectron spectrum contains an imprint of this matrix element, which can be extracted if the XUV wave packet used to ionize the molecules is known. This condition is no obstacle since we are well equipped to generate XUV pulses, for example in argon, which is a fairly efficient medium for harmonic orders up to ≈ 33, and measure them with a known detection gas. All that would be left to do, is to repeat the RABITT measurement, this time detecting with N_2 molecules in the MBES interaction volume. From this measurement, the molecular phase for N_2, still denoted $\Delta\phi_q^{\mathrm{at}}$ (cp. equation 1.68), can be extracted. The connection of this observable to the single-XUV-photon ionization matrix element we are actually interested in, remains, however, somewhat unclear (see end of section 1.3.4).

The experiment was done with the setup also used for the self-probing type experiments, i.e. the setup shown in figure 2.8. Attempts to observe alignment of molecules in the MBES interaction region via a possible dependence of the XUV photoionization yield on the angle between the internuclear axis and the XUV polarization direction [1] failed. This is somewhat surprising since even if the molecules injected by the effusive gas jet of the MBES remained at room temperature, a certain (low) degree of alignment should occur. The reason thus has to be that the XUV photoionization yield for N_2 molecules has a very weak dependence on alignment, as already observed by (Lépine et al. [114]). In any case, owing to the low degree of alignement that could be expected, the experiment was finally carried with unaligned N_2 molecules.

4.1.1 Deciphering the Spectra

When photoionizing N_2 molecules with XUV radiation, different photoelectron/ion pairs can be produced: An electron from the HOMO can be ejected into the continuum, leaving the N_2^+ ion in its fundamental $X\,^2\Sigma_g^+$ state. Alternatively, an electron from the HOMO-1 may be removed, leaving the ion in its first excited $A\,^2\Pi_u$ state, or an electron from the HOMO-2 is ejected, leaving the ion in its second excited $B\,^2\Sigma_u^+$ state. The BO potential curves for these three ion states as well as the neutral ground state are shown in figure 4.2. Ob-

[1] Note that the high harmonic emission from atoms has linear polarization parallel to that of the driving laser.

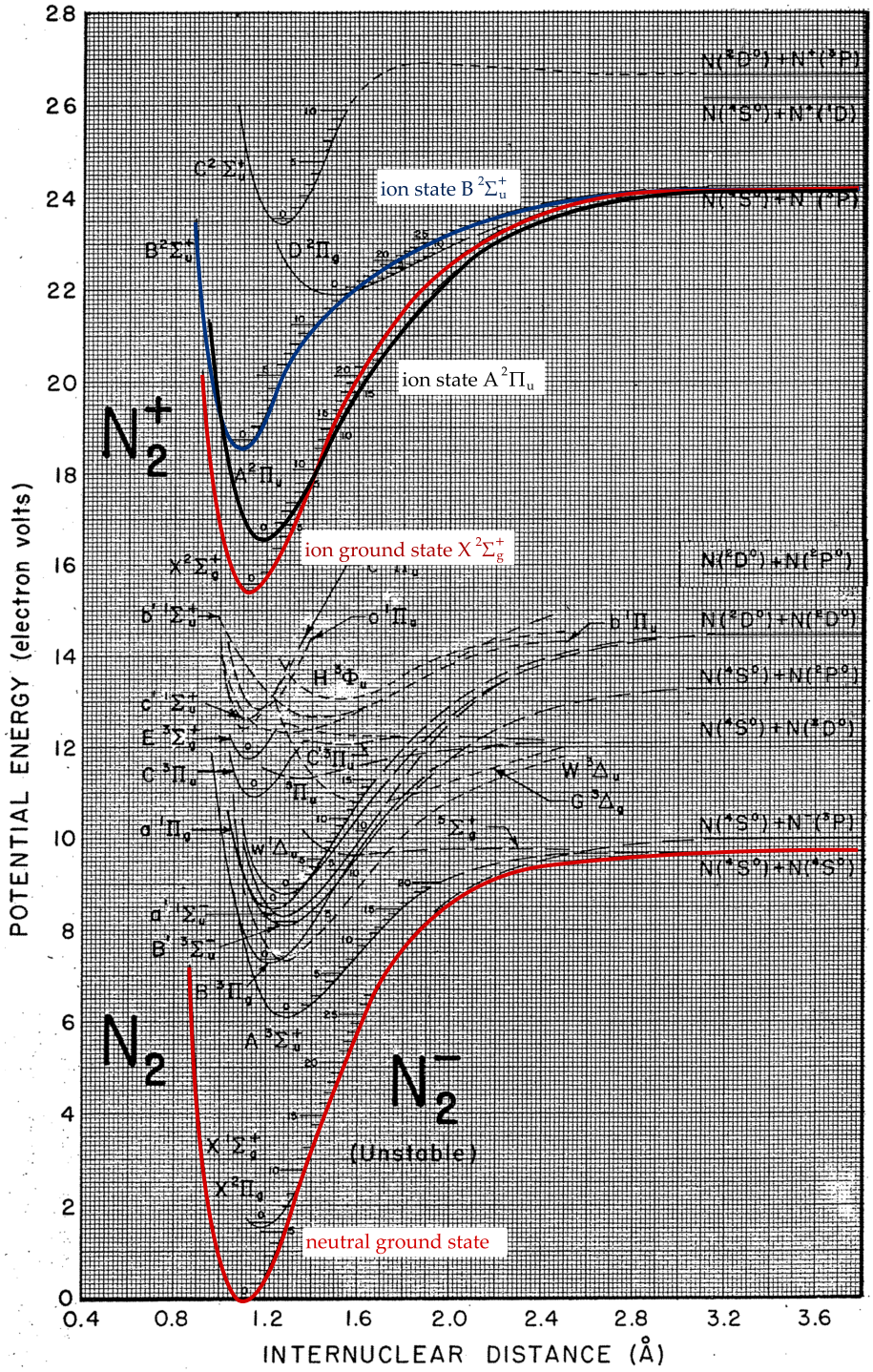

Figure 4.2. *Potentials energy curves for N_2 and N_2^+ according to (Lofthus and Krupenie [120]). The ground states and first two N_2^+ excited states are accentuated.*

viously, an enormous number of additional excited states of the ion and the neutral molecule exists, each corresponding to another excitation or ionization channel, but the three mentioned are those relevant for this experiment. The adiabatic ionization potentials for these three channels, in the following denoted as X, A and B channels according to the final ion state, are I_p^X = 15.58 eV, I_p^A = 16.7 eV and I_p^B = 18.7 eV, respectively.

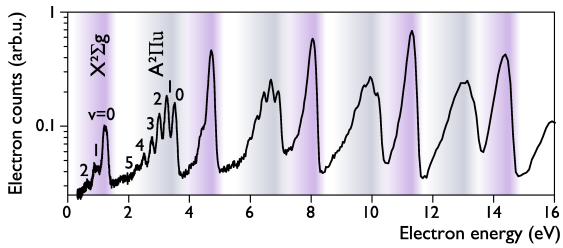

Figure 4.3. *Photoelectron spectrum obtained with molecular nitrogen, averaged over 2000 laser shots. The sets of peaks corresponding to ionization of the HOMO and HOMO-1 are shaded in violet and gray, respectively. Note that the ordinate shows electron counts in equally spaced* time *bins, i.e. it is not scaled to be proportional to the EWP spectral intensity. Note also that the time-of-flight → energy conversion was done with the simple equation 2.8, which is not accurate for the slowest electrons, which is why the very first peak actually appears at a too low energy in this figure.*

A photoelectron spectrum, produced by ionizing N_2 molecules with high-order harmonics generated in argon, is shown in figure 4.3. Essentially two sets of peaks appear, each corresponding to the comb of odd harmonics of the driving laser frequency, with photoelectron energies $q\omega_0 - I_p^X$ and $q\omega_0 - I_p^A$, respectively. The cross section for ionization from the HOMO-1 orbital is about 2 times higher in the considered spectral range than that for ionization from the HOMO (Itikawa et al. [81]). Ionization from the HOMO-2 produces a comb of photoelectron peaks that overlaps with that produced by ionization of the HOMO ($I_p^B - I_p^X = 3.12\,\text{eV} \approx 2\omega_0$). However, since the cross section for this channel is one order of magnitude lower that for the X channel (Itikawa et al. [81]), its contribution can be neglected.

For each of the two considered photoionization channels, X and A, the molecular ion can be excited to a series of vibrational states which are separated by about 250 meV (cp. figure 4.2). They appear as a substructure in broadened photoelectron peaks in the spectrum, clearly visible in figure 4.3. Note that the energy resolution of the electron time-of-flight measurement in the MBES decreases with electron energy, blurring the vibrational structure in the higher energy peaks. Obviously, there are more vibrational levels populated in the A- than in the X state. This is due to the fact that the equilibrium internuclear distance of 1.12 Å in the neutral molecule is very close to that in the ionic ground state X of 1.10 Å , whereas it is 1.17 Å in the first excited state $A\,^2\Pi_u$. In a Franck-Condon (i.e. vertical) transition, the projection of the vibrational ground state of the neutral onto the vibrational states of the ion thus populates a larger distribution for the A ion state. After proper calibration of both axes in figure 4.3, we find that for each harmonic peak, the integral over the A bands is about 1.8 times larger than that over the X band, in agreement with the photoionization cross sections.

To obtain the optimal spectral resolution, we have taken a series of spectra with retarding potentials in the MBES flight tube [2] increasing in steps of 3.1 eV, such that the electrons produced by different harmonic orders would be detected in the time-of-flight range with the best spectral resolution, corresponding to energies of 1–4 eV. The concatenated spectra give the high resolution spectrum shown in figure 4.4.

When the IR probe field is added, the spectrum is modified by additional sidebands appearing between the harmonic peaks. The sidebands from one ionization channel partly overlap with the harmonics from the other. In or-

[2] A grid of thin wires, which is traversed by the electrons, as they travel along the MBES flight tube, increases or decreases their energy according to the electrostatic potential it is set to.

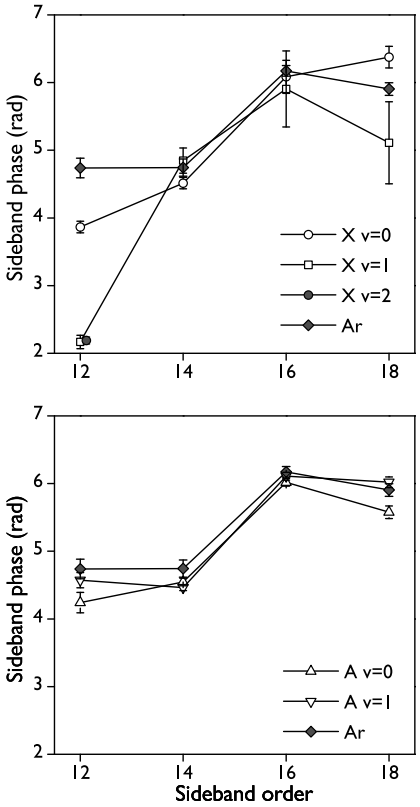

Figure 4.5. *Sideband phase* $(\varphi_{q+1} - \varphi_{q-1} - \Delta\phi_q^{at})$ *obtained for the different* N_2 *ionization channels. For each sideband order, a separate RABITT scan was performed with a retarding potential so that the spectral resolution is the same for all analyzed photoelectron peaks. A reference measurement with argon as detection gas is also shown.*

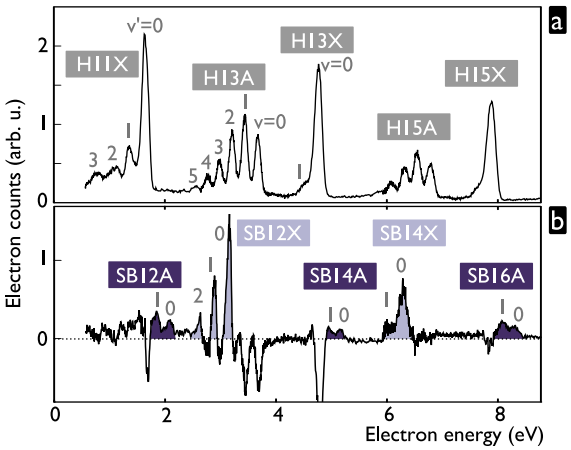

Figure 4.4. *High resolution spectrum, obtained by concatenating several spectra recorded with increasing retarding potential in the MBES flight tube. Spectrum obtained with the XUV beam only (a), and the difference of spectra obtained with and without the additionally present IR probe beam (b). The sidebands are identified as positive peaks in this difference.*

der to unambiguously identify them, we subtract the spectra obtained with and without the dressing field, as shown in figure 4.4b. The obtained trace is negative where the IR field has removed some population, i.e. where the harmonics are located, and positive where it has increased the signal, i.e. where the sidebands appear. Each sideband is labeled according to the corresponding photon energy and the final ion state.

4.1.2 Results

Already in the spectral intensities (figure 4.4a), it is apparent that, while there is an overall good agreement between the observed vibrational populations and the Franck-Condon factors, the X band produced by harmonic 11 runs over more vibrational levels than expected.

With high harmonics generated in argon with an intensity of $I = 1.2 \times 10^{14}$ W/cm^2, we performed series of RABITT scans with increasing retarding potentials in the same way as for the spectra shown in figure 4.4, so as to place the sidebands in the time-of-flight region were the spectral resolution is highest. Since the photoionization cross sections drop rather quickly with the XUV photon energy, such RABITT measurements could be performed for sidebands 12 to 18 only. This unfortunately limits the region where the results obtained here with photoionization of N_2 can be compared to those from the previous chapter concerning the recombination matrix elements. The particularity observed on the photoelectron peak corresponding to harmonic 11 and the X channel motivates a closer look to the phase measurement, though.

The result of such a series of RABITT scans is shown in figure 4.5. The measured sidebands phases are equal to $(\varphi_{q+1} - \varphi_{q-1} - \Delta\phi_q^{at})$, i.e. to the phase difference of two neighboring harmonics minus the molecular phase $\Delta\phi_q^{at}$ (cp. equations 1.67 or 2.6). Since $\Delta\phi_q^{at}$ is known for argon (see figure 1.13), the phase differences of the harmonics are measured from the reference RABITT scan detecting in argon. Subtracting them from the data obtained detecting in N_2 yields the molecular phase, $\Delta\phi_q^{at}$, for the different ionization channels, including the different vibrational states of the ion. This is the result shown in figure 3 in paper **V**. For the X channel, sideband 12 shows a remarkable

behavior: $\Delta\phi_{12}^{\text{at}} = -0.35\pi$ for $v = 0$ and reaches -0.9π for $v = 1$ and $v = 2$. For the A channel, $\Delta\phi_q^{\text{at}}$ is small for all sideband orders: between 0 and -0.2π. The large error bars for sideband 18 from the X channel are due to the low level of the signal.

These results have been reproduced in numerous RABITT scans from two different data acquisition campaigns one year apart, with the setup having been unmounted and re-mounted again for the second campaign. The molecular phase was consistently found as $\Delta\phi_{12}^{\text{at}} = (0.9 \pm 0.1)\pi$ for the (X,$v = 1$) channel, $\Delta\phi_{12}^{\text{at}} = (0.3 \pm 0.1)\pi$ for the (X,$v = 0$) channel, and $\Delta\phi_q^{\text{at}}$ between 0 and -0.2π for all other sidebands of channels X and A with $v = 0, 1$. As for the (X,$v = 2$) channel, only sideband 12 could be analyzed and the signal-to-noise ratio did not allow a reliable determination of $\Delta\phi_{12}^{\text{at}}$ for every scan. When it was possible, however, we found values very close to that for the (X,$v = 1$) channel, as was the case for the measurement shown in figure 4.5 and figure 3 in paper **V**.

This result is also very robust against variations of experimental conditions, in particular to the probe beam intensity. The pulse energy of the probe beam controls in particular the sideband amplitudes (see figure 1.11) and it indeed leads to an increase of the intensity of sideband 12 measured in the difference of spectra with and without the probe beam present (see figure 4.4b). The IR probe field could also influence the electronic states of the N_2 molecule, e.g. via Stark shift. Figure 4.6 shows the variation of sideband phases with the probe beam pulse energy. No significant dependence on this experimental parameter is observed.

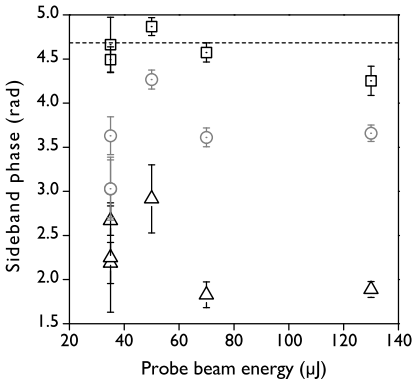

Figure 4.6. *Phase of sideband 12 for the ionization channels (A, $v = 0$) (⊡), (X, $v = 0$) (⊙) and (X, $v = 1$) (△), as a function of the probe beam pulse energy. The dashed line marks the relative phase of harmonics 11 and 13, $\varphi_{13} - \varphi_{11}$ determined by the reference scan detecting in argon. For the lowest probe beam energies, the error bars are rather large since the sidebands are very weak.*

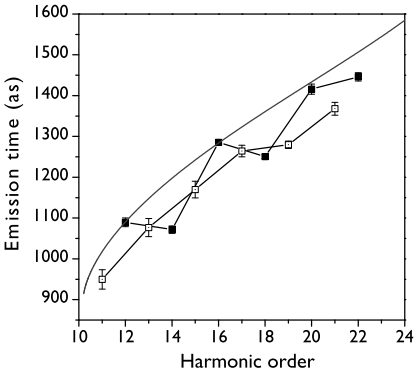

Figure 4.7. *Comparison of the emission times extracted from the sideband oscillations (filled squares) and oscillations of the harmonic peaks (empty squares) of a RABITT scan detecting in argon. The line shows the real part of the recollision times from an SFA calculation for an intensity of 1.2×10^{14} W/cm^2.*

4.1.3 Verification of the Measured Phase Shift

The sidebands to be analyzed in these measurements have the problem that they partially overlap with harmonic peaks in the photoelectron spectra. Both these types of peak oscillate in a RABITT scan, which could lead to a total oscillation with a phase that is different from the sought-for sideband phase.

The fact that using these 'problematic sidebands' we nonetheless extracted sideband phases (and thus measure emission times) that are compatible with those obtained detecting in argon, where this problem does not exist, suggests, though, that the selected sidebands are not too strongly perturbed by the underlying harmonics peaks. At least, this is true for the sideband orders > 14. For sideband 12 of channel X, however, we did consistently measure a large phase shift with respect to the reference given by the argon measurement. It should be verified whether this is a *real* effect owing to the photoionization process in N_2 or a mere consequence of the harmonic 13 peak of channel (A, $v = 2, 3$) blending in.

Simulation of overlapping sideband and harmonic peak

We will consider only the oscillating part of the sidebands and neglect their dc-component due to imperfect interferometric stability or differing amplitudes of the two interfering quantum paths. The atomic/molecular phase is set to zero. This oscillating part of sideband q then writes

$$I_q^{\text{SB}} = \cos\left(2\omega_0\tau + \varphi_{q+1} - \varphi_{q-1}\right), \tag{4.1}$$

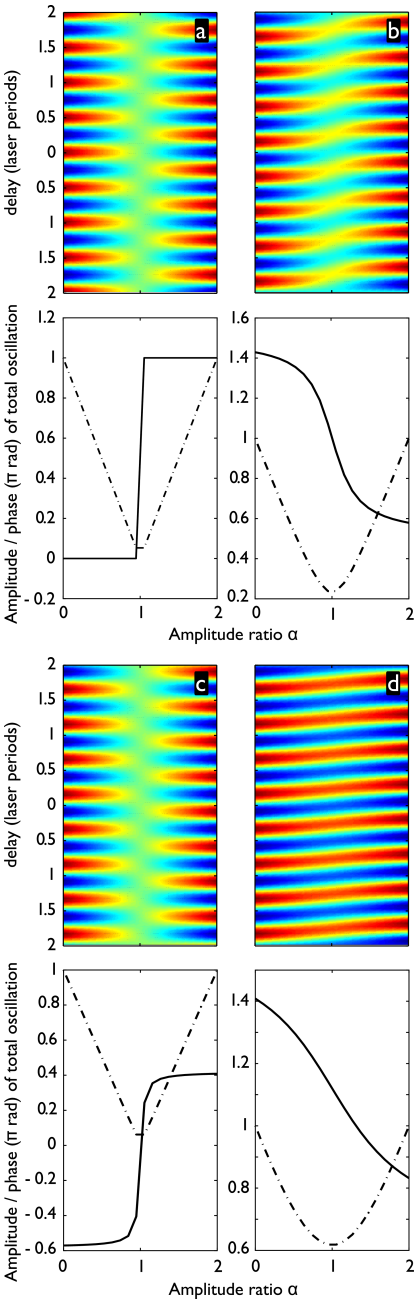

Figure 4.8. *Simulation of the oscillation of a sideband overlapping with a harmonic peak with relative strength α. (a) No GDD. (b) GDD of 100 as over $2\omega_0$. (c) sideband 12 + harmonic 13 with experimental phases for harmonics 11, 13 and 15, as determined in the reference measurement (figure 4.7). (d) Sideband 14 + harmonic 15, with experimental phases for harmonics 13, 15 and 17, as determined in the reference measurement (figure 4.7). Solid lines show the oscillation phase, dash-dotted lines show the oscillation contrast.*

with the same notation as in equations 1.67 and 2.6. The harmonic peaks oscillate due to population being transferred to the sidebands:

$$\begin{aligned} I^{\mathrm{H}}_{q+1} &= -\frac{1}{2}\left(I^{\mathrm{SB}}_{q} + I^{\mathrm{SB}}_{q+2}\right) \\ &= \frac{1}{2}\left(\cos\left(2\omega_0\tau + \varphi_{q+1} - \varphi_{q-1} + \pi\right) + \cos\left(2\omega_0\tau + \varphi_{q+3} - \phi_{q+1} + \pi\right)\right) \\ &= \cos\left(\frac{-\varphi_{q-1} + 2\varphi_{q+1} - \varphi_{q+3}}{2}\right)\cos\left(2\omega_0\tau + \frac{\varphi_{q+3} - \varphi_{q-1}}{2} + \pi\right), \end{aligned} \tag{4.2}$$

where the factor 1/2 accounts for equal probabilities of two-color transitions involving absorption or emission of one IR photon. There is a phase-dependent amplitude factor, which becomes unity when there is no attochirp, i.e. the spectral phase of the harmonics is linear. For typical values of the attochirp, the value is still close to unity, though. The oscillating term has a phase that turns out to be the mean value of the phases of the two sidebands above and below the harmonic peak. It thus gives a rougher, yet valid, approximation to the harmonic group delay than the sidebands' analysis. This is confirmed by figure 4.7, which compares the emission times obtained from $2\omega_0$ components of the sidebands and harmonic peaks oscillations.

Adding equations 4.1 and 4.2 with a variable weight α for the harmonic peak, i.e. $I^{\mathrm{tot}}_{j} = I^{\mathrm{SB}}_{q} + \alpha I^{\mathrm{H}}_{q+1}$, one can observe how the 'true' sideband phase is corrupted when a harmonic peak $q+1$ is superposed to sideband q. Results are shown in figure 4.8.

As already apparent from the oscillating term in equation 4.2, for a vanishing attochirp, i.e. a linear spectral phase, the harmonics oscillate exactly π out of phase with the sidebands. Superposing such an oscillation on a sideband will thus simply reduce the contrast of its oscillation until the harmonic peak contribution becomes dominant and the phase of the total oscillations jumps by π. This is the case in figure 4.8a.

In figure 4.8b, we assume a typical value for the attochirp at the generating intensity used in our experiments. Now, the harmonic peak oscillates 1.07π out of phase with the sideband, which is sufficient to alter the phase of the SB oscillation as soon as the harmonic peak blends in. Nonetheless, even for $\alpha = 0.5$, which reduces the oscillation contrast by a factor 2, the deviation from the correct sideband phase is only 0.07π, corresponding to 50 as of emission time. Such a deviation is slightly larger than the typical error bar in our measurements but does not wildly falsify the measurement. Increasing α to 1, however, leads to an oscillation contrast of 0.23 (i.e. still detectable) and a phase that is 0.42π off the correct sideband phase. Small variations of experimental conditions should change α, too, and thus lead to strongly fluctuating results for the determined phase in this region around $\alpha = 1$. The data shown in figure 4.6, where the probe beam intensity and thus α was varied, shows that we do not observe such fluctuations.

The best test is probably to compare different sideband orders based on experimentally determined harmonic phases. In figures 4.8c and 4.8d, sideband 12 and 14 blending with harmonic 13 and 15, respectively, are simulated with spectral phases obtained from the reference measurement shown by filled squares in figure 4.7. Figure 4.8c shows that for sideband 12 being superposed with harmonic 13, the situation is close to the case of 'no attochirp' (sidebands 12 and 14 *reproducibly* give almost the same emission time). Correspondingly, the transition from the correct sideband phase to the unwanted phase of the oscillating harmonic peak is very rapid and measuring a phase shift $\neq 0, \pi$ would be a mere coincidence that should be hard to reproduce (all the more as the oscillation contrast almost vanishes then). Since the same phase shifts (within a range of $\pm 0.1\pi$ rad) were obtained in numerous RABITT

scans from two different data acquisition campaigns, we can safely exclude such a coincidence.

Due to the strong increase of the emission time from sideband 14 to 16 in figure 4.7, sideband 14 superposed with harmonic 15 presents a completely different scenario. Figure 4.8d shows that the oscillation contrast always stays very good but the phase of the oscillation deviates rapidly when the harmonic peak blends in. Nevertheless measuring the correct sideband phase (i.e. no significant deviation from the phase of sideband 14 observed in the reference measurement), as is the case in the experiments, thus represents proof of a negligible influence of the oscillating harmonic peaks on the measurement.

In conclusion, these simulations strongly support the assumption that the distortion of the analyzed sideband phases due to superposing harmonic peaks is negligible and our measurements indeed yield a large molecular phase shift $\Delta\phi_{12}^{\mathrm{at}} = (-0.9 \pm 0.1)\pi$ for the (X,$v = 1, 2$) channels.

4.1.4 Origin of the Phase Shift

In paper **V**, we discuss the origin of the observed large molecular phase shift. Within the spectral width of harmonic 11, there is an autoionizing resonance at 17.12 eV attributed by (Zubek et al. [222]) to a member of the Hopfield Rydberg series (see also page 449 in (Herzberg [76])), converging to the B state of N_2^+ (cp. figure 4.2). This leads to the scheme shown in figure 4.9 for an additional photoionization channel via this autoionizing resonance, ending in the ground state X of N_2^+. In principle, autoioization might leave the ion in any state with energy below the resonance, but Frank-Condon factors strongly favor the X state.

A simple 1D model calculation in paper **V** shows that the molecular phase jumps by π when the photon energy scans over a resonance in the continuum and that this jump is smoothed by the finite lifetime of the resonance. In other words, the molecular phase is $\approx -\pi$ if the two consecutive harmonic orders correspond to (virtual) intermediate states that lie on opposite sides of the resonance. For all sidebands > 12, the intermediate states are above-resonance and are strongly detuned anyway. As for sideband 12, the situation is depicted in figure 4 of paper **V**: Harmonic 13 is above-resonance. Harmonic 11 is above-resonance as well for the $v = 0$ state of the autoionizing state, whereas it is below-resonance for the $v = 1$ state.

Based on Frank-Condon factors (see paper **V**), we can then argue that the quantum path passing via the $v = 1$ level of the autoionizing resonance gives a dominant contribution to the (X, $v = 1$) sideband, whereas its influence on the (X, $v = 0$) sideband is weaker. The latter is dominated by contributions from the direct path (harmonic 11 directly ionizing an electron from the HOMO, leaving the ion in the (X, $v = 0$) state) as well as the indirect path that passed via the $v = 0$ level of the autoionizing resonance.

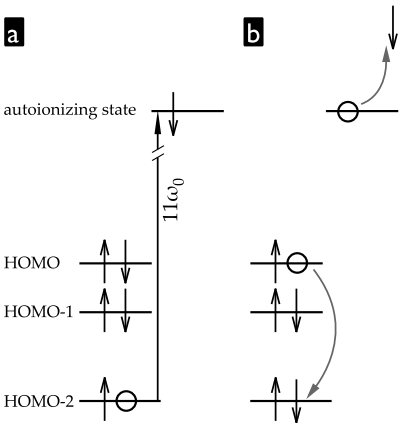

Figure 4.9. *Schematic of the photoionization channel via the autoionizing resonance: (a) Harmonic 11 resonantly excites the neutral molecule, promoting an electron from the HOMO-2 into a Rydberg orbit. This excited state of the neutral is located in the continuum of both the A and X states of the ion. (b) Eventually, an electron from the HOMO fills the hole in the HOMO-2 and the electron in the Rydberg orbit is ejected into the continuum, which leaves an ion in its ground state X.*

4.1.5 What was Actually Observed?

We observed a large molecular phase for some final ion states but not for others, and attributed this phase shift to an indirect ionization channel via an autoionizing resonance with a BO potential shape similar to the B ion state. Based on these points, we were able to develop a detailed description of the photoionization process. This conceptually simple (yet technically somewhat complex) explanation is certainly not the whole story, because the considered autoionizing resonance is a 'complex resonance', i.e. it involves a coupling with the highest members of another Rydberg series, converging to the $A\,^2\Pi_u$ $v \geq 2$ ion state (Dehmer et al. [25], Raoult et al. [164]).

One should, however, be careful when pushing the analysis further. Suppose that the atomic or molecular phase, $\Delta\phi_q^{\mathrm{at}}$, is equivalent to a group delay imposed on the released EWP by the *single-XUV-photon* ionization process (cf. the discussion at the end of section 1.3.4), in addition to that from the XUV wave packet. Then, the -0.9π phase shift observed for sideband 12 in the (X, $v = 1$) channel corresponds to a -600 as time-delayed emission of the EWP spectral component with energy $11\omega_0 - I_{\mathrm{p}}$. This would change the EWP temporal profile due to the presence of the resonance in the continuum. Our experiment would thus be conceptually very close to that of (Cavalieri et al. [15]), who observed a ≈ 100 as time-delayed electron emission from localized core states of solid tungsten as compared to those originating from delocalized conduction-band states. The sideband phase in our experiment is measured modulo 2π, corresponding to a group delay shift determined modulo 1.33 fs. If we further simplify the physical picture and imagine the electron to remain for a certain period in a Rydberg orbit before it is released into the continuum by autoionization, the time delay might be rather long (as can also be concluded from the width of the peak in the cross section associated with the resonance (Dehmer et al. [25])). Low-resolution IR-XUV cross-correlation measurements did, however, not show any significant temporal shift of the sideband envelope for the (X, $v = 1$) channel with respect to the others. These measurements suffered from rather low signal-to-noise and thus remain inconclusive.

Fine-tuning the driving laser wavelength would allow to scan the precise shape of the phase jump in the molecular phase and infer e.g. the resonance lifetime. Such an experiment is planned but requires modifications on the laser system that were not readily implementable.

A natural extension of the technique would be to detect photoelectrons with angular resolution and perform angle-resolved RABITT measurements, where photoionization channels can be further discerned according to the angular momentum of the final state (i.e. different partial waves). This leads to a direct connection to photoionization studies on synchrotrons, providing the complementary information not accessible otherwise.

Is this an *atto*physics experiment? We have used standard items from the experimental toolbox of attophysics and demonstrated a new approach, applying RABITT to measure the molecular phase of photoionization with a known XUV pulse. There is, however, no straightforward way to extract a quantity like an 'effective auto-ionization' time from the measured phase shift. This experiment is, however, clearly an ultrafast one, since it can in principle be applied to observe properties of transient states of molecules with a temporal resolution given by the femotsecond APT envelope duration.

Can we conclude on the original idea for the experiment, the comparison of the measured molecular phase to the phase of the recombination DME measured with the self-probing scheme (chapter 3)? One could look for a negative phase shift of sideband 12 for N_2 relative to that for HHG in argon. However, during the measurement campaigns that lead to the results discussed in chapter 3, we have always used neon as a detection gas so that sideband 16 was the lowest order. Referring to the results of (Wabnitz et al. [210]), obtained with a previous version of our setup, a small difference of the phase of sideband 12, 0.15π, was measured for unaligned N_2 as compared to the generation in argon.

CHAPTER 5

GENERATING ULTRASHORT XUV WAVEPACKETS IN ABLATION PLASMAS

In this chapter, the results of two measurement campaigns on HHG in low ionized ablation plasmas are presented. Instead of a gaseous medium, as in the experiments discussed in the previous part of this thesis, HHG takes place in the plume of ablated material that is created when a long (~ 100 ps) IR laser pulse is loosely focused to $I \sim 10^{10}\,\mathrm{W/cm^2}$ onto the surface of a solid target material. After letting the ablation plasma expand for ~ 100 ns, a strong femtosecond laser pulse, propagating parallel to the target surface at a distance of ~ 100 μm, generates high-order harmonics of the driving laser in the plasma. The plasma HHG medium predominantly contains singly charged ions and small amounts of neutral atoms and higher charged ions (Elouga Bom et al. [39]). The plasma is under-dense, i.e. the associated plasma-frequency of the collective free electron oscillation is below the laser frequency ω_0 such that the plasma is completely transparent.

The idea to use such a medium came up quite early in the quest for an optimized light source based on HHG and the first experiments were conducted by (Akiyama et al. [2]) and (Wahlström et al. [212]). At the time, the aim was to use the larger ionization potential of alcali ions as compared to rare-gas atoms to to extend the HHG plateau to very high photon energies. However, no real improvement was obtained, presumably due to the difficult plasma conditions. Recently, the method re-attracted attention when (Ganeev et al. [50, 51]) generated harmonics up to the 63rd order using boron and silver targets, and reported conversion efficiencies in the plateau region as high as ~ 10^{-5}. Such values had been obtained with gas harmonics, e.g. by (Hergott et al. [75]), after serious efforts optimizing phase matching, whereas they seemed to be 'easily' achievable with ablation plasmas. Soon after, (Ganeev et al. [53], Suzuki et al. [190]) beat this value for single harmonics by exploiting a resonant enhancement effect, leading to a ~ 10^{-4} conversion efficiency for harmonic 13 and 17 in indium and tin plasmas, respectively. Since very recently, nano-particle (Ganeev et al. [56]) and fullerene (Ganeev et al. [55]) containing targets are studied, because they can be highly polarizable and offer the possibility to tune plasmon resonances to a frequency of choice by varying the nano-particle size. A review of this approach as well as the general state-of-the-art of HHG in ablation plasma plumes is given by (Ganeev [49]).

Up to now, experiments focused on the maximization of generated XUV photon numbers and remained rather empirical. Few systematic studies have been conducted to shed light on the physical process responsible for the XUV

emission and the reported high efficiency. The best available support for the presumption that the generation mechanism would be the same three-step process as for gas harmonics is the observation of a similarly rapid drop of photon yield with increasing ellipticity of the driving laser that was observed for non-resonant (Ganeev et al. [50, 51]) as well as resonant (Suzuki et al. [190]) HHG in ablation plasma.

In particular, no temporal characterization had yet been done and there remained a doubt on the claims made in virtually all the above cited papers that ablation plasma harmonics would soon be the source of choice for experiments on non-linear optics in the XUV domain. We thus teamed up with Luc Elouga and Tsuneyuki Osaki of the INRS in Montréal to set up an experiment that would prove that this HHG medium is indeed a source of femtosecond and possibly attosecond XUV pulses. From the spectral phase that was to be measured, valuable information on the generation process may be extracted, in particular for the intriguing case of highly efficient resonant generation of single harmonics, which is the subject of section 5.3.

Résumé du Chapitre

Dans ce chapitre seront présentés les résultats de deux campagnes de mesure dédiées à la génération d'harmoniques élevées dans des plasmas d'ablation faiblement ionisés. Au lieu d'un milieu gazeux, comme dans les expériences discutées dans la partie précédente de cette thèse, la génération d'harmoniques élevées a lieu dans un panache de matériau ablaté, créé quand une impulsion laser infrarouge relativement longue (~ 100 ps) est focalisée faiblement à un éclairement de $I \sim 10^{10}$ W/cm^2 sur la surface d'une cible solide. Après expansion du plasma pendant ~ 100 ns, une impulsion laser femtoseconde intense, se propageant parallèlement à la surface de la cible à une distance de ~ 100 μm, génère des harmoniques élevées de la fréquence laser dans le plasma. Le mileu plasma est sous-dense, c.-à-d. que la fréquence plasma associée à l'oscillation collective des électrons libres est inférieure à la fréquence laser, ω_0, de sorte que le plasma est complètement transparent et contient en majorité des ions simplement et doublement chargés (Elouga Bom et al. [39], Ganeev et al. [50]).

La méthode a attiré l'attention quand (Ganeev et al. [50, 51]) ont pu générer des harmoniques jusqu'à l'ordre 63 en utilisant des cibles de bore et d'argent, et ont démontré des efficacités de conversion allant jusqu'à ~ 10^{-5} dans le plateau. Des telles valeurs n'avaient pu être obtenues avec des harmoniques gaz, par exemple par (Hergott et al. [75]), qu'après des efforts importants d'optimisation de l'accord de phase, alors qu'ils paraissaient 'facilement' atteignables avec les plasmas d'ablation. Peu après, (Ganeev et al. [53], Suzuki et al. [190]) amélioraient encore cette valeur pour certains ordres harmoniques en exploitant un effet d'augmentation résonnante, conduisant à une efficacité de ~ 10^{-4} pour les harmoniques 13 et 17 générées respectivement dans des plasmas d'indium et d'étain. Une revue de l'état de l'art de la génération d'harmoniques élevées dans les plasmas d'ablations est donnée dans (Ganeev [49]).

Motivation et but

Jusqu'ici, les expériences se sont concentrées sur la maximisation du nombre de photons XUV générés et sont restées plutôt empiriques. Peu d'études ont été effectuées afin d'éclairer le processus physique responsable de l'émission

XUV et de son efficacité élevée. Le meilleur soutien disponible pour la conjecture que le mécanisme de génération est le même processus en trois étapes que pour les harmoniques gaz est l'observation d'une chute rapide de l'intensité harmonique avec l'ellipticité du laser de génération, observée pour la génération d'harmoniques non-résonnante (Ganeev et al. [50, 51]) ainsi que résonnante (Suzuki et al. [190]) dans les plasmas d'ablation, similaire à ce qui est connu pour les harmoniques gaz.

En particulier, aucune caractérisation temporelle n'a été faite, ni à l'échelle femtoseconde ni à l'échelle attoseconde, si bien qu'il restait un doute sur les éclairements XUV réalisables avec les harmoniques générées dans les plasmas d'ablation et leur potentiel pour des expériences d'optique non-linéaire dans le domaine XUV. Nous nous sommes donc associés avec Luc Elouga et Tsuneyuki Osaki de l'INRS à Montréal, spécialistes de cette source, pour développer une expérience testant si ce milieu de génération d'harmoniques élevées est une source d'impulsions XUV femtosecondes et éventuellement attosecondes.

Résultats principaux

Il y avait deux difficultés majeures dans ces études expérimentales: (i) La qualité spatiale du faisceau laser de génération était assez fortement dégradée, principalement du fait de la longue propagation dans la ligne à retard nanoseconde (cf. figure 2.9). Bien que nous disposions de beaucoup plus d'énergie par impulsion que nous n'utilisons dans les expériences avec les gaz, nous n'avons pas pu atteindre un éclairement laser beaucoup plus élevé: nous estimons une valeur maximale de 2×10^{14} *W/cm*^{2}*, ce qui est inférieur aux éclairements couramment utilisés avec les plasmas d'ablation d'un facteur 2–5. C'est probablement pour cela que les signaux XUV obtenus dans nos expériences étaient très faibles et nous estimons l'efficacité de conversion infrarouge→XUV à* $\sim 10^{-8}$*. En outre, les orders harmoniques observés étaient plutôt faibles, faute d'un éclairement laser suffisant. (ii) Comme notre dispositif de mesure de phase spectrale par RABITT est très sensible aux gradients de densité d'électrons libres dans le milieu de génération, nous n'avons pas pu focaliser le faisceau laser générateur aussi proche de la surface de la cible que ce qui aurait été optimal, ce qui a limité la densité du milieu de génération et donc le signal.*

Néanmoins, il a été possible de faire des mesures avec différentes cibles, comme le plomb, l'or, et le chrome, ainsi qu'avec l'étain et l'indium – ces deux dernières cibles présentant des transitions radiatives fortes dans leurs ions simplement chargés et donc permettant l'observation de l'augmentation résonnante de l'efficacité de génération de certains ordres harmoniques. Avec toutes ces cibles, nous avons effectué des mesures de corrélation croisée entre une impulsion sonde fournie par le laser infrarouge et l'émission XUV générée dans le plasma d'ablation. Ces mesures ont mis en évidence une enveloppe femtoseconde de l'émission XUV, avec une largeur à mi-hauteur égale ou inférieure à l'impulsion laser génératrice. Sur cet aspect, aucune différence entre les harmoniques résonnantes et non-résonnantes n'a été observée.

Les mesures attosecondes n'ont donné des résultats fiables qu'avec la cible de chrome. Par la méthode RABITT nous avons mesuré l'intensité et la phase spectrale de l'émission XUV pour les ordres harmoniques 13 à 19, permettant de reconstruire une impulsion moyenne du train d'impulsions attosecondes émis. Sa durée est de 360 as, soit 1.4 fois la limite de Fourier.

Un resultat très intéressant a été obtenu avec l'étain: Les oscillations analysées dans la méthode RABITT étaient bien observées pour les ordres harmoniques non-résonnants, alors qu'elles étaient complètement absentes

pour l'harmonique 17 qui, elle, est résonnante. Cette absence pourrait être le résultat, pour l'harmonique résonnante, d'une dépendance différente de la phase avec l'éclairement de génération . Cela entraînerait une variation de la phase à l'intérieur de la largeur spectrale d'une harmonique très différente pour deux harmoniques consécutives dont l'une serait résonnante, brouillant l'interférence à la base des oscillations dans la méthode RABITT. Un tel effet est effectivement prévu dans la théorie de (Milošević [147, 148]) pour le mécanisme d'augmentation par résonance.

Conclusions

Ces résultats constituent la première caractérisation temporelle de l'émission harmonique générée dans des plasmas d'ablation. Le caractère complexe de ce milieu comportant différents états d'ionisation et une densité d'électrons libres relativement élevée ne permettait pas de faire des analogies directes avec la génération d'harmoniques élevées bien connue dans les gaz neutres. En particulier, un processus d'émission directement stimulé par le laser n'était pas évident.

Nous avons démontré que ce nouveau milieu de génération fournit une source de rayonnement XUV ultra-brève – femtoseconde et même attoseconde – comme les gaz neutres. Compte tenu des efficacités de conversion très élevés démontrées dans d'autres études, ces résultats ouvrent la voie vers une source XUV compacte à très haut flux crête. La longueur d'onde centrale de cette source pourrait être sélectionnée par le choix d'un matériau cible présentant une transition résonnante à l'énergie correspondante.

5.1 Specifics of the experimental setup

The setup is schematically shown in figure 2.9. Two major modifications had to be introduced to the setup: (i) The gas jet is replaced by a simple sample holder onto which are glued a range of different metal targets with reasonably polished surfaces. (ii) About 10% of the uncompressed (300 ps) laser beam is split off for the pre-pulse to be focused onto the metal surface, whereas the remaining part has to be delayed by ≈ 80 ns. The passage through the compressor imposes already a delay of ≈ 20 ns, leaving 60 ns, corresponding to 18 m of propagation to be added. Michel Perdrix, Olivier Gobert and David Garzella of the Saclay Laser Matter Interaction Center (SLIC), in charge of the laser facilities at our laboratory, designed and constructed this line. The precise length is not very important – as long as the delay between plasma creation and HHG is $\gtrsim 50$ ns, the ablation plasma conditions should be stable (Ganeev et al. [52]). In a first measurement campaign, the delay line was a simple four-times-passage through 4.5 m of air. Although the laser pulse is still rather long in this delay line and its peak power thus limited, the long propagation through air introduced (mainly spatial) pulse distortions. In the second campaign, in an attempt to improve on this issue, we installed an optical system which imaged the entrance point of the delay line onto the exit point, localized again after four passages over 4.5 m. Due to the occurence of intermediate focal spots, most of those 4.5 m were maintained in vacuum. Unfortunately, a new problem appeared: hot-spots in the laser beam profile (i.e. localized spikes in the spatial intensity profile), occurring somewhere before the laser amplifier chain exit, were imaged at points within the 18 m of the delay line. Some of these hot spots fell onto the folding mirrors of the delay line, regularly leaving burn marks, which then introduced new distortions to

the beam profile, creating even more hot spots, and so forth. The great effort has thus not been rewarded with an improved spatial beam quality. The pulse duration was barely affected, though, and was measured to be ≈ 55 fs at the entrance of our setup with an auto-correlator and at the exit (after the MBES) with SPIDER.

5.1.1 Experimental conditions

Due to the deteriorated spatial quality of the laser, we were, limited to an intensity of $\lesssim 2 \times 10^{14}\,\mathrm{W/cm^2}$ at the laser beam focus in the HHG chamber. This intensity was reached if the beam diameter, which is ≈ 35 mm at the compressor exit, was cut down to ≈ 17 mm just before the focusing lens, i.e. the focusing geometry was finally the same as in the gas-harmonics experiments. Only to reach this maximum value of $2 \times 10^{14}\,\mathrm{W/cm^2}$, two to three times more pulse energy was necessary compared to an optical setup without the delay line. Increasing the beam diameter and thus the pulse energy lead to a decreasing intensity at focus due the above-mentioned wave front distortions. The effective intensity at focus was estimated via the attochirp of high harmonics generated in argon gas by the laser beam that passed the delay line.

This limitation to an intensity a factor 2.5 to 5 below what is typically used for HHG in ablation plasma plumes may be one of the reasons that lead to a very low level of XUV signal in our experiments with all targets we have used. The rather bad phase matching in the HHG medium due to the strong wavefront distortions of the HHG driving beam will be another reason. We thus were far from the 10^{-5} conversion efficiency reported by (Ganeev et al. [50, 51]) for ablation plasma harmonics – rather, a signal one to two orders of magnitude weaker than that obtained with argon gas as HHG medium was observed under otherwise equal conditions. This leads us to estimate the conversion efficiency in our experiments as $\sim 10^{-8}$.

A further limitation was imposed by the minimum distance of the HHG beam to the target surface. We had to avoid the large gradient of the free electron density close to this surface as it refracts part of the annular HHG beam. Its energy is thus not completely blocked by the iris before the focusing into the MBES (cp. figure 2.9). To minimize this effect and thus perturbations due to a too strong refracted IR field interfering with the IR probe beam in the MBES interaction volume, we generated harmonics in the plasma plume at a distance of 200 – 300 μm from the target surface. This made sure that the refracted IR light from the HHG beam did not generate sidebands on its own, i.e. its intensity was considerably weaker than that of the IR probe beam in the MBES interaction volume. Due to the rapid drop of plasma density with the distance from the target surface, this resulted in a decrease by a factor of ≈ 2 in the generated XUV emission compared to focusing the HHG beam closer to the surface.

The low level of signal could hardly be dealt with by averaging more laser shots per photoelectron spectrum since the metal targets were not moved during data acquisition, i.e. the picosecond pre-pulse hit the surface always at the same spot. Very little material is actually ablated per laser shot and most targets could easily stand ~ 1000 shots without any degradation of the generated XUV signal. For a RABITT measurement, however, we typically use 10^4 laser shots (100 delay steps and averaging 100 shots per spectrum), so there was really no margin left to increase the averaging. On the contrary, the IR-XUV delay scans we made had to be kept rather short and always were accompanied by a gradual decline of signal during the scans.

All data were obtained by ionizing argon gas in the MBES which provides a relatively high photoionization cross-section.

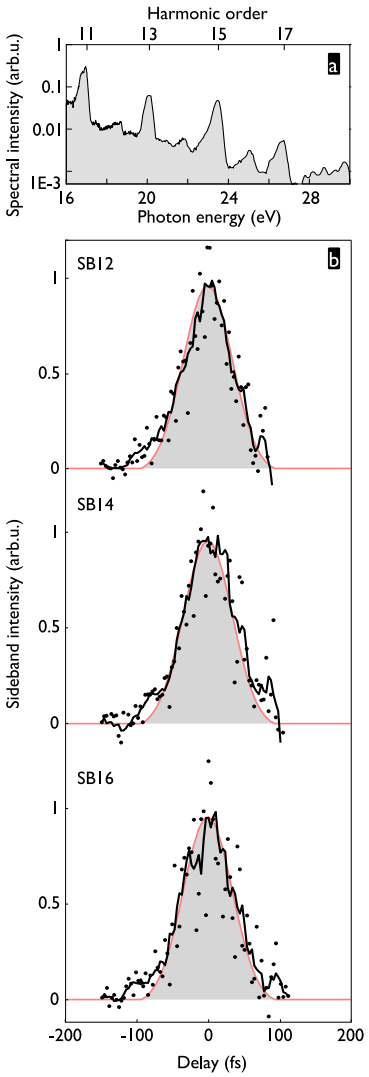

Figure 5.1. *Lead target. (a) Spectral intensity, obtained by summing up photoelecton spectra of a cross-correlation scan and correcting for the argon photoionization cross-section. The quantity shown is thus proportional to the generated XUV spectral intensity, except for the fact that sidebands are visible, which of course only occur in the photoelectron wave packets. (b) Intensities of sidebands 12, 14 and 16 as a function of the XUV-IR delay. Black dots are the data points and the black line is a 5-point running average. The grey shaded area and red line show a typical auto-correlation trace of the IR laser.*

5.2 Non-resonant Harmonic Emission

A number of different targets have been used, all of which had been shown to provide high conversion efficiencies and large spectra. The ones that turned out to yield a useable XUV emission were lead ($I_p(\mathrm{Pb}) = 7.4\,\mathrm{eV}$, $I_p(\mathrm{Pb}^+) = 15.0\,\mathrm{eV}$, $I_p(\mathrm{Pb}^{2+}) = 31.9\,\mathrm{eV}$), gold ($I_p(\mathrm{Au}) = 9.2\,\mathrm{eV}$, $I_p(\mathrm{Au}^+) = 20.5\,\mathrm{eV}$) and chrome ($I_p(\mathrm{Cr}) = 6.8\,\mathrm{eV}$, $I_p(\mathrm{Cr}^+) = 16.5\,\mathrm{eV}$, $I_p(\mathrm{Cr}^{2+}) = 31.0\,\mathrm{eV}$). The neutral atoms will in all three cases not contribute significantly to the high harmonic emission due to their low ionization potentials, leading to extremely low barrier suppression intensities $I_{BS} \approx 1 \times 10^{13}\,\mathrm{W/cm^2}$ (cp. equation 1.29). The doubly charged ions, on the other hand have $I_{BS} \approx 4 \times 10^{14}\,\mathrm{W/cm^2}$, and we probably do not come sufficiently close to this value with the experimental intensity. It should thus be the singly charged ions that give the dominating contribution to HHG in all three cases and the optimal conditions should be such that the effective intensity in the plasma plume is reasonably close to I_{BS} for the corresponding singly charged ions.

The same conclusion is reached by (Ganeev et al. [50]), studying HHG with a silver target ($I_p(\mathrm{Ag}) = 7.6\,\mathrm{eV}$, $I_p(\mathrm{Ag}^+) = 21.5\,\mathrm{eV}$, $I_p(\mathrm{Ag}^{2+}) = 34.8\,\mathrm{eV}$)), who observe a saturation of the cut-off position at harmonic 57 when increasing the HHG pulse energy above a value corresponding to an estimated intensity of $\approx 3.5 \times 10^{14}\,\mathrm{W/cm^2}$ (which is almost a factor 2 above the barrier suppression intensity for Ag^+ ions). This harmonic order corresponds to the cut-off position expected for an emission dominated by the singly charged ions and the saturation could be explained by two effects: the free electrons created by ionizing Ag^+ leading to self-defocusing of the HHG beam and to depletion of the ion ground state.

In the experiments reported so far, notably those were the intriguingly high conversion efficiencies had been observed, the HHG intensities were around $5 \times 10^{14}\,\mathrm{W/cm^2}$ (see e.g. (Elouga Bom et al. [38], Ganeev et al. [50])), i.e. a factor ≈ 2 above the barrier suppression intensity of the singly charged ions. Only in these conditions, strong XUV emission is observed and at lower intensities, the generated photon number drops very rapidly. This factor 2 is not too unsettling since I_{BS} is only a rough estimate based on a Coulomb potential and the experimental HHG saturation intensity depends in particular on the laser pulse duration.

Harmonic spectra generated with lead, gold, and chrome targets are shown in figures 5.1a, 5.2a and figure 2 of paper **VI**, respectively. The value of $I_p(\mathrm{Pb}^+)$ and the corresponding $I_{BS} = 5 \times 10^{13}\,\mathrm{W/cm^2}$ suggest a maximally achievable cut-off position at harmonic 15 for lead, in agreement with our observation. The same is true for the chrome target, where $I_{BS} = 7 \times 10^{13}\,\mathrm{W/cm^2}$ and thus the cut-off is to be expected at harmonic 19. For gold, $I_{BS} = 1.7 \times 10^{14}\,\mathrm{W/cm^2}$, leading to an expected cut-off at harmonic 33. I may be due to a particularly low effective intensity in the measurement shown in figure 5.2 that no harmonics above the 15th order could be observed with gold.

Assuming, on the other hand, that twice the barrier suppression intensity leads to the maximized cut-off position and conversion efficiency, we would expect that for lead, chrome and gold, we could achieve much stronger signal and harmonic orders up to 21, 27, and 53, respectively, if the effective HHG intensity was high enough. These are indeed approximately equal to the cut-off positions observed by (Ganeev et al. [54]) and (Elouga Bom [37]) under optimized conditions, using 35 fs laser pulses. With our measured intensity of $\lesssim 2 \times 10^{14}\,\mathrm{W/cm^2}$, we should not have been far from these optimal conditions for lead and chrome. In our case, however, the laser pulses were significantly longer and phase matching was deteriorated due to the above-mentioned wave front distortions. It turns out that high conversion efficien-

cies are not achieved so easily after all and that very intense and short laser pulses with excellent wave front quality are necessary.

5.2.1 Femtosecond XUV pulses

Despite the apparently suboptimal experimental conditions in our experiments, the main goal – the temporal characterization of high harmonic emission from ablation plasmas – could be tackled. Sidebands, created in photoelectron spectra by two-photon XUV+IR absorption (cp. section 1.3.4) provide a means to record cross-correlation traces of an IR probe pulse and the XUV pulses (Bouhal et al. [9, 10], Glover et al. [59], Mauritsson et al. [139], Norin et al. [155]). From the temporal width of a 1st order sideband[1], one can then estimate the average temporal width of the two adjacent odd harmonic orders if the IR probe pulse is known. For a proper de-correlation, the data has to be of exceptional quality, which is usually not the case. One thus typically assumes Gaussian temporal profiles for both the XUV and IR pulse, and estimates the FWHM duration, τ_{XUV}, of the XUV as

$$\tau_{XUV} = \sqrt{\tau_{SB}^2 - \tau_{IR}^2}, \tag{5.1}$$

where τ_{SB} and τ_{IR} are the measured sideband temporal width and the known IR probe pulse duration, respectively. In addition to this estimation, the temporal shape of the cross-correlation traces contains information about the pulse shapes (i.e. deviations from the assumed Gaussian profile) of IR and XUV.

Experimentally, this requires the same setup as for RABITT measurements, except that the scanned delay range will cover the complete temporal overlap of the XUV (APT envelope) and the IR probe pulse. Interferometric stability is not necessary. In our case, were the IR HHG driving beam and IR probe beam interfere in the HHG gas jet, it is in fact undesirable, since it would lead to an ω_0-modulation of the cross-correlation signal that would have to be removed afterwards. Our measurements were thus actually done with efforts to destabilize the RABITT-interferometer, which is obviously rather easy to do. Programming the piezo-electric transducer to do some jitter during the data acquisition would have been an option but having the air-conditioning blow onto the uncovered optical table already provided the required perturbation.

Measured cross-correlation traces for lead, gold and chrome samples are shown in figures 5.1b, 5.2b and 5.3, respectively. Positive delays correspond to the IR probe pulse preceding the XUV pulse. All traces have been normalized (i) by the spectrally integrated signal for all XUV-IR delays to remove signal fluctuations and (ii) by the average value of the three highest points around zero delay, thus restricting all cross-correlation traces to $[0, 1]$.

For all cases, the results are compared to a Gaussian fit of a typical auto-correlation trace of the IR probe pulse. Such auto-correlation traces are routinely taken at the exit of the laser compressor and hardly vary from day to day. We have also done SPIDER measurements (see e.g. (Walmsley and Dorrer [213])) of the IR probe pulses after the MBES, i.e. after propagation through the whole optical setup. These measurements revealed that the IR pulse shape was not a simple Gaussian: a small post-pulse immediately followed the main laser pulse. Higher-order phase terms acquired during propagation through the long delay line could be responsible for this. Otherwise, no significant pulse distortions were found – whether there was an ablation plasma plume to be traversed or not. It should thus be justified to always compare to the same "standard" auto-correlation curve.

[1] As for the RABITT measurement, one thus has to make sure that higher order sidebands are not generated (cp. section 1.3.4).

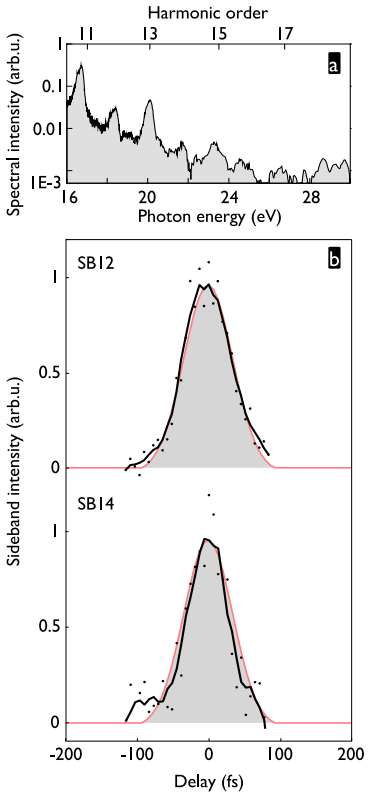

Figure 5.2. *Gold target. (a) Spectral intensity, obtained by summing up photoelecton spectra of a cross-correlation scan and correcting for the argon photoionization cross-section. The quantity shown is thus proportional to the generated XUV spectral intensity, except for the fact that sidebands are visible, which of course only occur in the photoelectron wave packets. (b) Intensities of sidebands 12 and 14 as a function of the XUV-IR delay. Black dots are the data points and the black line is a 3-point running average. The grey shaded area and red line show a typical auto-correlation trace of the IR laser.*

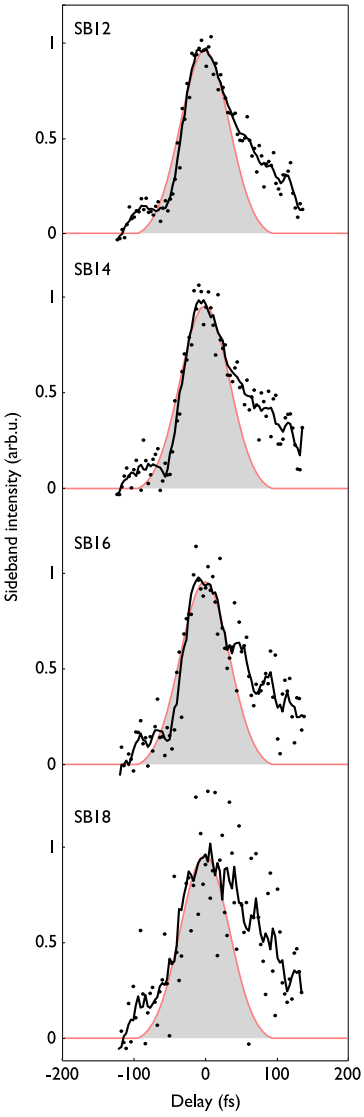

Figure 5.3. *Chrome target. Intensities of sidebands 12 to 18 as a function of the XUV-IR delay. Black dots are the data points and the black line is a 5-point running average. The grey shaded area and red line show a typical auto-correlation trace of the IR laser.*

For lead and gold, the measured cross-correlation traces very closely resemble the IR laser auto-correlation, which suggests that the XUV pulse duration is approximately equal to the IR pulse duration, i.e. ≈ 55 fs. The measurements with the chrome target were made in a different data acquisition run and present a strong asymmetry and a significantly increased width of the XUV-IR cross-correlation as compared to the IR auto-correlation. A clear distortion of the traces appears at positive delays, where the XUV overlaps with the falling edge of the IR and thus the post-pulse mentioned above. Therefore, it is most likely that the reason for the distortion is a longer and asymmetric IR probe pulse in this particular run rather than any effect specific to the chrome target.

Quantitative results?

Although the acquired traces have a reasonably good signal-to-noise ratio and have been been very well reproducible in several scans on the same day, there remains a doubt on how precise a quantitative result one should infer from them. Equation 5.1 could give an estimate for the XUV pulse length, although the IR probe pulse was certainly not Gaussian-shaped. What makes one hesitate is the fact that the cross-correlation traces are surprisingly large, i.e. the conclusion of an XUV pulse with the *same* length as the HHG driving pulse is somewhat unsettling, as with rare-gas harmonics one usually finds $\tau_{XUV} < \tau_{IR}$. However, in a saturated medium, were the harmonic yield has a very slow or even flat dependence on the driving laser intensity, the XUV pulse envelope may indeed have a larger FWHM duration than that of the IR driver. If we have reached such a saturated regime, though, why is the conversion efficiency so low?

A possible measurement error leading to over-estimation of the XUV pulse width could be a too high IR probe intensity. The IR probe intensity in these measurements was typically chosen to be a factor ≈ 3 higher than for usual RABITT measurements to ensure a sufficiently good signal-to-noise ratio even for a weak temporal IR-XUV overlap. However, for higher IR intensities, the 1st order sideband intensity starts saturating (cp. figure 1.11) as a function of IR intensity. This is the case when the intensities of the harmonic peaks and the sidebands in the photoelectron become similar (i.e. $|J_0'|^2 \approx |J_1'|^2$). This means that the traced sideband signal is no longer a cross-correlation of the XUV intensity envelope with the (known) IR intensity envelope but contains the IR intensity with an exponent < 1. So from a certain delay on, even if the overlap of XUV and IR pulse increases, the sideband intensity will not grow linearly with the overlap, the sideband signal starts to saturate leading to an effectively enlarged cross-correlation signal and thus an over-estimation of τ_{XUV}. We verify, however, that at all delays during the cross-correlation scans discussed here, the sideband intensity was at least about a factor of 2 smaller than the neighboring harmonic peak, suggesting that the above described effect should remain rather weak. The relation between piezo-steps and time delay is verified by a measured frequency of ω_0 of the total signal modulation in scans with interferometric stability and a delay jitter of several femotseconds induced by an 'exaggerated' blurring of interferences by means of the air conditioning seems very unlikely.

The traces shown here provide a definite upper limit to the XUV pulse duration: $\tau_{XUV} \leq \tau_{IR}$. This result provides evidence that the high-order harmonic emission from ablation plasmas results from a directly laser-driven process instead of some laser pumped plasma-transitions that would radiate long after the laser pulse has passed. It is thus very likely that the three step model of HHG can be applied here as well.

5.2.2 Attosecond Pulse Trains

Attosecond pulse measurements proved to be extremely hard and we encountered big difficulties in observing clean $2\omega_0$-oscillations of the sidebands. The mechanical stability of the setup was absolutely sufficient as proven by RABITT scans with harmonics generated in argon during the same measurement campaign as well as a very well resolved ω_0-modulation of the total signal in most scans with ablation plasma harmonics (originating from the interference of the probe and HHG driving beams in the generating medium). The reason for our difficulties were (i) the rather low spatial laser beam quality and energy stability, leading to noise and a decreased contrast of the $2\omega_0$-oscillations in the RABITT signal. (ii) Additional distortions of the IR probe beam during propagation in the plasma medium further reduce this contrast. (iii) Finally, the requirement that the sidebands be kept rather weak, together with the low XUV signal, the laser stability and beam quality problems and the limited acquisition times imposed by sample degradation resulted in quite unfavorable experimental conditions or RABITT measurements. Consequently, the largest part of the acquired data turned out to be unusable.

For one sample, though, chrome, a series of 4 RABITT scans with reproducible results and significant $2\omega_0$-amplitude in the sideband Fourier transform could be made. The Fourier-transformed sideband-signals of one of the RABITT scans are shown in figure 5.4. Clearly, the ω_0-component, remaining after normalization by the total signal (cp. section 2.3), is exceptionally strong, owing to the mentioned strong scattering of IR light from the HHG driving beam into the MBES interaction volume. The $2\omega_0$-peaks are much less pronounced than in the example shown in figure 2.6, but they are nonetheless clearly distinguishable from the surrounding noise. The reproducibility of the measured emission times finally gives confidence in this data.

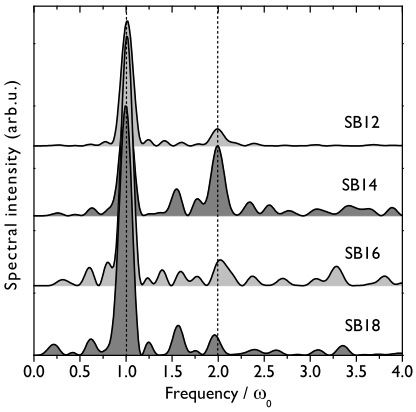

Figure 5.4. *Fourier transformed sidebands, measured in a RABITT scan with harmonics generated with a chrome target.*

These results are presented in paper **VI**. We were able to measure sideband phases and thus emission times for the orders 12 to 18, which, assuming a 'virtual band-pass filter' for harmonics 11 to 19, allows to reconstruct an average pulse in the train of attosecond pulses, generated in ablation plasma from a chrome target. We found a pulse duration of 360 as, corresponding to only 1.3 times the Fourier limit. The laser intensity used to generate these XUV pulses was not high enough to explain this very low attochirp. The free electron density in the plasma medium, which causes dispersion counter-acting the intrinsic attochirp, was also not high enough. Rather, we attribute the nearly linear spectral phase to the observed harmonic orders being in the cut-off region, where the emission times saturate.

5.3 Resonance-Enhanced Harmonic Emission

The probably most interesting aspect of ablation plasmas as an HHG medium is radiative transitions with large oscillator strengths in ions which have been shown to lead to strong enhancement of isolated harmonic orders with photon energy resonant with the transition energy. We have studied two targets where such resonances exist in the singly charged ions: indium ($I_p(\mathrm{In}) = 5.8\,\mathrm{eV}$, $I_p(\mathrm{In}^+) = 18.9\,\mathrm{eV}$, $I_p(\mathrm{In}^{2+}) = 28.0\,\mathrm{eV}$) and tin ($I_p(\mathrm{Sn}) = 7.3\,\mathrm{eV}$, $I_p(\mathrm{Sn}^+) = 14.6\,\mathrm{eV}$, $I_p(\mathrm{Sn}^{2+}) = 30.5\,\mathrm{eV}$). These are also the two targets used by (Ganeev et al. [53]) and (Suzuki et al. [190]), respectively. The strong radiative transitions to which the observed effect is attributed, are the $4d^{10}\,5s^2\,{}^1S_0 \rightarrow 4d^9\,5s^2\,5p\,({}^2D)\,{}^1P_1$ transition in In^+ at 19.92 eV, and the $4d^{10}\,5s^2\,5p\,{}^2P_{3/2} \rightarrow 4d^9\,5s^2\,5p^2\,({}^1D)\,{}^2D_{5/2}$ transition in Sn^+ at 26.27 eV. These two transitions have also been measured by photoabsorption spectroscopy by (Duffy and Dunne [34], Duffy

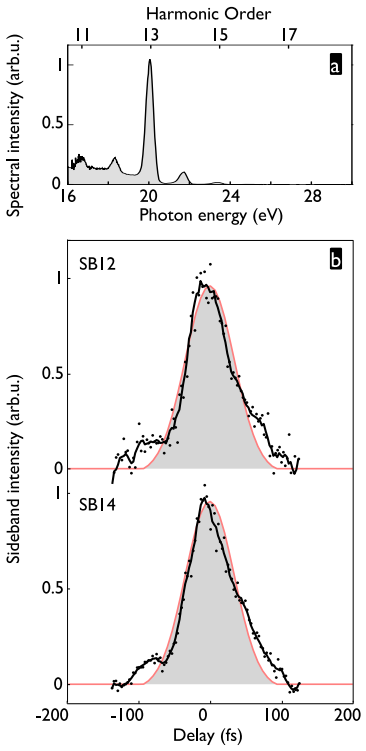

Figure 5.5. *Indium target. (a) Spectral intensity, obtained by summing up photoelecton spectra of a cross-correlation scan and correcting for the argon photoionization cross-section. The quantity shown is thus proportional to the generated XUV spectral intensity, except for the fact that sidebands are visible, which of course only occur in the photoelectron wave packets. (b) Intensities of sidebands 12 and 14 as a function of the XUV-IR delay. Black dots are the data points and the black line is a 5-point running average. The grey shaded area and red line show a typical auto-correlation trace of the IR laser.*

et al. [35]), and expectionally large gf values[2] have been calculated.

The transition energies for the indium and tin resonances are not exactly resonant with the 13th and 17th harmonic of a 795 nm laser ($\hbar\omega_0 = 1.565$ eV), respectively, but (Ganeev et al. [53]) and (Suzuki et al. [190]) suppose them to be driven into resonance by an AC Stark shift in the strong laser field. The mechanism for the enhancement has not yet been clearly identified. Recently, (Milošević [147]) addressed this question and proposed a simple scheme, based on HHG from a coherent superposition of bound states with different parity at energies ϵ_0 and ϵ_1. Then, a radiative bound-bound transition between the two states is allowed. The superposition is created by resonant harmonic photons with energy $\hbar\omega_r = \hbar q_r \omega_0 = \epsilon_1 - \epsilon_0$, which are generated through the usual three step process. The HHG spectrum from this coherent superposition contains a resonant part leading to stimulated emission at the frequency ω_r and, having the harmonic radiation and the stimulated emission at the same frequency ω_r, strong enhancement of radiation at the same frequency is obtained.

Harmonic spectra generated with indium and tin targets are shown in figures 5.5a and 5.6a, respectively. For indium, harmonic 13 completely dominates the spectrum and is actually generated with an efficiency comparable to that obtained with rare gas atoms in our setup. This is still orders of magnitude away from the $\sim 10^{-4}$ efficiency reported by (Ganeev et al. [53]), but it is a clear sign of a very efficient enhancement process. For tin, the intensity of the resonant harmonic 17 is clearly dominant over the neighboring orders, but the lower orders 13 and 11 are of comparable intensity. The resonant enhancement process in our experiments with tin is thus less efficient than in that of (Suzuki et al. [190]). The intensity was the same in both experiments, but the driving laser wavelength was slightly shorter in our case (792 nm as compared to 796 nm). Harmonic 17 may thus have been slightly less resonant in our conditions. Furthermore, the pulse duration of 150 fs was more than twice as long in the case of (Suzuki et al. [190]) than here.

5.3.1 Femtosecond XUV pulses

Since the mechanism of resonant enhancement is not quite clear yet, there is justified doubt on whether this efficient XUV emission process will provide ultrashort XUV pulses. The temporal characterization of this emission is thus of particular interest.

Results of cross-correlation scans analogous to those described in section 5.2.1 are shown in figures 5.5b and 5.6b-e for the indium and tin target, respectively. For indium, it is reasonable to assume that the sideband intensity involves essentially one contribution, namely that of a quantum path "harmonic 13 ± one IR photon". Both sidebands should thus give cross-correlation traces looking perfectly alike, which is confirmed in the experiment. The spectrum obtained with the tin target has the advantage that we can compare sidebands involving contributions from non-resonant harmonics (sidebands 12 and 14) to sidebands involving resonance-enhanced harmonics (sidebands 16 and 18). Both behave essentially in the same way. The temporal width appears to be decreased for the sidebands involving resonance-enhanced harmonics (clearly for sideband 16; for sideband 18, the data points are strongly scattered and it might be the smoothing that enlarges the trace). Such a shortening could, however, also be explained by the fact that cut-off harmonics are generated during a shorter time within the driving laser pulse.

[2] The gf value is the product of the oscillator strength g of a transition and the statistical weight g of the lower level.

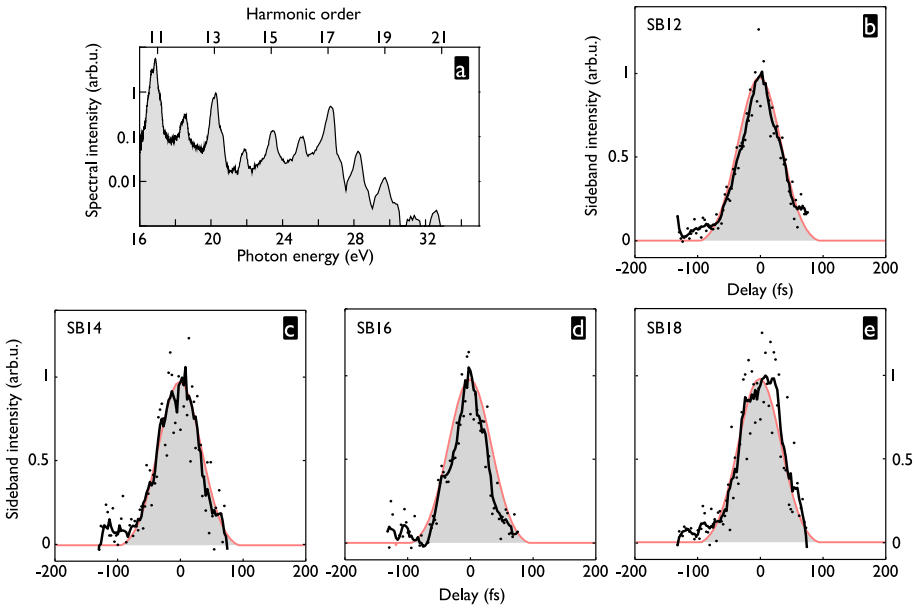

Figure 5.6. *Tin target. (a) Spectral intensity, obtained by summing up photoelecton spectra of a cross-correlation scan and correcting for the argon photoionization cross-section. The quantity shown is thus proportional to the generated XUV spectral intensity, except for the fact that sidebands are visible, which of course only occur in the photoelectron wave packets. (b)-(e) Intensities of sidebands 12 to 18 as a function of the XUV-IR delay. Black dots are the data points and the black line is a 5-point running average. The grey shaded area and red line show a typical auto-correlation trace of the IR laser.*

In general, the cross-correlation traces obtained here resemble very much those obtained for non-resonant harmonics, namely having approximately the same width as the laser auto-correlation trace and showing a signature of a post pulse in the IR probe pulse profile. The conclusions are thus also the same, i.e. we can give a definite upper limit to the XUV pulse duration: $\tau_{\mathrm{XUV}} \leq \tau_{\mathrm{IR}}$, which is evidence that the resonance-enhanced high-order harmonic emission from ablation plasmas results from a directly laser-driven process.

These measurements could be complemented by using a shorter IR probe pulse, such that $\tau_{\mathrm{XUV}} > \tau_{\mathrm{IR\,probe}}$, which would allow a more precise determination of the XUV pulse duration as well as a measurement of the harmonic chirp rate, as demonstrated by (Mauritsson et al. [137, 139], Norin et al. [155]). This will give information on the intensity dependence of the harmonic phase, which may be different for resonant and non-resonant harmonics, thus shedding more light on the mechanism behind resonant enhancement. Such a measurement requires a probe pulse shorter than the HHG driving pulse, i.e. post-compression in one of the interferometer arms.

5.3.2 RABITT measurements

RABITT measurements do not seem to make sense in the case of indium, where only harmonic 13 is efficiently generated. Given the extremely weak non-resonant harmonics, it thus does not seem surprising that no $2\omega_0$-oscillation was observed in the sidebands 12 and 14. However, an estimate of the $2\omega_0$-oscillation contrast expected from the relative intensities in figure 5.5a indicates that this modulation should still be observable.

With the tin target, one can compare sidebands involving contributions

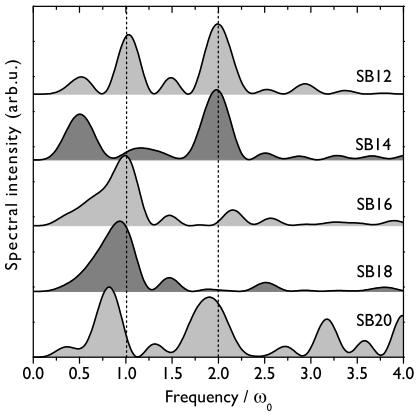

Figure 5.7. *Fourier transformed sidebands, measured in a RABITT scan with harmonics generated with a tin target, where harmonic 17 is resonance-enhanced. The $2\omega_0$-oscillation is not present on the sidebands around this harmonic order, although the interferometric stability was sufficient, as proven by the $2\omega_0$-peaks in the other sidebands.*

from non-resonant harmonics (sidebands 12, 14, and possibly 20) and sidebands involving resonance-enhanced harmonics (sidebands 16 and 18). Figure 5.7 shows Fourier transformed sidebands of a RABITT scan. Interestingly, the $2\omega_0$-oscillation, which is clearly present in the sidebands where only non-resonant harmonics beat, is absent in the two sidebands surrounding resonance-enhanced harmonic 17. This behavior is reproduced in every RABITT scan of this measurement run.

The necessary conditions for a working RABITT measurement – delay stability and wave front matching – are obviously fulfilled since the other sidebands show a very clean oscillation. Additionally, the intensity ratio of harmonic 13 to 15 is as high as that of the resonant harmonic 17 to 15, which implies that if the $2\omega_0$-oscillation contrast is sufficient to be observed on sideband 14, so should it for sideband 16. A possible explanation would be that the intensity dependence of the phase of resonant and non-resonant harmonics is very different and thus the phase variation within the spectral width of the harmonic peak differs strongly. The fulfillment of a third necessary condition for RABITT – an (almost) parallel phase variation within neighboring peaks – is thus questioned. Indeed, the model of (Milošević [148]) predicts an almost intensity independent phase for resonance-enhanced harmonics. One can thus simply no longer define 'a relative phase' of the two neighboring harmonics because its value varies rapidly within the spectral width of the sideband. Analyzing only narrow spectral regions of sidebands 16 and 18 in our data did, however, not lead to the re-appearance of the missing $2\omega_0$-oscillation, possibly due to the low signal-to-noise ratio.

5.4 Conclusions

These results constitute the first temporal characterization of the high-order harmonics generated in ablation plasma plumes. The complex nature of this medium containing different kinds of ions and a rather high free electron density does not allow to rely on straightforward analogies with the well known HHG in neutral gases. The confirmation, found in these results, that the non-resonant and resonant XUV emission process in ablation plasma plumes is directly laser driven thus constitutes an important advance.

For non-resonant HHG, we have been able to show that the generation of attosecond pulse trains with femtosecond envelopes is possible just as in neutral gases. Concerning resonant HHG, probably the most interesting aspect of ablation plasmas as an HHG medium, we have shown that femtosecond XUV pulses can be produced, which, in view of the very high conversion efficiencies of 10^{-4}, observed in other experiments, opens the perspective of a very high peak flux tabletop XUV source. The central wavelength of these pulses could be selected by choosing a target material with a strong transition at the desired energy.

Finally, the absence of attosecond synchronization between resonant and non-resonant harmonics points to specific phase properties of the resonant orders.

General Conclusions and Outlook

Since the beginning of this thesis work in 2006, the field of attosecond physics and in particular the study of molecular structure and dynamics using HHG has made impressive progress.

Self-probing

Many new experimental studies of different aspects of HHG in aligned molecules have been published. Our measurements of the amplitudes and phases of the DME component parallel to the driving laser polarization direction, done for CO_2 and N_2, provide very valuable experimental reference and constitute a major step forward in the imaging of electrons in molecules. The technique of molecular orbital tomography had been a subject of intense debate in the community. We demonstrate in paper **II** its experimental feasibility using data measured with N_2.

Several other groups are now measuring the phase of the HHG emission from aligned molecules with methods different from ours: far-field interference with a reference source (Mairesse et al. [131], Smirnova et al. [186], Zhou et al. [220]) as well as gas mixtures (Kanai et al. [88, 90], Wagner et al. [211]) allow to trace the phase change of each individual harmonic order as a function of the molecular alignment angle, whereas RABITT measures the phase change as a function of the harmonic order for a fixed alignment angle. The new methods thus provide complementary information to our results presented in papers **I** and **II** and we are eager to combine RABITT with them.

Measurements of the polarization state of the XUV emission were reported for instance by (Levesque et al. [115]) and in paper **III**, addressing the vector properties of the DME. Elliptically polarized harmonics generated with a linearly polarized driving laser in N_2 were observed by (Mairesse [125], Zhou et al. [221]), which came as a surprise and provides an important benchmark for theoretical models that are currently being developed.

The foundations of the self-probing scheme have been strengthened by measurements of (Levesque et al. [116]), who found (for argon, neon and helium) that the EWP amplitude is largely independent of the atom, thus supporting the idea of calibration via a reference atom.

Theoretically, the self-probing scheme has been studied as well, and is further reinforced by the theory of (Le et al. [102]), who showed for that the high harmonic emission from molecules can be expressed as the product of an EWP and an accurate (i.e. non-plane-wave) recombination DME. Based on these results, (Le et al. [104, 105]) of the group of Chi-Dong Lin developed a 'Quantitative Rescattering Theory', focusing on the correct treatment of scattering states. Similarly, (Ciappina et al. [19]) of Manfred Lein's group published a theoretical study replacing plane waves by two-center Coulomb waves, observing essentially the same 'acceptable' distortions as we did in paper **II**.

The most 'exact' description of HHG in molecules is obviously obtained by solving the TDSE, which has, however, to date only been possible for single

electron molecules (i.e. H_2^+, (H-He)$^{2+}$ and the like). These calculations – with a focus on molecular orbital imaging – are mainly done in Manfred Lein's group and the application of the plane-wave based tomographic reconstruction procedure (see (van der Zwan et al. [202])) turned out to work perfectly well even for asymmetric orbitals.

(Smirnova et al. [186, 187]) have developed a different, rather complex model combining a whole range of building blocks from quantum chemistry and strong-field physics. Contributions of different orbitals are included as well as their laser-induced coupling (i.e. coupling between different ionic states). While this is probably the most advanced model available for 'complex molecules' to date, it has yet to be tested against a greater number of experiments. This model could explain the spectral shift of the interference positions observed both in CO_2 and N_2 as an interplay of 'structural interference' in the recombination step and 'dynamic interference' between multi-orbital contributions. If both could be disentangled, information about the structure as well as the dynamics of a molecular system could be extracted from measurements.

Experimental evidence for multi-orbital contributions to HHG have been reported by (Akagi et al. [1], McFarland et al. [141], Smirnova et al. [186]) as well as by us in paper **II**. This had initially been considered to be in conflict with the tomographic imaging. However, we show in paper **II**, that while physics certainly gets more complex when several orbitals come into play, it also gets more interesting and actually allows to observe intra-molecular dynamics. In section 3.4, we conclude that this is the direction molecular imaging based on the self-probing scheme has to evolve to be relevant since spatial resolution will always be rather limited.

If electron dynamics are to be imaged, there will in general be a loss of spatial symmetry in the electron wavefunctions. As discussed in section 3.4.6, this requires an extension of currently available techniques for the complex DME measurement. A promising method to be examined for achieving this has been demonstrated by (Shafir et al. [184]), and is currently being applied to molecules by Hiromishi Niikura of the NRC Canada to experimentally determine the symmetry of the dominating 'active orbital'.

Efforts to extract the structure of more complicated, polyatomic molecules are made for example by (Torres et al. [198]). A technical development crucial to these studies but also for dynamical imaging is the use of longer wavelength (mid-infrared, i.e. typically 1-4 μm) driving lasers, see e.g. (Bandulet et al. [8], Doumy et al. [30], Marangos et al. [134], Vozzi et al. [207]). Due to the scaling of the ponderomotive potential as $U_p \propto I\lambda^2$, they offer the advantage of generating harmonic spectra with higher cut-off energies while keeping the intensity at a level below the barrier suppression intensity of large molecules with often small I_p. This will help to improve the reliability and spatial resolution of molecular imaging experiments. It will also increase the time-window during which dynamics can be followed in the 'chirp-encoded recollision' scheme (Baker et al. [5, 6]), where pump-probe delays are mapped onto the XUV frequency. The drawback of mid-infrared drivers comes as a $\propto \lambda^{-5}$ to $\propto \lambda^{-6}$ drop of the generation efficiency, predicted by (Tate et al. [194]), which will have to be dealt with by increasing the repetition rate of the laser systems to multi-kHz or even MHz. A breakthrough in that direction has been achieved by (Boullet et al. [11]), who demonstrated HHG at 1 MHz driven by a fiber amplification system.

The acetylene-vinylidene isomerization, an example given by (Le et al. [106]) for a very fast molecular transformation (a proton changing its place) coming with a significant change of the HOMO, is an interesting candidate for imaging the changing electronic orbital. The movement of the nucleus in

this transformation has been traced for the deuterated version of acetylene dication, $C_2D_2^{2+}$, by Coulomb explosion imaging by (Hishikawa et al. [77]), who found a duration of ≈ 90 fs for the acetylene→vinylidene isomerization and another ≈ 190 fs for the isomerization back to acetylene. Dynamic molecular imaging with HHG could instead interrogate the electrons in the molecule. Nuclear movement is dictated by an electronic potential and while tracing the nuclei tells us *how* they move, being able to actually 'see' the electron(s) during the transformation will answer the question *why* they move the way they do.

The PACER method, capable of probing with attosecond resolution the change of the nuclear configuration in the ion during electron excursion in the HHG process, has been used by (Baker et al. [6]) to observe transient two-center interference. (Patchkovskii [157]) presented a simplified theory for the calculation of nuclear correlation functions that may allow to apply PACER and the associated genetic algorithm to more complex molecules in the future. Again, longer driving laser wavelengths can extend the accessible time window. In paper **IV**, we have studied the phase as an observable for PACER. The observable effect is very small but, besides confirming the time-frequency mapping, we present experimental data that may suggest that the XUV phase encodes information that goes beyond the assumptions made for the SFA-based model of (Lein [109]).

Although not directly related to this thesis, experiments by (Meckel et al. [143]) should be mentioned. Here, the self-probing scheme is also used but the information is not encoded by recombination into light emission, but by electron diffraction on the ionic potential. This electron re-scattering is also observed by (Mauritsson et al. [140]), but using a continuum EWP created by XUV single-photon ionization and made to re-scatter on its parent ion by a strong IR laser field. These experiments could lead to coherent diffraction imaging of the ionic potential.

Probing with ultra-short XUV pulses

The generation of isolated attosecond pulses is becoming a mature tool, based on different gating methods such as IR few-cycle driver pulses (Goulielmakis et al. [64]) (who reported the current record duration of 80 as) or polarization gating (Sansone et al. [174], Sola et al. [188]), sometimes in combination with two-color fields (Mashiko et al. [136]). Attosecond pulse trains are more than just a preliminary stage to single attosecond pulse generation but offer specific advantages. Such are the achievable spectral resolution in XUV photoionization experiments, pointed out in paper **V**, or the coherent signal enhancement obtainable in a 'stroboscopic measurement', proposed by (Mauritsson et al. [140]). APT are also generated and shaped with great control today, see for instance (Gustafsson et al. [66], Mansten et al. [132]). We have shown in paper **I** how the control over intra-molecular quantum interference can be used to shape attosecond pulses and prepare them e.g. for coherent-control experiments.

In paper **V**, we have demonstrated how RABITT can be used to measure the characteristic phase imposed upon the ejected photoelectron wave packet by the photoionization process itself. This experiment bears some conceptual resemblance to the attosecond spectroscopy of photoelectron emission from condensed matter demonstrated in 2007 by (Cavalieri et al. [15]), in the sense that a phase shift in the photo electron wave packet is measured and attributed to dynamics of the XUV photo-ionization process. For this type of experiment an important theoretical question remains open: the equivalence of the observable atomic/molecular phase and the phase of the single-XUV-

photon DME has yet to established. In other words, how directly can actual time delays be extracted from phase shifts observed in two-photon two-color transitions?

New experiments

The results on HHG in ablation plasma media discussed in chapter 5 and paper **VI** have been the first temporal characterization of this type of XUV source, proving its ultra-short duration. The observation of an interesting phase effect on resonance-enhanced harmonics may help to unravel the mechanism behind the enhancement. It will certainly be necessary to repeat these experiments in conditions that lead to the very high HHG conversion efficiencies that were the main motivation for these studies. These experiments will be developed in a joint effort of our group and the INRS Montréal.

A new attosecond beamline has been developed and tested in Saclay during the last two years of this thesis. It is installed on a different laser system, the 'Plate-forme Lasers Femtosecondes Accordables' (PLFA), delivering up to 13 mJ per pulse with 35 fs duration at 1 kHz repetition rate. Post-compression techniques will allow to generate driving laser pulses of ≈ 10 fs duration and several mJ energy for our experiments. The new beamline is optimized for very high long-term stability, i.e. the optical table carrying the entire beam path is now completely decoupled from the vacuum chambers and their pumps. This more stable system together with the new laser will allow increasing the accessible harmonic spectral range while greatly reducing acquisition times of RABITT or FROG-CRAB measurements.

Taking the data for one tomographic reconstruction took about 90 minutes on the 'old' beamline using a 20 Hz (but very high energy) laser. The improvement by a factor 50 of laser repetition rate will soon allow taking several such 'frames' of a 'molecular movie' during a reasonable measurement time, thus implementing one of the technical prerequisites for time-resolved molecular imaging using an external pump (i.e. an additional laser pulse launching the dynamics at some delay before the HHG driving pulse). Also, the systematic variation of different experimental parameters can be achieved in a more reliable way as data acquisition series become less sensitive to long term drifts. The shorter pulse duration will allow exploring a greater intensity range and study in detail the intriguing spectral shifts of the interference features discussed in chapter 3. Higher achievable cut-off positions will probably allow the observation of such interference features in the HHG amplitude and phase for more molecules, such as N_2O. For a significant improvement of spatial resolution in orbital tomography, however, the use of mid-IR lasers will be inevitable.

For the follow-up experiments proposed to continue the study of paper **V**, a collaboration with the Anne L'Huillier's group at Lund University has been started. A velocity map imaging spectrometer will provide angular resolution for the photoelectron emission. The tunability of central wavelength of the laser system in Lund can be used to scan the harmonic photon energy over the resonance and thus infer more information about the complex resonance.

I hope to have convincingly shown in this thesis that the tool set of attosecond physics, based in particular on high harmonic generation, is getting more and more complete and suitable for observing electron dynamics in molecules with . Such observations will help to understand *how* and *why* these quantum systems work the way they do.

Appendix A

Atomic Units

Atomic units greatly simplify formulae and render typical values appearing in calculations on atomic-scale systems more computer-friendly. In atomic units, the four fundamental quantities *electron rest mass*, m_e, *elementary charge*, e, the *reduced Planck's constant*, $\hbar$, and *Coulomb's constant*, $1/4\pi\epsilon_0$, are set to unity:

$$m_e = e = \hbar = 4\pi\epsilon_0 = 1\,.$$

This means, that one atomic unit, (a.u.), of the following quantities correspond in SI units to:

Angular momentum, Action		$\hbar$	=	$1.054\,571\,68 \times 10^{-34}$ J s
Mass		m_e	=	$9.109\,383 \times 10^{-31}$ kg
Charge		e	=	$1.602\,176\,53 \times 10^{-19}$ C
Length	$a_0 =$	$\frac{4\pi\epsilon_0\hbar^2}{m_e e^2}$	=	$5.291\,772\,06 \times 10^{-11}$ m = 0.53 Å
Velocity	$v_B =$	$\frac{e^2}{4\pi\epsilon_0\hbar}$	=	$2.187\,691\,26 \times 10^{6}$ m s^{-1}
Momentum		$m_e v_B$	=	$1.992\,851\,66 \times 10^{-24}$ kg m s^{-1}
Time	$\tau_0 =$	$\frac{a_0}{v_B}$	=	$2.418\,884\,30 \times 10^{-17}$ s = 24.2 as
Frequency		τ_0^{-1}	=	$4.134\,137\,38 \times 10^{16}$ Hz
Energy	$E_h =$	$\frac{m_e e^4}{(4\pi\epsilon_0)^2\hbar^2}$	=	$4.359\,744\,2 \times 10^{-18}$ J = 27.2 eV
Electric field	$\mathcal{E}_0 =$	$\frac{e}{4\pi\epsilon_0 a_0^2}$	=	$5.142\,206\,51 \times 10^{11}$ V m^{-1}
Intensity		$\frac{1}{2}\epsilon_0 c\mathcal{E}_0^2$	=	$3.509\,445\,2 \times 10^{16}$ W cm^{-2}

Appendix B

Exact scattering states for a 1D square well potential

Consider the Schrödinger equation 1.14 in one dimension, with $V(x)$ being a square potential as shown in Fig. B.1. Piecewise, the situation of a free electron is recovered, where the solutions are plane waves, $e^{\pm ikx}$, with $k = \sqrt{2(E-V)}$. Solving the Schrödinger equation 1.14 now means finding the coefficients that fulfill the condition of continuously connecting the three ansatz on either edge of the potential well. The solution for bound states with $E < 0$ is found in virtually any quantum mechanics text book. For $E > 0$, this is less often the case. The ansatz are plane waves for all x:

$$\phi(x)^{\text{scat}}_{|k|} = \begin{cases} A^{(+)}e^{ikx} + A^{(-)}e^{-ikx} & \text{for } x \le 0, \\ B^{(+)}e^{ik_2 x} + B^{(-)}e^{-ik_2 x} & \text{for } 0 \le x \le a, \\ C^{(+)}e^{ikx} + C^{(-)}e^{-ikx} & \text{for } a \le x, \end{cases} \tag{B.1}$$

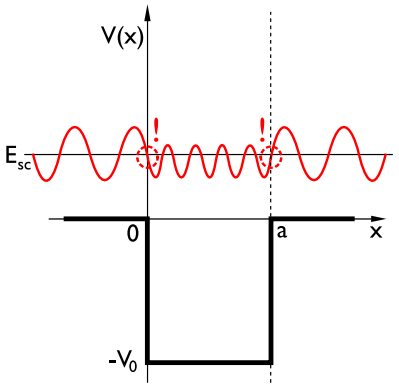

Figure B.1. *Textbook example of a one-dimensional square potential. For bound states ($E < 0$), the wavefunction has to be square integrable and the connection conditions can only be fulfilled for discrete E, whereas for continuum states ($E > V_0$), the plane waves can always be continuously connected.*

where $k = \sqrt{2E}$ and $k_2 = \sqrt{2(E+V_0)}$. There are 2 linearly independent solutions, $\phi(x)^{\text{scat}}_{+|k|}$ and $\phi(x)^{\text{scat}}_{-|k|}$, for each $|k|$: They are chosen such that they go as $e^{\pm ikx}$ as $x \to \pm\infty$. There are four connection conditions for the six coefficients. Two coefficients can thus be chosen freely and for $\phi(x)^{\text{scat}}_{+|k|}$,a clever choice is $A^{(-)} = 0$ and $C^{(+)} = 1$. For the remaining four coefficients, with $\alpha = e^{ika}$ and $\beta = e^{ik_2 a}$, the connection conditions are:

$$\begin{aligned} A^{(+)} &= B^{(+)} + B^{(-)}, & B^{(+)}\beta + B^{(-)}/\beta &= \alpha + C^{(-)}/\alpha, \\ kA^{(+)} &= k_2(B^{(+)} - B^{(-)}), & k_2(B^{(+)}\beta - B^{(-)}/\beta) &= k(\alpha - C^{(-)}/\alpha). \end{aligned}$$

This finally leads to:

$$\begin{aligned} A^{(+)} &= \frac{4e^{i(k+k_2)a}kk_2}{e^{2ik_2a}(k_2+k)^2 - (k_2-k)^2} & B^{(+)} &= \frac{2e^{i(k+k_2)a}k(k_2+k)}{e^{2ik_2a}(k_2+k)^2 - (k_2-k)^2} \\ B^{(-)} &= \frac{2e^{i(k+k_2)a}k(k_2-k)}{e^{2ik_2a}(k_2+k)^2 - (k_2-k)^2} & C^{(-)} &= \frac{e^{2ika}(e^{2ik_2a}-1)(k^2-k_2^2)}{e^{2ik_2a}(k_2+k)^2 - (k_2-k)^2} \end{aligned} \tag{B.2}$$

For $\phi(x)^{\text{scat}}_{-|k|}$, one simply exchanges the results $A^{(-)} \leftrightarrow C^{(+)}$, $B^{(+)} \leftrightarrow B^{(-)}$ and $A^{(+)} \leftrightarrow C^{(-)}$.

It is noteworthy that the coefficients B.2 contain E-dependent phase factors, i.e. the scattering states for different energies will have different phases.

This property of exact continuum states for a given potential plays a crucial role in papers **I** and **II**.

The frequency content of exact scattering states obviously depends on the spatial region. This spatial chirp is particularly prominent in regions where the potential varies rapidly.

Appendix C

Symmetry properties of the Fourier transform: Oddness and Imaginarity

The Fourier transformation, $\mathcal{F}$, between a complex valued function $f(\boldsymbol{r})$ in real space with the Cartesian coordinates $\boldsymbol{r} = (x, y, z)$ and the function $F(\boldsymbol{k})$ in frequency space of wave vectors $\boldsymbol{k} = (k_x, k_y, k_z)$ is defined as

$$F(\boldsymbol{k}) = \mathcal{F}_{\boldsymbol{r}\to\boldsymbol{k}}[f(\boldsymbol{r})] = \frac{1}{\sqrt{2\pi}} \int_{-\infty}^{\infty} \mathrm{d}\boldsymbol{r}\, f(\boldsymbol{r}) \mathrm{e}^{-\mathrm{i}\boldsymbol{k}\cdot\boldsymbol{r}}, \tag{C.1}$$

$$f(\boldsymbol{r}) = \mathcal{F}_{\boldsymbol{k}\to\boldsymbol{r}}[F(\boldsymbol{k})] = \frac{1}{\sqrt{2\pi}} \int_{-\infty}^{\infty} \mathrm{d}\boldsymbol{k}\, F(\boldsymbol{k}) \mathrm{e}^{\mathrm{i}\boldsymbol{k}\cdot\boldsymbol{r}}. \tag{C.2}$$

It will be sufficient to discuss properties of a one-dimensional case since $\mathcal{F}$ in a higher dimensional space can simply be written as a series of one-dimensional transforms, e.g.

$$F(\boldsymbol{k}) = \frac{1}{\sqrt{2\pi}} \int_{-\infty}^{\infty} \mathrm{d}z \left\{ \int_{-\infty}^{\infty} \mathrm{d}y \left[\int_{-\infty}^{\infty} \mathrm{d}x\, f(x,y,z) \mathrm{e}^{-\mathrm{i}k_x x} \right] \mathrm{e}^{-\mathrm{i}k_y y} \right\} \mathrm{e}^{-\mathrm{i}k_z z}. \tag{C.3}$$

Splitting $f(x)$ in its real and imaginary part:

$$f(x) = a(x) + \mathrm{i}b(x) \quad : a(x), b(x) \in \mathbb{R}\ \forall x, \tag{C.4}$$

and using the Euler's formula $\mathrm{e}^{\pm\mathrm{i}\phi} = \cos\phi \pm \mathrm{i}\sin\phi$, equation C.1 writes:

$$\begin{aligned} F(k_x) = \frac{1}{\sqrt{2\pi}} \int_{-\infty}^{\infty} \mathrm{d}x \,[\, a(x)\cos(k_x x) + b(x)\sin(k_x x)\,] \\ + \frac{\mathrm{i}}{\sqrt{2\pi}} \left\{ \int_{-\infty}^{\infty} \mathrm{d}x \,[\, b(x)\cos(k_x x) - a(x)\sin(k_x x)\,] \right\}. \end{aligned} \tag{C.5}$$

Taking a close look at equation C.5 and bearing in mind that the integrals vanish for integrands odd in x, one is readily convinced of the following handy symmetry properties of the Fourier transform:

$f(x)\ldots$		$F(k_x)\ldots$
real valued and even in x	$\Leftrightarrow$	is real valued and even in k_x
real valued and odd in x	$\Leftrightarrow$	is imaginary valued and odd in k_x
imaginary valued and even in x	$\Leftrightarrow$	is imaginary valued and even in k_x
imaginary valued and odd in x	$\Leftrightarrow$	is real valued and odd in k_x
real valued	$\Leftrightarrow$	has an even real part and an odd imaginary part
imaginary valued	$\Leftrightarrow$	has an odd real part and an even imaginary part

The author's contribution to the papers

I **Coherent control of attosecond emission from aligned molecules**
I did the measurements of the experimental data used in the paper with the setup developed by Willem Boutu and I performed the data analysis. I contributed a major part to the writing of the paper and the reply to the referees, and I made the figures (as well as the Nature physics cover image).

II **Attosecond imaging of molecular electronic wave-packets**
I did the measurements of the experimental data used in this paper with the setup developed by Willem Boutu. I performed the data analysis and the simulations of the attosecond-pulse profiles based on SFA-calculations by Thierry Auguste. I made extensive simulations on the tomography-scheme, implemented in software by Jérémie Caillat, which were relevant to the progress of our understanding. I played a major role in the 2 years of discussions among the authors as well as other colleagues, and the finding and exploration of the final physical interpretation proposed in the paper. I also wrote parts of the manuscript and the experimental part of the supplementary information.

III **Polarization-resolved pump-probe spectroscopy with high harmonics**
I extended the setup in Saclay for these experiments, proposed by Yann Mairesse, and did the measurements and analysis of the data shown in figures 3, 5 and 6. I also participated in the experiments done in Bordeaux, leading to the data shown in figures 4 and 7. I contributed to some extent to the writing of the paper.

IV **Attosecond chirp encoded dynamics of light nuclei**
I participated in the preparation of these experiments and I did the measurements of the experimental data used in this paper. I played the leading role in the interpretation of the results and the theoretical analysis of Manfred Lein's SFA-based model. Except for the solution of the TDSE for the nuclear dynamics (equation 4 in the paper), done by Richard Taïeb, I did all the calculations and the data analysis. The calculation of molecular alignment distributions was based on a program developed by Sébastien Weber. I wrote the paper and the reply to the referees – obviously with the help of comments from the co-authors.

V **Phase-resolved attosecond near-threshold photoionization of molecular nitrogen**
I played a leading role in the two measurement campaigns leading to the experimental data used in this paper. I participated in the extension of the data analysis software and performed most of the data analysis. I contributed an important part to the discussions of the theoretical interpretation, lead by Yann Mairesse. I wrote a preliminary manuscript and participated to some extent to the writing of the final paper and the communication with the referees.

VI **Attosecond pulse generation in chromium ablation plasma**
I took part in the planning of the two measurements campaigns and the design of the experimental setup. I had the primary responsibility for the temporal-characterization part of the experiments and carried out the measurements together with Luc Elouga. I did the data analysis and wrote some of the necessary software. I played a major part in the interpretation of the results and the writing of the manuscript.

Acknowledgments

It is my privilege to thank Jon Marangos and Manfred Lein, who accepted the burden of being my thesis reviewers, as well as Danielle Dowek, Anne L'Huillier, Eric Mével and John Tisch for being members of my jury.

Doing a thesis work in Paris can be tough because there are so many equally important things to do. Like Lunch. Apéro. And dinner. Or go see this concert and that exhibition. Only under very special conditions – such as those in the *groupe attophysique* of the SPAM – a *thésard* will get to do some science nonetheless. Didier Normand, *le chef de l'institut*, Cécile Reynaud, *la chef du labo*, and Bertrand Carré, the kindest *chef de groupe* there is, make the SPAM a place for high quality science and non-science and fight behind the scenes with all those administrative and budgetary issues.

I am deeply indebted to Pascal Salières, my supervisor, and Willem Boutu, my predecessor as a graduate student. Pascal has been a tremendous source of inspiration and ideas, continuously offering encouragement and great opportunities to his students. He also never got tired of correcting (minor) errors in my french. Willem has done all the hard and lengthy work of developing the original setup and the experimental success I finally could show off at conferences and in this manuscript is as much his as it is mine.

The great conditions in the *groupe attophysique* are also ensured by all its other members, to whom I am very grateful, namely:
To the ever energetic Sébastien Weber, for theoretically and experimentally aligning molecules with me. To Docteur Thierry Ruchon, for the time spent together in the lab, for after-work-beer-and-pizza and explaining rugby. To the 'old hand' Patrick Monchicourt and the spectrometer whisperer and H-index king of the group Pierre Breger, who have probably seen your problem before and can think back how they solved it last time. To the amazingly de-localized Hamed Merdji. To Zsolt Diveki, who keeps asking until he finds something I can't answer. To David Gauthier, for moving *doucement* in his side of the lab and being fun to be around. To Alessandra Ravasio, for Gnocchi, Tiramisu and her italian charm. To Christian Cornaggia, who explains H_2 so well and knows so many examples where the Germans do better than the French. To Thierry Auguste, who cares for the physics not the fuss. And to Marie Géléoc, who bought us great wine in Bad Honnef.

None of the experiments would have worked out without Marc Billon and Gilles Le Chevallier, who do all of that electronics–cable-pulling–vacuum-pumping magic and always know a joke. I am also grateful to Eric Caprin for fixing the **☆↯☠* gas-jet again and again, and to Didier and André of the work-shop. Michel Bougeard has been of great of help in designing the new setup that will turn out to be totally *impeccable*. Your

support was indispensable for the APTM experiment and its spin-offs.

I owe a lot to the SLIC team, Jeff, Olivier, Michel, David, Fabien and Delphine for taking care of brave LUCA, spending time and energy on the nanosecond delay line, providing some of the best beams on the planet and letting me borrow €€-optical components.

Merci Jacqueline et Véronique for always having been helpful and concerned about the *thésards'* well-being.

Very special thanks go to our theorist-friends Richard, Jérémie, Alfred and Cécilia, who have taught me a lot during entertaining discussions in their cosy mansard right in Paris' quartier latin. They have worked with us during the full three years of my thesis, and without their knowledge, rigor and programming skills, our experimental results would have just remained *bizarre*.

I thank the group of CELIA Bordeaux, in particular Julien, Baptiste and Yann, with whom I had the privilege to work on several experiments. It was fun, *messieurs*! Special thanks to Yann, *le docteur Mairesse* and holder of the title *theśard de référence* in Saclay. Not only that but also his frank and passionate, yet thoughtful attitude on and off physics has often impressed me and has been a strong inspiration to me.

Thanks to the programmers of gnuplot and inkscape for these fabulous free toys to make spiffy figures.

Many more wonderful people have accompanied me during the adventures of the past three years – whether they were geographically close or far – and I am grateful to everyone of you. *Mes amis parisiens* have often inquired about the well-being of my electrons, but most of the time they have brought my mind off physics and towards journalists' issues, music and food, thus keeping me from becoming a nerd. Very special and warm thanks go to my dear friends Stephan, Norman and Marko, who have always remained close to me and helped me to remain in good spirits although they are dispersed over Germany and Sweden. Way to go, men!

Zu guter Letzt will ich von ganzem Herzen meiner Familie danken. Euer beständiges Vertrauen, Eure Unterstützung und Ermutigung, nicht nur während der letzten drei Jahre, bedeuten mir viel. Danke auch für das Hinwegsehen über zu lange Kontaktpausen wenn ich mich für zu beschäftigt hielt. Ma belle Sabrina, tu partages mes hauts et mes bas et je te remercie de tout mon cœur pour ton soutien, ta sincérité admirable, ta chaleur et ton regard. Merci d'être fière de moi - rien ne me rend plus heureux.

Thank you all.
S.

REFERENCES

[1] Akagi H, Otobe T, Staudte A, Shiner A, Turner F, Dorner R, Villeneuve DM, and Corkum PB. *Laser tunnel ionization from multiple orbitals in HCl*. Science **325**, 1364–1367 (2009).

[2] Akiyama Y, Midorikawa K, Matsunawa Y, Nagata Y, Obara M, Tashiro H, and Toyoda K. *Generation of high-order harmonics using laser-produced rare-gas-like ions*. Phys. Rev. Lett. **69**, 2176–2179 (1992).

[3] Ammosov MV, Delone NB, and Krainov VP. *Tunnel ionization of complex atoms and of atomic ions in an alternating electromagnetic field*. Sov. Phys. - JETP **64**, 1191–1194 (1986).

[4] Antoine P, L'Huillier A, and Lewenstein M. *Attosecond pulse trains using high-order harmonics*. Phys. Rev. Lett. **77**, 1234–1237 (1996).

[5] Baker S, Robinson JS, Haworth CA, Teng H, Smith RA, Chirilă CC, Lein M, Tisch JWG, and Marangos JP. *Probing proton dynamics in molecules on an attosecond time scale*. Science **312**, 424–427 (2006).

[6] Baker S, Robinson JS, Lein M, Chirilă CC, Torres R, Bandulet HC, Comtois D, Kieffer JC, Villeneuve DM, Tisch JWG, and Marangos JP. *Dynamic two-center interference in high-order harmonic generation from molecules with attosecond nuclear motion*. Phys. Rev. Lett. **101**, 053901 (2008).

[7] Balcou P, Cornaggia C, Gomes ASL, Lompre LA, and L'Huillier A. *Optimizing high-order harmonic generation in strong fields*. J. Phys. B **25**, 4467–4485 (1992).

[8] Bandulet HC, Comtois D, Shiner AD, Trallero-Herrero C, Kajumba N, Ozaki T, Corkum PB, Villeneuve DM, Kieffer JC, and Légaré F. *High harmonic generation with a spatially filtered optical parametric amplifier*. J. Phys. B **41**, 245602 (2008).

[9] Bouhal A, Evans R, Grillon G, Mysyrowicz A, Breger P, Agostini P, Constantinescu RC, Muller HG, and von der Linde D. *Cross-correlation measurement of femtosecond noncollinear high-order harmonics*. J. Opt. Soc. Am. B **14**, 950–956 (1997).

[10] Bouhal A, Salières P, Breger P, Agostini P, Hamoniaux G, Mysyrowicz A, Antonetti A, Constantinescu R, and Muller HG. *Temporal dependence of high-order harmonics in the presence of strong ionization*. Phys. Rev. A **58**, 389–399 (1998).

[11] Boullet J, Zaouter Y, Limpert J, Petit S, Mairesse Y, Fabre B, Higuet J, Mével E, Constant E, and Cormier E. *High-order harmonic generation at a megahertz-level repetition rate directly driven by an ytterbium-doped-fiber chirped-pulse amplification system*. Opt. Lett. **34**, 1489–1491 (2009).

[12] Boutu W. *Dynamique de la génération d'harmoniques dans les atomes et les molécules*. PhD thesis, Université Paris-Sud 11, (2007).

[13] Bransden BH and Joachain CJ. *Physics of Atoms and Molecules*. Pearson Education, Harlow, UK (2003).

[14] Breidbach J and Cederbaum LS. *Universal attosecond response to the removal of an electron*. Phys. Rev. Lett. **94**, 033901 (2005).

[15] Cavalieri A, Muller N, Uphues T, Yakovlev V, Baltuska A, Horvath B, Schmidt B, Blumel L, Holzwarth R, Hendel S, Drescher M, Kleineberg U, Echenique P, Kienberger R, Krausz F, and Heinzmann U. *Attosecond spectroscopy in condensed matter*. Nature **449**, 1029–1032 (2007).

[16] Chirilă C and Lein M. *Assessing different forms of the strong-field approximation for harmonic generation in molecules*. J. Mod. Opt. **54**, 1039–1045 (2007).

[17] Chirilă CC and Lein M. *Effect of dressing on high-order harmonic generation in vibrating h_2 molecules*. Phys. Rev. A **77**, 043403 (2008).

[18] Chirilă CC and Lein M. *Explanation for the smoothness of the phase in molecular high-order harmonic generation*. Phys. Rev. A **80**, 013405 (2009).

[19] Ciappina MF, Chirilă CC, and Lein M. *Influence of coulomb continuum wave functions in the description of high-order harmonic generation with* H_2^+. Phys. Rev. A **75**, 043405 (2007).

[20] Cohen-Tannoudji C, Diu B, and Laloë F. *Méchanique Quantique, tomes I et II*. Hermann, Paris, France (1986).

[21] Constant E, Garzella D, Breger P, Mével E, Dorrer C, Le Blanc C, Salin F, and Agostini P. *Optimizing high harmonic generation in absorbing gases: Model and experiment*. Phys. Rev. Lett. **82**, 1668–1671 (1999).

[22] Corkum PB. *Plasma perspective on strong field multiphoton ionization*. Phys. Rev. Lett. **71**, 1994–1997 (1993).

[23] Cormier E, Walmsley IA, Kosik EM, Wyatt AS, Corner L, and Dimauro LF. *Self-referencing, spectrally, or spatially encoded spectral interferometry for the complete characterization of attosecond electromagnetic pulses*. Phys. Rev. Lett. **94**, 033905 (2005).

[24] de Nalda R, Heesel E, Lein M, Hay N, Velotta R, Springate E, Castillejo M, and Marangos JP. *Role of orbital symmetry in high-order harmonic generation from aligned molecules*. Phys. Rev. A **69**, 031804 (2004).

[25] Dehmer PM, Miller PJ, and Chupka WA. *Photoionization of* N_2 $X\ ^1\Sigma_g^+$, $v'' = 0$ *and* 1 *near threshold. Preionization of the Worley–Jenkins Rydberg series*. J. Chem. Phys. **80**, 1030–1038 (1984).

[26] Descamps D, Roos L, Delfin C, Lchar39huillier A, and Wahlström CG. *Two- and three-photon ionization of rare gases using femtosecond harmonic pulses generated in a gas medium*. Phys. Rev. A **64**, 031404+ (2001).

[27] Dinu LC, Muller HG, Kazamias S, Mullot G, Augé F, Balcou P, Paul PM, Kovacev M, Breger P, and Agostini P. *Measurement of the subcycle timing of attosecond XUV bursts in high-harmonic generation*. Phys. Rev. Lett. **91**, 063901 (2003).

[28] Dion CM, Bandrauk AD, Atabek O, Keller A, Umeda H, and Fujimura Y. *Two-frequency ir laser orientation of polar molecules. numerical simulations for hcn*. Chem. Phys. Lett. **302**, 215–223 (1999).

[29] Dooley PW, Litvinyuk IV, Lee KF, Rayner DM, Spanner M, Villeneuve DM, and Corkum PB. *Direct imaging of rotational wave-packet dynamics of diatomic molecules*. Phys. Rev. A **68**, 023406 (2003).

[30] Doumy G, Wheeler J, Roedig C, Chirla R, Agostini P, and DiMauro LF. *Attosecond synchronization of high-order harmonics from midinfrared drivers*. Phys. Rev. Lett. **102**, 093002 (2009).

[31] Drescher M, Hentschel M, Kienberger R, Uiberacker M, Yakovlev V, Scrinzi A, Westerwalbesloh T, Kleineberg U, Heinzmann U, and Krausz F. *Time-resolved atomic inner-shell spectroscopy*. Nature **419**, 803–807 (2002).

[32] Dudovich N, Oron D, and Silberberg Y. *Coherent transient enhancement of optically induced resonant transitions*. Phys. Rev. Lett. **88**, 123004 (2002).

[33] Dudovich N, Smirnova O, Levesque J, Mairesse Y, Ivanov, Villeneuve D, and Corkum P. *Measuring and controlling the birth of attosecond xuv pulses*. Nature Physics **advanced online publication**, 781–786 (2006).

[34] Duffy G and Dunne P. *The photoabsorption spectrum of an indium laser produced plasma*. Journal of Physics B: Atomic, Molecular and Optical Physics **34**, L173–L178 (2001).

[35] Duffy G, van Kampen P, and Dunne P. *4d→5p transitions in the extreme ultraviolet photoabsorption spectra of Sn II and Sn III*. J. Phys. B **34**, 3171–3178 (2001).

[36] Durfee CG, Rundquist AR, Backus S, Herne C, Murnane MM, and Kapteyn HC. *Phase matching of high-order harmonics in hollow waveguides*. Phys. Rev. Lett. **83**, 2187–2190 (1999).

[37] Elouga Bom LB. , private communication, (2008).

[38] Elouga Bom LB, Kieffer J, Ganeev R, Suzuki M, Kuroda H, and Ozaki T. *Influence of the main pulse and prepulse intensity on high-order harmonic generation in silver plasma ablation*. Phys. Rev. A **75**, 033804–033808 (2007).

[39] Elouga Bom LB, Bouzid F, Vidal F, Kieffer JC, and Ozaki T. *Correlation of plasma ion densities and phase matching with the intensities of strong single high-order harmonics*. J. Phys. B **41**, 215401 (2008).

[40] Enos MJ, editor. *Fields Institute Communications: Dynamics and Control of Mechanical Systems: The Falling Cat and Related Problems*, volume 1. American Mathematical Society, Toronto, Ontario, Canada (1993).

[41] Fabre B. *Paquets d'onde vibrationnels créés par ionisation de H_2 en champ laser intense*. PhD thesis, Université Catholique de Louvain, (2005).

[42] Ferray M, L'Huillier A, Li X, Lompre L, Mainfray G, and Manus C. *Multiple-harmonic conversion of 1064 nm radiation in rare gases*. J. Phys. B **21**, L31–L35 (1988).

[43] Fick E. *Einführung in die Grundlagen der Quantentheorie*. Aula Verlag, Wiesbaden, Germany (1988).

[44] Fleming GR, Ratner MA, and Robinson AL, editors. *Directing Matter and Energy : Five challenges for Science and the Imagination*. U.S. Department of Energy, Washington, DC, USA, available online at `http://www.sc.doe.gov/bes/reports/list.html` (2007).

[45] Flettner A, König J, Mason MB, Pfeifer T, Weichmann U, Düren R, and Gerber G. *Ellipticity dependence of atomic and molecular high harmonic generation*. Eur. Phys. J. D **21**, 115–119 (2002).

[46] Friedrich B and Herschbach D. *Alignment and trapping of molecules in intense laser fields*. Phys. Rev. Lett. **74**, 4623 (1995).

[47] Gaarde M, Tate J, and Schafer K. *Macroscopic aspects of attosecond pulse generation*. J. Phys. B **41**, 132001 (2008).

[48] Gamow G. *Zur quantentheorie des atomkernes*. Zeitschr. f. Physik A **51**, 204–212 (1928).

[49] Ganeev R. *High-order harmonic generation in a laser plasma: a review of recent achievements*. J. Phys. B **40**, R213–R253 (2007).

[50] Ganeev R, Baba M, Suzuki M, and Kuroda H. *High-order harmonic generation from silver plasma*. Phys. Lett. A **339**, 103–109 (2005).

[51] Ganeev R, Suzuki M, Baba M, Kuroda H, and Ozaki T. *High-order harmonic generation from boron plasma in the extreme-ultraviolet range*. Opt. Lett. **30**, 768–770 (2005).

[52] Ganeev R, Singhal H, Naik P, Arora V, Chakravarty U, Chakera J, Khan R, Kulagin I, Redkin P, Raghuramaiah M, and Gupta P. *Harmonic generation from indium-rich plasmas*. Phys. Rev. A **74**, 063824 (2006).

[53] Ganeev R, Suzuki M, Baba M, Kuroda H, and Ozaki T. *Strong resonance enhancement of a single harmonic generated in the extreme ultraviolet range*. Opt. Lett. **31**, 1699–1701 (2006).

[54] Ganeev R, Bom E, Kieffer J, Suzuki M, Kuroda H, and Ozaki T. *Demonstration of the 101st harmonic generated from a laser-produced manganese plasma*. Phys. Rev. A **76**, 023831–023837 (2007).

[55] Ganeev RA, Elouga Bom LB, Abdul Hadi J, Wong MCH, Brichta JP, Bhardwaj VR, and Ozaki T. *Higher-order harmonic generation from fullerene by means of the plasma harmonic method*. Phys. Rev. Lett. **102**, 013903 (2009).

[56] Ganeev RA, Elouga Bom LB, and Ozaki T. *Comparison of high-order harmonic generation from various cluster- and ion-containing laser plasmas*. J. Phys. B **42**, 055402 (2009).

[57] Gianturco FA and Lucchese RR. *Cross sections and asymmetry parameters in gas-phase photoionization of C_{60}*. Phys. Rev. A **64**, 032706 (2001).

[58] Gibson GN and Biegert J. *Influence of orbital symmetry on high-order-harmonic generation and quantum tomography*. Phys. Rev. A **78**, 033423 (2008).

[59] Glover TE, Schoenlein RW, Chin AH, and Shank CV. *Observation of laser assisted photoelectric effect and femtosecond high order harmonic radiation*. Phys. Rev. Lett. **76**, 2468–2471 (1996).

[60] Goban A, Minemoto S, and Sakai H. *Laser-field-free molecular orientation*. Phys. Rev. Lett. **101**, 013001 (2008).

[61] Gordon A and Kärtner F. *Quantitative modeling of single atom high harmonic generation*. Phys. Rev. Lett. **95**, 223901 (2005).

[62] Goulielmakis E, Uiberacker M, Kienberger R, Baltuska A, Yakovlev V, Scrinzi A, Westerwalbesloh T, Kleineberg U, Heinzmann U, Drescher M, and Krausz F. *Direct measurement of light waves*. Science **305**, 1267–1269 (2004).

[63] Goulielmakis E, Schultze M, Hofstetter M, Yakovlev V, Gagnon J, Uiberacker M, Aquila A, Gullikson E, Attwood D, Kienberger R, Krausz F, and Kleineberg U. *Single-cycle nonlinear optics*. Science **320**, 1614–1617 (2008).

[64] Goulielmakis E, Schultze M, Hofstetter M, Yakovlev VS, Gagnon J, Uiberacker M, Aquila AL, Gullikson EM, Attwood DT, Kienberger R, Krausz F, and Kleineberg U. *Single-cycle nonlinear optics*. Science **320**, 1614–1617 (2008).

[65] Gurney RW and Condon EU. *Wave mechanics and radioactive disintegration*. Nature **122**, 439–4339 (1928).

[66] Gustafsson E, Ruchon T, Swoboda M, Remetter T, Pourtal E, López-Martens R, Balcou P, and L'Huillier A. *Broadband attosecond pulse shaping*. Opt. Lett. **32**, 1353–1355 (2007).

[67] Haessler S and Swoboda M. Optimization and application of high-order harmonics of an ultrashort terawatt laser. Lund Reports on Atomic Physics LRAP-324, Lund Institute of Technology, Sweden, (2004).

[68] Hall G. *Computational quantum chemistry - then and now*. J. Mol. Struct.: THEOCHEM **234**, 13–18 (1991).

[69] Hay N, Castillejo M, de Nalda R, Springate E, Mendham KJ, and Marangos JP. *High-order harmonic generation in cyclic organic molecules*. Physical Review A **61**, 053810 (2000).

[70] Hay N, de Nalda R, Halfmann T, Mendham KJ, Mason MB, Castillejo M, and Marangos JP. *Pulse-length dependence of high-order harmonic generation in dissociating cyclic organic molecules*. Phys. Rev. A **62**, 041803 (2000).

[71] Hay N, Velotta R, Lein M, de Nalda R, Heesel E, Castillejo M, and Marangos JP. *High-order harmonic generation in laser-aligned molecules*. Phys. Rev. A **65**, 053805 (2002).

[72] Henke BL, Gullikson EM, and Davis JC. *X-Ray Interactions: Photoabsorption, Scattering, Transmission, and Reflection at E = 50-30,000 eV, Z = 1-92*. Atomic Data and Nuclear Data Tables **54**, 181–342 (1993), also accesssible through `http://henke.lbl.gov/optical_constants/`.

[73] Hentschel M, Kienberger R, Spielmann C, Reider G, Milosevic N, Brabec T, Corkum P, Heinzmann U, Drescher M, and Krausz F. *Attosecond metrology*. Nature **414**, 509–513 (2001).

[74] Hergott JF. *Optimisation de la génération dharmoniques d'orde élevé et application à l'interférometrie UVX résolue en temps*. PhD thesis, Université Paris-Sud 11, (2001).

[75] Hergott JF, Kovacev M, Merdji H, Hubert C, Mairesse Y, Jean E, Breger P, Agostini P, Carré B, and Salières P. *Extreme-ultraviolet high-order harmonic pulses in the microjoule range*. Phys. Rev. A **66**, 021801 (2002).

[76] Herzberg G. *Molecular Spectra and Molecular Structure*. Krieger Publishing Company, Malabar, Florida, USA (1989).

[77] Hishikawa A, Matsuda A, Fushitani M, and Takahashi EJ. *Visualizing recurrently migrating hydrogen in acetylene dication by intense ultrashort laser pulses*. Phys. Rev. Lett. **99**:258302 (2007).

[78] Huber KP and Herzberg G. *"Constants of Diatomic Molecules" (data prepared by J.W. Gallagher and R.D. Johnson, III) in NIST Chemistry WebBook, NIST Standard Reference Database Number 69, Eds. P.J. Linstrom and W.G. Mallard*. National Institute of Standards and Technology, Gaithersburg MD, USA, `http://webbook.nist.gov` (2008).

[79] Itatani J, Quéré F, Yudin GL, Ivanov, Krausz F, and Corkum PB. *Attosecond streak camera*. Phys. Rev. Lett. **88**, 173903 (2002).

[80] Itatani J, Levesque J, Zeidler D, Niikura H, Pepin H, Kieffer JC, Corkum PB, and Villeneuve DM. *Tomographic imaging of molecular orbitals*. Nature **432**, 867–871 (2004).

[81] Itikawa Y, Hayashi M, Ichimura A, Onda K, Sakimoto K, Takayanagi K, Nakamura M, Nishimura H, and Takayanagi T. *Cross sections for collisions of electrons and photons with nitrogen molecules*. J. Phys. Chem. Ref. Data **15**, 985–1010 (1986).

[82] Jin C, Le AT, and Lin CD. *Retrieval of target photorecombination cross sections from high-order harmonics generated in a macroscopic medium*. Phys. Rev. A **79**, 053413 (2009).

[83] Jordan G and Scrinzi A. *Core-polarization effects in molecular high harmonic generation*. New J. Phys. **10**, 025035 (2008).

[84] Kamta L and Bandrauk AD. *Three-dimensional time-profile analysis of high-order harmonic generation in molecules: Nuclear interferences in H_2^+*. Phys. Rev. A **71**, 053407–053419 (2005).

[85] Kanai T and Sakai H. *Numerical simulations of molecular orientation using strong, nonresonant, two-color laser fields*. J. Chem. Phys. **115**, 5492–5497 (2001).

[86] Kanai T, Minemoto S, and Sakai H. *Quantum interference during high-order harmonic generation from aligned molecules*. Nature **435**, 470–474 (2005).

[87] Kanai T, Minemoto S, and Sakai H. *Ellipticity dependence of high-order harmonic generation from aligned molecules*. Physical Review Letters **98**, 053002 (2007).

[88] Kanai T, Takahashi EJ, Nabekawa Y, and Midorikawa K. *Destructive interference during high harmonic generation in mixed gases*. Phys. Rev. Lett. **98**, 153904 (2007).

[89] Kanai T, Takahashi E, Nabekawa Y, and Midorikawa K. *Observing the attosecond dynamics of nuclear wavepackets in molecules by using high harmonic generation in mixed gases*. New J. Phys. **10**, 025036 (2008).

[90] Kanai T, Takahashi EJ, Nabekawa Y, and Midorikawa K. *Observing molecular structures by using high-order harmonic generation in mixed gases*. Phys. Rev. A **77**, 041402 (2008).

[91] Keldysh LV. *Ionization in the field of a strong electromagnetic wave*. Sov. Phys. JETP **20**, 1307–1314 (1965).

[92] Kim KT, Kang KS, Park MN, Imran T, Umesh G, and Nam CH. Comparison of RABITT and FROG measurements in the temporal characterization of attosecond pulse trains, (2007). URL `http://arxiv.org/abs/0707.4228`.

[93] Kitzler M, Milosevic N, Scrinzi A, Krausz F, and Brabec T. *Quantum theory of attosecond xuv pulse measurement by laser dressed photoionization*. Phys. Rev. Lett. **88**, 173904 (2002).

[94] Koopmans T. *Über die zuordnung von wellenfunktionen und eigenwerten zu den einzelnen elektronen eines atoms*. Physica **1**, 104–113 (1934).

[95] Kopold R, Becker W, and Kleber M. *Model calculations of high-harmonic generation in molecular ions*. Phys. Rev. A **58**, 4022–4038 (1998).

[96] Kovacev M. *Rayonnement harmonique dordre élevé: Génération dimpulsions attosecondes. Applications de la cohérence.* PhD thesis, Université Paris-Sud 11, (2003).

[97] Krause JL, Schafer KJ, and Kulander KC. *High-order harmonic generation from atoms and ions in the high intensity regime*. Phys. Rev. Lett. **68**, 3535–3538 (1992).

[98] Kroll NM and Watson KM. *Charged-particle scattering in the presence of a strong electromagnetic wave*. Phys. Rev. A **8**, 804–809 (1973).

[99] Kruit P and Read FH. *Magnetic field paralleliser for 2π electron-spectrometer and electron-image magnifier*. J. Phys. E **16**, 313–324 (1983).

[100] Lappas DG and Marangos JP. *Orientation dependence of high-order harmonic generation in hydrogen molecular ions*. J. Phys. B **33**, 4679–4689 (2000).

[101] Le AT, Tong XM, and Lin CD. *Evidence of two-center interference in high-order harmonic generation from* co_2. Phys. Rev. A **73**, 041402 (2006).

[102] Le AT, Della, Fainstein P, Telnov D, Lein M, and Lin C. *Theory of high-order harmonic generation from molecules by intense laser pulses*. J. Phys. B **41**, 081002 (2008).

[103] Le AT, Morishita T, and Lin CD. *Extraction of the species-dependent dipole amplitude and phase from high-order harmonic spectra in rare-gas atoms*. Phys. Rev. A **78**, 023814 (2008).

[104] Le AT, Lucchese RR, Lee MT, and Lin CD. *Probing molecular frame photoionization via laser generated high-order harmonics from aligned molecules*. Phys. Rev. Lett. **102**, 203001 (2009).

[105] Le AT, Lucchese RR, Tonzani S, Morishita T, and Lin CD. *Quantitative rescattering theory for high-order harmonic generation from molecules*. Phys. Rev. A **80**, 013401 (2009).

[106] Le VH, Le AT, Xie RH, and Lin CD. *Theoretical analysis of dynamic chemical imaging with lasers using high-order harmonic generation*. Phys. Rev. A **76**, 013413 (2007).

[107] Le Déroff L. *Etude des propriétés de cohérence de la génération d'harmoniques d'ordre élevé : qualité du faisceau, cohérence spatiale et temporelle et application*. PhD thesis, Université Paris 06, (1999).

[108] Lebech M, Houver JC, Lafosse A, Dowek D, Alcaraz C, Nahon L, and Lucchese RR. *Complete description of linear molecule photoionization achieved by vector correlations using the light of a single circular polarization*. J. Chem. Phys. **118**, 9653–9663 (2003).

[109] Lein M. *Attosecond probing of vibrational dynamics with high-harmonic generation*. Phys. Rev. Lett. **94**, 053004 (2005).

[110] Lein M, Hay N, Velotta R, Marangos JP, and Knight PL. *Interference effects in high-order harmonic generation with molecules*. Phys. Rev. A **66**, 023805 (2002).

[111] Lein M, Hay N, Velotta R, Marangos JP, and Knight PL. *Role of the intramolecular phase in high-harmonic generation*. Phys. Rev. Lett. **88**, 183903 (2002).

[112] Lein M, Kreibich T, Gross EKU, and Engel V. *Strong-field ionization dynamics of a model H_2 molecule*. Phys. Rev. A **65**, 033403 (2002).

[113] Lennard-Jones JE. *The electronic structure of some diatomic molecules*. Trans. Faraday Soc. **25**, 668–686 (1929).

[114] Lépine F, Kling M, Ni Y, Khan J, Ghafur O, Martchenko T, Gustafsson E, Johnsson P, Varjú K, Remetter T, L'Huillier A, and Vrakking M. *Short xuv pulses to characterize field-free molecular alignment*. J. Mod. Opt. **54**, 953–966 (2007).

[115] Levesque J, Mairesse Y, Dudovich N, Pepin H, Kieffer J, Corkum PB, and Villeneuve DM. *Polarization state of high-order harmonic emission from aligned molecules*. Phys. Rev. Lett. **99**, 243001 (2007).

[116] Levesque J, Zeidler D, Marangos JP, Corkum PB, and Villeneuve DM. *High harmonic generation and the role of atomic orbital wave functions*. Phys. Rev. Lett. **98**, 183903 (2007).

[117] Lewenstein M, Balcou P, Ivanov MY, L'Huillier A, and Corkum PB. *Theory of high-harmonic generation by low-frequency laser fields*. Phys. Rev. A **49**, 2117–2132 (1994).

[118] L'Huillier A, Schafer KJ, and Kulander KC. *Theoretical aspects of intense field harmonic generation*. J. Phys. B **24**, 3315–3341 (1991).

[119] Liang Y, Augst S, Chin SL, Beaudoin Y, and Chaker M. *High harmonic generation in atomic and diatomic molecular gases using intense picosecond laser pulses-a comparison*. J. Phys. B **27**, 5119–5130 (1994).

[120] Lofthus A and Krupenie PH. *The spectrum of molecular nitrogen*. J. Phys. Chem. Ref. Data **6**, 113–307 (1977).

[121] Lucchese RR, Raseev G, and Mckoy V. *Studies of differential and total photoionization cross sections of molecular nitrogen*. Phys. Rev. A **25**, 2572–2587 (1982).

[122] Lyngå C, L'Huillier A, and Wahlström CG. *High-order harmonic generation in molecular gases*. J. Phys. B **29**, 3293–3302 (1996).

[123] Machholm M and Henriksen NE. *Field-free orientation of molecules*. Physical Review Letters **87**, 193001 (2001).

[124] Madsen LB. *Strong-field approximation in laser-assisted dynamics*. Am. J. Phys. **73**, 57–62 (2005).

[125] Mairesse Y. , private communication, (2008).

[126] Mairesse Y and Quéré F. *Frequency-resolved optical gating for complete reconstruction of attosecond bursts*. Phys. Rev. A **71** (2005).

[127] Mairesse Y, de Bohan A, Frasinski L, Merdji H, Dinu L, Monchicourt P, Breger P, Kovacev M, Taïeb R, Carré B, Muller H, Agostini P, and Salières P. *Attosecond synchronization of high-harmonic soft x-rays*. Science **302**, 1540–1543 (2003).

[128] Mairesse Y, Gobert O, Breger P, Merdji H, Meynadier P, Monchicourt P, Perdrix M, Salières P, and Carré B. *High harmonic xuv spectral phase interferometry for direct electric-field reconstruction*. Phys. Rev. Lett. **94**, 173903 (2005).

[129] Mairesse Y, Dudovich N, Smirnova O, Patchkovski S, Zeidler D, Levesque J, Ivanov YM, Villeneuve DM, and Corkum PB. Interferometric measurements of molecular structure. Talk at the "International workshop on Attosecond Physics", (2007).

[130] Mairesse Y, Dudovich N, Levesque J, Ivanov M, Corkum P, and Villeneuve D. *Electron wavepacket control with elliptically polarized laser light in high harmonic generation from aligned molecules*. New J. Phys. **10**, 025015 (2008).

[131] Mairesse Y, Zeidler D, Dudovich N, Spanner M, Levesque J, Villeneuve DM, and Corkum PB. *High-order harmonic transient grating spectroscopy in a molecular jet*. Phys. Rev. Lett. **100**, 143903 (2008).

[132] Mansten E, Dahlström JM, Johnsson P, Swoboda M, L'Huillier A, and Mauritsson J. *Spectral shaping of attosecond pulses using two-colour laser fields*. New J. Phys. **10**, 083041 (2008).

[133] Maquet A and Taïeb R. *Two-colour IR+XUV spectroscopies: the soft-photon approximation*. J. Mod. Opt. **54**, 1847–1857 (2007).

[134] Marangos J, Torres R, Siegel T, Brugnera L, Frank F, Chipperfield L, Hoffmann D, and Tisch J. Optimising fields for HHG. Talk at the "International Conference on Attosecond Physics", (2009).

[135] Martens RL, Varjú K, Johnsson P, Mauritsson J, Mairesse Y, Salières P, Gaarde MB, Schafer KJ, Persson A, Svanberg S, Wahlström CG, and L'Huillier A. *Amplitude and phase control of attosecond light pulses*. Phys. Rev. Lett. **94**, 033001 (2005).

[136] Mashiko H, Gilbertson S, Li C, Khan SD, Shakya MM, Moon E, and Chang Z. *Double optical gating of high-order harmonic generation with carrier-envelope phase stabilized lasers*. Phys. Rev. Lett. **100**, 103906 (2008).

[137] Mauritsson J, Johnsson P, Martens RL, Varjú K, Kornelis W, Biegert J, Keller U, Gaarde MB, Schafer KJ, and Lchar39huillier A. *Measurement and control of the frequency chirp rate of high-order harmonic pulses*. Phys. Rev. A **70**, 021801 (2004).

[138] Mauritsson J, Gaarde M, and Schafer K. *Accessing properties of electron wave packets generated by attosecond pulse trains through time-dependent calculations*. Phys. Rev. A **72**, 013401 (2005).

[139] Mauritsson J, Johnsson P, Lopez-Martens R, Varjú K, L'Huillier A, Gaarde MB, and Schafer KJ. *Probing temporal aspects of high-order harmonic pulses via multi-colour, multi-photon ionization processes*. J. Phys. B **38**, 2265–2278 (2005).

[140] Mauritsson J, Johnsson P, Mansten E, Swoboda M, Ruchon T, L'Huillier A, and Schafer K. *Coherent electron scattering captured by an attosecond quantum stroboscope*. Phys. Rev. Lett. **100**, 073003 (2008).

[141] McFarland BK, Farrell JP, Bucksbaum PH, and Gühr M. *High harmonic generation from multiple orbitals in n2*. Science **322**, 1232–1235 (2008).

[142] Mcpherson A, Gibson G, Jara H, Johann U, Luk TS, Mcintyre IA, Boyer K, and Rhodes CK. *Studies of multiphoton production of vacuum-ultraviolet radiation in the rare gases*. J. Opt. Soc. Am. B **4**, 595–601 (1987).

[143] Meckel M, Comtois D, Zeidler D, Staudte A, Pavicic D, Bandulet HC, Pepin H, Kieffer JC, Dorner R, Villeneuve DM, and Corkum PB. *Laser-induced electron tunneling and diffraction*. Science **320**, 1478–1482 (2008).

[144] Merdji H, Salières P, Le Déroff L, Hergott JF, Carrè; B, Joyeux D, Descamps D, Norin J, Lyngå, L'Huillier A, Wahlström CG, Bellini M, and Huller S. *Coherence properties of high-order harmonics: Application to high-density laser–plasma diagnostic*. Laser Part. Beams **18**, 495–502 (2000).

[145] Miller KJ. *Additivity methods in molecular polarizability*. J. Am. Chem. Soc. **112**, 8533–8542 (1990).

[146] Miller KJ. *Calculation of the molecular polarizability tensor*. J. Am. Chem. Soc. **112**, 8543–8551 (1990).

[147] Milošević DB. *High-energy stimulated emission from plasma ablation pumped by resonant high-order harmonic generation*. J. Phys. B **40**, 3367 (2007).

[148] Milošević DB. , private communication, (2008).

[149] Monmayrant A and Chatel B. *New phase and amplitude high resolution pulse shaper*. Rev. Scient. Instr. **75**, 2668–2671 (2004).

[150] Muller HG. *Numerical simulation of high-order above-threshold-ionization enhancement in argon*. Phys. Rev. A **60**, 1341–1350 (1999).

[151] Muller HG. *Reconstruction of attosecond harmonic beating by interference of two-photon transitions*. Appl. Phys. B **74**, s17–s21 (2002).

[152] Nabekawa Y, Shimizu T, Okino T, Furusawa K, Hasegawa H, Yamanouchi K, and Midorikawa K. *Interferometric autocorrelation of an attosecond pulse train in the single-cycle regime*. Phys. Rev. Lett. **97**, 153904 (2006).

[153] Niikura H, Légaré F, Hasbani R, Bandrauk A, Ivanov MY, Villeneuve D, and Corkum P. *Sub-laser-cycle electron pulses for probing molecular dynamics*. Nature **417**, 917–922 (2002).

[154] Niikura H, Légaré F, Hasbani R, Ivanov MY, Villeneuve D, and Corkum P. *Probing molecular dynamics with attosecond resolution using correlated wave packet pairs*. Nature **421**, 826–829 (2003).

[155] Norin J, Mauritsson J, Johansson A, Raarup MK, Buil S, Persson A, Dühr O, Gaarde MB, Schafer KJ, Keller U, Wahlström CG, and L'Huillier A. *Time-frequency characterization of femtosecond extreme ultraviolet pulses*. Phys. Rev. Lett. **88**, 193901 (2002).

[156] Odžak S and Milošević DB. *Interference effects in high-order harmonic generation by homonuclear diatomic molecules*. Phys. Rev. A **79**, 023414 (2009).

[157] Patchkovskii S. *Nuclear dynamics in polyatomic molecules and high-order harmonic generation*. Phys. Rev. Lett. **102**, 253602 (2009).

[158] Patchkovskii S, Zhao Z, Brabec T, and Villeneuve DM. *High harmonic generation and molecular orbital tomography in multielectron systems: Beyond the single active electron approximation*. Phys. Rev. Lett. **97**, 123003–123004 (2006).

[159] Patchkovskii S, Zhao Z, Brabec T, and Villeneuve DM. *High harmonic generation and molecular orbital tomography in multielectron systems*. J. Chem. Phys. **126**, 114306 (2007).

[160] Paul PM, Toma ES, Breger P, Mullot G, Auge F, Balcou P, Muller HG, and Agostini P. *Observation of a train of attosecond pulses from high harmonic generation*. Science **292**, 1689–1692 (2001).

[161] Press WH, Flannery BP, Teukolsky SA, and Vetterling WT. *Numerical Recipes*. Cambridge University Press, Cambridge, England, 2nd edition (1992).

[162] Quéré F, Mairesse Y, and Itatani J. *Temporal characterization of attosecond xuv fields*. J. Mod. Opt. **52**, 339–360 (2005).

[163] Ramakrishna S and Seideman T. *Information content of high harmonics generated from aligned molecules*. Phys. Rev. Lett. **99**, 113901 (2007).

[164] Raoult M, Le Rouzo H, Raseev G, and Brion LH. *Ab initio approach to the multichannel quantum defect calculation of the electronic autoionisation in the hopfield series of N_2*. Journal of Physics B: Atomic and Molecular Physics **16**, 4601 (1983).

[165] Ravasio A, Gauthier D, Maia FRNC, Billon M, Caumes JP, Garzella D, Geleoc M, Gobert O, Hergott JF, Pena AM, Perez H, Carre B, Bourhis E, Gierak J, Madouri A, Mailly D, Schiedt B, Fajardo M, Gautier J, Zeitoun P, Bucksbaum PH, Hajdu J, and Merdji H. *Single-shot diffractive imaging with a table-top femtosecond soft x-ray laser-harmonics source*. Phys. Rev. Lett. **103**, 028104 (2009).

[166] Raymer MG. *Measuring the quantum mechanical wave function*. Contemp. Phys. **38**, 343–355 (1997).

[167] Remacle F and Levine RD. *An electronic time scale in chemistry*. PNAS USA **103**, 6793–6798 (2006).

[168] Remetter T, Johnsson P, Mauritsson J, Varjú K, Ni Y, Lepine F, Gustafsson E, Kling M, Khan J, Martens LR, Schafer K, Vrakking M, and L'Huillier A. *Attosecond electron wave packet interferometry*. Nature Physics **2**, 323–326 (2006).

[169] Roothaan CCJ. *New developments in molecular orbital theory*. Rev. Mod. Phys. **23**, 69–89 (1951).

[170] Rosca-Pruna F and Vrakking MJJ. *Experimental observation of revival structures in picosecond laser-induced alignment of i2*. Phys. Rev. Lett. **87**, 153902 (2001).

[171] Ruchon T, Hauri CP, Varjú K, Mansten E, Swoboda M, Lopez-Martens R, and L'Huillier A. *Macroscopic effects in attosecond pulse generation*. New J. Phys. **10**, 025027 (2008).

[172] Salières P, L'Huillier A, and Lewenstein M. *Coherence control of high-order harmonics*. Phys. Rev. Lett. **74**, 3776 (1995).

[173] Salières P, Le Déroff L, Auguste T, Monot P, D'Oliveira P, Campo D, Hergott JF, Merdji H, and Carré B. *Frequency-domain interferometry in the xuv with high-order harmonics*. Phys. Rev. Lett. **83**, 5483–5486 (1999).

[174] Sansone G, Benedetti E, Calegari F, Vozzi C, Avaldi L, Flammini R, Poletto L, Villoresi P, Altucci C, Velotta R, Stagira S, De Silvestri S, and Nisoli M. *Isolated single-cycle attosecond pulses*. Science **314**, 443–446 (2006).

[175] Santra R and Gordon A. *Three-step model for high-harmonic generation in many-electron systems*. Phys. Rev. Lett. **96**, 073906 (2006).

[176] Schafer KJ, Yang B, Dimauro LF, and Kulander KC. *Above threshold ionization beyond the high harmonic cutoff*. Phys. Rev. Lett. **70**, 1599–1602 (1993).

[177] Schleich WP and Raymer MG. *Special issue on quantum state preparation and measurement*. J. Mod. Opt. **44**, 2021–2022 (1997).

[178] Schmidt MW, Baldridge KK, Boatz JA, Elbert ST, Gordon MS, Jensen JH, Koseki S, Matsunaga N, Nguyen KA, Su S, Windus TL, Dupuis M, and Montgomery JA. *General atomic and molecular electronic structure system*. J. Comput. Chem. **14**, 1347–1363 (1993).

[179] Schneider F and Merkel A. *The lowest bound states of triplet $(BH_2)^+$*. Chem. Phys. Lett. **161**, 527–531 (1989).

[180] Schwarz WHE. *Measuring orbitals: Provocation or reality?* Angew. Chem. Int. Ed. **45**, 1508–1517 (2006).

[181] Schwenke J, Mai A, Miranda M, He X, Genoud G, Mikkelsen A, Pettersson, Persson A, and L'Huillier A. *Single-shot holography using high-order harmonics*. J. Mod. Opt. **55**, 2723–2730 (2008).

[182] Seideman T. *Revival structure of aligned rotational wave packets*. Phys. Rev. Lett. **83**, 4971–4974 (1999).

[183] Sekikawa T, Kosuge A, Kanai T, and Watanabe S. *Nonlinear optics in the extreme ultraviolet*. Nature **432**, 605–608 (2004).

[184] Shafir D, Mairesse Y, Villeneuve DM, Corkum PB, and Dudovich N. *Atomic wavefunctions probed through strong-field light-matter interaction*. Nature Phys. **5**, 412–416 (2009).

[185] Shan B, Tong XM, Zhao Z, Chang Z, and Lin CD. *High-order harmonic cutoff extension of the o_2 molecule due to ionization suppression*. Phys. Rev. A **66**, 061401 (2002).

[186] Smirnova O, Mairesse Y, Patchkovskii S, Dudovich N, Villeneuve D, Corkum P, and Ivanov MY. *High harmonic interferometry of multi-electron dynamics in molecules*. Nature **460**, 972–977 (2009).

[187] Smirnova O, Patchkovskii S, Mairesse Y, Dudovich N, and Ivanov MY. *Strong-field control and spectroscopy of attosecond electron-hole dynamics in molecules*. PNAS USA (2009).

[188] Sola I, Mevel E, Elouga L, Constant E, Strelkov V, Poletto L, Villoresi P, Benedetti E, Caumes JP, Stagira S, Vozzi C, Sansone G, and Nisoli M. *Controlling attosecond electron dynamics by phase-stabilized polarization gating*. Nature Physics **2**, 319–322 (2006).

[189] Stewart I. *Nonlinear dynamics: Quantizing the classical cat*. Nature **430**, 731–732 (2004).

[190] Suzuki M, Baba M, Ganeev R, Kuroda H, and Ozaki T. *Anomalous enhancement of a single high-order harmonic by using a laser-ablation tin plume at 47 nm*. Opt. Lett. **31**, 3306–3308 (2006).

[191] Svanberg S. *Atomic and Molecular Spectroscopy*. Springer, Berlin and Heidelberg, Germany (2004).

[192] Svelto O. *Principles of Lasers*. Plenum Press, New York and London (1998).

[193] Szabo A and Ostlund NS. *Modern Quantum Chemistry: Introduction to Advanced Electronic Structure Theory*. Dover Publications, New York, USA (1996).

[194] Tate J, Auguste T, Muller HG, Salières P, Agostini P, and DiMauro LF. *Scaling of wave-packet dynamics in an intense midinfrared field*. Phys. Rev. Lett. **98**, 013901 (2007).

[195] Thomann I, Bahabad A, Liu X, Trebino R, Murnane MM, and Kapteyn HC. *Characterizing isolated attosecond pulses from hollow-core waveguidesusing multi-cycle driving pulses*. Opt. Express **17**, 4611–4633 (2009).

[196] Toma ES and Muller HG. *Calculation of matrix elements for mixed extreme-ultraviolet & infrared two-photon above-threshold ionization of argon*. J. Phys. B **35**, 3435–3442 (2002).

[197] Torres R and Marangos JP. *Mapping of orbital structure from high harmonic generation through the molecular dipole moment*. Journal of Modern Optics **54**, 1883–1899 (2007).

[198] Torres R, Kajumba N, Underwood J, Robinson J, Baker S, Tisch J, Nalda DR, Bryan W, Velotta R, Altucci C, Turcu I, and Marangos J. *Probing orbital structure of polyatomic molecules by high-order harmonic generation*. Phys. Rev. Lett. **98**, 203007 (2007).

[199] Trebino R, editor. *Frequency-Resolved Optical Gating: The Measurement of Ultrashort Laser Pulses*. Kluwer Academic Publishers, Dordrecht, The Netherlands (2002).

[200] Tzallas P, Charalambidis D, Papadogiannis NA, Witte K, and Tsakiris GD. *Direct observation of attosecond light bunching*. Nature **426**, 267–271 (2003).

[201] Uiberacker M, Uphues T, Schultze M, Verhoef A, Yakovlev V, Kling M, Rauschenberger J, Kabachnik N, Schroder H, Lezius M, Kompa K, Muller HG, Vrakking M, Hendel S, Kleineberg U, Heinzmann U, Drescher M, and Krausz F. *Attosecond real-time observation of electron tunnelling in atoms*. Nature **446**, 627–632 (2007).

[202] van der Zwan EV, Chirilă CC, and Lein M. *Molecular orbital tomography using short laser pulses*. Phys. Rev. A **78**, 033410 (2008).

[203] Varjú K, Mairesse Y, Carré B, Gaarde MB, Johnsson P, Kazamias S, López-Martens R, Mauritsson J, Schafer KJ, Balcou P, L'Huillier A, and Salières P. *Frequency chirp of harmonic and attosecond pulses*. J. Mod. Opt. **52**, 379–394 (2005).

[204] Velotta R, Hay N, Mason MB, Castillejo M, and Marangos JP. *High-order harmonic generation in aligned molecules*. Phys. Rev. Lett. **87**, 183901 (2001).

[205] Véniard V, Taïeb R, and Maquet A. *Phase dependence of (N+1)-color (N>1) ir-uv photoionization of atoms with higher harmonics*. Phys. Rev. A **54**, 721–728 (1996).

[206] Vozzi C, Calegari F, Benedetti E, Caumes JP, Sansone G, Stagira S, Nisoli M, Torres R, Heesel E, Kajumba N, Marangos JP, Altucci C, and Velotta R. *Controlling two-center interference in molecular high harmonic generation*. Phys. Rev. Lett. **95**, 153902–153904 (2005).

[207] Vozzi C, Calegari F, Frassetto F, Poletto L, Sansone G, Villoresi P, Nisoli M, De Silvestri S, and Stagira S. *Coherent continuum generation above 100 ev driven by an ir parametric source in a two-color scheme*. Phys. Rev. A **79**, 033842 (2009).

[208] Vrakking M. *Chemical physics: Electronic movies*. Nature **460**, 960–961 (2009).

[209] Vrakking MJ and Stolte S. *Coherent control of molecular orientation*. Chem. Phys. Lett. **271**, 209–215 (1997).

[210] Wabnitz H, Mairesse Y, Frasinski L, Stankiewicz M, Boutu W, Breger P, Johnsson P, Merdji H, Monchicourt P, Salières P, Varjú K, Vitteau M, and Carré B. *Generation of attosecond pulses in molecular nitrogen*. Eur. Phys. J. D **40**, 305–311 (2006).

[211] Wagner N, Zhou X, Lock R, Li W, Wuest A, Murnane M, and Kapteyn H. *Extracting the phase of high-order harmonic emission from a molecule using transient alignment in mixed samples*. Phys. Rev. A **76**, 061403 (2007).

[212] Wahlström CG, Borgström S, Larsson J, and Pettersson SG. *High-order harmonic generation in laser-produced ions using a near-infrared laser*. Phys. Rev. A **51**, 585–591 (1995).

[213] Walmsley IA and Dorrer C. *Characterization of ultrashort electromagnetic pulses*. Adv. Opt. Photon. **1**, 308–437 (2009).

[214] Walmsley IA and Wong V. *Characterization of the electric field of ultrashort optical pulses*. J. Opt. Soc. Am. B **13**, 2453–2463 (1996).

[215] Walters ZB, Tonzani S, and Greene CH. *Limits of the plane wave approximation in the measurement of molecular properties*. J. Phys. Chem. A **112**, 9439–9447 (2008).

[216] Wörner HJ, Niikura H, Bertrand JB, Corkum PB, and Villeneuve DM. *Observation of electronic structure minima in high-harmonic generation*. Phys. Rev. Lett. **102**, 103901 (2009).

[217] Yu H and Bandrauk AD. *Three-dimensional cartesian finite element method for the time dependent schr[o-umlaut]dinger equation of molecules in laser fields*. J. Chem. Phys. **102**, 1257–1265 (1995).

[218] Zaïr A, Holler M, Guandalini A, Schapper F, Biegert J, Gallmann L, Keller U, Wyatt AS, Monmayrant A, Walmsley IA, Cormier E, Auguste T, Caumes JP, and Salières P. *Quantum path interferences in high-order harmonic generation*. Phys. Rev. Lett. **100**, 143902 (2008).

[219] Zewail AH. *Femtochemistry: Atomic-scale dynamics of the chemical bond†*. J. Phys. Chem. A **104**, 5660–5694 (2000).

[220] Zhou X, Lock R, Li W, Wagner N, Murnane M, and Kapteyn H. *Molecular recollision interferometry in high harmonic generation*. Phys. Rev. Lett. **100**, 073902 (2008).

[221] Zhou X, Lock R, Wagner N, Li W, Kapteyn HC, and Murnane MM. *Elliptically polarized high-order harmonic emission from molecules in linearly polarized laser fields*. Phys. Rev. Lett. **102** (2009).

[222] Zubek M, King GC, and Rutter PM. *Near-threshold photoionisation studies of N_2*. J. Phys. B **21**, 3585 (1988).

Papers

PAPER I

Coherent control of attosecond emission from aligned molecules

W. Boutu, S. Haessler, H. Merdji, P. Breger, G. Waters, M. Stankiewicz, L. J. Frasinski, R. Taïeb, J. Caillat, A. Maquet, P. Monchicourt, B. Carré and P. Salières.

Nature Physics **4**, 545–549 (2008).

LETTERS

Coherent control of attosecond emission from aligned molecules

W. BOUTU[1], S. HAESSLER[1], H. MERDJI[1], P. BREGER[1], G. WATERS[2], M. STANKIEWICZ[3], L. J. FRASINSKI[4], R. TAIEB[5,6], J. CAILLAT[5,6], A. MAQUET[5,6], P. MONCHICOURT[1], B. CARRE[1] AND P. SALIERES[1]*

[1]CEA-Saclay, DSM, Service des Photons, Atomes et Molécules, 91191 Gif sur Yvette, France
[2]J.J. Thomson Physical Laboratory, University of Reading, Whiteknights, Reading RG6 6AF, UK
[3]Institute of Physics, Jagiellonian University, ul. Reymonta 4, 30-059 Kraków, Poland
[4]The Blackett Laboratory, Imperial College London, Prince Consort Road, London SW7 2BW, UK
[5]UPMC Univ Paris 06, UMR 7614, Laboratoire de Chimie Physique-Matière et Rayonnement, 11 rue Pierre et Marie Curie, 75231 Paris Cedex 05, France
[6]CNRS, UMR 7614, LCPMR F-75005 Paris, France
*e-mail: pascal.salieres@cea.fr

Published online: 4 May 2008; doi:10.1038/nphys964

Controlling attosecond electron wave packets and soft X-ray pulses represents a formidable challenge of general implication to many areas of science[1–4]. A strong laser field interacting with atoms or molecules drives ultrafast intra-atomic/molecular electron wave packets on a subfemtosecond timescale, resulting in the emission of attosecond bursts of extreme-ultraviolet light[5,6]. Controlling the intra-atomic/molecular electron dynamics enables steering of the attosecond emission[7,8]. Here, we carry out a coherent control in linear molecules, where the interaction of the laser-driven electron wave packet with the core leads to quantum interferences[9–12]. We demonstrate that these interferences can be finely controlled by turning the molecular axis relative to the laser polarization, that is, changing the electron recollision angle. The wave-packet coulombic distortion modifies the spectral phase jump measured in the extreme-ultraviolet emission. Our attosecond control of the interference results in attosecond pulse shaping, useful for future applications in ultrafast coherent control of atomic and molecular processes.

High harmonic generation in gases[13,14] is a spectacular process arising when a strong laser field tunnel ionizes an atom/molecule, creating an attosecond electron wave packet that is subsequently accelerated and driven back to the core by the laser field[15,16]. It may then recombine to the ground state, releasing its accumulated kinetic energy in the form of an attosecond burst of extreme-ultraviolet light. In a multicycle laser field, this process is repeated every half-cycle leading to a train of attosecond pulses, the spectrum of which contains only the odd harmonics of the laser frequency. The precise characterization of this attosecond emission gives insight into the ultrafast electron dynamics[17]. A control of the continuum electron dynamics—and of the resulting extreme-ultraviolet emission—can be carried out by shaping the laser field, through a time-varying polarization[7] or a multicolour superposition[8]. Our approach is to coherently control the recombination step in linear molecules, when the returning electron wave packet interacts with the multicentre core, leading to quantum interferences[9–12].

A simple way to describe such interferences in diatomic molecules is the two-centre interference model[9,18]: the recolliding electron wave packet is modelled by a plane wave $\Psi_c \propto \exp[i\mathbf{kr}]$, and the ground state (the highest occupied molecular orbital, HOMO) by a linear combination of atomic orbitals. For an antisymmetric combination: $\Psi_0 \propto \Phi_0(\mathbf{r}-\mathbf{R}/2) - \Phi_0(\mathbf{r}+\mathbf{R}/2)$, where $\mathbf{R}$ is the internuclear vector, the recombination dipole moment in the velocity form[19] reads:

$$\langle \Psi_c|\mathbf{p}|\Psi_0\rangle \propto i\mathbf{k}\sin(\mathbf{kR}/2)\langle \exp[i\mathbf{kr}]|\Phi_0\rangle, \quad (1)$$

where $\mathbf{p}$ is the dipole momentum operator.

A destructive interference is obtained at $\mathbf{kR}/2 = n\pi$, that is, when

$$R\cos\theta = n\lambda_e, \quad (2)$$

where θ is the angle between the molecular axis and the electron propagation direction given by the laser polarization, n is an integer and λ_e is the electron de Broglie wavelength. The molecule then behaves like a two-point emitter, the emissions of which are dephased owing to the path difference between the centres and the symmetry of the orbital.

The CO_2 molecule, although triatomic, provides good conditions for observing this quantum interference. Indeed, its HOMO is a Π orbital dominated by the antisymmetric combination of two p orbitals centred on the O atoms. Moreover, the O–O distance ($R_{O-O} = 4.39$ a.u.) corresponds to an electron wavelength typical of the harmonic generation process. The recombination dipole moment exhibits a clear minimum close to that expected from equation (2)—however, for $R = 3.9$ a.u. $< R_{O-O}$ (Fig. 1). This deviation is due to a non-negligible contribution to the HOMO from the d_{xy} carbon orbital, and also to a lesser extent from the d_{xy} oxygen orbitals, the symmetry of which does not correspond to the interference condition (2).

The electron de Broglie wavelength $\lambda_e = 2\pi/k$ is directly related to the energy of the emitted photon by: $\hbar^2k^2/2m_e = \hbar\omega$ (this heuristic relation predicts an interference position that agrees well with that obtained from accurate simulations[10,19] for H_2^+). The destructive interference will thus appear in the harmonic spectrum as a clear minimum at a specific harmonic order (harmonic 23 for $\theta = 0$). Recent measurements in aligned CO_2 molecules have given indications of the presence of such a minimum[11,12]. However, those

© 2008 Macmillan Publishers Limited. All rights reserved.

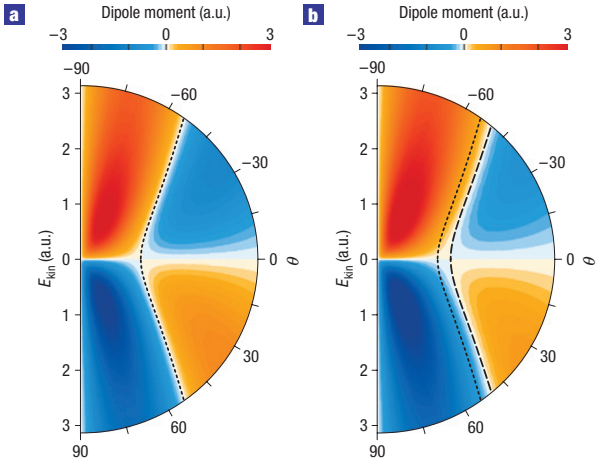

Figure 1 Theoretical dependence of the CO_2 recombination dipole on the angle and energy of the free-electron plane wave. Transition matrix element $\langle \exp[i\mathbf{kr}]|\mathbf{p}|\Psi_0\rangle$ where $\Psi_0 = \Psi_0(\theta, \mathbf{r})$ is the HOMO of CO_2, shown in polar coordinates as a function of the angle θ (°) between the electron wave vector **k** and the molecular axis, and the kinetic energy $k^2/2$ (atomic units) of the electron at recollision. **a**, In Ψ_0, only the *p* orbitals of the oxygen atoms are included. The dipole moment changes sign when the recollision angle θ follows equation (2) with $n = 1$ and $R = 4.3$ a.u. (dotted line). **b**, Total Ψ_0 as obtained from a Hartree–Fock calculation (GAMESS, General Atomic and Molecular Electronic Structure System code). The non-negligible contribution of the d_{xy} (*x* along the internuclear axis) carbon orbital (~7%), and also to a lesser extent of the d_{xy} oxygen orbitals (~2%), shifts the position of the interference to higher energy (equivalent to smaller *R* in equation (2): the prediction for $R = 3.9$ a.u. is shown by the dashed line). The dipole contribution of the d_{xy} carbon orbital obviously does not present any interference. As for the d_{xy} oxygen orbitals, they contribute to the total HOMO as a symmetric combination and thus give rise to a destructive interference following $R\cos\theta = (n-1/2)\lambda_e$. The sum of these different terms leads to the observed deviation. Note that the dipoles in **a** and **b** are real valued.

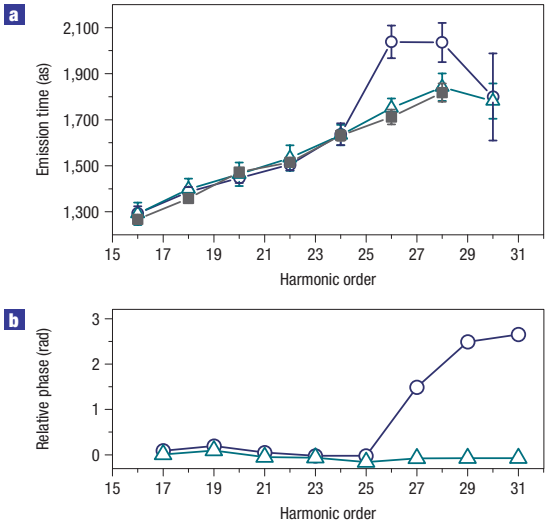

Figure 2 Experimentally measured phase of the harmonic emission from aligned CO_2 molecules. a, Harmonic emission time, that is, frequency derivative of the spectral phase, for molecules aligned parallel (open circles) and perpendicular (open triangles) to the laser polarization, and for krypton atoms (filled squares), under the same generating conditions (intensity of 1.25×10^{14} W cm^{-2}). The error bars indicate the accuracy of the relative phase determination (standard deviation of the phase within the FWHM of the $2\omega_0$ peak in the RABITT trace Fourier transform). Krypton and perpendicularly aligned CO_2 present the same linear dependence of the emission times, corresponding to the free-electron wave-packet dynamics in the continuum[17]. The emission from molecules aligned parallel to the laser exhibits an extra delay between harmonics 25 and 29, corresponding to a rapid increase of the spectral phase. **b**, Difference of spectral phases φ between CO_2 molecules and krypton. Using this reference atom, the subtraction uncovers the phase solely due to the recombination process in the molecule. The phases are obtained from the data shown in **a** by the rectangular integration method. To show the relative phase at harmonic 31, we assumed the emission time at $30\omega_0$ of krypton (that could not be measured owing to the low signal in the cutoff) to be equal to that of perpendicularly aligned CO_2 (measured owing to the slightly higher cutoff). See the Methods section for the choice of the phase zero.

observations rely only on spectral amplitude measurements, and hence could be explained by the interplay between the distribution of the partially aligned molecules and the angular dependence of the harmonic yield[20].

Our analysis is based on the measurements of both amplitude and phase of the harmonic emission from aligned molecules. The spectral phase, although more difficult to measure, contains important information on the interference process. In particular, a phase jump of π is expected at the position of destructive interference[9,18]. Indeed, the sign of the dipole moment in Fig. 1 changes at the amplitude minimum. The harmonic phase is also a crucial element for recovering the symmetry of the molecular orbitals in the tomographic reconstruction procedure[21]. Finally, it gives insight into the ultrafast electron dynamics and enables the reconstruction of the attosecond emission temporal profile.

We have characterized the harmonic emission from non-adiabatically aligned[22] CO_2 molecules (see the Methods section). The 'reconstruction of attosecond beating by interference of two-photon transition' (RABITT) technique[5,17,23] gives access to the relative phases of neighbouring harmonics, and thus to the group delay, also called the emission time:

$$t_e(\omega_{q+1}) := \frac{\partial\varphi}{\partial\omega} \approx \frac{\varphi_{q+2} - \varphi_q}{2\omega_0}.$$

In rare-gas atoms, this emission time varies linearly with the harmonic order in the plateau region, and coincides with the recollision time of the electron trajectories[17]. The resulting frequency chirp of the harmonic emission is a direct signature of the continuum electron dynamics. This is shown in Fig. 2a for krypton, which has a similar ionization potential to CO_2 ($I_p(Kr) = 14.00$ eV, $I_p(CO_2) = 13.77$ eV). Such a reference atom can be used to calibrate the recolliding electron wave packet[21,24]: the first two steps of the harmonic emission process (tunnel ionization and continuum dynamics) are expected to be similar in the two gases (except for the ionization angular dependence; see the Methods section). Indeed, the emission times of the CO_2 molecules aligned perpendicularly to the laser field match very closely with those of Kr (Fig. 2a). However, for parallel alignment, a strong deviation is observed between harmonics 25 and 29. Integrating the difference between the emission times in CO_2 and in Kr gives the phase associated solely with the recombination process (Fig. 2b). It presents a clear jump starting at harmonic 25, close to the prediction of the dipole calculation for the destructive interference. However, there are two remarkable features that are generic to all of our measurements. First, the total phase jump is 2.7 rad in this data set, and not π

© 2008 Macmillan Publishers Limited. All rights reserved.

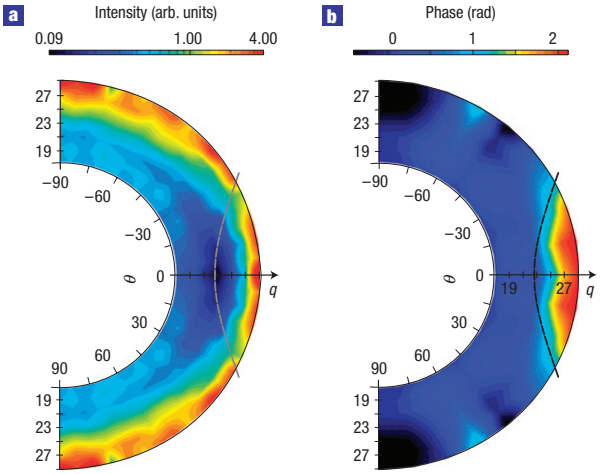

Figure 3 Experimental spectral intensity and phase of the CO_2 harmonic emission normalized by that of Kr. CO_2 harmonic intensity and phase (measured for molecule angles from 90° to 0°) normalized to the krypton data taken under the same experimental conditions (intensity of 0.95×10^{14} W cm^{-2}). To prevent the dispersion effects due to the larger ionization rate of Kr, the corresponding data were taken at lower pressure (25 torr versus 60 torr for CO_2) ensuring good phase-matching conditions. The dashed lines are the same as the one shown in Fig. 1b converted to harmonic order. The relation between the measured data and the recombination dipole moment is given in the Methods section. **a**, Intensity ratio versus alignment angle θ (measured in steps of 5°) and harmonic order q. The ratio is not corrected for the different pressures. A clear intensity minimum is measured around harmonic 23 for $\theta = 0$ that disappears when the molecule is rotated. **b**, Spectral phase difference (as in Fig. 2b), measured in steps of 10°. A phase jump of 2 rad is observed at the same position as the intensity minimum.

(value averaged over eight measurements: 2.0 ± 0.6 rad). Second, this jump is not step-like but is spread over three harmonic orders.

Such deviations cannot be explained by an imperfect experimental alignment: the convolution of the rotational wave-packet angular distribution with the dipole in Fig. 1b (both real-valued functions) would only induce a shift of the interference position but neither a spread nor a reduced value of the phase jump that both correspond to a complex dipole value. Such deviations appeared in early simulations[9,18] in H_2^+ and H_2 single molecules: a reduced phase jump of 2.7 rad spread over five orders was found in H_2^+ and even stronger deviations appeared in H_2. A recent dipole calculation replacing the plane waves in equation (1) by two-centre Coulomb wavefunctions has reproduced this behaviour[19]: the incorporation of the Coulomb binding potential of the atomic centres modifies the prediction of two-centre interference, in particular the shape of the phase jump. Our measured phase jump would thus contain a direct signature of the coulombic distortion of the recolliding electron wave packet, uncovered by the high sensitivity of the quantum interference.

We have carried out careful measurements of the phase jump as a function of the alignment angle (Fig. 3b). It reaches 2 rad for angles below 30° and quickly decreases to 0 with increasing angle. This may correspond to a shift to harmonic orders outside our accessible spectral range, in agreement with the dipole calculation in Fig. 1b. The harmonic amplitudes (Fig. 3a), normalized to those measured in krypton, exhibit a clear minimum around harmonic 23–25 at small angles, which disappears at large angles. The consistency of the amplitude and phase data is excellent and demonstrates a fine control of the quantum interference by turning the molecular axis. Note that the exact position of the interference may change significantly with intensity (phase jump for parallel alignment starting at harmonic 25 in Fig. 2b instead of harmonic 23 in Fig. 3b owing to the larger intensity), as also observed in recent amplitude measurements (Y. Mairesse *et al.*, manuscript in preparation). This extra deviation from the two-point emitter model may explain the different interference positions reported in ref. 11 (harmonic 25) and ref. 12 (harmonic 33).

The temporal characteristics of the quantum interference reveal an unexpected behaviour. With the measured amplitudes and phases, we reconstruct the temporal profile of the extreme-ultraviolet emission[5,17,23], and thus the acceleration of the dipole moment that mirrors the intramolecular electron dynamics. The temporal profile corresponding to orders 17–23 below the phase jump is very similar to that of krypton and does not vary significantly with the alignment angle (Fig. 4a). In contrast, the emission of harmonics 23–29 undergoing the phase jump is delayed in time with respect to krypton by 150 as for small angles and gradually converges to it with increasing angle (Fig. 4b). This delay is due to the quantum interference in the recombination process, and not to the transit time of the electron wave packet between the two oxygen atoms, which is twice as small. The spreading of the phase jump over three harmonic orders shifts the corresponding emission times to larger values (Fig. 2a), resulting in a delayed attosecond emission (Fig. 4b) with a barely modified pulse shape (slightly reduced full-width at half-maximum, FWHM, as compared with perpendicular alignment). This surprising result is a consequence of both the spreading and the occurrence of the quantum interference in the harmonic cutoff. There, the amplitude drops quickly with order, so that the destructive interference between spectral components on either side of the phase jump is not efficient enough to distort the temporal profile. The pulse reconstruction using the experimentally measured phases but assuming equal amplitudes for harmonics 17–29 results in a strong distortion with the expected double peak (Fig. 4c). The strongest distortion of the pulse (double peak with zero amplitude in between) would be obtained for a step-like π phase jump positioned in the middle of a flat spectrum.

The full potential of pulse shaping offered by the measured phase jump can be reached by simultaneously carrying out amplitude shaping. For instance, a clean double pulse could be obtained either using thin filters, or by placing the phase jump in the plateau region of the harmonic spectrum, which should be possible by generating with higher intensity and shorter pulses. By combining amplitude control and phase control (as the position and height of the phase jump depend on molecular structure and orientation), we extend the possibility of coherent quantum control to the extreme-ultraviolet and attosecond domains. For example, coherent transient enhancement of a resonant transition[25] could be carried out if the phase jump of $\sim\pi$ is placed at the transition energy. The below- and above-resonance contributions to the excited state population then interfere constructively.

We have shown how molecular structure and orientation affect the attosecond shape of the total (continuum + bound) electron wave packet during recollision. Further effects could also play a role in shaping the wave packet: (1) interplay of the molecular potential with the strong laser field (Coulomb–laser coupling)[26], (2) Π symmetry of the CO_2 HOMO reflected in the structure of the recolliding electron wave packet[27], (3) ionization dynamics involving many orbitals[27] and in particular orbitals below the HOMO (Y. Mairesse *et al.*, manuscript in preparation), and (4) exchange effects with core electrons[28,29]. At present, the relative importance of these factors is unknown. Our measurements thus

© 2008 Macmillan Publishers Limited. All rights reserved.

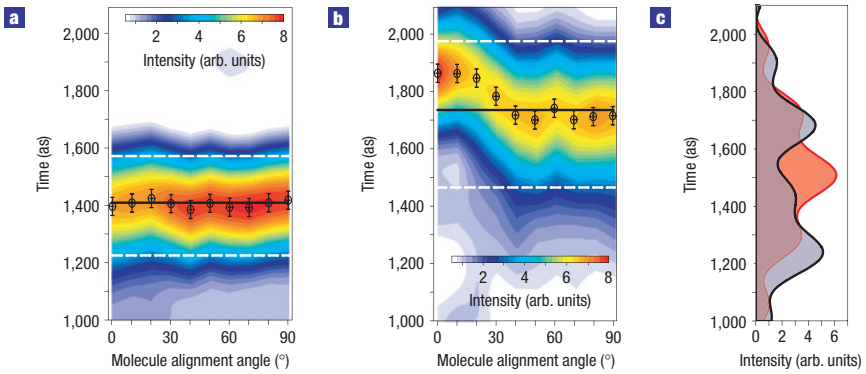

Figure 4 Attosecond dynamics of the harmonic emission from aligned CO_2 molecules. Intensity of a typical attosecond pulse in the generated train mapped as a function of the alignment angle θ and time t, with $t = 0$ at the maximum of the generating field. This dynamics is reconstructed from the spectral information in Fig. 3. Circles give the peak position of the pulse for ten θ values in a series of RABITT scans, and the error bars represent the standard deviation of the emission time of sideband 16, indicating the error in absolute timing of the attosecond pulses[17]. Black and dashed white lines indicate the positions of peak and half-maximum, respectively, of the attosecond pulse generated in krypton under the same experimental conditions. **a**, Using harmonics 17–23, located below the phase jump. The attosecond pulses generated in CO_2 and krypton are the same, with a duration of 320 as FWHM. **b**, Using harmonics 23–29, undergoing the phase jump. For the parallel alignment ($\theta = 0°$), the pulse is shifted by 150 as owing to the phase jump and gradually moves to the same timing as krypton as the molecules are rotated towards the perpendicular alignment. **c**, Time profile for harmonics 17–29 assuming constant spectral amplitudes for $\theta = 0°$ (black) and $\theta = 90°$ (red). Note that we shifted the absolute timing of the pulses in **a–c** with respect to the generating field by +200 as. All emission times in this series including the Kr reference data were measured to be 200 as too low with respect to the data in Fig. 2 and to previous findings[17]. However, the atto-chirp (slope of the emission time versus frequency) in both Figs 2 and 4 was as expected for the intensities used[17]. The small shift of time reference is presumably due to macroscopic effects (dispersion during propagation) and is compensated for here to present the single-atom/molecule response.

provide crucial information to benchmark improved models of the interaction of molecules with strong laser fields.

Our demonstrated control on the attosecond timescale provides a way to generalize the use of the continuum electron wave packet as a probe of molecular systems, in particular for accurate *ab initio* tomographic imaging of molecular orbitals. The extreme-ultraviolet spectral phase could also be used to probe coulombic recolliding electron wave packets. Finally, the control of the attosecond emission is a further step towards the extreme-ultraviolet pulse shaping that will open a new class of experiments, such as extreme-ultraviolet coherent control of atomic and molecular systems.

METHODS

We used the Laser Ultra-Court Accordable (LUCA) laser facility, which delivers to our experiment infrared pulses of 50 fs duration and up to 30 mJ in energy. A supersonic gas jet of CO_2, cooled in expansion to a rotational temperature of about 90 K, provides the molecular sample. An aligning laser pulse focused up to 5×10^{13} W cm^{-2} with a lens of 1 m focal length creates a rotational wave packet in the medium[22]. This wave packet periodically rephases, giving at the revival times a strong molecular alignment along the polarization direction (angular distribution of the rotational wave packet confined in a cone angle of ~20°). At the half revival time (equal to half the rotational period of the molecule), a second, more intense laser pulse of approximately 1×10^{14} W cm^{-2} generates high harmonics from the aligned molecules. A micrometric motorized translation stage is used to control the delay, and the angle between the axis of molecular alignment and the polarization of the generating beam is monitored by a motorized half-wave plate inserted in the aligning beam. To implement the RABITT technique, we need a third, weaker pulse of intensity about 10^{11} W cm^{-2}, the synchronization of which with the generating pulse is controlled by a piezoelectric translation stage. After harmonic generation, a diaphragm blocks the aligning and generating beams. A broadband toroidal mirror under grazing incidence focuses the harmonics and dressing beam in a detecting neon jet placed in the source volume of a magnetic-bottle electron spectrometer (see ref. 17, Fig. 2 for the phase measurement part of the set-up).

This demanding set-up requires precise alignment of three laser beams (aligning, generating and dressing), the intensities, delays and polarization of which should be controlled independently. In particular, the interferometric stability needed by the RABITT measurements must be preserved for more than 1.5 h to carry out the acquisition of the data shown in Fig. 3.

The RABITT technique measures the derivative of the harmonic phase, not the phase itself. To get a phase reference for Figs 2b and 3b, we assume that the phase of harmonic 15 generated in CO_2: (1) does not vary with angle and (2) for convenience, is the same as the one in Kr. The first assumption is supported by recent interferometric experiments (Y. Mairesse *et al.*, manuscript in preparation) demonstrating a very weak angular dependence of the phase of low harmonics in CO_2.

Within the plane-wave approximation, the transition dipole moment $d_{CO_2}(\omega,\theta)$ between a continuum state and the CO_2 HOMO can be directly related to the harmonic intensity ratio $S_{CO_2}(\omega,\theta)/S_{Kr}(\omega)$ and phase difference $\varphi_{CO_2}(\omega,\theta) - \varphi_{Kr}(\omega)$ measured in CO_2 and the krypton reference gas using[21]:

$$d_{CO_2}(\omega,\theta) = \langle \Psi_c|\mathbf{p}|\Psi_{CO_2}\rangle = \sqrt{\frac{P_{Kr}}{P_{CO_2}(\theta)}}\sqrt{\frac{S_{CO_2}(\omega,\theta)}{S_{Kr}(\omega)}}$$

$$\times \exp[i(\varphi_{CO_2}(\omega,\theta) - \varphi_{Kr}(\omega))]\langle \Psi_c|\mathbf{p}|\Psi_{Kr}\rangle,$$

where Ψ_{CO_2} is the CO_2 HOMO wavefunction, Ψ_{Kr} is the 4p orbital of krypton, Ψ_c is a plane wave $\exp[i\mathbf{k}(\omega)\mathbf{r}]$ propagating along the laser polarization direction, P_{CO_2} is the angle-dependent ionization yield of CO_2 and P_{Kr} is the ionization yield of Kr. As the Kr dipole is real valued and presents a smooth behaviour, it does not significantly modify the structures observed in Fig. 3 that can thus be attributed to the CO_2 dipole. Note finally that the above formula does not apply at $\theta = 0$ and 90° where the ionization is suppressed in CO_2 owing to the HOMO symmetry.

Received 21 December 2007; accepted 3 April 2008; published 4 May 2008.

References

1. Drescher, M. *et al.* Time-resolved atomic inner-shell spectroscopy. *Nature* **419**, 803–807 (2002).
2. Remetter, T. *et al.* Attosecond electron wave packet interferometry. *Nature Phys.* **2**, 323–326 (2006).
3. Baker, S. *et al.* Probing proton dynamics in molecules on an attosecond time scale. *Science* **312**, 424–427 (2006).

© 2008 Macmillan Publishers Limited. All rights reserved.

4. Cavallieri, A. *et al*. Attosecond spectroscopy in condensed matter. *Nature* **449**, 1029–1032 (2007).
5. Paul, P. M. *et al*. Observation of a train of attosecond pulses from high harmonic generation. *Science* **292**, 1689–1692 (2001).
6. Hentschel, M. *et al*. Attosecond metrology. *Nature* **414**, 509–513 (2001).
7. Sola, I. *et al*. Controlling attosecond electron dynamics by phase-stabilized polarization gating. *Nature Phys.* **2**, 319–322 (2006).
8. Pfeifer, T. *et al*. Single attosecond pulse generation in the multicycle-driver regime by adding a weak second-harmonic field. *Opt. Lett.* **31**, 975–977 (2005).
9. Lein, M., Velotta, R., Marangos, J. P. & Knight, P. L. Role of the intramolecular phase in high-harmonic generation. *Phys. Rev. Lett.* **88**, 183903 (2002).
10. Lagmago Kamta, G. & Bandrauk, A. D. Three-dimensional time-profile analysis of high-order harmonic generation in molecules: Nuclear interferences in H_2^+. *Phys. Rev. A* **71**, 053407 (2005).
11. Kanai, T., Minemoto, S. & Sakai, H. Quantum interference during high-order harmonic generation from aligned molecules. *Nature* **435**, 470–474 (2005).
12. Vozzi, C. *et al*. Controlling two-center interference in molecular high harmonic generation. *Phys. Rev. Lett.* **95**, 153902 (2005).
13. McPherson, A. *et al*. Studies of multiphoton production of vacuum-ultraviolet radiation in the rare gases. *J. Opt. Soc. Am. B* **4**, 595–601 (1987).
14. Ferray, M. *et al*. Multiple-harmonic conversion of 1064 nm radiation in rare gases. *J. Phys. B* **21**, L31–L35 (1988).
15. Corkum, P. B. Plasma perspective on strong field multiphoton ionization. *Phys. Rev. Lett.* **71**, 1994–1997 (1993).
16. Schafer, K. J., Yang, B., DiMauro, L. F. & Kulander, K. C. Above threshold ionization beyond the high harmonic cutoff. *Phys. Rev. Lett.* **70**, 1599–1602 (1993).
17. Mairesse, Y. *et al*. Attosecond synchronization of high-harmonic soft X-rays. *Science* **302**, 1540–1543 (2003).
18. Lein, M., Hay, N., Velotta, R., Marangos, J. P. & Knight, P. L. Interference effects in high-order harmonic generation with molecules. *Phys. Rev. A* **66**, 023805 (2002).
19. Ciappina, M. F., Chirila, C. C. & Lein, M. Influence of Coulomb continuum wave functions in the description of high-order harmonic generation with H_2^+. *Phys. Rev. A* **75**, 043405 (2007).
20. Le, A.-T., Tong, X.-M. & Lin, C. D. Evidence of two-center interference in high-order harmonic generation from CO_2. *Phys. Rev. A* **73**, 041402 (2006).
21. Itatani, J. *et al*. Tomographic imaging of molecular orbitals. *Nature* **432**, 867–871 (2004).
22. Rosca-Pruna, F. & Vrakking, M. Experimental observation of revival structures in picosecond laser-induced alignment of I_2. *Phys. Rev. Lett.* **87**, 153902 (2001).
23. Wabnitz, H. *et al*. Generation of attosecond pulses in molecular nitrogen. *Eur. Phys. J. D* **40**, 305–311 (2006).
24. Levesque, J., Zeidler, D., Marangos, J. P., Corkum, P. B. & Villeneuve, D. M. High harmonic generation and the role of atomic orbital wave functions. *Phys. Rev. Lett.* **98**, 183903 (2007).
25. Dudovich, N., Oron, D. & Silberberg, Y. Coherent transient enhancement of optically induced resonant transitions. *Phys. Rev. Lett.* **88**, 123004 (2002).
26. Smirnova, O., Mouritzen, A. S., Patchkovskii, S. & Ivanov, M. Yu. Coulomb–laser coupling in laser-assisted photoionization and molecular tomography. *J. Phys. B* **40**, F197–F206 (2007).
27. Xie, X. *et al*. Subcycle dynamics in the laser ionization of molecules. *Phys. Rev. A* **76**, 023426 (2007).
28. Patchkovskii, S., Zhao, Z., Brabec, T. & Villeneuve, D. M. High harmonic generation and molecular orbital tomography in multielectron systems: Beyond the single active electron approximation. *Phys. Rev. Lett.* **97**, 123003 (2006).
29. Zhao, Z., Yuan, J. & Brabec, T. Multielectron signatures in the polarization of high-order harmonic radiation. *Phys. Rev. A* **76**, 031404 (2007).

Acknowledgements

We acknowledge financial support from the EU-FP6 XTRA (MRTN-CT-2003-505138) and LASERLAB (RII3-CT-2003-506350) programmes, the ANR Attoscience and the Engineering and Physical Sciences Research Council (UK) (GR/S22424/01).

Author contributions

P.S. with B.C., H.M. and P.M. planned the project. W.B., H.M., P.B., P.M., B.C. and P.S. designed and installed the experiment. W.B. and S.H., with assistance from H.M., P.B., G.W., M.S., L.J.F., P.M. and P.S. carried out the measurements. W.B., S.H., H.M. and P.S. analysed the data. R.T., J.C. and A.M. carried out the dipole simulations. All authors discussed the results and contributed to the final manuscript. W.B. and S.H. contributed equally to this work.

Author information

Reprints and permission information is available online at http://npg.nature.com/reprintsandpermissions. Correspondence and requests for materials should be addressed to P.S.

© 2008 Macmillan Publishers Limited. All rights reserved.

PAPER II

Attosecond imaging of molecular electronic wave-packets

S. Haessler, J. Caillat, W. Boutu, C. Giovanetti-Teixeira, T. Ruchon, T. Auguste, Z. Diveki, P. Breger, A. Maquet, B Carré, R. Taïeb and P. Salières.

Nature Physics, accepted (2009).

Attosecond imaging of molecular electronic wave-packets

S. Haessler[1], J. Caillat[2, 3], W. Boutu[1], C. Giovanetti-Teixeira[2, 3], T. Ruchon[1], T. Auguste[1], Z. Diveki[1], P. Breger[1], A. Maquet[2, 3], B. Carré[1], R. Taïeb[2, 3], P. Salières[1]

1 CEA-Saclay, IRAMIS, Service des Photons, Atomes et Molécules, 91191 Gif-sur-Yvette, France.

2 UPMC Univ. Paris 06, UMR 7614, Laboratoire de Chimie Physique-Matière et Rayonnement, 11 rue Pierre et Marie Curie, 75231 Paris Cedex 05, France.

3 CNRS, UMR 7614, LCPMR F-75005 Paris, France.

A strong laser field may tunnel ionize a molecule from several orbitals simultaneously, forming an attosecond electron-hole wave-packet. Both temporal and spatial information on this wavepacket can be obtained through the coherent soft X-ray emission resulting from the laser-driven recollision of the liberated electron with the core. By characterizing the emission from aligned N_2 molecules, we evidence the attosecond contributions of the two highest occupied molecular orbitals. We determine conditions where they are disentangled in the real and imaginary parts of the emission dipole moment. This allows us to perform a tomographic reconstruction of both orbitals with Ångström spatial resolution. Their coherent superposition provides experimental images of the attosecond wavepacket created in the ionization process. Our results open the perspective of imaging ultrafast intra-molecular dynamics combining attosecond and Ångström resolutions.

The recent development of attosecond sources of coherent soft X-rays has opened the perspective of observing and controlling the fastest electronic processes in matter. In this rapidly evolving field, the attosecond processes explored up to now may be grouped in two categories. The first one encompasses the dynamics driven by a strong laser field in atoms and molecules. The laser period being a few femtoseconds, the timescale of sub-cycle electron dynamics is attosecond, as in tunnelling ionization[1,2] and continuum dynamics[3-7]. The second category deals with 'intrinsic' (laser-free) dynamics that is characteristic of the system: conduction band dynamics[8] or bound-state dynamics related to ultrashort lived transient states[9-11]. Attosecond 'intrinsic' dynamics could also be driven by coherent superposition of bound states. Such coherent superposition of bound states determines, e.g., intra-molecular electron transfer via non-adiabatic transitions in chemical reactions[12]. Theoretical studies investigated for instance electron-electron correlation[13,14] or charge migration in small peptides[15], and only recently both theoretical and experimental work has been performed in the context of tunnel ionization[16,17]. .

Imaging such coherent wavepackets localized in time and space would allow a better understanding of their dynamics. High-order harmonic generation (HHG) can be an efficient tool for such purpose. HHG occurs when a strong laser pulse, of frequency ω_L, tunnel-ionizes a gas target, creating an electron wave-packet (EWP) that is subsequently accelerated and driven back to the core where it recombines, emitting an attosecond burst of coherent soft X-rays[18-20]. Advanced characterization of the latter gives extremely precise information on both the structure and the dynamics of the radiating system. As the EWP associated with the observed photon emission has a duration at recollision of a few hundred attoseconds, it allows probing ultrafast dynamics in the excited molecular system (ion and correlated continuum electron) such as ultrafast nuclear motion[21,22], or attosecond electron dynamics in the recombination process[23]. As the EWP de Broglie wavelength λ_{dB} is of the order of molecular internuclear distances (~1 Å), it allows observing quantum interferences in the recombination process[23-27]. It may also lead to a tomographic reconstruction of the radiating orbital with Å resolution, as first proposed by Itatani et al[28]. This fascinating possibility of spatially imaging the wave function of a quantum object in

amplitude and phase attracted much attention. However both the assumptions made in the theoretical treatment and the incomplete experimental data raised intense discussions[29-34] on the feasibility of the technique that is still to be demonstrated.

Here we study an attosecond wavepacket created in aligned nitrogen molecules by tunnel ionization from both the highest occupied molecular orbital (HOMO), and the lower-lying orbital (referred to as HOMO-1). The HHG emission resulting from the freed EWP recollision is characterized in amplitude and phase. In our generation conditions, the signatures of the two orbitals can be disentangled, allowing their tomographic reconstruction. Exploiting further the measured relative phase of their contributions allows us to reconstruct the dynamic superposition of the orbitals left empty after tunnel ionization (so called "hole"), which evolves on the attosecond time-scale before recombination. This hole can be seen as a "negative" image of the ion left in a coherent superposition of the ground (X) and excited (A) states.

Creating and probing a bound attosecond wavepacket

Recent experimental and theoretical studies[16,17,35] have revealed that molecules interacting with a strong laser field could be tunnel ionized from several valence orbitals simultaneously due to their small energy separations and different geometries. This was observed in the resulting HHG emission, where the different orbitals lead to interfering contributions in the qth harmonic total dipole moment $\vec{D}(\theta, q\omega_L)$, where θ is the angle between the laser polarization and the molecular axis. In the strong field approximation (SFA), when only the HOMO, ψ^{HOMO}, and HOMO-1, $\psi^{HOMO\text{-}1}$, contribute without coupling, $\vec{D}(\theta, q\omega_L)$ reads[28,36]:

$$\vec{D}(\theta, q\omega_L) = a_1(\theta, k_q) \int [\psi^{HOMO}(\vec{r})]^* \, \vec{r} \, e^{i\vec{k}_q \cdot \vec{r}} \, d\vec{r} + a_2(\theta, k_q) \int [\psi^{HOMO\text{-}1}(\vec{r})]^* \, \vec{r} \, e^{i\vec{k}_q \cdot \vec{r}} \, d\vec{r}$$
$$\equiv a_1(\theta, k_q) \, \vec{d}^{HOMO}(\theta, k_q) + a_2(\theta, k_q) \, \vec{d}^{HOMO\text{-}1}(\theta, k_q) \quad (1)$$

where the bound wave functions are expressed in the Koopmans approximation[37] and the scattering state in the plane-wave approximation, with $q\omega_L = k_q^2/2$ (discussed later, atomic units are used throughout). The complex wave packet amplitude $a_{1/2}$ of each contribution results from the tunnel-ionization and continuum excursion steps. The angle θ determines the ratio of the orbital contributions in both the ionization amplitude and the recombination dipole moment[16,17]. The HHG emission thus contains rich structural and dynamical information on the complex ionic system but this information is not accessible through measurement of the harmonic intensity only.

Our experimental setup achieves laser-driven non-adiabatic molecular alignment, subsequent attosecond pulse generation and characterization in the spectral domain in amplitude and phase of the HHG polarization component parallel to the driving laser (see Methods). The temporal intensity profile of the attosecond emission from N_2 molecules is shown in Fig. 1a for different θ. The pulse shape hardly varies but the peak timing presents a gradual shift by -50 as when θ increases from 0° to 90°.

Understanding the origin of this temporal shift and its relation to multi-orbital contributions requires a detailed analysis of the effective recombination dipole $d^{exp}(\theta,q)$ extracted from the measured spectra. To this end, one has to remove the complex amplitude accumulated by the EWP prior to recombination, which induces a chirp in the attosecond emission[5], i.e., $d^{exp}(\theta,q) = D^{exp}(\theta,q)/a_1$. This is achieved by normalizing the measured XUV spectrum (amplitude and phase) for nitrogen by the spectrum for argon (same ionization potential I_p) obtained under the same experimental conditions, and multiplying this ratio by the theoretical recombination dipole $d_{Ar}(q)$ for argon[23,28].

The obtained normalized amplitude (Fig. 2a) reproduces the results of ref. 28 with a spectral minimum at harmonic 25 at all alignment angles. However, the assumption made in ref. 28 of a π phase jump associated to structural interferences (expected to be θ-dependent[24]) is not confirmed here. Our measured phase difference (Fig. 2b) presents a more complex behaviour with two identified jumps.

In the following, we show that this non-trivial phase is driven by not only structural interferences but also multi-orbital effects favoured by both energy and geometry criteria.

Disentangling the orbital contributions to HHG

In N_2, the HOMO (σ_g symmetry) and HOMO-1 (π_u symmetry) are separated by only[38] $\Delta\varepsilon \approx$ -1.4 eV. The differences in symmetry and geometry result in a strong angular dependence of the ratio of their ionization probabilities[39,40], that is maximum at $\theta = 90°$. They also lead to a larger plane-wave recombination dipole moment for the HOMO-1 at high energy, and consequently an overall significant contribution to the high-harmonic emission at 90°. Our analysis, focused on the dipole *phase*, follows the chronology of the SFA model: we address for each contribution the phase $\phi_d=\phi_c+\phi_r$, with (i) the phase $\phi_c=\arg(a_{1/2})$ acquired by the ionic system during the continuum excursion and (ii) the phase $\phi_r=\arg(d^{\mathrm{HOMO/HOMO\text{-}1}})$ added by recombination.

The dipole normalization procedure removed the phase ϕ_c, *but only for the HOMO contribution*. The HOMO-1 contribution is left, after calibration, with a phase equal to[41] $\Delta\phi_c(q\omega_L) = \arg(a_2/a_1) = \phi_c^{\mathrm{HOMO\text{-}1}}(q\omega_L) - \phi_c^{\mathrm{HOMO}}(q\omega_L) \approx \Delta\varepsilon\ \tau_q$ (see Supplementary Information), where τ_q is the electron excursion time associated with harmonic order q. The difference $\Delta\phi_c(q\omega_L)$ is plotted in Fig.3a for our experimental conditions. It evolves slowly around -π, value reached in the middle of the experimental spectral range, at H25.

The recombination dipole expressed in the plane-wave (PW) approximation (appearing in Eq. (1)) turns out to be the Fourier transform of the bound wave-function times the dipole operator[28,36] $\vec{r}$. Due to the symmetry properties of the orbitals and of the dipole operator (antisymmetric) on the one hand, and of the Fourier transform on the other hand, the recombination dipole is purely *imaginary-valued* for the HOMO (σ_g) and purely *real-valued* for the HOMO-1 (π_u), resulting in $\Delta\phi_r = \pi/2$. At this stage, the accumulated phase difference $\Delta\phi_d = \Delta\phi_c + \Delta\phi_r$ is close to -π/2: the HOMO and HOMO-1 contributions to the normalized dipole $d^{\mathrm{exp}}(\theta,q)$ are *practically* disentangled in the imaginary and real part, respectively. The measured phase variation around H25 at θ =90° could be a signature of a significant contribution of HOMO-1 coming into play for the high harmonics.

However, the PW approximation assumes the recolliding electron to be free, although it is accelerated by the parent ionic core, inducing a distortion of the EWP, which may cancel out the disentanglement of the HOMO and HOMO-1 contributions. Computing exact values of molecular recombination dipoles requires a precise knowledge of the continuum states, which is by no means a simple task in such multi-electron multi-center systems[30,42]. Nevertheless, valuable insight can be gained through a relatively simple model, that uses Coulomb waves[37] (CWs) for the continuum. This approach is motivated by the fact that the ionic core acts asymptotically as an effective point charge $Z^* = 1$. Figure 3b,c presents the phase variation of the dipole against the electron momentum k computed for the HOMO within the CW approximation, for three illustrative θ values. Two representative cases are considered: the plane wave limit $Z^* = 0$ (Fig. 3b) and $Z^* = 1$ corresponding to the effective N_2^+ charge (Fig. 3c). As expected from the symmetry criteria mentioned before, in the case of PWs, the phase is an odd multiple of π/2, the sudden jumps being a manifestation of structural sign changes in the purely imaginary dipole. For $Z^* = 1$ and k>0.5 a.u, the evolution tends to follow the variations observed for $Z^*= 0$, with the following differences: (i) besides being smoothed, the π-jumps are translated towards lower k by an amount $\delta k\approx$0.4 a.u. and (ii) the phases are vertically shifted by a global term which decays smoothly as k increases. By assigning to each harmonic frequency $q\omega_L$ an asymptotic momentum k_q using[36] $k_q^2/2 = q\omega_L - I_p$, one finds that our measurements were performed in the window 0.9 a.u.< k < 1.54 a.u. In this range, the phase variations are dominantly governed by the structural jumps also observed in the PW approximation, with a global phase shift $\delta\phi_r\approx\pi/4$. We performed the same study for the HOMO-1, and obtained similar conclusions both on the jump translation and on the global phase shift. Therefore we conclude that (i) we can base our interpretation on the PW approximation, provided a proper translation is made on the electron momentum scale, and (ii) we can still consider the HOMO and HOMO-1 contributions to be disentangled in the imaginary and real parts of $d^{\mathrm{exp}}(\theta,q)$ respectively, provided a $-\delta\phi_r$ rotation in the complex plane. Within the experimental k-range, the momentum

translation in (i) corresponds to a kinetic energy translation of ≈ 15 eV. This is consistent with the heuristic relation $k_q^2/2 = q\omega_L$ generally used in the SFA interpretation of molecular harmonic spectra[24]. The removal of I_p from the energy conservation law is interpreted as a compensation for the absence of electron acceleration close to the core in the PW treatment. In (ii), performing a global phase shift assumes that the *exact* scattering phase shift is practically independent of energy in the studied spectral range, molecular alignment, and ionized orbital – as suggested by the CW model. This is consistent with numerical experiments[31] based on the time-dependent Schrödinger equation for a single contributing orbital, where such an overall dipole rotation allowed quasi-suppression of the imaginary part of the reconstructed orbital. The physical origin of this rotation was, however, not identified in ref. 31. The global phase shift, $\delta\phi_r$, for *exact* N_2 scattering states is probably different from the CW based prediction, we thus empirically chose the phase origin that provided the most consistent reconstructions (see Fig.2 and Supplementary Information).

Tomographic imaging of the dynamic hole

Our understanding of the complex dipole structure allows us to exploit the measured data and (i) to simulate the temporal profiles of the attosecond emission, (ii) to reconstruct the involved orbitals by a tomographic procedure, and, merging the temporal and structural aspects, (iii) to image, at the instant of recombination, the dynamic "hole" formed by the coherent ionization channels.

Combining the predicted phases ϕ_d and experimental harmonic amplitudes, we simulated the temporal intensity profile of the attosecond emission as a function of the relative weight $|a_2|:|a_1|$ of both contributions. Figure 1b reproduces very well the experimental negative temporal shift of the attosecond pulse peak when a significant HOMO-1 contribution is gradually added to the HOMO contribution as the angle is increased from 0° to 90°. This regular evolution is consistent with the phase difference close to $-\pi/2$ that minimizes the interference of the two contributions. Different experimental conditions (laser intensity and wavelength, selection of long trajectories) can lead to stronger interferences and much more distorted temporal profiles, as illustrated by the simulations presented in Fig.1c where $\Delta\phi_r=\pi/2$ was omitted leading to a total phase difference centered around $-\pi$.

Following the tomographic procedure suggested by Itatani *et al.*[28], we now define the 2D reconstructed functions:

$$f_\alpha(x,y) = \frac{1}{\alpha}\sum_q\sum_j 2\omega_L\Delta\theta\ \left[d_\alpha^{\exp}(\theta_j,k_q)\right]^*\ \exp[ik_q(x\cos\theta_j + y\sin\theta_j)] \qquad (\alpha = x,y), \tag{2}$$

where q and j span the harmonic and angular samplings respectively, $\Delta\theta$ is the angular step (10°), $[d^{\exp}{}_\alpha]^*$ is the complex-conjugated α-component of the normalized dipole and the discretized inverse Fourier transform is restricted to the *(x,y)* plane. If the transform were performed exactly, both f_x and f_y would be equal to the wavefunction contributing to the dipole, integrated over the transverse direction *z*.

We present in Fig.4a,b the 2D orbitals reconstructed from our data shown in Fig.2, taken as the half sum of f_x and f_y in order to average the errors due to the discrete sampling. The measurements were done for angles between 0° and 90°. The tomographic procedure requires the experimental dipole to be extrapolated up to 360°, by imposing the assumed symmetry associated with the orbital to be imaged. Note that new methods are currently developed to detect experimentally the orbital symmetries by controlling the EWP trajectory[43,44]. The disentanglement of the multi-orbital contributions in the experimental dipole allows us to reconstruct both the HOMO (from its imaginary part when selecting the σ_g symmetry), and the HOMO-1 (from its real part when selecting the π_u symmetry). As seen in Fig. 4a, our reconstructed σ_g orbital possesses the main characteristics of the nitrogen HOMO (Fig. 4e), namely three main lobes with alternating signs, separated by two nodal surfaces passing through each nucleus. The visual aspect of the HOMO-1 reconstruction (Fig. 4b) is dominated by the imposed symmetry and possesses little particular structure.

We performed simulated reconstructions for the HOMO and HOMO-1 in the PW approximation, based on orbitals calculated with GAMESS[45]. To mimic the experimental conditions, we computed

the dipoles over the span corresponding to the harmonic and orientation samplings using the relation $k_q^2/2 = q\omega_L$, restricting the dipoles to the laser polarization orientation. The simulated HOMO reconstruction, shown in Fig. 4c, is strikingly similar to the experimental one (Fig. 4a): both present very similar distorted lobes, with extrema and nodes at the same locations. For the HOMO-1, the experimental and simulated reconstructions (Fig. 4b,d) both present a main central lobe, but with notably different sizes. We relate this to the fact that the HOMO-1 reconstructions had to be done using the velocity-form of the dipole operator, in order to avoid numerical singularities appearing when reconstructing π orbitals in the length gauge. This was confirmed by very similar discrepancies obtained when reconstructing the HOMO in the velocity gauge (see Supplementary Information).

The main distortions and extra oscillations in our reconstructions, compared to *exact* Hartree-Fock orbitals (shown in Fig. 4e,f), thus result essentially from the restricted harmonic span. Our analysis cannot account for the remaining deviations, in particular the HOMO:HOMO-1 contrasts (the ratio of the maximum amplitudes is 1:10 in the experiment, while 3:10 in the simulations). Our simulations do not take into account the different ionization yields of the two orbitals and possibly different continuum wavepacket spreading. Deviations may also be related to approximations inherent to the SFA, such as neglecting bound- and continuum-state distortions by the strong external field[46,47]. For systems with little relaxation, such as N_2, the Dyson orbital (which is the orbital to be considered in a rigorous treatment) does not differ significantly from the ionized Hartree-Fock orbital and the exchange terms[48,49], the magnitude of which is considerably overestimated in the plane-wave approximation, are negligible. Distortions may also result from properties of the *exact* dipole absent in our model[30,42], though we expect relatively long-lived resonances to have little impact on the HHG recombination dipole due to the sub-cycle time-scale of the electron excursion.

The HOMO and HOMO-1 experimental reconstructions, ψ_{exp}^{HOMO} and ψ_{exp}^{HOMO-1} (Fig. 4a,b), provide snapshots of the orbitals at the recombination instant $\tau \approx 1.5$ fs after tunnel-ionization, *i.e.* they contain the relative phase $\Delta\phi_c$ accumulated during the EWP excursion. These images are averaged over $\Delta\tau \approx 600$ as, as given by the electron excursion times spanned by the harmonics (cf. Fig. 3a). The coherent superposition of ψ_{exp}^{HOMO} and ψ_{exp}^{HOMO-1} provides time-resolved experimental images of the wave-packet left empty after coherent tunnel ionization from both orbitals[16,17]. Figure 5a shows $\psi_{exp}^{HOMO} + \psi_{exp}^{HOMO-1}$, *i.e.* the "hole" at the recombination time. The same wave-packet taken at the tunnel-ionization instant ($\tau = 0$), reconstructed by removing from the HOMO-1 the phase difference $\Delta\phi_c = -\pi$ acquired until recombination, *i.e.* as $\psi_{exp}^{HOMO} - \psi_{exp}^{HOMO-1}$, is shown in Fig. 5b. Since the value of τ coincides approximately with one half-period $\pi/|\Delta\varepsilon|$ of the HOMO-HOMO-1 beating, we observe the motion of the 'hole' from one side of the molecule to the other.

Intra-molecular time-resolved imaging

Varying the generation parameters (laser intensity and wavelength, selection of the long trajectories) provides different ways for controlling the EWP recombination time, and thus makes it possible to probe the hole at different instants. Combining various phase measurement techniques[5,16,23,27] (RABITT, 2-source interferometry, gas mixing) with the driving-field polarization control[43,44] will allow lifting the assumptions made in the tomographic reconstructions, in particular *a priori* knowledge of the orbital symmetry. This imaging of a dynamic hole wave-packet serves as a test bench for intra-molecular time-resolved imaging. This is a general technique that can be applied to follow the "frontier" orbital of a system during, e.g., a photo-excited process in a conventional pump-probe scheme. Our progress towards time-resolved tomography thus opens the perspective of imaging ultrafast dynamics of valence electrons and light nuclei at various stages of chemical reactions.

Methods

We use the 'Laser UltraCourt Accordable' (LUCA) of the 'Saclay Laser Matter Interaction Center' (SLIC), delivering pulses centered around 795 nm with up to 30 mJ energy and ≈55 fs duration at a repetition rate of 20 Hz.

Our setup is based on a Mach-Zehnder type interferometer for the `Reconstruction of Attosecond Beating by Interference of Two-photon Transitions' (RABITT) measurement (see Supplementary Information). Drilled mirrors (8 mm hole diameter) separate the annular generating beam (outer diameter cut to 17 mm by an iris), which contains most of the energy (≈ 1 mJ), and the weak central part (≈ 50 μJ, diameter ≈ 4 mm). The latter can be delayed by a piezoeletric translation stage with interferometric stability (~ 10 nm). In both arms, combinations of half-wave plate and polarizer allow to finely control the pulse energy. The two beams are then collinearly focused by the same lens of 1 m focal length ($F_{\#} \approx 60$ for the generating beam and $F_{\#} \approx 250$ for the probe beam). The beam focus is placed ≈ 5 mm before the HHG gas jet, thus selecting the short trajectory contribution[50]. An iris of ≈ 4 mm diameter blocks the annular generating beam in the far field. The source point of the XUV emission together with the on-axis probe beam is then imaged by a broad-band gold-coated toroidal mirror into the detection volume of a magnetic bottle electron spectrometer (MBES).

This toroidal mirror together with a flat mirror cause two grazing-incidence (11.5°) reflections of the HHG radiation on Au-surfaces, preferentially transmitting the s-polarized component into the electron spectrometer (with a 2:1 contrast). The generating laser is kept s-polarized while the molecular alignment axis is rotated in order to predominantly detect the HHG polarization component parallel to the driving laser.

In the spectrometer interaction volume, the neon target gas, injected by a permanent leak, is photoionized by the high harmonics. With the HHG and detection gas jet running, the pressure is $\sim 10^{-3}$ - 10^{-2} mbar in the HHG chamber, $\sim 10^{-5}$ mbar in the toroidal mirror chamber, $\sim 10^{-4}$ mbar in the MBES interaction volume and $\sim 10^{-6}$ mbar in the MBES flight tube.

To align molecules in the HHG gas jet, a third laser pulse with controllable delay, polarization and intensity is needed. To this end, a larger interferometer, based on amplitude beam splitters, is set up around the compact RABITT interferometer. One fifth of the incoming pulse energy is transmitted into the arm for the aligning beam and passes a motorized delay stage. Here, the stability requirements are much less severe than for the RABITT interferometer, since the variation of the angular distribution of the molecules varies on a ~10 fs timescale. The central part (≈ 4 mm diameter) of this beam is blocked so as to limit the amount of its energy passing into the MBES and thus prevent above-threshold ionization. The polarization direction of the aligning beam is set by a motorized half-wave plate, thus controlling directly the alignment angle of the molecular ensemble with respect to the HHG driving laser polarization direction at the half-revival delay. The pulse energy in the aligning beam is limited by a diaphragm (cutting the beam to typically 12 mm diameter), thereby limiting the aligning beam intensity to $\approx 5 \cdot 10^{13}$ Wcm^{-2} in the HHG gas jet. This also ensures that the aligning beam focal spot is larger than that of the generating beam.

The HHG gas jet has an orifice of 300 μm diameter backed with 3 bar pressure. This leads to an estimated 90 K rotational temperature of the nitrogen molecules at ≈ 1 mm distance from the orifice, where the generating beam is focused. This estimate is obtained by Fourier transforming the revival trace (dependence of the total harmonic yield on the aligning beam – generating beam delay), and comparing to the Fourier transform of calculated $\langle\cos^2\theta\rangle$-traces.

Acknowledgements:

We thank O. Smirnova, M. Ivanov and Y. Mairesse for fruitful discussions. Financial support from the LASERLAB2 program and from the ANR ATTO-WAVE is acknowledged. Parts of the computations have been performed at the Institut du Développement et des Ressources en Informatique Scientifique IDRIS.

Author Contributions :
P.S. with B.C. planned the project. W.B., P.B. B.C. and P.S. designed and installed the experiment. S.H. with assistance of W.B. P.B. and P.S. performed the measurements. S.H. and J.C. with assistance from W.B.,T.R., Z.D. and P.S. analyzed the data. J.C., C.G.-T., T.A., A.M. and R.T. performed the calculations. All authors discussed the results and contributed to the final manuscript.

Competing financial interests :
The authors declare that they have no competing financial interests.

References:

1. Uiberacker, M. *et al.* Attosecond real-time observation of electron tunnelling in atoms. *Nature* **446,** 627-632 (2007).
2. Eckle, P. *et al.* Attosecond ionization and tunnelling delay time measurements in Helium. *Science* **322**, 1525-1529 (2008).
3. Niikura, H. *et al.* Probing molecular dynamics with attosecond resolution using correlated wave packet pairs. *Nature* **421**, 826-829 (2003).
4. Mauritsson, J. *et al*. Coherent Electron Scattering Captured by an Attosecond Quantum Stroboscope. *Phys. Rev. Lett.* **100**, 073003 (2008).
5. Mairesse, Y. *et al.* Attosecond synchronization of high harmonic soft X-ray. *Science* **302**, 1540-1543 (2003).
6. Sola, I. *et al*. Controlling attosecond electron dynamics by phase-stabilized polarization gating. *Nature Phys.* **2**, 319–322 (2006).
7. Dudovich, N. L. *et al*. Measuring and controlling the birth of attosecond XUV pulses. *Nature Phys.* **2**, 781-786 (2006).
8. Cavallieri, A. *et al*. Attosecond spectroscopy in condensed matter. *Nature* **449**, 1029–1032 (2007).
9. Drescher, M. *et al*. Time-resolved atomic inner-shell spectroscopy. *Nature* **419**, 803–807 (2002).
10. Fohlisch, A. *et al*. Direct observation of electron dynamics in the attosecond domain. *Nature* **436,** 373-376 (2005).
11. Haessler *et al.* Phase-resolved attosecond near-threshold photoionization of molecular nitrogen. Phys. Rev. A **80**, 011404 (2009).
12. H. Nakamura. *Nonadiabatic Transitions. Concepts, Basic Theories and Applications.* (World Scientific Publishing, Singapore, 2002).
13. Breidbach, J. & Cederbaum, L. S. Universal Attosecond Response to the Removal of an Electron. *Phys. Rev. Lett.* **94**, 033901 (2005).
14. Hu, S. X. & Collins, L. A. Attosecond Pump Probe: Exploring Ultrafast Electron Motion inside an Atom. *Phys. Rev. Lett.* **96**, 073004 (2006).
15. Remacle, F. & Levine, R. D. An electronic time scale in chemistry. *PNAS* **103**, 6793-6798 (2006).
16. Smirnova, O. *et al.* High harmonic interferometry of multi-electron dynamics in molecules. *Nature* **460**, 972-977 (2009).
17. Smirnova, O. Patchkovskii, S., Mairesse, Y., Dudovich, N. & Ivanov, M. Yu Strong-field control and spectroscopy of attosecond electron-hole dynamics in molecules. *PNAS USA* **106**, 16556-16561 (2009).
18. Schafer, K. J., Yang, B., DiMauro, L. F. & Kulander K. C. Above threshold ionization beyond the high harmonic cutoff. *Phys. Rev. Lett.* **70**, 1599-1602 (1993).
19. Corkum, P. B. Plasma perspective on strong field multiphoton ionization. *Phys. Rev. Lett.* **71**, 1994-1997 (1993).
20. Krausz, F. & Ivanov M. Yu. Attosecond physics. *Rev. Mod. Phys.* **81**, 163-245 (2009).
21. Baker S. *et al.* Dynamic two-center interference in high-order harmonic generation from molecules with attosecond nuclear motion. *Phys. Rev. Lett.* **101**, 053901 (2008).
22. Li, W. *et al.*, Time-resolved dynamics in N_2O_4 probed using high harmonic generation. *Science* **322**, 1207-1211 (2008).
23. Boutu, W. *et al.* Coherent control of attosecond emission from aligned molecules. *Nature Phys.* **4**, 545-549 (2008).
24. Lein, M. Molecular imaging using recolliding electrons. *J. Phys. B* **40**, R135-R173 (2007).
25. Kanai, T., Minemoto, S. & Sakai, H. Quantum interference during high-order harmonic generation from aligned molecules. *Nature* **435**, 470 474 (2005).

26. Vozzi, C. *et al.* Controlling two-center interference in molecular high harmonic generation. *Phys. Rev. Lett.* **95**, 153902 (2005).
27. Wagner, N. *et al*. Extracting the phase of high-order harmonic emission from a molecule using transient alignment in mixed samples. *Phys. Rev. A* **73**, 061403 (2007).
28. Itatani, J. *et al.* Tomographic imaging of molecular orbitals. *Nature* **432**, 867-871 (2004).
29. Schwarz, W. H. E. Measuring Orbitals: Provocation or Reality? *Angewandte Chemie* **45**, 1508-1517 (2006).
30. Walters, Z. B., Tonzani, S. & Greene, C. H. Limits of the plane wave approximation in the measurement of molecular properties. *J. Phys. Chem.* **112** 9439-9447 (2008).
31. van der Zwan, E., Chirila, C. C. & Lein, M. Molecular orbital tomography using short laser pulses. *Phys. Rev. A* **78**, 033410 (2008).
32. Le, V.-H., Le, A.-T., Xie, R.-H. & Lin, C. D. Theoretical analysis of dynamic chemical imaging with lasers using high-order harmonic generation. *Phys. Rev. A* **76** 013413 (2007).
33. Torres, R. & Marangos, J. P. Mapping of orbital structure from high harmonic generation through the molecular dipole moment. *J. Mod. Opt.* **54**, 1883-1899 (2007).
34. Gibson, G. N. & Biegert, J. Influence of orbital symmetry on high-order-harmonic generation and quantum tomography. *Phys. Rev. A* **78**, 033423 (2008).
35. McFarland, B. K., Farrell, J. P., Bucksbaum, P. H. & Gühr, M. High harmonic generation from multiple orbitals in N_2. *Science* **322**, 1232-1235 (2008).
36. Lewenstein, M., Balcou, Ph., Ivanov, M. Yu, L'Huillier, A. & Corkum, P. B. Theory of high harmonic generation by low-frequency laser fields. *Phys. Rev. A* **49**, 2117-2132 (1994).
37. Bransden, B. H. & Joachain, C. J. *Physics of Atoms and Molecules* (Pearson Education, Harlow, 2003).
38. Lofthus, A. & Krupenie, P.H. Spectrum of molecular nitrogen. *J. Phys. Chem. Ref. Data* **6**, 113-307 (1977).
39. Tong, X. M., Zhao, Z. X. & Lin, C. D. Theory of molecular tunneling ionization. *Phys. Rev. A* **66**, 033402 (2002).
40. Pavicic, D., Lee, K., Rayner, D. M., Corkum, P. B. & Villeneuve, D. M. Direct Measurement of the Angular Dependence of Ionization for N_2, O_2, and CO_2 in Intense Laser Fields. *Phys. Rev. Lett.* **98**, 243001 (2007).
41. Kanai, T., Takahashi, E. J., Nabekawa, Y. & Midorikawa, K. Destructive interference during high harmonic generation in mixed gases. *Phys. Rev. Lett.* **98**, 153904 (2007).
42. Le, A.T., Lucchese, R. R., Tonzani, S., Morishita, T. & Lin C. D. Quantitative rescattering theory for high-order harmonic generation from molecules. *Phys. Rev. A* **80**, 013401 (2009).
43. Shafir, D., Mairesse, Y., Villeneuve, D. M., Corkum, P. B. & Dudovitch, N. Atomic wavefunctions probed through strong-field light–matter interaction. *Nature Phys.* **5**, 412-416 (2009).
44. Mairesse, Y. *et al*. Electron wavepacket control with elliptically polarized laser light in high harmonic generation from aligned molecules. *New J. Phys.* **10,** 025015 (2008).
45. Schmidt, M. W. *et al.* General atomic and molecular electronic-structure system. *J. Comput. Chem.* **14**, 1347- 1363 (1993).
46. Smirnova, O. A., Moritzen, S., Patchkovskii, S. & Ivanov, M. Yu. Coulomb–laser coupling in laser-assisted photoionization and molecular tomography *J. Phys. B* **40**, F197-F206 (2007).
47. Jordan, G. & Scrinzi, A. Core-polarization effects in molecular high harmonic generation. *New J. Phys.* **10**, 025035 (2008).
48. Patchkovskii, S., Zhao, Z., Brabec, T. & Villeneuve, D. M. High Harmonic Generation and Molecular Orbital Tomography in Multielectron Systems: Beyond the Single Active Electron Approximation. *Phys. Rev. Lett.* **97**, 123003 (2006).
49. Santra, R. & Gordon, A. Three-Step Model for High-Harmonic Generation in Many-Electron Systems. *Phys. Rev. Lett.* **96**, 073906 (2006).
50. Balcou, P., Salières, P., L'Huillier, A. & Lewenstein, M. Generalized phase-matching conditions for high harmonics: The role of field-gradient forces. *Phys. Rev. A* **55**, 3204-3210 (1997).

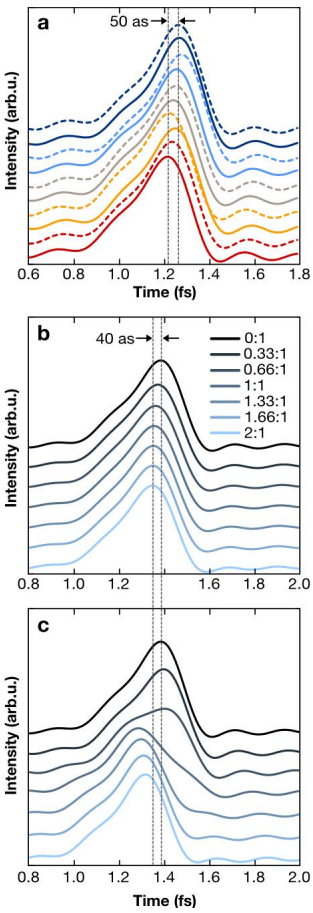

Figure 1. Attosecond emission of aligned N_2 molecules. (**a**): Temporal intensity profile of an average pulse in the attosecond pulse train emitted by N_2 molecules aligned at angles θ=0° to 90°, reconstructed from a series of RABITT measurements, taking into account harmonics 17 to 27. Line colours correspond to alignment angles as indicated in Fig. 2. Relative timing calibration was ensured by setting the group delay for the lowest harmonic (H17) to the same value for all angles (see Supplementary Information). The observed evolution thus results from the phase variations within the considered spectral range. While close to our experimental sensitivity limit (±20 as for the pulse peak positions, see Supplementary Information), the 50-as shift is reliable in view of its regular, almost monotonic (except for the fluctuation at θ = 60°) evolution in the 10 independent measurements. (**b, c**) Simulated intensity profiles resulting from a coherent superposition of two contributions whose relative weight ($|a_2|$:$|a_1|$) is varied from 0:1 to 2:1 for all harmonics 17 to 27. The continuum spectral phases are computed as in Fig. 3a. For the spectral amplitudes (not a sensitive parameter), we used an experimental spectrum (N_2 at θ=0°) for all curves. In (**b**), $\Delta\phi_r = \pi/2$ is taken into account by correspondingly shifting the spectral phase for the HOMO contribution, whereas this additional phase is omitted in (**c**). The ≈150 as overall time-shift between the measured (**a**) and simulated (**b**) pulse profiles is presumably due to macroscopic effects (dispersion during propagation), not accounted for in our simulations.

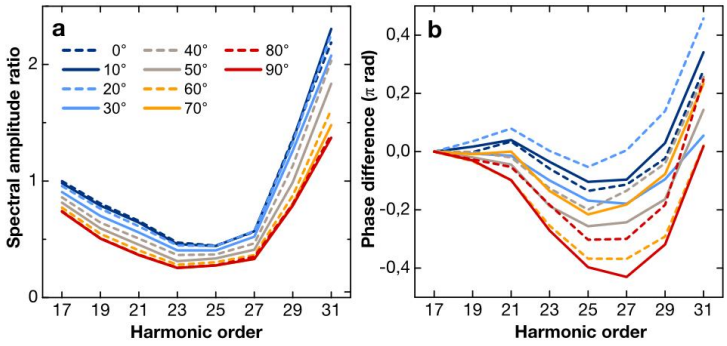

Figure 2. Experimental recombination dipole for N_2 molecules. (**a**): Amplitude and (**b**) phase of the complex XUV field for N_2 at various alignment angles normalized by that for argon. For perpendicular alignment (θ = 90°), the phase decreases by $\pi/2$ between harmonic 17 and 27. This jump gradually disappears when rotating the molecules towards parallel alignment (θ = 0°). For all angles, the phase increases by $\pi/2$ from harmonic 27 on, which might be the beginning of a larger jump not completely contained in our spectral range. The phase difference is set to 0 at the lowest harmonic order 17; see Supplementary Information for details on the data analysis.

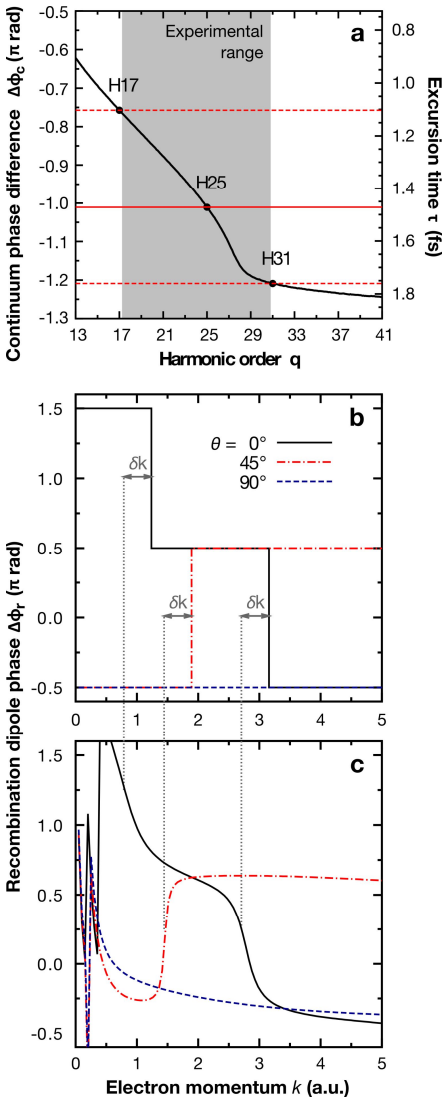

Figure 3. Phase of the harmonic emission. (**a**): Continuum phase difference $\Delta\phi_c(q\omega_L)$ computed within SFA for an 800 nm laser field with intensity $1.2\cdot10^{14}$ Wcm^{-2} and binding energies ε_1=-15.58 eV and ε_2=-17.00 eV, corresponding to the HOMO and HOMO-1 contributions (short trajectories are considered). Horizontal lines indicate the phase differences and excursion times for the first (H17), middle (H25) and last (H31) harmonics of the experimental range (grey area). (**b**, **c**): Phases of the HOMO recombination dipole computed with Coulomb-waves, at 3 different orientations θ, vs. electron momentum k. For computational purposes, the orbital was expressed as a combination of single-center Slater functions. Two values of the effective charge are considered for the Coulomb waves: (**b**) $Z^* = 0$, corresponding to plane waves, and (**c**) $Z^* = 1$, corresponding to the asymptotic charge of N_2^+. For k>0.5 a.u., both series of curves show similar patterns, up to a k-dependent global phase shift and a translation $\delta k\approx0.4$ a.u. on the momentum scale. For k<0.5 a.u., the fast oscillations in (**c**) are a direct imprint left by the Coulomb-waves, as can be seen from their partial wave-expansion[37], where each angular momentum l contributes with a phase $\eta_l(Z^*,k) = \arg[\Gamma(l+1+iZ^*/k)]$.

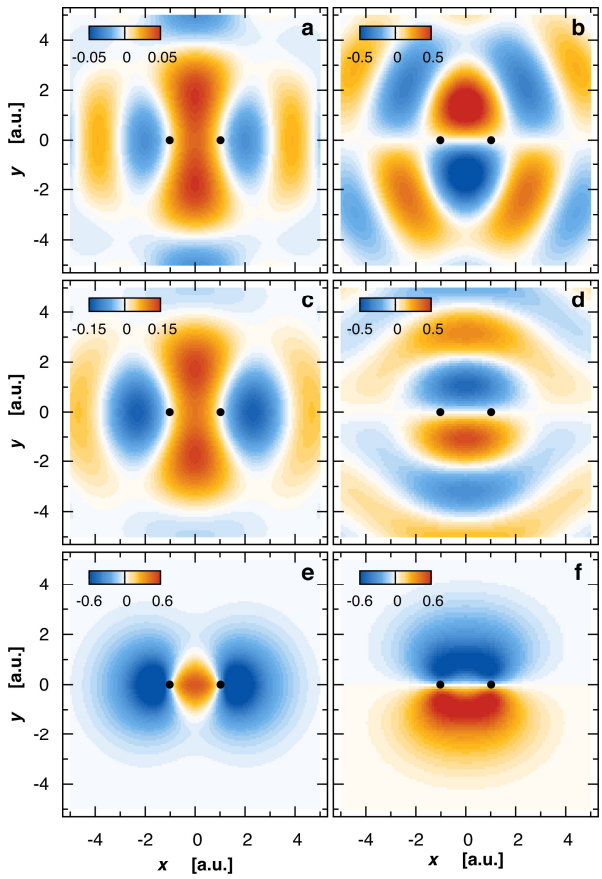

Figure 4. Orbital tomographic reconstructions. (**a**): from the imaginary part of the experimental dipole imposing σ_g-symmetry; (**b**) : from the real part of the experimental dipole imposing π_u-symmetry; (**c**) : simulated reconstruction with the HOMO PW-dipole; (**d**) : simulated reconstruction with the HOMO-1 PW-dipole. For the sake of comparison, simulations were done with the experimental sampling (harmonics and angles, see Fig. 2), using the dispersion relation $k_q^2/2 = q\omega_L$, and by restricting the theoretical dipole to its component along the laser polarization. Black dots indicate the nuclei position at equilibrium distance. Reconstructions in (**b,d**), are based on the `velocity-form' of the dipole to avoid division by x/y in real space and thus numerical problems with the orbital nodes at y=0. (**e**): Hartree-Fock HOMO and (**f**): HOMO-1, calculated with GAMESS[45].

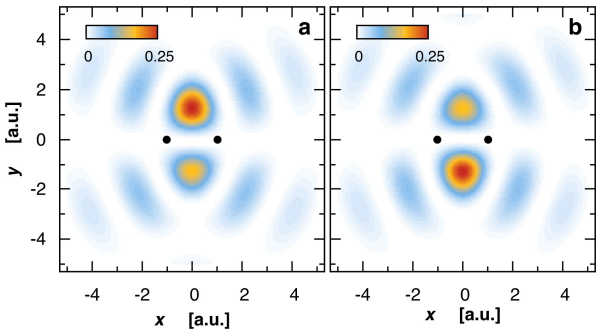

Figure 5. Reconstructions of the dynamic hole. (**a**): Squared sum and (**b**): squared difference of the wavefunctions shown in Figure 4a,b. These can be interpreted as the hole-density in the ion at the recollision / tunnel-ionization instants (see text) for a relative weight of the HOMO:HOMO-1 contributions corresponding to the relative amplitudes of the wavefunctions in Figure 4a,b. Although we have access to *wave-packets*, we plot the corresponding densities so as to visually emphasize their asymmetries.

Supplementary Information to the article "Attosecond imaging of molecular electronic wave-packets"

Experimental setup

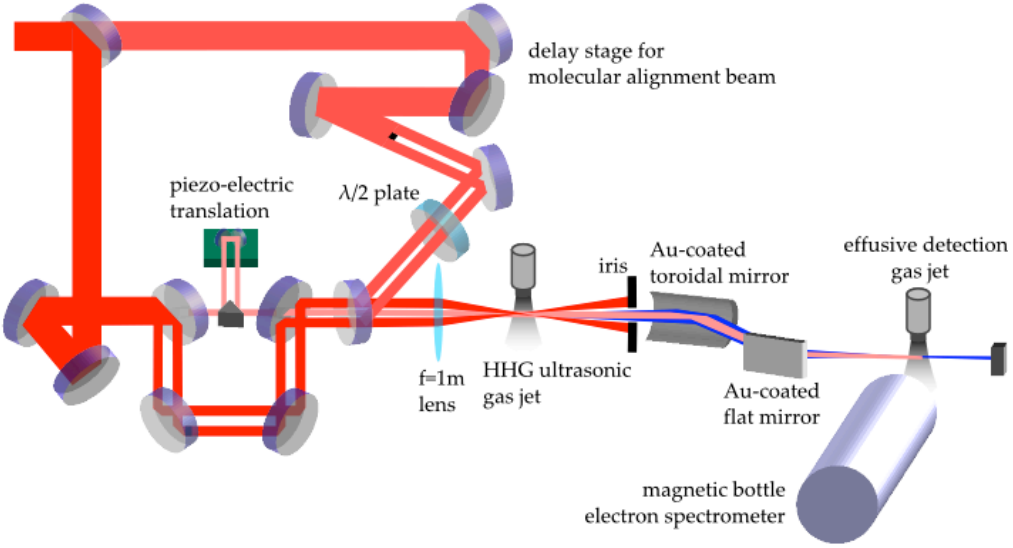

Supplementary Figure 1: **Schematic of the experimental setup.** The laser beam enters at the upper left of the scheme. The part transmitted through the first beam splitter is the beam producing nonadiabatic alignment[1] of the molecules in the HHG gas jet. In the lower left part of the figure, the drilled mirror based interferometer for the RABITT measurement is depicted. Here, the large annular beam is the harmonic generating beam, whereas the small central part is the probe beam for RABITT. From the focusing lens on, the setup is placed under vacuum.

The RABITT method

We detect the harmonic emission with photon energies larger than I_p^{Ne} = 21.6 eV by photoionizing neon atoms and detecting the released photoelectrons with a magnetic bottle electron spectrometer. Intensity spectra, corrected for the energy-dependent ionization cross-section of neon, readily yield the XUV spectral intensities.

The spectral phase $\varphi(\omega)$ of the harmonics is measured with the RABITT technique[2-5]. It is based on the analysis of sidebands, created in the photoelectron spectrum by absorption of one harmonic photon and simultaneous absorption or stimulated emission of one infrared (IR) photon from a weak probe beam, which is also present in the detection volume. This probe beam having the same frequency ω_L as the generating beam, this leads to the interference of two quantum paths "absorption of harmonic q and absorption of 1 IR photon" and "absorption of harmonic q+2 and stimulated emission of 1 IR photon" at the same photoelectron energy, $(q+1)\omega_L - I_p^{Ne}$. Varying the phase of the IR probe field by varying its delay τ relative to the generating beam and thus the harmonic beam leads to a modulation of the sideband intensity $S_{q+1}(\tau)$ as

$$S_{q+1}(\tau) \propto \cos(2\omega_L\tau + \varphi_{q+2} - \varphi_q - \Delta\phi^{at}), \quad \text{(S1)}$$

where φ_{q+2} and φ_q are the spectral phases of harmonics q+2 and q, respectively, and $\Delta\phi^{at}$ is a small phase correction, characteristic of the target gas, which can be calculated for rare gas atoms[3,4].

Extracting the phase of the oscillating sidebands via a Fourier transform thus yields the relative phase of neighbouring harmonic orders q and $q+2$, and thus the group delay, also called emission time

$$t_e(q+1) = (\partial\varphi/\partial\omega)|_{q+1} \approx (\varphi_{q+2} - \varphi_q)/(2\omega_L). \quad \text{(S2)}$$

The RABITT method can be complemented by using the interference of the probe beam with the generating beam in the HHG medium, that leads to a small modulation of the total harmonic yield $\propto \cos(\omega_L\tau + \alpha_0)$. The phase of this modulation serves as a reference for the sideband phases in our measurements[3,6] leading to the determination of a 'time reference' for the group delay values, modulo π/ω_L, on a scale where t=0 is located at an extremum of the generating IR field.
The experimental observable is thus the derivative of the spectral phase $\varphi(\omega)$ with respect to frequency and $\varphi(\omega)$ is obtained by concatenating the measured relative phases. The spectral phase is thus determined up to an integration constant φ_0.

Details on the phase data analysis

In a series of RABITT scans where the molecule alignment angle is varied and experimental conditions otherwise remain the same, the 'time reference' fluctuates over a narrow range (typically ±50 as), see Supplementary Fig. 2a. For instance, at 30° and 80°, almost all group delays are shifted downwards, indicating a modification of the 'time reference'. We have never observed a *systematic* shift of the 'time reference' with the angle: in another series of measurements, such shifts occur at different angles. Therefore, the observed shifts are probably a measurement error rather than a real single-molecule effect. Albeit being small, these fluctuations induce rather large errors in the integration performed to obtain the spectral phases. This is the reason why we usually remove them.
To this end, we choose a sideband order where we suppose that the group delay does not vary with the angle – in general the lowest order: sideband 16 – and normalize all curves in the series to the average value for this sideband. The chosen value for the 'time reference' is thus not arbitrary but an average over random fluctuations. The result is shown in Supplementary Fig. 2b. These data are then integrated to obtain the spectral phases for each alignment angle. Note that the same integration constant is used for all angles.
For the argon reference scan (shown in the Supplementary Fig. 3), it turns out that the group delay at sideband 16 is almost the *same* (+2.7 as) as the average value for sideband 16 obtained from the different N_2 curves. In the integration of the group delay to obtain the spectra phase, the integration constant is set to the same value as in N_2.

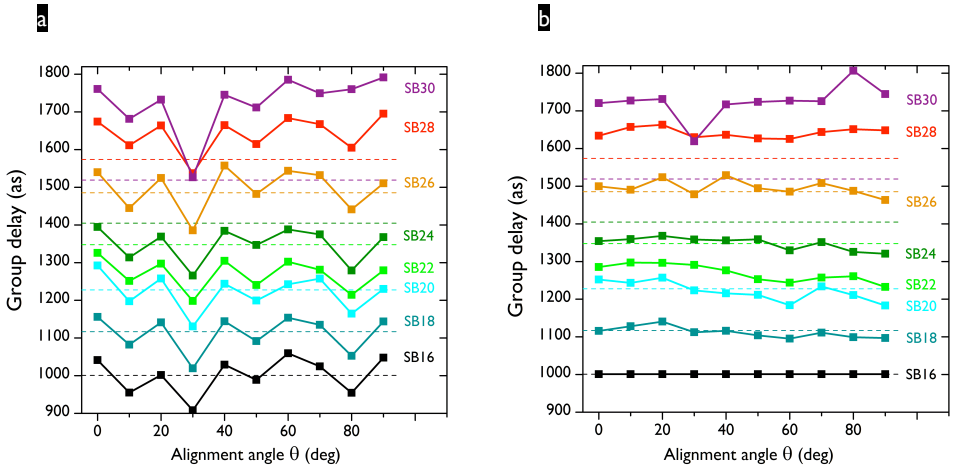

Supplementary Figure 2: **Fluctuation of the 'time reference' for the group delays.** In both panels, dashed lines mark the group delays measured for the argon reference, with the line colors corresponding to the sideband order. (a) 'Raw' group delays extracted for each sideband in a series of RABITT scans for N_2 for alignment angles from 0° to 90°. Clearly, the dominating variation of the group delay with angle is irregular and reproduced by every sideband. It is due to fluctuations of the 'time reference'. (b) Group delays after the values for each individual angle were shifted such that the group delay at sideband 16 is the same and equal to the average value of the fluctuating data. Integrating these data (i.e. concatenating the group delays of subsequent sidebands for each individual alignment angle) yields the spectral phases for nitrogen at the individual alignment angles and for the argon reference. The *difference* between the two is then the sought-for dipole phase, shown in Fig. 2b of the main paper.

In summary: (i) the recombination dipole phase, obtained as the *difference* between the spectral phases for the molecule and the reference atom, is *set to* to zero at harmonic 15 for all angles (by always using the same integration constant). (ii) The linear slope beween harmonics 15 and 17 of the recombination dipole phase is also *set to* zero for all alignment angles (by setting the same group delay at sideband 16 for all scans).

Point (i) concerns two issues. First, it contains the 'absolute' phase difference between the H15 emissions from N2 and argon as a function of alignment angle. In our experiments, we do not measure it but it could be accessed through the gas mixing method[7-9]. We assume an angle-independent H15 phase, which is supported by recent interferometric experiments[10] demonstrating a very weak angular dependence of the phase of low harmonics in N_2. Second, it also implicitly includes any constant phase such as the theoretical correction $-\delta\phi_r$, which removes the scattering phase shift and allows a plane-wave tomographic reconstruction. Since the latter correction is not known, the H15 phase difference is an adjustable parameter which is chosen in order to get the most consistent tomographic reconstructions. Obviously, a global phase shift transfers amplitude from the real to the imaginary part and vice versa, i.e. if it has the 'wrong' value, the separation into HOMO and HOMO-1 is lost.

In point (ii), we decide to dismiss the 'angle-dependent time reference' information that can in principle be extracted from RABITT measurements, because we are convinced that in our data, this information is dominated by noise. Note that the group delay variation is obtained from the interference of two-photon transitions *in the detection gas*, visible on the sidebands (see paragraph 'The RABITT method'), whereas the 'time reference' is obtained from the interference of the IR generating and probe beams *in the HHG medium* – so the two pieces of information really stem from different processes occuring at different parts of the setup. Setting the *same* 'time reference' for all angles due to the limited precision of its measurement simply means that we neglect a possible (small) angle-dependent linear component of the dipole phase.

The phases resulting from the above procedure is shown in Fig. 2b) and used for the reconstructions presented in Fig. 4.

Intensity calibration

The effective harmonic generation intensity for the measurements reported here is determined via both the experimentally observed cut-off position and the 'attochirp', i.e. the slope of the measured group delay vs. harmonic order. For rare gas atoms, it has been shown that the harmonic group delay, also called emission time, agrees with recombination instants calculated with the SFA model[3]. The slope of

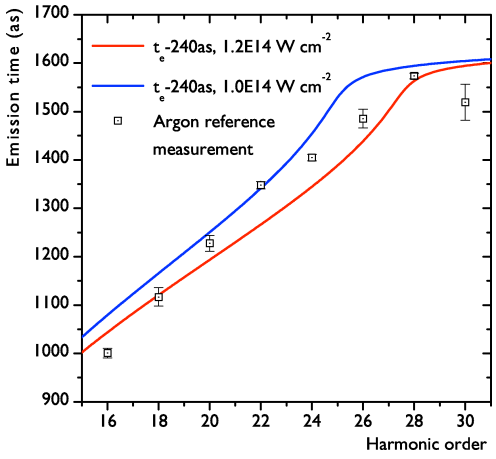

Supplementary Figure 3: **Determination of the effective experimental intensity.** The red and blue lines show recombination times for argon (I_p=15.76 eV), calculated by solving the saddle-point equations of the SFA model for an intensity of $1.2 \cdot 10^{14}$ W cm^{-2} and $1.0 \cdot 10^{14}$ W cm^{-2}, respectively. Only the points for the short trajectory contribution are shown. They have been shifted by -240 as in order to facilitate direct comparison with the experimental group delay of the argon reference measurement (squares), used for the study presented in this paper.

the calculated recombination times is inversely proportional to the generating laser intensity. Comparing to the measured emission times thus allows determining the effective generation intensity in the experiment. Supplementary Figure 3 shows such a comparison with the argon reference measurement used in the study reported here. The spectral position where the emission time saturates marks the cut-off position and agrees best with a calculation for $1.2 \cdot 10^{14}$ W cm^{-2}. The mean slope of the experimental emission time falls between the simulations for $1.2 \cdot 10^{14}$ W cm^{-2} and $1.0 \cdot 10^{14}$ W cm^{-2}. Had we used the smaller intensity for the calculations discussed in this paper, the conclusions would have been the same. Notably, the harmonic order where the continuum-phase difference $\Delta\phi_c$ takes the value of $-\pi$ (cf. Fig. 3a of the main paper), would only shift from 25 to 23 in this case. A calculation analogous to that shown in Fig. 1b of the main paper would give a shift of -50 as of the attosecond pulse peak when varying the HOMO-1:HOMO ratio of the contributions to HHG from 0:1 to 2:1.

Error estimation for the attosecond pulse timing

The error bar for individual group delay measurements is given by the standard deviation of the phase within the FWHM of the $2\omega_0$ peak in the RABITT trace Fourier transform. This error amounts to typically ±30 as (see, e.g., Supplementary Figure 3). This value gives an upper limit for the fluctuations of the attosecond pulse peak position due to experimental uncertainties. Another way of testing the reliability of the temporal shift shown in Fig. 1a of the main paper is to perform a statistical study of the pulse peak positions obtained with several measurements under same conditions. The result is shown in Supplementary Figure 4. In panel a, we show the pulse peak positions obtained in two series of RABITT scans for alignment angles θ from 0° to 90° in steps of 10° under same experimental conditions (i.e. gas pressure, pulse energies and focusing conditions), but independent from another on different days. For each point, the group delay for H17 was normalized to the same value. The two series show the same trend, as confirmed by the linear fits, which are almost parallel. The smooth, almost monotonic shift is thus reproduced in a second data acquisition run. The data used in the main paper is the one represented by the diamonds in Supplementary Figure 4a. The small offset between the two series may be due to a small difference of the effective HHG driving laser intensity.
To improve statistics somewhat, we average in Supplementary Figure 4b the pulse peak positions from these two series and several other measurements done for $\theta = 0°$ and $\theta = 90°$. All these data have been obtained under equal experimental conditions (i.e. gas pressure, pulse energies and focusing conditions), but independent from each other on different days. The error bars attributed to the averaged pulse peak positions indicate the range over which the averaged values fluctuate.
Including more measurements in the analysis, the value of the temporal shift between $\theta = 0°$ and

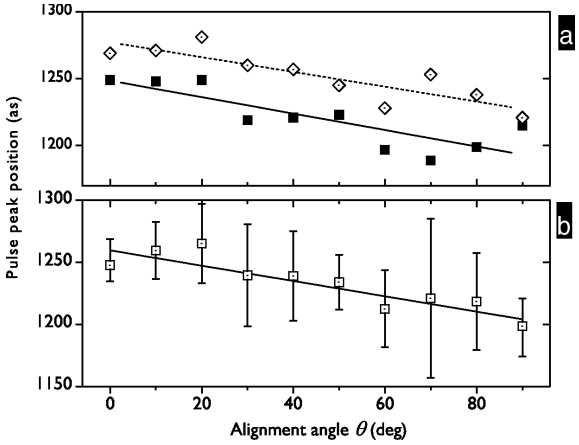

Supplementary Figure 4: **Error estimation for the attosecond pulse peak position.** (**a**) Two independent series of RABITT scans with 10° steps in θ show the same trend, confirmed by the linear fits that are almost parallel. (**b**) Averaging these two series as well as other scans for $\theta = 0°$ and $\theta = 90°$ obtained under same conditions confirms the shift between the attosecond emission for $\theta = 0°$ and $\theta = 90°$, and its significance compared to the timing fluctuations due to experimental uncertainties.

θ = 90° remains -50 as, with error bars of ±20 as on each point. For the intermediate angles, the error is essentially given by the offset between the two series shown in panel a.

Influence of the Cooper minimum on the argon reference

Using argon as a reference in order to calibrate the re-colliding wavepacket complex amplitude becomes questionable in the region of the Cooper-minimum[11,12]. In HHG, this leads to a minimum of the spectral intensity at a photon energy of 51 eV as well as a (theoretically predicted) phase variation of 2.6 rad over a width of 20 eV around this position[13]. For a 795 nm laser, this leads to the spectral minimum appearing at H33 and the phase variation would spread from H27 to H39. This corresponds to an average variation of 0.4 rad between two odd harmonic orders, and thus a group delay shift of 0.4 rad / $2\omega_L$= 90 as.

In our argon reference scan, the last group delay value, measured for SB30, is indeed ≈80 as lower than the previous point instead of saturating as expected from the SFA result (see Supplementary Figure 2). This variation is reproduced in other measurements done with argon on the same day, i.e. under (as close as possible) equal conditions, without, however appearing systematically. We thus consider it as a variation linked to the precise experimental conditions rather than due to a phase jump linked to the Cooper minimum. Data taken with the same laser and a similar setup as used for our experiments show that no significant deviation of the group delay measured for argon from the SFA calculation is observed up to[14] SB32.

If there is a signature of the Cooper minimum in our argon reference data, then it only appears on the very last harmonic order, H31. It may thus amplify the increase of the amplitude ratio (Fig. 2a of the main paper) as well as the increase of the phase difference (Fig. 2b of the main paper). However, it cannot explain the qualitative features discussed in our paper.

Phase difference, $\Delta\phi_c$, accumulated during the continuum excursion

The quantum paths contributing to HHG are associated with an accumulated phase given by the action along the path[3]

$$S([t_i, t_r, \vec{p}]) = q\omega_L t_r - \int_{t_i}^{t_r} \left[\frac{(\vec{p} + \vec{A}(t'))^2}{2} - \varepsilon \right] dt' , \tag{S3}$$

where t_i and t_r are the instants of ionization and recombination, respectively, $\vec{p}$ is the electron drift momentum, $\vec{A}(t')$ is the vector potential of the driving laser field and ε is the bound state energy (e.g. for the HOMO, $\varepsilon = -I_p$).

An infinite number of quantum paths contribute to the emission of each harmonic order. However, in the strong field regime[15], only a few closed quantum paths with stationary phase dominate, meaning that they satisfy $\delta S([t_i, t_r, \vec{p}]) = 0$. We only consider the quantum paths with the shortest electron excursion times $\tau = (t_r - t_i)$ (i.e. the `short' trajectories dominating our experimental signal), thus associating each harmonic frequency $q\omega_L$ with a single quantum path. Varying ε, the phase for this quantum path changes by (for $\Delta\varepsilon$ small against $p^2/2$):

$$\Delta\phi_c(\omega) = \left.\frac{dS}{d\varepsilon}\right|_{\omega=\text{const.}} \Delta\varepsilon = \left[(t_r - t_i) + \underbrace{\frac{\partial S}{\partial t_r}}_{=0} \frac{\partial t_r}{\partial \varepsilon} + \underbrace{\frac{\partial S}{\partial t_i}}_{=0} \frac{\partial t_i}{\partial \varepsilon} + \underbrace{\frac{\partial S}{\partial p}}_{=0} \frac{\partial p}{\partial \varepsilon} \right] \Delta\varepsilon = \Delta\varepsilon\tau . \tag{S4}$$

Gauge dependence of orbital tomography

The recombination dipole, for a single orbital ψ of energy ε, reads in the length and velocity form respectively:

$$\vec{d}_{len}(\vec{k}) = \int [\psi(\vec{r})]^* \, \vec{r} \, e^{i\vec{k}\cdot\vec{r}} \, d\vec{r} \tag{S5}$$

$$\vec{d}_{vel}(\vec{k}) = \frac{i\vec{k}}{\frac{k^2}{2} - \varepsilon} \int [\psi(\vec{r})]^* \, e^{i\vec{k}\cdot\vec{r}} \, d\vec{r} \tag{S6}$$

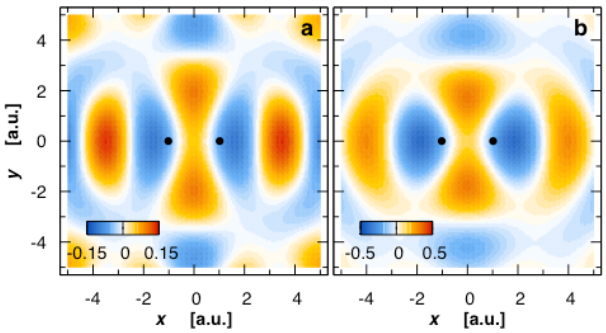

Supplementary Figure 5: **Tomography in the velocity gauge.** (**a**) Experimental and (**b**) simulated reconstructions of the HOMO in the velocity gauge. The agreement is less satisfactory than in the length gauge (Fig. 4a,c).

Expressions (1) and (2) in the main text make use of the former. Both forms would be rigorously equal if plane waves were molecular scattering eigenstates. This is however not the case, which makes the tomographic procedure gauge dependent. When confronting the experimental and simulated reconstructions for the HOMO in the length gauge (Fig 4a,c) on the one hand, and in the velocity gauge (Supplementary Fig 5a,b) on the other hand, it is noticeable that the length gauge is more suited to our study, confirming previous predictions[16].

Imaginary part of the experimental reconstructions

Imposing a σ_g (respectively π_u) symmetry to both real and imaginary parts of the experimental dipole transfers the inappropriate HOMO-1 (respectively HOMO) contribution into the *imaginary* part of the reconstructed orbital. We show in Supplementary Figure 6a the imaginary part associated with the experimental real-valued HOMO reconstruction (Fig. 4a in the main text). It has to be compared to the imaginary-valued simulated reconstruction obtained by computing the *HOMO-1* dipole from 0° to 90° and extrapolating it up to 360° enforcing the *HOMO* symmetry (Supplementary Figure 6b). Despite being *a priori* unphysical, these reconstructions, when compared to each other, confirm the analysis and interpretation of our experimental data.

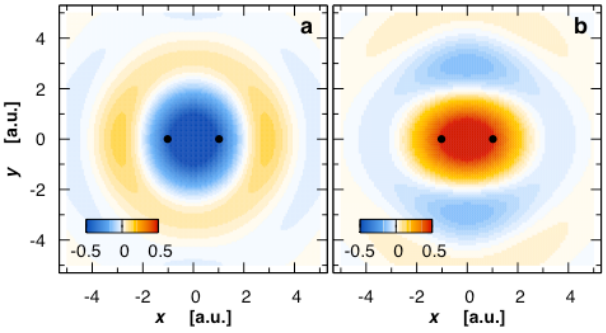

Supplementary Figure 6: Spurious contributions to the reconstructions. (a) Imaginary part of the experimental reconstruction in the HOMO symmetry and (b) imaginary-valued simulated reconstruction from the HOMO-1 dipole with the HOMO symmetry enforced, see text. Both were performed in the length gauge. The difference in sign, also seen in Fig. 4b,d is consistent with the -π phase accumulated by the HOMO-1 contribution in the HHG process (see main text). The agreement between experiment and simulation supports the main conclusions of our work.

Importance of the phase in the reconstructions

In order to emphasize the major role of the dipole *phases* in obtaining correct reconstructions, we have applied the tomographic procedure to the experimental dipole with enforced *constant* phases, which has the consequence to merge the HOMO and HOMO-1 contributions, and to smooth out all structural phase jumps. Supplementary Figure 7 displays the result obtained when enforcing the HOMO symmetry: the signatures characterizing the HOMO, that are present in the correct experimental reconstruction (Fig. 4a in the main text), have now disappeared in favour of the dominating HOMO-1 contribution (displayed alone in Supplementary Figure 6a with the same symmetry).

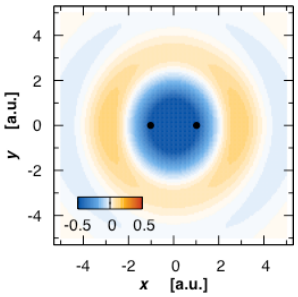

Supplementary Figure 7: **Experimental reconstruction without the phase.** Reconstruction from the experimental dipole with the HOMO symmetry, when enforcing a constant phase over the whole span. The results now contains both HOMO and HOMO-1 contributions, and is dominated by the latter (relative weights can be seen in the color-scales of Fig. 4a,b)

References

1. Rosca-Pruna, F. & Vrakking, M. Experimental Observation of Revival Structures in Picosecond Laser-Induced Alignment of I_2. *Phys. Rev. Lett.* **87**, 153902 (2001).
2. Paul, P.M. *et al.,* Observation of a Train of Attosecond Pulses from High Harmonic Generation *Science* **292**, 1689-1692 (2001).
3. Mairesse, Y. *et al.,* Attosecond Synchronization of High-Harmonic Soft X-rays. *Science* **302**, 1540-1543 (2003).
4. Véniard, V., Taïeb, R. & Maquet, A. Phase dependence of (N+1)-color (N>1) ir-uv photoionization of atoms with higher harmonics. *Phys. Rev. A* **54**, 721-728 (1996).
5. E. S. Toma, E.S. & Muller, H.G. Calculation of matrix elements for mixed extreme-ultraviolet–infrared two-photon above-threshold ionization of argon. *J. Phys. B* **35**, 3435-3442 (2002).
6. Dinu, L.C. *et al.* Measurement of the Subcycle Timing of Attosecond XUV Bursts in High-Harmonic Generation. *Phys. Rev. Lett.* **91**, 063901 (2003).
7. Kanai, T., Takahashi, E. J., Nabekawa, Y. & Midorikawa, K. Destructive interference during high harmonic generation in mixed gases. *Phys. Rev. Lett.* **98**, 153904 (2007).
8. Wagner, N. *et al.* Extracting the phase of high-order harmonic emission from a molecule using transient alignment in mixed samples. *Phys. Rev. A* **73**, 061403 (2007).
9. McFarland, B. *et al.* High-order harmonic phase in molecular nitrogen. *Phys. Rev. A* **80**, 033412 (2009).
10. Bertrand, J., Wörner, H.-J., Villeneuve, D., Corkum, P.B., Molecular frame high harmonic dipole amplitude and phase measurements, F42, *Conference on Attosecond Physics*, Kansas (2009).
11. Cooper, J.W. Photoionization from Outer Atomic Subshells. A Model Study. *Phys. Rev.* **128**, 681-693 (1962).
12. Mauritsson, J., Gaarde, M.B. & Schafer, K.J. Accessing properties of electron wave packets generated by attosecond pulse trains through time-dependent calculations. *Phys. Rev. A* **72**, 013401 (2005).
13. Wörner, H.J., Niikura, H., Bertrand, J., Corkum, P.B. & Villeneuve, D.M. Observation of Electronic Structure Minima in High-Harmonic Generation. *Phys. Rev. Lett.* **102**, 103901 (2009).
14. Mairesse, Y. *et al.* Optimization of Attosecond Pulse Generation. *Phys. Rev. Lett.* **93**, 163901 (2004).
15. Salières, P. *et al.* Feynman's Path-Integral Approach for Intense-Laser-Atom Interactions. *Science* **292**, 902-905 (2001).
16. Xie, X., Jordan, G., Wickenhauser, M. & Scrinzi, A. Time and momentum distributions of rescattering electrons *J. Mod. Opt.* **54**, 999-1010 (2007).

PAPER III

Polarization-resolved pump-probe spectroscopy with high harmonics

Y. Mairesse, S. Haessler, B. Fabre, J. Higuet, W. Boutu, P. Breger, E. Constant, D. Descamps, E. Mével, S. Petit and P. Salières.

New J. Phys. **10**, 025028 (2008).

New Journal of Physics
The open-access journal for physics

Polarization-resolved pump–probe spectroscopy with high harmonics

Y Mairesse[1,3], S Haessler[2], B Fabre[1], J Higuet[1], W Boutu[2], P Breger[2], E Constant[1], D Descamps[1], E Mével[1], S Petit[1] and P Salières[2]

[1] CELIA, Université Bordeaux I, UMR 5107 (CNRS, Bordeaux 1, CEA), 351 Cours de la Libération, 33405 Talence Cedex, France
[2] CEA-Saclay, DSM, Service des Photons, Atomes et Molécules, 91191 Gif-sur-Yvette, France
E-mail: mairesse@celia.u-bordeaux1.fr

New Journal of Physics **10** (2008) 025028 (11pp)
Received 22 October 2007
Published 29 February 2008
Online at http://www.njp.org/
doi:10.1088/1367-2630/10/2/025028

Abstract. High harmonic generation in gases can be used as a probe of the electronic structure of the emitting medium, with attosecond temporal resolution and angström spatial resolution. The prospect of measuring molecular dynamics by pump–probe spectroscopy with such precision is attracting a lot of interest. An important issue in pump–probe spectroscopy lies in the ability to detect small signals: the detected signal can be easily dominated by the contributions from non-excited molecules or from a carrier gas. In this paper, we demonstrate that polarization-resolved pump–probe spectroscopy can be used to overcome this issue. We study high harmonic generation from rotationally excited molecules. We show that by measuring the harmonic field that is generated orthogonally to the driving laser field, the contrast in the detection of alignment revivals in nitrogen can be increased by a factor 4. We use this configuration to measure alignment revivals in an argon–nitrogen mixture, in which the total harmonic signal is dominated by the contributions from argon.

[3] Author to whom any correspondence should be addressed.

© IOP Publishing Ltd and Deutsche Physikalische Gesellschaft

Contents

1. Introduction 2
2. Principle 3
3. Polarization state of high harmonics from aligned nitrogen molecules 5
4. Pump–probe measurements in pure N_2 6
5. Detection of the alignment revival in an Ar–N_2 mixture 9
6. Conclusion 10

Acknowledgments 10

References 10

1. Introduction

High harmonic generation from molecules is a three step process [1, 2]. Firstly, part of the highest occupied molecular orbital (HOMO) tunnels out into the continuum under the influence of the strong laser field. This free electron wavepacket is then accelerated by the field. Lastly, it comes back to the vicinity of the parent ion, where it interferes with the part of the HOMO that remained bound. The interference of the propagating free electron wavepacket and the HOMO leads to an oscillation of the electron density, resulting in the emission of a burst of light. This process is periodic and leads to the generation of a train of attosecond pulses separated by half the driving laser period [3, 4]. A single attosecond pulse can be isolated by using single cycle driving pulses [5, 6] or polarization gating techniques [7, 8].

The spectrum of the emitted light is determined by the two interfering components: the free electron wavepacket and the HOMO. The characteristics of the free electron wavepacket mainly depend on the propagation into the continuum, i.e. on the laser field intensity [9, 10]. The typical de Broglie wavelength of the recolliding electrons is in the angström domain. Thus, the harmonic signal is a very accurate probe of the HOMO. This property was recently used to perform the tomographic reconstruction of the HOMO of N_2 [11]. By extending such measurements to the case of molecular dynamics, it would be possible to follow the evolution of electron wavefunctions in chemical reactions.

Recent experiments have shown that the high harmonic signal could be used to encode rotational [11]–[13] and vibrational [14]–[16] molecular dynamics. The extension to more complex processes such as electronic excitations and photochemical dynamics will face the problem of the contrast in the measurements, especially for high temporal resolutions. In the case of a low cross-section excitation process, the harmonic signal will be dominated by the contributions from non-excited molecules. Furthermore, a carrier gas is often used in experiments and it can also create a strong background signal. In order to extract the contribution of excited molecules from the background, different techniques have been developed and are extensively used in conventional femtosecond pump–probe spectroscopy [17, 18]. One solution is transient grating spectroscopy, which has recently been transposed to high harmonic generation [19]. In the following, we show that polarization-resolved pump–probe spectroscopy can be used to increase the contrast in the detection of the harmonic emission from excited molecules. We consider the particular case of rotational wavepackets, but this technique could be used with any excitation process leading to anisotropy of the generating medium.

IOP Institute of Physics DEUTSCHE PHYSIKALISCHE GESELLSCHAFT

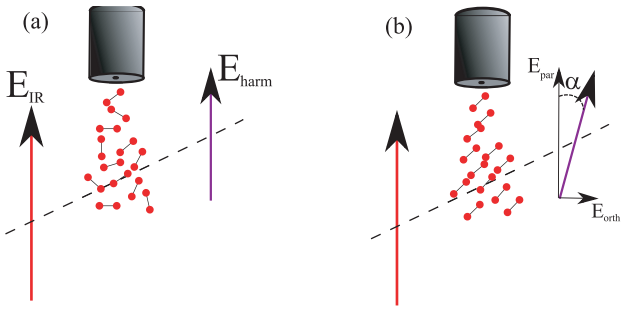

Figure 1. Principle of polarization-resolved pump–probe spectroscopy. When the generating medium is isotropic (a), the high harmonics are polarized parallel to the driving laser field. When anisotropy exists in the medium (b), the polarization of the high harmonics can be rotated with respect to the driving field by an angle α. The orthogonal polarization component is then non-zero.

2. Principle

In this paper, we study rotational excitation of molecular samples with high harmonic generation. Rotational wavepackets can be excited by focusing a femtosecond laser pulse at a few 10^{13} W cm^{-2} in a gas sample [20, 21]. A coherent superposition of rotational states is then populated. The molecular alignment distribution presents a characteristic temporal evolution: the molecules are aligned along the pump-laser polarization every half-rotational period of the considered molecule [22]. Since the harmonic generation process is sensitive to the alignment of the molecule with respect to the laser polarization, revivals of molecular alignment can be probed by monitoring the high harmonic signal produced in the rotationally excited gas sample [11]–[13].

In previous pump–probe studies, the revivals of molecular alignment were detected by measuring the total harmonic intensity. In the following, we show that the contrast can be significantly enhanced by performing polarization-resolved measurements. The principle of our measurement is described in figure 1. In an isotropic medium, the high harmonics generated by a linearly polarized laser pulse are polarized parallel to the laser polarization (figure 1(a)). If anisotropy exists in the medium, for example, a particular molecular alignment, then an orthogonal polarization component can be generated (figure 1(b)). Thus, measuring the orthogonal polarization of the harmonic light provides a sensitive way of probing any anisotropy of the generating medium.

The experiment was performed on two laser systems: the 1 kHz Ti:sapphire AURORE laser facility from CELIA, which provides 35 fs and 9 mJ pulses at 800 nm, and the 20 Hz Ti:sapphire LUCA laser from CEA which delivers 50 fs and 50 mJ pulses. Our experimental set-up is shown in figure 2. A two-arm interferometer splits the incoming laser pulse in two: one part for molecular alignment (pump pulse) and one for harmonic generation (probe pulse). The two pulses can be delayed by a motorized translation stage placed in the probe arm.

A zero-order half waveplate hwp1 (aligning waveplate) is placed in the pump arm, allowing control of the alignment direction of the molecules in the generating medium. A rotation of $\theta/2$ of hwp1 leads to a rotation of θ of the pump polarization axis, i.e. a rotation of θ between the alignment direction of the molecules and the polarization of the probe pulse.

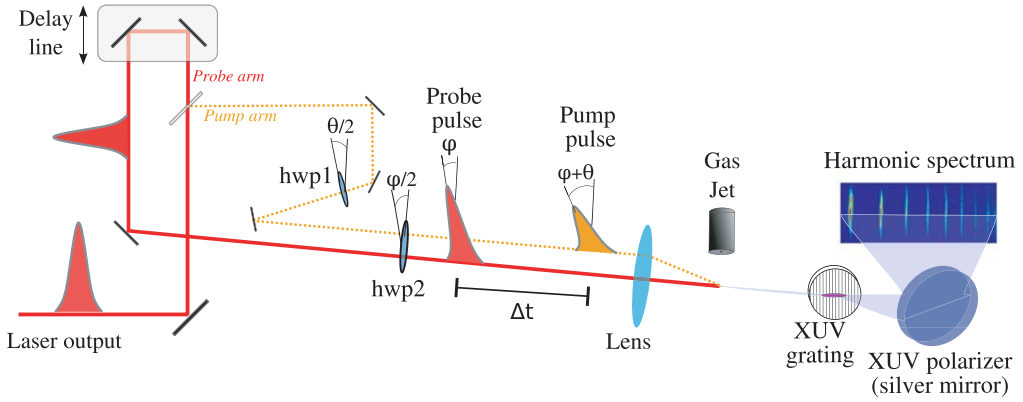

Figure 2. Experimental set-up (see text).

At the output of the interferometer the two beams are parallel and separated by 15 mm. They pass through a second zero-order broadband half waveplate hwp2. This 'analyzing' waveplate is used to rotate the polarization of the two pulses by the same angle φ, which is equivalent to rotating the whole experimental chamber.

The two outcoming beams are then focused by a 500 mm lens into a pulsed gas jet with a backing pressure of 2 bar. The probe beam is on-axis and generates high-order harmonics. The pump beam is tilted by 30 mrad with respect to the axis of the probe beam and thus to the axis of the vacuum chamber. This ensures that the high harmonics that it may generate will not reach the detector.

The harmonic spectrum generated by the probe pulse is measured by an XUV spectrometer consisting of a grazing incidence grating and a set of dual microchannel plates in front of a phosphor screen. The signal emitted by the phosphor screen is recorded by an 8-bit CCD camera. A typical spectrally resolved far field harmonic profile is presented in figure 2, showing harmonics 21–35 generated in N_2.

In order to analyze the polarization of the generated high-order harmonics, we placed a silver mirror with no protective coating at 45° incidence between the grating and the microchannel plates [23]. This silver mirror acts as a polarizer: at this incidence, the ratio between the XUV reflectivity for S ($\varphi = 0°$) and P ($\varphi = 90°$) polarizations, i.e. its extinction ratio, is about 30. This mirror cannot be rotated which justifies the use of hwp2 to change the axis of the detected polarization.

Figure 3 shows the calibration of our polarizer. The harmonic 21 signal generated in argon is monitored as a function of the angle of the analyzing waveplate. The signal follows a $\cos^2(\varphi)$ modulation, characteristic of Malus' law. In the general case of an imperfect polarizer with extinction ratio A and XUV light polarized at an angle α from the probe laser pulse, the measured intensity follows:

$$I = I_0 \left(\cos^2(\varphi - \alpha) + \frac{1}{A} \sin^2(\varphi - \alpha) \right). \quad (1)$$

Here, the generating medium (argon) is isotropic, so that $\alpha = 0°$ (figure 1(a)). A fit of the experimental data allows us to determine the orientations of the analyzing waveplate that

IOP Institute of Physics DEUTSCHE PHYSIKALISCHE GESELLSCHAFT

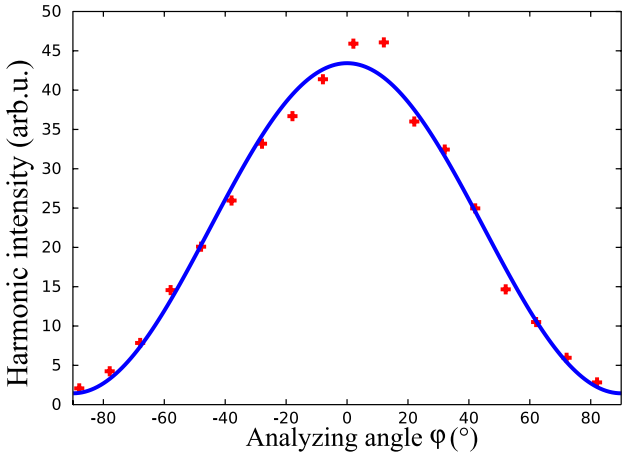

Figure 3. Evolution of the harmonic 21 intensity generated in argon as a function of the orientation of the analyzing waveplate $\varphi/2$. The red crosses are the experimental data points. The blue line is a fit using equation (1) which is used to calibrate the polarizer.

minimize and maximize the signal. They correspond to P and S polarizations, respectively. The measured extinction ratio of our polarizer is about 30 at this wavelength.

3. Polarization state of high harmonics from aligned nitrogen molecules

The polarization state of high harmonics in aligned molecules was recently measured [24], showing that when molecules are not parallel or perpendicular to the driving laser field the direction of the harmonic polarization can be tilted with respect to that of the probe laser. We have repeated these measurements in nitrogen with our experimental set-up.

We set the pump–probe delay to 4.1 ps (close to the half-rotational period of N_2) to maximize the degree of molecular alignment in the gas jet. For a given orientation of the aligning waveplate, we measure the harmonic intensity as a function of the orientation of the analyzing waveplate. A fit of the experimental data (similar to that shown in figure 3) allows us to extract the angle α, i.e. the direction of the harmonic polarization. We repeat this procedure for 15 orientations of the alignment waveplate, from -52.5° to 52.5°, which corresponds to molecular alignments from -105° to 105°

Figure 4 shows a polar plot of the experimental results. The radial dimension is the harmonic order, from 19 to 33. The polar angle is the molecular alignment angle θ with respect to the probe laser field. The colormap encodes the angle α between the harmonic polarization direction and the probe laser polarization. This picture is in qualitative agreement with previous experiments [24], even though the angles between the harmonic and laser polarizations are smaller in our measurements (between -2.5° and 2.5°). A remarkable feature appears when molecules are aligned around 30°: the polarization angle α changes sign from positive (red) to negative (blue) values. Around harmonic 25 the polarization angle is zero, which means that the harmonics are polarized parallel to the probe pulse polarization: the orthogonal component of the harmonic dipole is zero.

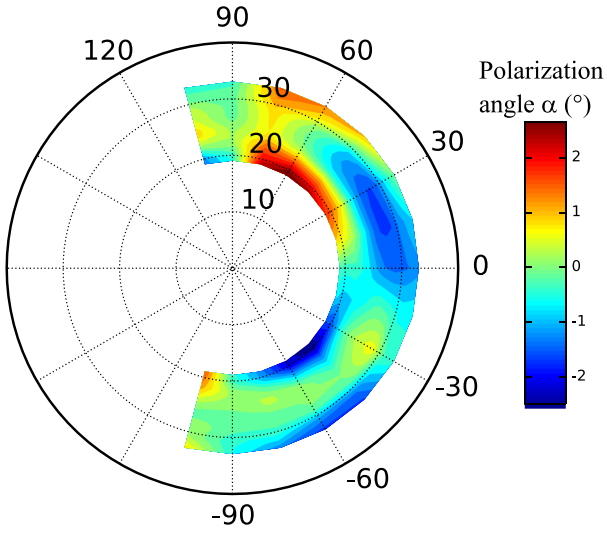

Figure 4. Polarimetry of high harmonic generation in aligned N_2. The colormap shows the angle α between the laser polarization and the harmonic polarization, in degrees. The radial direction is the harmonic order, from 19 to 33. The polar coordinate corresponds to the molecular alignment angle θ with respect to the probe laser field ($\theta = 0^\circ$ is along the horizontal direction).

At intermediate alignment, except around H25, the harmonic dipole has a non-zero orthogonal component. Our polarization resolved measurements are based on the detection of this component. We will focus on the region of the spectrum where the orthogonal component is maximum, i.e. on harmonics 19 and 21. In the case presented in figure 4, the angle α is about 2° and the orthogonal component is very small. This is certainly due to a poor degree of alignment in the experiment. The quality of alignment is very sensitive to the rotational temperature in the gas jet. This temperature can be decreased by adjusting the backing pressure, the nozzle aperture, and the distance between the laser focus and the nozzle. In figure 5, we present the evolution of the harmonic signal detected when $\varphi = 90^\circ$ (referred to as orthogonal signal) as a function of molecular alignment angle θ for harmonic 21, for optimized molecular alignment conditions. The orthogonal signal is maximum when molecules are aligned around 45° from the laser polarization. Therefore, we chose molecular alignments in this range for the polarization-resolved pump–probe spectroscopy. We estimate that in this case the harmonics polarization is around 18° from the laser polarization (the derivation of this value is given in the following section).

4. Pump–probe measurements in pure N_2

In order to illustrate the principle of polarization-resolved spectroscopy, we have performed a pump–probe study of high harmonic generation in rotationally excited nitrogen molecules. The evolution of the molecular alignment distribution around the half revival of N_2 is well known: the molecules are aligned parallel to the pump-laser polarization slightly before the half revival

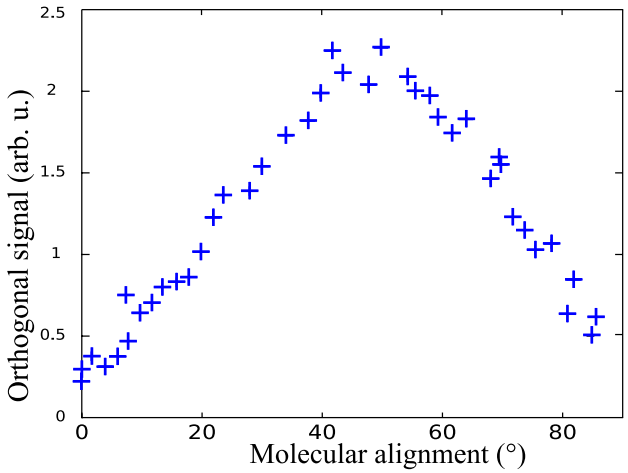

Figure 5. Evolution of the harmonic 21 orthogonal signal ($\varphi = 90^\circ$) as a function of the molecular alignment angle θ.

and anti-aligned slightly after [22]. In addition, the pump pulse induces a slight permanent molecular alignment along its polarization, known as incoherent alignment.

We compare two situations. In what we refer to as the 'conventional situation', the pump and probe pulses have parallel polarization. The analyzing waveplate is set to maximize the reflection on the polarizer (S polarization). This configuration is very close to what would be obtained without any polarizer, since the parallel component of the harmonic field is always dominant. The evolution of the harmonic 21 signal with the pump–probe delay Δt is shown in figure 6(a). The average value of the signal between $\Delta t = 3.4$ ps and $\Delta t = 3.6$ ps is normalized to 1. In this range of delay the molecular alignment distribution is almost isotropic because the permanent alignment is weak at this pump intensity ($\langle \cos^2 \theta \rangle = 0.35$ while it is 0.33 for an isotropic distribution [19, 22]). The harmonic signal is maximum at $\Delta t = 4.1$ ps, when the molecules are aligned parallel to the laser polarization, and minimum at $\Delta t = 4.3$ ps, when the molecules are anti-aligned. The contrast in the detection of the alignment revival, defined as the ratio between the signal off and on the revival, is 2 (which is similar to what has been reported in other experiments).

In the second part of the experiment, we perform polarization-resolved spectroscopy. We rotate the aligning waveplate by 20°, so that the pump-pulse polarization is at 40° to the probe pulse polarization. In this configuration an orthogonal polarization component of the harmonic field can be generated by the molecules that are aligned. In order to detect this orthogonal signal, we rotate the analyzing waveplate by 45° ($\varphi = 90^\circ$) so that the probe pulse is P polarized on the polarizer. The evolution of the harmonic intensity as a function of delay is shown in figure 6(a). The signal is normalized to one away from the revival. Before this normalization, the harmonic intensity is 30 times lower in this configuration than in the conventional configuration. When the molecules are aligned ($\Delta t = 4.1$ ps), the orthogonal polarization of the harmonic field goes through a maximum. The contrast in the detection of the molecular alignment is here 8: the implementation of polarization-resolved spectroscopy allows us to enhance the sensitivity by a factor 4. The contrast is set by the extinction ratio of the polarizer and could be further enhanced by increasing this extinction ratio.

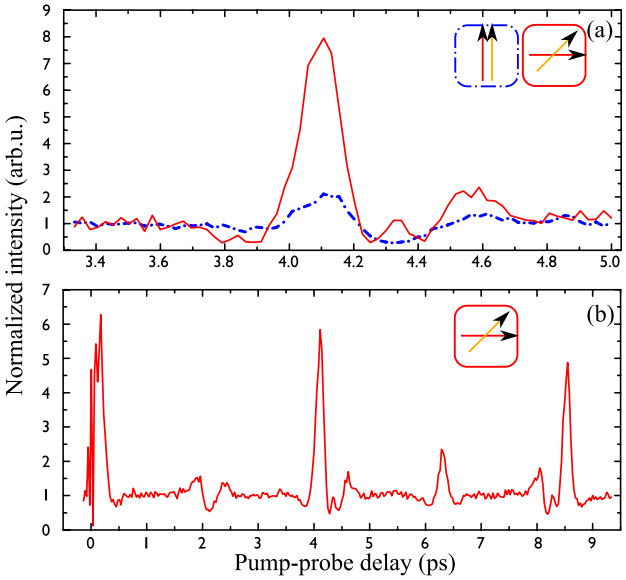

Figure 6. Pump–probe scans in N_2, with a pump intensity of $5 \times 10^{13}\,\mathrm{W\,cm^{-2}}$ and a probe intensity of $1.2 \times 10^{14}\,\mathrm{W \cdot cm^{-2}}$. (a) Evolution of the H21 signal as a function of pump–probe delay in two configurations. Conventional configuration (blue): the pump and probe pulse polarizations are parallel and the analyzing waveplate is rotated to maximize the reflection on the polarizer (S polarization). Polarization-resolved spectroscopy (red): the pump-pulse polarization is rotated by 40° with respect to the probe. The analyzing waveplate is rotated so that the probe pulse is P polarized on the polarizer. (b) Evolution of the H19 intensity as a function of pump–probe delay over a full-rotational period of N_2, in the polarization resolved spectroscopy configuration.

We can estimate the polarization angle α of harmonic 21 at the revival with respect to the probe pulse polarization by deriving the ratio of intensities on and off the revival $C = I_{\mathrm{on}}/I_{\mathrm{off}}$ from Malus' law (equation (1)). Off the revival, $I_{0,\mathrm{off}}$ is normalized to 1 and $\alpha = 0°$, i.e. $I_{\mathrm{off}} = 1/A$. On the revival, we observed in the 'conventional situation' that the total harmonic signal is doubled: $I_{0,\mathrm{on}} = 2$. Hence $C = 2A(\cos^2(90° - \alpha) + \frac{1}{A}\sin^2(90° - \alpha))$, yielding $\alpha \approx 18°$ for $A = 30$ and the observed contrast of $C = 8$.

The orthogonal signal presents a secondary maximum at $\Delta t = 4.3\,\mathrm{ps}$. This delay corresponds to the molecular anti-alignment. The molecules are then contained in a plane perpendicular to the pump-pulse polarization. These molecules can produce harmonic light polarized perpendicular to the probe pulse, which leads to a significant orthogonal harmonic signal.

Figure 6(b) presents a similar measurement for harmonic 19. The delay is, here, scanned over a full-rotational period of nitrogen. The orthogonal harmonic signal is peaked when the molecules are aligned around the full and half revivals. A significant modulation is also measured around quarter revivals, with a contrast that reaches 2 at the 3/4 revival. This shows that polarization-resolved pump–probe spectroscopy provides a sensitive characterization of the rotational wavepacket dynamics.

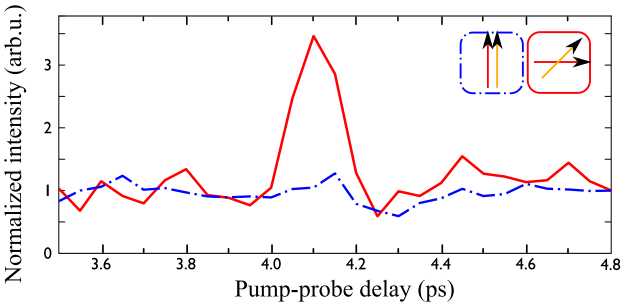

Figure 7. Pump-probe scans for H21 in a 50/50 mixture of argon and nitrogen, around the half revival of N_2. The blue line corresponds to the conventional configuration and the red line to the polarization-resolved configuration.

We have shown that polarization-resolved spectroscopy could be used to increase the contrast in the detection of alignment revivals in nitrogen. Performing complete polarimetric measurements as a function of the pump–probe delay would allow an additional contrast enhancement. Small variations of the polarization angle can be determined with a very high accuracy through the fits with the Malus' law (figure 4). Knowing the total harmonic signal, it is then possible to calculate the value of the orthogonal component of the harmonic field. In that case there is no background: the orthogonal component is zero if the polarization angle is zero. As soon as a small degree of molecular alignment exists, the polarization angle deviates and creates a non-zero orthogonal background. This method could be used to study subtle effects in the rotational wavepacket dynamics.

In the next section, we show that polarization-resolved pump–probe spectroscopy can be employed to detect revivals in a case where the total harmonic signal is dominated by a continuous background.

5. Detection of the alignment revival in an Ar–N_2 mixture

Polarization-resolved spectroscopy should be used to extract a signal generated by excited molecules from a strong background generated by non-excited molecules or by a carrier gas. In the particular case studied here, the rotational excitation is a very efficient process and the total harmonic signal is sufficient to detect the alignment revivals with a decent contrast. In order to study a less favorable case, we have performed a similar experiment in a mixture of argon and nitrogen.

The high harmonic signal generated in argon is typically about three times more important than the one produced in nitrogen under the same experimental conditions. In a 50/50 mixture, we expect the harmonic yield to be dominated by argon. Figure 7 (blue dashed-dotted line) shows the evolution of the harmonic 21 signal in the conventional configuration (parallel alignment and parallel polarization) as the delay is scanned around the half revival. The modulation of the harmonic signal induced by the evolution of the rotational wavepacket is hardly distinguishable. The red continuous line is the evolution of the orthogonal signal in the case of a pump polarization at 30° from the probe polarization. A clear maximum is observed at $\Delta t = 4.1$ ps. The polarization-resolved measurement allows us to detect the revival

of molecular alignment in the mixture with a contrast of 3.5, greatly improving the sensitivity of the measurement.

6. Conclusion

We have shown that polarization-resolved pump–probe spectroscopy could be used to study high harmonic generation from rotationally excited molecules. We have measured the state of polarization of high harmonics from aligned nitrogen molecules. We observe remarkable features, such as sign changes in the orthogonal component of the harmonic field. These features should be further analyzed, since the polarization of high harmonics was recently predicted to contain signatures of multielectron effects in the generation process [25].

In pump–probe scans, we have demonstrated an enhancement by a factor 4 of the contrast in the detection of alignment revivals in pure nitrogen. We have also shown that polarization-resolved measurements could be used to extract the signal from excited nitrogen molecules from a strong background generated by argon atoms. The contrast could be further enhanced by increasing the extinction ratio of our polarizer, e.g. by using several reflections on silver surfaces. The extension of this technique to other types of excitation is straightforward, as soon as the excited medium presents some anisotropy. This is thus an important step towards the investigation of molecular dynamics initiated by low cross-section processes.

Acknowledgments

We thank N Dudovich for fruitful discussions and S Weber for his help on the experiment. We acknowledge financial support from the European XTRA network (MRTN-CT-2003-505138), ANR Attoscience, Réseau des Technologies Femtoseconde de la Mission des Ressources et Compétences Technologiques du CNRS and the Conseil Régional d'Aquitaine (COLA).

References

[1] Corkum P B 1993 *Phys. Rev. Lett.* **71** 1994
[2] Schafer K J, Yang B, DiMauro L F and Kulander K C 1993 *Phys. Rev. Lett.* **70** 1599
[3] Paul P M, Toma E S, Breger P, Mullot G, Augé F, Balcou Ph, Muller H G and Agostini P 2001 *Science* **292** 1689
[4] Mairesse Y *et al* 2003 *Science* **302** 1540
[5] Hentschel M *et al* 2001 *Nature* **414** 509
[6] Kienberger R *et al* 2004 *Nature* **427** 817
[7] Sola I J *et al* 2006 *Nat. Phys.* **2** 319
[8] Sansone G *et al* 2006 *Science* **314** 443
[9] Zeidler D, Bardon A B, Staudte A, Villeneuve D M, Dörner R and Corkum P B 2006 *J. Phys. B: At. Mol. Opt. Phys.* **39** L159
[10] Levesque J, Zeidler D, Marangos J P, Corkum P B and Villeneuve D M 2007 *Phys. Rev. Lett.* **98** 183903
[11] Itatani J, Levesque J, Zeidler D, Niikura H, Pépin H, Kieffer J C, Corkum P B and Villeneuve D M 2004 *Nature* **432** 867
[12] Kanai T, Minemoto S and Sakai H 2005 *Nature* **435** 470
[13] Vozzi C *et al* 2005 *Phys. Rev. Lett.* **95** 153902
[14] Lein M 2005 *Phys. Rev. Lett.* **94** 053004

[15] Baker S, Robinson J S, Haworth C A, Teng H, Smith R A, Chirila C C, Lein M, Tisch J W G and Marangos J P 2006 *Science* **312** 424
[16] Wagner N, Wuest A, Christov I, Popmintchev T, Zhou X, Murnane M and Kapteyn H 2006 *Proc. Natl Acad. Sci.* **103** 13279
[17] Levenson M D 1982 *Introduction to Nonlinear Laser Spectroscopy* (New York: Academic)
[18] Mukamel S 1995 *Principles of Nonlinear Optical Spectroscopy* (New York: Oxford University Press)
[19] Mairesse Y, Zeidler D, Dudovich N, Spanner M, Levesque J, Villeneuve D M and Corkum P B submitted
[20] Rosca-Pruna F and Vrakking M J J 2001 *Phys. Rev. Lett.* **87** 153902
[21] Stapelfeldt H and Seideman T 2003 *Rev. Mod. Phys.* **75** 543
[22] Dooley P W, Litvinyuk I V, Lee K F, Rayner D M, Spanner M, Villeneuve D M and Corkum P B 2003 *Phys. Rev.* A **68** 023406
[23] Antoine P, Carré B, L'Huillier A and Lewenstein M 1997 *Phys. Rev.* A **55** 1314
[24] Levesque J, Mairesse Y, Dudovich N, Pépin H, Kieffer J-C, Corkum P B and Villeneuve D M 2007 *Phys. Rev. Lett.* **99** 243001
[25] Zhao Z, Yuan J and Brabec T 2007 *Phys. Rev.* A **76** 031404

PAPER IV

Attosecond chirp encoded dynamics of light nuclei

S. Haessler, W. Boutu, M. Stankiewicz, L.J. Frasinski, S. Weber, J. Caillat, R. Taïeb, A. Maquet, P. Breger, P. Monchicourt, B Carré and P. Salières.

J. Phys. B **42**, 134002 (2009).

IOP PUBLISHING JOURNAL OF PHYSICS B: ATOMIC, MOLECULAR AND OPTICAL PHYSICS

J. Phys. B: At. Mol. Opt. Phys. **42** (2009) 134002 (8pp) doi:10.1088/0953-4075/42/13/134002

Attosecond chirp-encoded dynamics of light nuclei

S Haessler[1], W Boutu[1,5], M Stankiewicz[2], L J Frasinski[3], S Weber[1,6], J Caillat[4], R Taïeb[4], A Maquet[4], P Breger[1], P Monchicourt[1], B Carré[1] and P Salières[1]

[1] CEA Saclay, IRAMIS, Service des Photons, Atomes et Molécules, 91191 Gif-sur-Yvette, France
[2] Institute of Physics, Jagiellonian University, ul. Reymonta 4, 30-059 Kraków, Poland
[3] The Blackett Laboratory, Imperial College London, South Kensington Campus, London SW7 2AZ, UK
[4] UMPC Université Paris 06, CNRS, UMR 7614, LCPMR, 11 rue Pierre et Marie Curie, 75231 Paris Cedex 05, France

E-mail: pascal.salieres@cea.fr

Received 30 January 2009, in final form 31 March 2009
Published 12 June 2009
Online at stacks.iop.org/JPhysB/42/134002

Abstract
We study the spectral phase of high-order harmonic emission as an observable for probing ultrafast nuclear dynamics after the ionization of a molecule. Using a strong-field approximation theory that includes nuclear dynamics, we relate the harmonic phase to the phase of the overlap integral of the nuclear wavefunctions of the initial neutral molecule and the molecular ion after an attosecond probe delay. We determine experimentally the group delay of the high harmonic emission from D_2 and H_2 molecules, which allows us to verify the relation between harmonic frequency and the attosecond delay. The small difference in the harmonic phase between H_2 and D_2 calculated theoretically is consistent with our experimental results.

1. Introduction

Dynamic imaging of a molecular structure with ångström space and attosecond time resolution is one of the most exciting recent developments in attosecond science. The attosecond timescale is inherent to intra-atomic/molecular electron dynamics and to the movement of the lightest nuclei. The ultimate goal of this research might be tomographic imaging [1] of an evolving molecular orbital. A challenging goal in chemical physics is to trace ultrafast nuclear re-arrangements or vibrations. In particular, the transfer of protons within large molecules plays an important role in many chemical reactions relevant to life sciences [2, 3], combustion and astrophysics [4]. A great deal of research has thus been devoted to the observation of such nuclear re-arrangements achieving femtosecond [5–7] or attosecond [8, 9] time resolution.

A technically fairly simple, yet powerful method termed PACER (probing attosecond dynamics by chirp encoded recollision) has been proposed for observing the expansion of a vibrating hydrogen molecular ion immediately after ionization. It was studied first numerically [10] and then demonstrated experimentally two years ago [9]. Briefly, the ratio of high harmonic spectra generated under the same conditions in protonated and deuterated species of a molecule is measured, and the nuclear dynamics are retrieved by means of a genetic algorithm. The three steps, commonly used to describe high harmonic generation (HHG) [11, 12], are considered as a pump, a delay stage and a probe process: a strong laser field ionizes the molecule, launching simultaneously an electron wavepacket of attosecond duration into the continuum and a time-dependent nuclear wavepacket onto the electronic ground-state potential surface of the molecular ion. The continuum electron wavepacket is subsequently accelerated and driven back to the ion by the laser field, while the nuclear wavepacket evolves in parallel. At recollision, there is a certain probability for recombination to the ground state, releasing the accumulated kinetic energy of the electron in the form of an attosecond burst of XUV

[5] Present address: Department of Chemistry, University of California, Berkeley, CA 94720, USA and Chemical Sciences Division, Lawrence Berkeley National Laboratory, Berkeley, CA 94720, USA.
[6] Present address: CNRS, Université de Toulouse, UPS, Laboratoire Collisions Agrégats Réactivité, IRSAMC, France.

 © 2009 IOP Publishing Ltd Printed in the UK

J. Phys. B: At. Mol. Opt. Phys. **42** (2009) 134002 S Haessler *et al*

light. For *coherent* emission, recombination has to lead back to the initial state, the nuclear part of which is the vibrational ground state of the neutral molecule. The probability of this transition depends on the overlap of this ground-state nuclear wavefunction with the evolved nuclear wavepacket of the molecular ion at the recombination time, i.e. recombination will be all the less likely the further the ion has evolved. Only this *coherent* light will be detectable as a macroscopic signal produced by many emitters. Obviously, recombination can lead back to an excited state of the molecule, like an electronic state with the same symmetry as the initial state, or a vibrationally excited state. This excited state would, however, have an arbitrary phase relative to the continuum electron, which is 'phase locked' to the ground state, and the light emission would consequently be *incoherent*, adding only a weak background to the high harmonic emission.

Scanning the pump-probe delay is achieved by the inherent chirp of the recolliding electron wavepacket: for the short electron trajectories, higher harmonics are associated with larger electron excursion times and thus larger recollision times. In [9], this chirp was assumed to be the same as for rare-gas atoms, as measured in [13]. The latter study showed that the measured recollision times are very well described by the Lewenstein model [14]. Recently, it has been shown that the atomic and molecular recollision times may be equal provided that (i) the nuclear movement can be neglected on a sub-laser-cycle timescale (which is true for heavier molecules such as N_2 and CO_2), (ii) the sample is unaligned [15] or aligned in such a way that two-centre interference [16] does not occur, and (iii) the two species have the same ionization potential [17].

The aim of this work is twofold: first, using the reconstruction of attosecond beating by interference of two-photon transitions (RABITT) [18, 19] technique, we want to verify experimentally for H_2 and D_2 molecules that the frequency–time mapping, which is at the heart of the PACER method, is not affected by the molecular ion's expansion. Second, and more generally, we will address the question how the rapid nuclear dynamics affect the phase of the high harmonic emission, and whether it could be linked more directly to the nuclear dynamics than the harmonic intensity. The second of these points has been studied in [20] using a different experimental technique, which will be discussed and compared to our experimental findings.

In our paper, we first review the theoretical basis of PACER in section 2.1, followed by a detailed analysis of the result with regard to the phase differences between H_2 and D_2 in section 2.2. We then present our experimental configuration and results in sections 3 and 4, respectively. Finally, we draw conclusions of our study in section 5.

2. Theoretical description

2.1. Overview of the strong-field approximation theory including nuclear dynamics

The theoretical basis for PACER is thoroughly described in [10, 21] but to address the above questions we will briefly review the essential points. The two wavepackets launched in the ionization step of the three-step model are correlated, and their evolution is followed in [10] by considering the simplest case of H_2 and D_2 molecules and solving numerically the time-dependent Schrödinger equation (TDSE), including the interaction of the single active electron with the screened nuclei, i.e. non-Born–Oppenheimer couplings. The authors then derive a modified Lewenstein model [14], also called the strong-field approximation (SFA) model, incorporating the nuclear motion within the Born–Oppenheimer (BO) approximation. The results of this model agree very well with the exact TDSE calculation, justifying the approximations made for the considered parameters (780 nm, six-cycle pulse with 4×10^{14} W cm^{-2}). It is hardly possible to rigorously deduce a range of laser parameters where the SFA and the BO approximation are valid. The SFA approach has been extensively compared with TDSE calculations and experiments in rare-gas atoms, and was shown to be in satisfactory agreement for a Keldysh parameter, $\gamma \leqslant 1$. The same should hold for the simplest molecules such as H_2. The BO approximation on the other hand obviously becomes questionable for the lightest nuclei, and indeed there are deviations observed, e.g., from the Franck–Condon principle for the tunnel ionization step [22, 23].

Following the assumptions of the SFA and assuming that only one electron can become active, one makes an ansatz for the full wavefunction (atomic units are used unless stated otherwise):

$$\psi(\boldsymbol{r}_1, \boldsymbol{r}_2, R, t) = \mathrm{e}^{-\mathrm{i}E_0 t}\left\{\chi_0(R)\psi_R(\boldsymbol{r}_1, \boldsymbol{r}_2) + \int \frac{\mathrm{d}^3k}{(2\pi)^3}\phi(\boldsymbol{k}, R, t) \times \left[\exp(\mathrm{i}\boldsymbol{k}\cdot\boldsymbol{r}_1)\psi_R^+(\boldsymbol{r}_2) + \exp(\mathrm{i}\boldsymbol{k}\cdot\boldsymbol{r}_2)\psi_R^+(\boldsymbol{r}_1)\right]\right\}, \quad (1)$$

where $\boldsymbol{r}_1, \boldsymbol{r}_2$ are the coordinates of the two electrons, $\chi_0(R)\psi_R(\boldsymbol{r}_1, \boldsymbol{r}_2)$ is the real-valued ground-state wavefunction of H_2 (or its isotopes) in the BO approximation, i.e. written as a product of a nuclear part χ_0 and an electronic part ψ_R, and $\psi_R^+(\boldsymbol{r}_{1/2})$ is the electronic ground-state BO wavefunction of H_2^+. $\phi(\boldsymbol{k}, R, t)$ describes the time dependence of the continuum electron as well as the nuclear part of the H_2^+ wavefunction. E_0 is the ground-state energy eigenvalue. We choose the origin of energy such that the lowest BO potential of H_2^+, $V_{\mathrm{BO}}^+(R)$, takes the value zero at the average internuclear distance $\bar{R}_0$ in the vibrational ground state of the neutral molecule. We thus subtract $V_{\mathrm{BO}}^+(\bar{R}_0)$ from all curves, which consequently replaces E_0 in (1) by $E_0 - V_{\mathrm{BO}}^+(\bar{R}_0) = -I_{\mathrm{p}}$, where I_{p} is an effective vertical ionization potential.

The TDSE for an H_2 molecule with fixed orientation, driven by a linearly polarized laser field $E(t)$ along the x-axis is then solved analytically, neglecting non-BO couplings and laser field interaction with ψ_R^+, leading to an expression for $\phi(\boldsymbol{k}, R, t)$ that allows calculating the time-dependent dipole momentum along x:

$$\begin{aligned} V_x(t) &= -\mathrm{i}\langle\psi(t)|\partial_{x_1} + \partial_{x_2}|\psi(t)\rangle \\ &= 2\mathrm{i}\int_0^t \mathrm{d}t' \int \frac{\mathrm{d}^3p}{(2\pi)^3} E(t')\bar{d}_{\mathrm{i}}[\boldsymbol{p} + \boldsymbol{A}(t')]\,\exp[\mathrm{i}S(\boldsymbol{p}, t, t')] \\ &\quad \times \int \mathrm{d}R\,\chi_0(R)v_{\mathrm{r}}[\boldsymbol{p} + \boldsymbol{A}(t), R]\chi(R, t - t') + \mathrm{c.c.}, \end{aligned} \quad (2)$$

where

$$S(\boldsymbol{p}, t, t') = -\int_{t'}^{t} \mathrm{d}t'' \left\{ \frac{[\boldsymbol{p} + \boldsymbol{A}(t'')]^2}{2} + I_\mathrm{p} \right\} \tag{3}$$

is the semiclassical action of the continuum electron, $\boldsymbol{p} = \boldsymbol{k} - \boldsymbol{A}(t)$ is its canonical momentum, and $\boldsymbol{A}(t) = -\int_{-\infty}^{t} \boldsymbol{E}(t')\,\mathrm{d}t'$ is the vector potential of the laser field. The evolution of the nuclear wavepacket, $\chi(R, t - t')$, in the molecular ion is obtained by solving the Schrödinger equation,

$$\mathrm{i}\dot{\chi}(R, t) = \left[-\partial_R^2 \big/ M + V_{\mathrm{BO}}^+(R)\right]\chi(R, t), \tag{4}$$

where M is the mass of one nucleus. For the initial condition, the Franck–Condon principle is applied: $\chi(R, t') = \chi_0(R)$. This is a good approximation for laser intensities on the order of 10^{14} W cm^{-2} and molecules aligned perpendicular to the laser polarization direction [22, 23], and should thus also hold for an unaligned molecular sample. Note that the interaction with the strong laser field is neglected in (4) although the laser field significantly modifies the potential curve the nuclear wavepacket moves on and may couple different electronic states. The effect, however, is strongest at internuclear separations R of the molecular ion above its equilibrium value $R_0 = 2$ au and, in particular, close to the avoided crossings of the field dressed σ_g and σ_u states of the molecular ion around $R = 4$ au, leading to bond softening and bond hardening [24, 25]. Within the time window covered by the excursion times in HHG with an 800 nm laser (<1.8 fs), the nuclear wavepacket cannot evolve very far and, in fact, still remains on the falling edge of the σ_g potential curve. At these R, the potential is barely affected (see figure 13 in [24], where H_2^+ potentials are shown for an intensity of 1×10^{14} W cm^{-2}) and the field-free calculation using (4) should be valid for the nuclear wavepacket evolution accessible in the experiment. The effect of laser dressing on the outcome of PACER-like experiments has also been studied theoretically by Chirilă and Lein [26] and found to be negligible for 800 nm lasers due to the short time between ionization and recombination. For mid-IR lasers (e.g., 1.5 or 2 μm), however, dressing leads to significant modifications of the nuclear dynamics.

In expression (2) for the dipole momentum, the three steps described in the introduction are recovered as follows:

(i) At time t' the active electron tunnels into the continuum with a probability amplitude of $E(t')\bar{d}_\mathrm{i}$. Here, a simplification has been introduced: the R-dependence of the matrix element d_i has been neglected and instead the effective matrix element,

$$\bar{d}_\mathrm{i}(\boldsymbol{k}) = \left(\int |\langle \exp(\mathrm{i}\boldsymbol{k}\cdot\boldsymbol{r}_1)\psi_R^+(\boldsymbol{r}_2)|x_1| \times \psi_R(\boldsymbol{r}_1, \boldsymbol{r}_2)\rangle\, \chi_0(R)|^2\, \mathrm{d}R \right)^{1/2}, \tag{5}$$

averaged over all possible values of the internuclear distance R, is used. (ii) The active electron moves in the continuum under the influence of the laser field only, until time t, acquiring a phase *relative to the ground state* of $S(\boldsymbol{p}, t, t')$. (iii) At time t, the continuum electron recombines with the molecular ion to the neutral ground state, the amplitude of which is given by

$$v(\boldsymbol{k}) = -\mathrm{i}\int \chi_0(R)\big\langle \psi_R(\boldsymbol{r}_1, \boldsymbol{r}_2)|\partial_{x_1}| \times \exp[\mathrm{i}\boldsymbol{k}\cdot\boldsymbol{r}_1]\psi_R^+(\boldsymbol{r}_2)\big\rangle \chi(R, t - t')\,\mathrm{d}R. \tag{6}$$

Note that the bra–ket matrix element implies integration over both $\boldsymbol{r}_1$ and $\boldsymbol{r}_2$, and that its functional form is identical for H_2 and D_2. It is still parametrically R-dependent, and is written here for a specific alignment angle θ of the molecular axis with respect to the laser polarization. Adopting a linear combination of atomic orbitals (LCAO) for the electronic ground states of the neutral molecule and the molecular ion with $\psi_R = \psi_R^+(\boldsymbol{r}_1)\psi_R^+(\boldsymbol{r}_2)$ [21], one can reduce its R-dependence to an interference kernel $\cos(kR\cos(\theta)/2)$. Any possible difference between the recombination amplitudes for H_2 and D_2 with an alignment distribution of $\sigma(\theta)$ must then be contained in

$$c(k, R) = \int \sigma(\theta) \int \chi_0(R)\cos(kR\cos(\theta)/2) \times \chi(R, t - t')\,\mathrm{d}R\,\mathrm{d}\theta. \tag{7}$$

The interference kernel is real valued and will change sign at $k_0 = \pi/[R\cos(\theta)]$, which translates to a sudden π phase jump. For H_2 molecules, partly aligned along the laser polarization direction, two-centre interference will indeed play a role when using an 800 nm laser [27]. Detecting the phase jump at some harmonic order q associated with the excursion time τ_q, as was recently demonstrated for CO_2 molecules [17], would be an observation of dynamic two-centre interference [27] on the observable 'harmonic phase'. This would provide a means of observing when the centre of mass $\tilde{R}(t - t')$ of the product of the nuclear wavefunctions $\chi_0(R)$ and $\chi(R, t - t')$ passes through the value $\tilde{R} = \pi/[\sqrt{2q\omega_0}\cos(\theta_\mathrm{m})]$ satisfying the destructive interference condition, where θ_m is the modal value of the alignment distribution $\sigma(\theta)$, and ω_0 is the driving laser frequency. For D_2 molecules, this dynamic two-centre interference then occurs at a larger time and hence larger harmonic order. This would, however, only provide a measurement of one point $\tilde{R}(\tau_q)$ for each isotope and does not directly allow us to continuously trace the nuclear dynamics.

For randomly aligned molecules, the θ-integral in (7) reduces to $\sin(kR/2)/(kR/2)$, the sign change of which would occur at too high harmonic orders to be observed using an 800 nm laser. Dropping the interference kernel thus still gives a reasonably good approximation for unaligned molecules [9]. This has the great advantage of reducing the R-dependence of (7) to a k-independent nuclear overlap integral:

$$C(t - t') = \int \chi_0(R)\chi(R, t - t')\,\mathrm{d}R. \tag{8}$$

The intensity of a harmonic that is dominated by a single excursion time $\tau = t - t'$ is therefore proportional to $|C(\tau)|^2$, which monotonically decreases with time when the molecular ion expands. The decrease is obviously slower in the heavier isotope since the nuclear dynamics is slower. When the contribution of the short trajectories is isolated in the experiment, the measured ratio of harmonic intensities for D_2 and H_2, being proportional to $|C^{\mathrm{D_2}}(\tau)/C^{\mathrm{H_2}}(\tau)|^2$, will thus monotonically increase with harmonic order. This has been experimentally confirmed [9, 20].

2.2. Analysis of phase effects

The three steps of the high harmonic emission process influence the phase of the radiation emitted in the following manner:

(i) The term (5) is essentially the same for the two isotopes, since the electronic wavefunctions ψ_R and ψ_R^+ are identical. There is a small difference in the width of the initial nuclear wavepackets $\chi_0(R)$, but as they are purely real valued this will not translate to a phase difference.

(ii) In (3), the ionization potential for D_2 is, in fact, about 40 meV higher than for H_2 [28], but this difference is negligible. At this point, Kanai *et al* [20] introduced to the action an ionization potential being a function of the internuclear distance $R(t'')$, which then gave a different contribution for H_2 and D_2 due to the different nuclear dynamics. They described this term as 'the interaction between the molecular ion and the electron'. We think such a modification of the action is incorrect, because any ion–electron interaction is explicitly excluded in the SFA and thus cannot appear in the result. Note that the influence of the ion's Coulomb potential has been shown to be noticeable only for the lowest harmonics with energies close to I_p [29]. Second, the I_p in the action is nothing else but the energy eigenvalue of the neutral molecule BO ground state after a recalibration of the energy axis. This ground state is stationary and its energy does not change with time. We thus conclude that, within the framework of the SFA, the continuum electron dynamics is not only the same in H_2 and D_2 but it is also the same as in an atom of equal ionization potential. It is thus perfectly justified to use the frequency–time mapping as calculated from the three-step model as was done in the experiments [9, 27].

(iii) We have now established that the recolliding continuum electron wavepacket is, within the framework of the SFA, identical in the cases of H_2 and D_2. Along the lines proposed by Itatani *et al* [1], we can now directly obtain the phase difference of the harmonic emissions from the two isotopes from the phase difference of the recombination amplitudes $v(\boldsymbol{k})$ given in (6). As discussed earlier, when neglecting two-centre interference, the difference between H_2 and D_2 is contained in (8). It is thus the phase of the integral $C(\tau)$ that is passed on to the harmonic emission and potentially contains a signature of the nuclear dynamics. As $\chi_0(R)$ is real valued, the evolved nuclear wavepackets $\chi(R,\tau)$ are the only remaining source of phase difference.

We first treat the nuclear evolution classically and hence take R as a sharply defined variable depending on the excursion time τ. The nuclei only convert potential energy $V_{\mathrm{BO}}^+(R)$ into kinetic energy T_n. Using $V_{\mathrm{BO}}^+(\bar{R}_0)=0$, the Lagrangian reads $\mathcal{L}(\tau)=T_\mathrm{n}-V_{\mathrm{BO}}^+=-2V_{\mathrm{BO}}^+[R(\tau)]$. We can thus write the quasiclassical action of the nuclei in the molecular ion as $S_\mathrm{n}(t-t')=-2\int_{t'}^{t}\mathrm{d}t''\,V_{\mathrm{BO}}^+[R(t'')]$. The quasiclassical estimate for the harmonic phase difference $\Delta\varphi_{\mathrm{qcl}}^{\mathrm{D_2-H_2}}$ between D_2 and H_2 is the difference of the quasiclassical actions S_n of their evolving nuclear wavepackets. Linearizing the potential curve of the ion around the average internuclear distance $\bar{R}_0$ of the ground state, i.e. $V_{\mathrm{BO}}^+(R)=\partial_R V_{\mathrm{BO}}^+(R)\big|_{\bar{R}_O}\Delta R$, approximating the nuclear movement by classical uniformly accelerated motion, $\Delta R^{\mathrm{H_2/D_2}}(\tau)=-\partial_R V_{\mathrm{BO}}^+(R)\big|_{\bar{R}_O}/(2M^{\mathrm{H,D}})\,\tau^2$, and using $M^\mathrm{D}=2M^\mathrm{H}$, we find the simple relation,

$$\Delta\varphi_{\mathrm{qcl}}^{\mathrm{D_2-H_2}}(\tau)=\Delta S_\mathrm{n}^{\mathrm{D_2-H_2}}=\partial_R V_{\mathrm{BO}}^+(R)\big|_{\bar{R}_O}\,\Delta R^{\mathrm{H_2}}(\tau)\frac{\tau}{3}. \qquad (9)$$

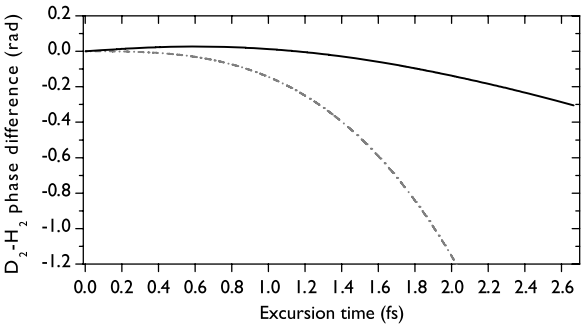

Figure 1. Theoretical phase difference from a full quantum-mechanical calculation (full line) and from the quasiclassical expression (9) (dash-dotted line).

The slope of the BO potential of the molecular ion at $\bar{R}_0=1.4$ au is $\partial_R V_{\mathrm{BO}}^+(R)\big|_{\bar{R}_O}=-0.15$ au. Equation (9) turns out to be—up to a factor of 2—the same as the phase difference calculated by Kanai *et al* [20]. The difference is that we identify its origin as the phase of the evolved nuclear wavepacket in the molecular ion and conclude that it only comes into play during the recombination step, whereas the continuum electron dynamics remain unaffected.

Nevertheless, this quasiclassical approach allows us to find only a rough estimate. Recombination and thus high harmonic emission are only possible as long as there is an overlap of $\chi_0(R)$ and $\chi(R,\tau)$. The quantum nature of the nuclear movement, i.e. the finite width of the nuclear wavefunctions, is thus absolutely essential. Equation (9) can only give an upper limit for the phase difference between the harmonic emissions from the two isotopes, because, roughly speaking, the nuclear position where the product $\chi_0(R)\chi(R,\tau)$ is maximum evolves considerably slower than the classical trajectory of the nuclei in the ion. For a reliable result, we thus have to calculate $C(\tau)$ exactly. Since the Hamiltonian in (4) is time independent, it is fairly straightforward to compute the evolution of $\chi(R,\tau)$. Once eigenstates $\chi_n(R)$ and eigenenergies E_n of the Hamiltonian are found, one can project the initial wavepacket $\chi(R,0)=\chi_0(R)$ onto this basis and calculate $\chi(R,\tau)=\sum_n \exp[-\mathrm{i}E_n\tau]a_n\chi_n(R)$ with $a_n=\langle\chi_n|\chi_0\rangle$. We have done this calculation for n up to 105, which has given us the complex $C(\tau)$ for H_2 and D_2 according to (8), i.e. neglecting two-centre interference. We checked that our ratio $|C^{\mathrm{D_2}}(\tau)/C^{\mathrm{H_2}}(\tau)|^2$ (shown in figure 3) agrees very well with that by Lein [9, 10]. In figure 1, we compare the D_2–H_2 phase difference of the $C(\tau)$ obtained from this full calculation with the phase difference $\Delta\varphi_{\mathrm{qcl}}^{\mathrm{D_2-H_2}}(\tau)$ from the quasiclassical treatment. Obviously, the quasiclassical result is a gross overestimation, and only the full quantum-mechanical treatment is adequate.

3. Experimental configuration

The experiments were carried out using the LUCA laser at CEA Saclay, delivering up to 30 mJ in 55 fs pulses at

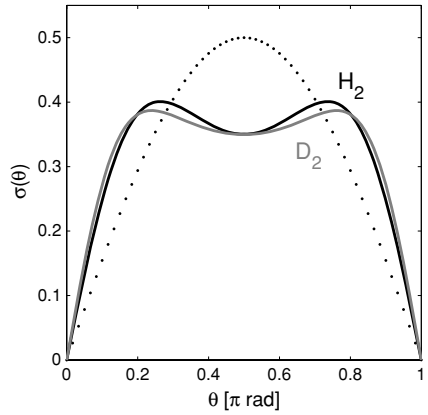

Figure 2. Calculated alignment distributions $\sigma(\theta)$ at the generating pulse peak for our experimental conditions. Black and grey lines show $\sigma(\theta)$ for H_2 and D_2, respectively. The dotted line shows an isotropic distribution for comparison.

20 Hz repetition rate. The setup is shown in figure 2 in [13]. A supersonic gas jet provides the molecular sample with an effective medium length of ≈1 mm. The Mach–Zehnder-type interferometer for the RABITT [18, 19] measurement is based on drilled mirrors separating the laser beam in two parts: an annular generating beam (outer diameter cut to 17 mm by an iris) and a central probe beam (diameter ≈4 mm). The latter can be delayed by a piezoeletric translation stage with interferometric stability. Both beams are then collinearly focused by a 1 m focal length lens ≈5 mm before the gas jet, making sure that the short trajectory contribution to the HHG emission is selected by phase matching [30]. In the gas jet, the intensities of generating and probe beam are 1.2×10^{14} W cm^{-2} and $\sim 10^{11}$ W cm^{-2}, respectively. An iris then blocks the annular generating beam, whereas the high harmonics together with the on-axis probe beam are focused by a broad-band Au-coated toroidal mirror into an effusive neon gas jet. A magnetic-bottle electron spectrometer (MBES) [31] detects the photoelectron spectrum. With the weak IR probe pulse present, spectral sidebands occur, created by two-photon ionization involving a high harmonic photon and an IR photon. Analysis of these sidebands as a function of the probe beam delay gives access to the relative phase of two successive harmonic orders, $\varphi_{q+2} - \varphi_q$, and thus to the group delay [13]:

$$\tau_g(\omega_{q+1}) := \left.\frac{\partial\varphi}{\partial\omega}\right|_{q+1} \approx \frac{\varphi_{q+2} - \varphi_q}{2\omega_0}. \quad (10)$$

Note that the small modulation of the HHG intensity due to interference with the probe beam in the generating medium allows us to determine absolute group delay values with respect to the generating laser field maximum [32].

We verified that partial alignment induced by the generating pulse is negligible by calculating the angular distributions $\sigma(\theta)$ at the peak of the pulse by the method described in the appendix of [33], using the fourth-order Runge–Kutta method [34] for the TDSE integration. We use a $\sin^2$ pulse of 55 fs FWHM duration and a temperature of 90 K for D_2 and 150 K for H_2 due to the different backing pressures necessary to achieve equal gas densities. The result is shown in figure 2. Obviously, the alignment distributions are modified during the generating pulse but not strongly enough for dynamic two-centre interference [27] to play a role.

4. Experimental results

Using the RABITT technique, we have measured intensity and group delay of the high harmonic emission from unaligned H_2 and D_2 molecules $\left(I_p^{H_2/D_2} = 15.43 \text{ eV}\right)$ as well as for Ar atoms, which have a very similar ionization potential $\left(I_p^{Ar} = 15.76 \text{ eV}\right)$. We were able to measure the group delay for harmonic orders between 15 and 31, and obtain harmonic intensities from photoelectron spectra recorded without the IR probe beam present for orders 17–33. We had no means of directly measuring the density in the generating gas jet. As the efficiency of turbo molecular pumps rapidly drops with decreasing molecular weight, the residual pressure in the vacuum chambers was rather high when generating harmonics in D_2 and even more so for H_2. We first determined the maximum possible gas jet backing pressure for H_2 by observing its characteristic trace in the recorded photoelectron spectra. With a significant density of H_2 molecules having migrated about 2 m down to the interaction region of the MBES and mixing with the injected neon, the peaks in the photoelectron spectrum are broadened on the red side with a substructure corresponding to the vibrational levels of H_2^+ ions. We then lowered the backing pressure until this distortion completely disappeared to minimize reabsorption of the harmonics. In this case, we read $\approx 5 \times 10^{-2}$ mbar residual pressure in the HHG chamber. With D_2, even when the residual pressure reading is the same as for H_2 in the HHG chamber, we never observed such distortions. Due to its larger weight it is pumped somewhat more efficiently than H_2 in the differential pumping stage halfway between generating gas jet and MBES.

Figure 3 shows D_2/H_2 intensity ratios measured in the same generating conditions except for the gas pressures. The harmonic orders have been associated with electron excursion times as calculated with the SFA for argon, shown by the dashed line in figure 4(a). With the same residual pressure readings for H_2 and D_2, we reproduce reasonably well for the plateau harmonics 17–27 the ratio of nuclear correlation functions $|C^{D_2}(\tau)/C^{H_2}(\tau)|^2$ from the full quantum-mechanical calculation described in section 2.2. We compare to the theory neglecting two-centre interference because only then is the calculation independent of experimental parameters, in particular, the intensity. This leads to a small under-estimation of the slope in the theoretical ratio, which is compatible with our observation. The agreement shows that we have found conditions giving approximately equal jet densities. When the D_2 backing pressure is reduced such that the residual pressure readings for the two isotopes give $p_{H_2}/p_{D_2} = 1.3$, we still obtain an increasing intensity ratio but at too low absolute values. Assuming phase-matched HHG and thus a quadratic dependence of HHG intensity on the medium density, the unequal experimental densities can be corrected for by

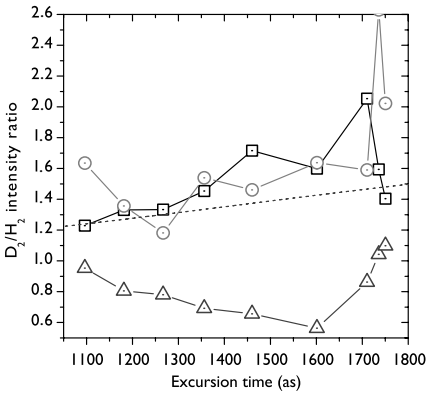

Figure 3. D_2/H_2 intensity ratios for harmonics 17–33 measured with different gas pressures. Residual pressure readings $p_{H_2} = p_{D_2} = 5 \times 10^{-2}$ mbar in the HHG chamber (□), $p_{H_2} = 5 \times 10^{-2}$ mbar, $p_{H_2}/p_{D_2} = 1.3$ and the D_2 spectrum has been corrected by multiplication with $(1.3)^2$ (○), $p_{H_2} = 8 \times 10^{-2}$ mbar, $p_{H_2}/p_{D_2} = 1.3$(△). The dashed line is the squared ratio of nuclear overlap integrals $|C^{D_2}(\tau)/C^{H_2}(\tau)|^2$ from our full quantum-mechanical calculation. The harmonic order excursion time mapping is taken from an SFA calculation for Ar at an intensity of 1.2×10^{14} W cm^{-2}, shown in figure 4(a).

multiplying the D_2 spectrum by $(1.3)^2$. Indeed, this correction brings the measured intensity ratio to an agreement with theory, which also shows that reabsorption within our thin gas jet is negligible. However, such a simple correction will not be possible anymore for too high residual pressure in the vacuum chambers because reabsorption on the way from the source of the harmonics to the detector becomes important. We expect this to be the case when the H_2 residual pressure causes traces of H_2^+ ions in the MBES spectra. The photoionization cross sections [35] of H_2 and D_2 decrease from ≈3.7 Mbarn at harmonic 17 to ≈1 Mbarn at harmonic 27. For an averaged residual pressure of 10^{-2} mbar over 2 m, this would result in a transmission of $T = 83\%$ for harmonic 17 and $T = 95\%$ for harmonic 27, which significantly flattens the measured spectrum as compared to the spectrum emitted at the source. As the transmission increases exponentially with decreasing density of the absorbing gas, the quicker drop of residual pressure for D_2 over the propagation distance will result in a much less pronounced flattening of the spectrum due to reabsorption. The slope of the D_2/H_2 intensity ratio obtained in these conditions will then be decreased or even inversed. We indeed measure a ratio that decreases with harmonic order (triangles in figure 3) for an H_2 residual pressure reading of $p_{H_2} = 8 \times 10^{-2}$ mbar. Figure 4(a) shows the group delay measured for the three gases in the conditions of the squares in figure 3. In rare-gas atoms, these group delays have been called *emission times* because they correspond to the real part of the recollision times calculated with the SFA [13]. This should hold, in particular, for argon but nevertheless there is an offset of about −250 as between the emission times given by the SFA and the measurement. The calculation is done for the correct effective intensity since the theoretical and experimental slopes of the emission time curves (that vary as 1/intensity [13]) agree perfectly in the plateau region. We consistently observe such a shift of the measured absolute timing (reported already in [17]) and attribute it to a yet unidentified macroscopic effect in the HHG gas jet rather than physics on the single atom/molecule level. In particular, the fact that the experimental group delay curves seem to fit the theoretical excursion time curve is presumably coincidental. A striking result of figure 4 is the agreement of all three group delay curves within our error bars. We can thus conclude that the continuum electron dynamics are the same for the very

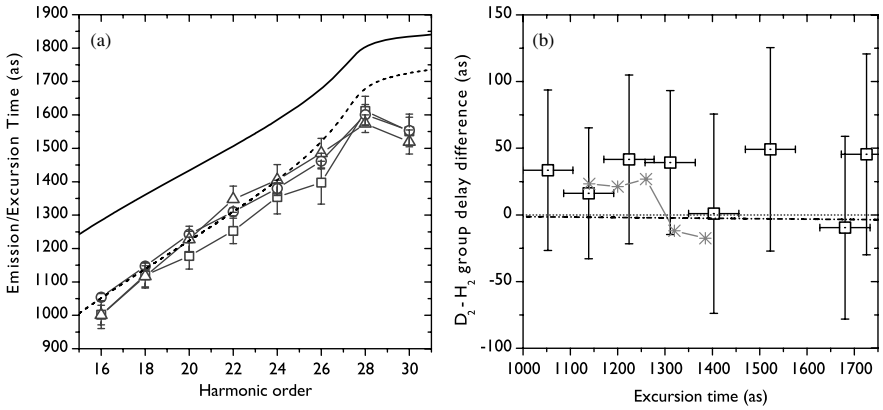

Figure 4. (a) Measured group delay or emission times for H_2(□), D_2 (○) and Ar (△). The error bars represent the accuracy of the τ_g-determination (standard deviation of the phase within the FWHM of the $2\omega_0$ peak in the RABITT trace Fourier transform). The full and the dashed line show recollision and excursion times, respectively, as calculated with the SFA for Ar and an intensity of 1.2×10^{14} W cm^{-2}. (b) Group delay differences, $\Delta\tau_g$, plotted as a function of the excursion time according to the q–τ mapping from the SFA calculation shown in figure 4(a). Squares are mean values over three measurements. Vertical error bars are given by the span covered by these three measurements. Stars mark results from Kanai *et al* [20] scaled to correct for the different q–τ mappings (see the text). The dash-dotted line is the theoretical group delay difference, derived from the full quantum mechanical treatment of the nuclear dynamics (see the text).

light molecules and argon, which experimentally confirms the conclusion drawn from the analysis of equation (3) and validates the time–frequency mapping that is the basis of the PACER method.

For a closer analysis, we show in figure 4(b) the difference of group delays $\Delta\tau_g = \tau_g^{D_2} - \tau_g^{H_2}$. We plot it as a function of the excursion time, justified by the conclusion from section 2.2: the frequency–time mapping is identical for the two isotopes, and any potential difference between the group delays is due to the recombination process. Different data acquisitions gave slightly varying results, differing mainly by a constant offset. We show the difference of the average over three acquisition runs for D_2 (one of which is shown in figure 4(a)) obtained in conditions of approximately equal gas density to one acquisition run for H_2, shown also in figure 4(a).

Kanai *et al* [20] have measured the D_2–H_2 phase difference $\Delta\varphi$ by generating harmonics in a mixture of the two gases. Their interfering emissions allow extracting the quantity $\cos(\Delta\varphi)$ from the measured spectral intensities, which leads to a sign ambiguity for $\Delta\varphi$. To compare these results to ours, we can write $\tau_g = \partial\varphi/\partial\omega = \partial\varphi/\partial\tau \times \partial\tau/(\omega_0\partial q)$. We then have to correct for the difference in $\partial\tau/(\omega_0\partial q)$ between our experiments, imposed by the different HHG intensities. In our case, $\partial\tau/\partial q \approx 44$ as in the plateau region, whereas $\partial\tau/\partial q \approx 30$ as for the conditions in [20]. We thus calculate the group delay difference from Kanai's data according to (10) and scale it by 44/30. The calculated points fall within our error margins.

We also compare to the group delay difference derived from the phase difference of the $C(\tau)$ (see (8) and figure 1) calculated in section 2.2. To this end, we take the derivative of the D_2–H_2 phase difference with respect to τ and multiply by $\partial\tau/(\omega_0\partial q)$ corresponding to the frequency–time mapping for our experimental conditions. The expected group delay difference is almost zero for these excursion times which is within our error margins.

5. Conclusions

We experimentally confirmed that the time–frequency mapping at the heart of the PACER technique is identical for H_2 and D_2 molecules as well as for argon atoms, which have almost the same ionization potential. This is supported by our theoretical analysis, suggesting that there is no influence of the nuclear dynamics on the recolliding continuum electron wavepacket.

The error bars in our current measurements do not yet allow us to discern the influence of the nuclear dynamics in the H_2^+ molecule on the high harmonic phase. Future measurements with improved accuracy should allow a more precise comparison of experiment and theory. These improvements could be gained by RABITT scans over a longer delay range and more precise control over experimental parameters such as the gas density in the generating jet.

Acknowledgments

We thank John Marangos, Yann Mairesse and Christian Cornaggia for fruitful discussions. We acknowledge financial support from the EU-FP6 program LASERLAB (RII3-CT-2003-506350), the ANR Attoscience (ANR-05-BLAN-0295) and the Engineering and Physical Sciences Research Council UK (grant no EP/C530772/2).

References

[1] Itatani J, Levesque J, Zeidler D, Niikura H, Pepin H, Kieffer J C, Corkum P B and Villeneuve D M 2004 Tomographic imaging of molecular orbitals *Nature* **432** 867–71

[2] Schultz T, Samoylova E, Radloff W, Hertel I V, Sobolewski A L and Domcke W 2004 Efficient deactivation of a model base pair via excited-state hydrogen transfer *Science* **306** 1765–8

[3] Sobolewski A L, Domcke W and Hättig C 2005 Tautomeric selectivity of the excited-state lifetime of guanine/cytosine base pairs: the role of electron-driven proton-transfer processes *Proc. Natl Acad. Sci. USA* **102** 17903–6

[4] Kaiser R, Balucani N, Charkin D and Mebel A 2003 A crossed beam and *ab initio* study of the $C_2(X^1\Sigma_g^+/a^3\Pi_u)$+ C_2 $H_2(X^1\Sigma_g^+)$ reactions *Chem. Phys. Lett.* **382** 112–9

[5] Markevitch A N, Romanov D A, Smith S M and Levis R J 2006 Rapid proton transfer mediated by a strong laser field *Phys. Rev. Lett.* **96** 163002

[6] Hishikawa A, Matsuda A, Fushitani M and Takahashi E J 2007 Visualizing recurrently migrating hydrogen in acetylene dication by intense ultrashort laser pulses *Phys. Rev. Lett.* **99** 258302

[7] Hishikawa A, Matsuda A, Takahashi E J and Fushitani M 2008 Acetylene–vinylidene isomerization in ultrashort intense laser fields studied by triple ion-coincidence momentum imaging *J. Chem. Phys.* **128** 084302

[8] Niikura H, Légaré F, Hasbani R, Ivanov M Y, Villeneuve D and Corkum P 2003 Probing molecular dynamics with attosecond resolution using correlated wave packet pairs *Nature* **421** 826–9

[9] Baker S, Robinson J S, Haworth C A, Teng H, Smith R A, Chirilă C C, Lein M, Tisch J W G and Marangos J P 2006 Probing proton dynamics in molecules on an attosecond time scale *Science* **312** 424–7

[10] Lein M 2005 Attosecond probing of vibrational dynamics with high-harmonic generation *Phys. Rev. Lett.* **94** 053004

[11] Schafer K J, Yang B, DiMauro L F and Kulander K C 1993 Above threshold ionization beyond the high harmonic cutoff *Phys. Rev. Lett.* **70** 1599–602

[12] Corkum P B 1993 Plasma perspective on strong field multiphoton ionization *Phys. Rev. Lett.* **71** 1994–7

[13] Mairesse Y *et al* 2003 Attosecond synchronization of high-harmonic soft x-rays *Science* **302** 1540–3

[14] Lewenstein M, Balcou Ph, Ivanov M Y, L'Huillier A and Corkum P B 1994 Theory of high-harmonic generation by low-frequency laser fields *Phys. Rev.* A **49** 2117–32

[15] Wabnitz H *et al* 2006 Generation of attosecond pulses in molecular nitrogen *Eur. Phys. J.* D **40** 305–11

[16] Lein M, Hay N, Velotta R, Marangos J P and Knight P L 2002 Role of the intramolecular phase in high-harmonic generation *Phys. Rev. Lett.* **88** 183903

[17] Boutu W *et al* 2008 Coherent control of attosecond emission from aligned molecules *Nat. Phys.* **4** 545–9

[18] Véniard V, Taïeb R and Maquet A 1996 Phase dependence of (n+1)-color ($n > 1$) IR-UV photoionization of atoms with higher harmonics *Phys. Rev.* A **54** 721–8

[19] Paul P M, Toma E S, Breger P, Mullot G, Auge F, Balcou Ph, Muller H G and Agostini P 2001 Observation of a train of attosecond pulses from high harmonic generation *Science* **292** 1689–92

[20] Kanai T, Takahashi E, Nabekawa Y and Midorikawa K 2008 Observing the attosecond dynamics of nuclear wavepackets

in molecules by using high harmonic generation in mixed gases *New J. Phys.* **10** 025036

[21] Chirilă C C and Lein M 2006 Influence of nuclear vibration on harmonic generation in molecules *J. Phys. B: At. Mol. Opt. Phys.* **39** S437–44

[22] Urbain X, Fabre B, Staicu-Casagrande E M, de Ruette N, Andrianarijaona V M, Jureta J, Posthumus J H, Saenz A, Baldit E and Cornaggia C 2004 Intense-laser-field ionization of molecular hydrogen in the tunneling regime and its effect on the vibrational excitation of H_2^+ *Phys. Rev. Lett.* **92** 163004

[23] Chirilă C C and Lein M 2006 High-order harmonic generation in vibrating molecules *J. Mod. Opt.* **53** 113–24

[24] Posthumus J H 2004 The dynamics of small molecules in intense laser fields *Rep. Prog. Phys.* **67** 623–65

[25] Feuerstein Th B, Rudenko A, Zrost K, Schröter C D, Moshammer R, Ullrich J, Niederhausen T and Thumm U 2007 Complete characterization of molecular dynamics in ultrashort laser fields *Phys. Rev. Lett.* **99** 153002

[26] Chirilă C C and Lein M 2008 Effect of dressing on high-order harmonic generation in vibrating H_2 molecules *Phys. Rev.* A **77** 043403

[27] Baker S *et al* 2008 Dynamic two-center interference in high-order harmonic generation from molecules with attosecond nuclear motion *Phys. Rev. Lett.* **101** 053901

[28] Shiner D, Gilligan J M, Cook B M and Lichten W 1993 H_2, D_2, and HD ionization potentials by accurate calibration of several iodine lines *Phys. Rev.* A **47** 4042–5

[29] Ivanov M Y, Brabec T and Burnett N 1996 Coulomb corrections and polarization effects in high-intensity high-harmonic emission *Phys. Rev.* A **54** 742–5

[30] Mairesse Y *et al* 2004 Optimization of attosecond pulse generation *Phys. Rev. Lett.* **93** 163901

[31] Kruit P and Read F H 1983 Magnetic field paralleliser for 2π electron-spectrometer and electron-image magnifier *J. Phys. E: Sci. Instrum.* **16** 313–24

[32] Dinu L C, Muller H G, Kazamias S, Mullot G, Augé F, Balcou Ph, Paul P M, Kovacev M, Breger P and Agostini P 2003 Measurement of the subcycle timing of attosecond XUV bursts in high-harmonic generation *Phys. Rev. Lett.* **91** 063901

[33] Dooley P W, Litvinyuk I V, Lee K F, Rayner D M, Spanner M, Villeneuve D M and Corkum P B 2003 Direct imaging of rotational wave-packet dynamics of diatomic molecules *Phys. Rev.* A **68** 023406

[34] Press W H, Flannery B P, Teukolsky S A and Vetterling W T 1992 *Numerical Recipes* 2nd edn (Cambridge: Cambridge University Press)

[35] Latimer C J, Dunn K F, O'Neill F P, Macdonald M A and Kouchi N 1995 Photoionization of hydrogen and deuterium *J. Chem. Phys.* **102** 722–5

PAPER V

Phase-resolved attosecond near-threshold photoionization of molecular nitrogen

S. Haessler, B. Fabre, J. Higuet, J. Caillat, T. Ruchon, P. Breger, B. Carré, E. Constant, A. Maquet, E. Mével, P. Salières, R. Taïeb and Y. Mairesse.

Phys. Rev. A **80**, 011404(R) (2009).

RAPID COMMUNICATIONS

PHYSICAL REVIEW A **80**, 011404(R) (2009)

Phase-resolved attosecond near-threshold photoionization of molecular nitrogen

S. Haessler,[1] B. Fabre,[2] J. Higuet,[2] J. Caillat,[3] T. Ruchon,[1] P. Breger,[1] B. Carré,[1] E. Constant,[2] A. Maquet,[3] E. Mével,[2] P. Salières,[1] R. Taïeb,[3] and Y. Mairesse[2]

[1]*CEA-Saclay, IRAMIS, Service des Photons, Atomes et Molécules, 91191 Gif-sur-Yvette, France*

[2]*CELIA, Université Bordeaux I, UMR 5107 (CNRS, Bordeaux 1, CEA), 351 Cours de la Libération, 33405 Talence Cedex, France*

[3]*UPMC, Université Paris 06, CNRS, UMR 7614, LCPMR, 11 rue Pierre et Marie Curie, 75231 Paris Cedex 5, France*

(Received 21 November 2008; published 28 July 2009)

We photoionize nitrogen molecules with a train of extreme ultraviolet attosecond pulses together with a weak infrared field. We measure the phase of the two-color two-photon ionization transition (molecular phase) for different states of the ion. We observe a 0.9π shift for the electrons produced in the ionization channels leading to the $X\ ^2\Sigma_g^+$, $v'=1$, and $v'=2$ states. We relate this phase shift to the presence of a complex resonance in the continuum. By providing both a high spectral and temporal resolution, this general approach gives access to the evolution of extremely short-lived states, which is often not accessible otherwise.

DOI: 10.1103/PhysRevA.80.011404 PACS number(s): 33.80.Eh, 33.60.+q, 42.65.Ky, 82.53.Kp

Ionization of atoms and molecules by absorption of ultrashort extreme ultraviolet (xuv) radiation provides rich structural information on the considered species. The ionization process releases an electron wave packet, which can be described as a coherent superposition of partial waves. The relative contributions and phases of the partial waves can be extracted from photoelectron angular distributions at a given energy [1]. However, the temporal structure of the ejected wave packet, which is imposed by the phase relation between different energy components, is not accessible with such experiments. To access this phase, one needs to couple two energy components of the electron wave packet and record the resulting interference. This can be achieved by absorption of high-order harmonics of an infrared laser pulse in the presence of the fundamental field.

An intense laser pulse propagating in a gas jet produces coherent xuv radiation constituted of odd harmonics $(2q+1)\omega_0$ of the fundamental frequency ω_0. These harmonics are all approximately phase locked with the fundamental and form an attosecond pulse train (APT) [2]. In photoionization experiments with high harmonics, the photoelectron spectrum exhibits equidistant lines resulting from single-photon ionization [Fig. 1(a)]. If an additional laser field with frequency ω_0 is added, two-photon ionization can occur: absorption of a harmonic photon accompanied by either absorption or stimulated emission of one photon ω_0. New lines (sidebands) appear in the spectrum, in between the harmonics [Fig. 1(a)]. Since two coherent quantum paths lead to the same sideband, interferences occur. They are observed in an oscillation of the sideband amplitude as the delay τ between the probe (ir) and harmonic fields is scanned [2,3]. This is the basis of the reconstruction of attosecond beating by interference of two-photon transitions (RABBITT) technique. The phase of the oscillation is determined by the phase difference between consecutive harmonics (phase locking) and by additional phase characteristics of the ionization process.

The same process can be described in the time domain. The APT creates a train of attosecond electron wave packets. The additional laser field acts as an optical gate on the electrons, which can be used to retrieve the temporal profile of the electron wave packets [4,5]. This temporal structure is set by the temporal shape of the APT but also by the photoionization process. Thus, RABBITT measurements with a well-characterized APT give access to the spectral phase of the photoionization [6,7], i.e., the temporal dynamics of photoionization.

Recently Cavalieri *et al.* [8] reported a time-resolved measurement of photoionization of a solid target by a single attosecond pulse. Conceptually this is close to RABBITT [4,5] but using of an APT rather than a single pulse has major advantages: (i) the production of APT is much less demanding; (ii) the spectrum of APT is a comb of narrow harmonics that can be used to identify different photoionization channels; (iii) the intensity of the ir beam must be of $\approx 10^{11}$ W cm^{-2} for RABBITT and about 10^{13} W cm^{-2} with single pulses [9], which can perturb the system.

Here we study the photoionization of nitrogen molecules with an APT and characterize the outgoing electron wave packets using the RABBITT technique. We probe the region just above the ionization threshold of N_2, which is spectroscopically very rich [10–12]. We show that the "complex resonance" (at 72.3 nm) [10,12,13] induces a $\approx\pi$ phase change in the molecular phase. This effect strongly depends

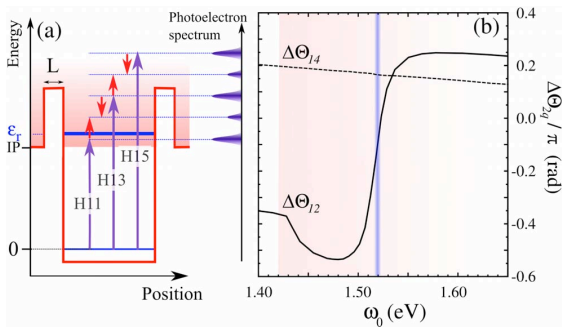

FIG. 1. (Color online) Theoretical model of a RABBITT experiment in presence of a resonance. (a) Principle of RABBITT and model potential that is used for the simulations. (b) Evolution of the molecular phase difference $\Delta\theta_{12}$ (solid line) and $\Delta\theta_{14}$ (dashed line) as a function of the fundamental laser frequency. Harmonic 11 is in the continuum for $\omega_0 > 1.43$ eV and hits the resonance when $\omega_0 = 1.52$ eV.

 ©2009 The American Physical Society

on the final ionic state, revealing the complex nature of the photoionization process.

We first present a theoretical study of the influence of resonances on RABBITT measurements. The oscillations as a function of the delay τ of the sideband S_{2q} between harmonics $2q-1$ and $2q+1$, integrated over all electron ejection angles Ω, are given by [3]

$$S_{2q}(\tau) = \int d\Omega |T_{2q}^{(+)} + T_{2q}^{(-)}|^2 \propto a + b \times \cos(2\omega_0\tau + \varphi_{2q+1} - \varphi_{2q-1} + \theta_{2q+1} - \theta_{2q-1}). \quad (1)$$

In this expression, $\varphi_{2q\pm1}$ are the phases of the harmonics $H(2q\pm1)$. The quantities $\theta_{2q\pm1}$, usually referred to as atomic or molecular phases [6,7,14], stem from the second-order transition matrix elements $T_{2q}^{(\pm)}$ corresponding to the absorption of harmonics $2q\pm1$ accompanied by either the emission $(-)$ or absorption $(+)$ of one fundamental ir photon, both paths leading to S_{2q}:

$$T_{2q}^{(\pm)} = \sum_n \langle \vec{k}_{2q}|\mathcal{D}|n\rangle\langle n|\mathcal{D}|0\rangle \times \left[\frac{1}{-I_p + (2q \pm 1)\omega_0 - \bar{\epsilon}_n} + \frac{1}{-I_p \mp \omega_0 - \bar{\epsilon}_n}\right], \quad (2)$$

where $\mathcal{D}$ is the dipole operator, $|0\rangle$ is the initial state, and $|\vec{k}_{2q}\rangle$ is the final continuum state labeled by the momentum of the outgoing electron ($k_{2q}^2/2 = -I_p + 2q\omega_0$). The sum is running over all states (discrete and continuum) $|n\rangle$. The real part of $\bar{\epsilon}_n$ is the energy of $|n\rangle$, while its imaginary part η is a signature of its width: $\eta=0$ for a discrete state, $\eta\to0^+$ in the continuum, and $\eta=\Gamma_r/2$ for a resonance of lifetime Γ_r^{-1}.

In conventional RABBITT measurements, performed in rare gas atoms presenting structureless continua, $\Delta\theta_{2q} = \theta_{2q+1} - \theta_{2q-1}$ tends to vanish, and the phases of sideband oscillations directly provide the phase differences of consecutive harmonics. Here, the situation is reversed: we perform a RABBITT experiment on N_2 using harmonics with known phases in presence of a resonance. The outcome is the measurement of nontrivial molecular phases $\theta_{2q\pm1}$.

In order to quantify the effect of a resonance on the molecular phases, we have simulated RABBITT electron spectra by solving the time-dependent Schrödinger equation for a one-dimensional (1D) electron in a model potential interacting with a perturbative ir pulse and several of its odd harmonics [Fig. 1(a)]. The potential shape was adapted to get the same ionization energy as N_2 ($I_p=15.58$ eV) and an autoionizing resonant state $|r\rangle$ with energy $\epsilon_r=16.7$ eV which can be reached by the 11th harmonic of a 800 nm laser pulse. The resonance width Γ_r can be tuned by adjusting the barrier width L. We show in Fig. 1(b) the molecular phase differences, extracted from the computed spectra, as a function of ω_0 for a barrier width $L=6$ a.u. corresponding to a lifetime $\Gamma_r^{-1} \approx 57$ fs.

While $\Delta\theta_{14}$ slightly varies with the ir frequency, $\Delta\theta_{12}$ is strongly dependent on the detuning of H11 relative to the resonance energy. When H11 is below the resonance, i.e., $\omega_0 < 1.52$ eV, there is an important difference between $\Delta\theta_{12}$ and $\Delta\theta_{14}$, while when H11 is above the resonance, $\Delta\theta_{12}$ is close to $\Delta\theta_{14}$. This can be understood by looking at Eq. (2). In the first component of the sum, the term corresponding to the resonant state becomes dominant over all other states when $-I_p + 11\omega_0 \approx \epsilon_r$, as the real part of its denominator changes sign. In the limit of an isolated resonance with infinite lifetime ($\Gamma_r=0$), this would lead to a π jump in the molecular phase. With a finite lifetime, the imaginary part $\Gamma_r/2$ smoothens the phase variation and reduces the magnitude of the jump.

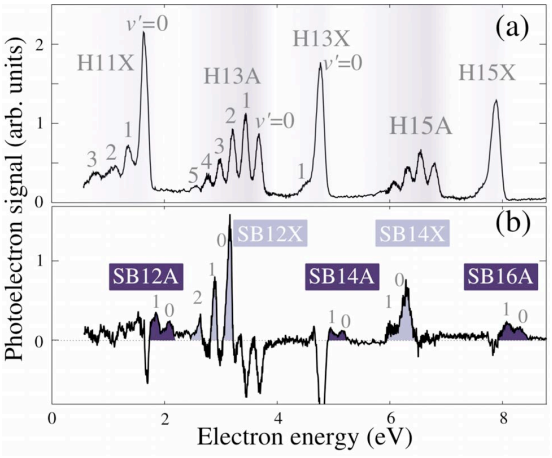

FIG. 2. (Color online) Photoionization of N_2 by a comb of high-order harmonics and influence of the ir field. (a) Spectrum obtained with harmonics alone. (b) Difference between the photoelectron spectra obtained with and without the ir probe field.

The measurements were performed with the setup described in [15]. We used a 20-Hz 50-mJ 50-fs laser system. The laser beam is split into a generating beam and a delayed probe beam. The annular generating beam is focused into a pulsed argon jet and generates an APT. The generating ir is filtered out and the xuv radiation is focused by a grazing incidence Au-coated toroidal mirror in a molecular nitrogen effusive jet. The photoelectrons are detected with a magnetic bottle time-of-flight spectrometer. The probe beam is focused together with the xuv in the nitrogen jet and the ir-xuv delay is adjusted with a piezoelectric transducer.

Figure 2(a) shows a photoelectron spectrum obtained without the probe field. The energy resolution of the spectrometer is maximal in the range 1–3 eV. We have applied different voltages to the flight tube so that the electrons produced by different harmonics would be detected in this optimal energy range. We concatenate the spectra to get the high-resolution spectrum shown in Fig. 2(a). Each spectrum was averaged over 2000 laser shots.

The harmonics are separated by twice the fundamental frequency, i.e., 3.13 eV. Each harmonic produces two photoelectron bands, corresponding to two ionization channels: one correlated with the fundamental electronic state $X\ ^2\Sigma_g^+$ of the N_2^+ ion ($I_p=15.58$ eV), and the other to the excited $A\ ^2\Pi_u$ state ($I_p=16.69$ eV). For each harmonic, the integral of the A band is about 1.8 times larger than that of the X band, in agreement with measured photoionization cross sections [16].

The photoelectron bands show fine structures revealing the vibrational states of the ion. The A and X states of N_2^+ have different equilibrium distances [17] and the corresponding bands present different shapes. For the ion ground state X, in which the equilibrium distance (1.12 Å) is about the same as for the molecular ground state (1.10 Å), we observe a narrow vibrational distribution. By contrast, for the first excited state of the ion A, the larger equilibrium distance (1.17 Å) results in a broader vibrational distribution. While there is an overall good agreement between the observed vibrational populations and the Franck-Condon factors, the X band produced by H11 runs over more vibrational levels than expected.

The spectrum of the fundamental laser pulse was centered at 1.565 eV, leading to a central energy of 17.22 eV for H11 with a spectral width of about 0.15 eV. The photoionization spectrum of N_2 shows a resonance within this width, around 17.12 eV [13], which was attributed to the $B\ ^2\Sigma_u^+(3d\sigma_g)^1\Sigma_u^+$ Hopfield Rydberg state [10,12]. It is of particular interest because it is a "complex resonance," i.e., it involves a coupling with the highest members of another Rydberg series converging to the $A\ ^2\Pi_u v^+ \geq 2$ [10,13].

Such quasibound autoionizing states are known to significantly modify the vibrational repartition, transferring part of the $v'=0$ population to higher vibrational states as $v'=1$, 2, and 3 [11]. Assuming that the states of the Hopfield series have the same shape as the B, we calculated the Franck-Condon factors for a transition from the molecular ground state to the different vibrational levels of the X state of the ion, via the first two vibrational levels of a B-like autoionizing state. We obtain the following populations for $v'=0,1,2,3$: 58%, 26%, 12%, 4%. This is in fair agreement with the measured populations: 58%, 20%, 12%, and 10%.

When the ir probe field is added, sidebands appear between the harmonics. The sidebands from one ionization channel partly overlap with the harmonics from the other ionization channel. In order to unambiguously identify them, we subtracted the spectra obtained with and without the probe field [Fig. 2(b)]. The resulting signal is negative where the ir field has removed some population, i.e., where harmonics are located, and positive where it has increased the signal, i.e., where sidebands are. We have labeled each sideband according to the corresponding photon energy and ion state.

We scanned the delay between xuv and ir and measured the phase of the sideband oscillations by fast-Fourier-transform. This operation was performed for each sideband and each ionization channel. Different sidebands were measured with different retarding voltages, here again to achieve a correct resolution of the vibrational levels. In order to extract the molecular phase from the phase of the sideband oscillation [Eq. (1)], one has to remove the difference $\varphi_{2q+1}-\varphi_{2q-1}$. This difference is inherent to the harmonic generation process and is independent of the target gas. It was measured by RABBITT of the same APT in a reference atom (argon) whose atomic phases are known from theory [15]. The term $\varphi_{2q+1}-\varphi_{2q-1}$ was then subtracted from the sideband phase to obtain $\Delta\theta_{2q}$.

The evolution of $\Delta\theta_{2q}$ as a function of sideband order is shown in Fig. 3. For the X channel, sideband 12 shows a

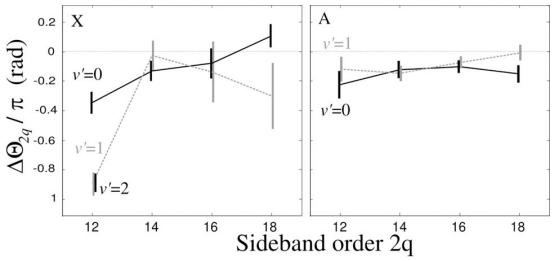

FIG. 3. Molecular phase difference $\Delta\theta_{2q}$ as a function of the sideband order for different ionization channels.

remarkable behavior: $\Delta\theta_{12}$ is -0.35π for $v'=0$ and reaches -0.9π for $v'=1$ and $v'=2$. This variation in $\Delta\theta_{12}$ is due to a phase jump in the two-photon matrix element associated to the absorption of H11. This phase shift was found to be very robust even by varying the intensity of the ir probe field by a factor 3. For the A channel $\Delta\theta_{2q}$ stays small for all sideband orders, between 0 and -0.2π. The absence of signature of the resonance in this channel is due to a poor coupling of the autoionizing state with the A continuum [10].

While the signature of the vibrationally dependent influence of the resonance already appears in the amplitude distribution of the vibrational states (Fig. 2), these measurements bring additional information on the photoionization process. Indeed, as shown in Fig. 1, the effect of the resonance on the molecular phase is strongest when the energy of the harmonic is below the resonance. We can use this information to schematically represent the photoionization process (Fig. 4). The initial wave packet is projected onto the first two vibrational levels ($v''=0,1$) of the B-like resonance that are contained within the bandwidth of H11. The central energy reached by absorption of H11 (horizontal dotted line in Fig. 4) is above the $v''=0$ level so that the molecular phase is weakly affected by the resonance for this path. On the other hand, H11 is below the $v''=1$ level and the molecular phase presents a phase shift $\approx\pi$ for this path. Franck-Condon factors show that the population from the $v''=0$ of a B-like state will mainly end in the $v'=0$ of the X ionic state, while the overlap of the $v''=1$ is good with the $v'=0,1,2$ states. Thus, for the $X, v'=0$ state, the signal is a mixture of direct and resonant contributions from the $v''=0$, for which there is no phase shift, and contributions from the $v''=1$

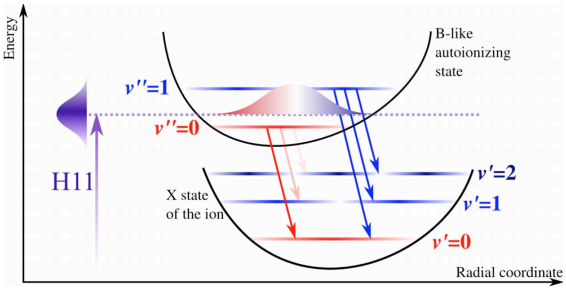

FIG. 4. (Color online) Schematic description of the photoionization process via the vibrational levels of the autoionizing state.

which are shifted. The resulting phase is only slightly affected by the resonance. By contrast, for the $X,v'=1$ and $X,v'=2$ states, the contributions from the $v''=1$ level dominate and there is a strong phase shift. The simple picture presented in Fig. 4 is schematic since it does not explain why the phase shift for the $v'=1$ and $v'=2$ are equal. This is probably a signature of the coupling to Rydberg states converging to the $A\ ^2\Pi_u v^+ \geq 2$.

Our results show that RABBITT is very sensitive to the location of the one-photon ionization level with respect to the vibrational states and to the shape of the autoionizing state potential-energy surface. Thus, it can be used to reveal subtle information on the phase of the xuv photoionization process. The observed behavior of the two-photon molecular phases for different sidebands can be interpreted as a modification of the electron release time by the presence of the resonance. In the single xuv photoionization process, this would correspond to a change in the electron wave-packet temporal profile, admitting that the ir probe beam does not significantly perturb this process and does not induce an additional phase shift. While this assumption is consistent with our measurements of molecular phases independent of the probe beam intensity, it remains to be formally established.

In conclusion, we have used interference of two-photon transitions to measure the amplitude and phase of electron wave packets produced by attosecond xuv photonionization of N_2 molecules. We have shown the influence of a complex resonance on the ionization phase for different vibrational states of the ion.

A natural extension of our work would be to measure the photoelectron angular distributions [18]. This would provide the relative phases between the partial waves constituting the electron wave packet, which are inaccessible in our angle-integrated measurement. In addition, tuning the harmonic wavelength by tuning the ir wavelength [19] would enable us to measure the phases while scanning the resonance. The extension of our work to the study of dynamics is quite straightforward and would give access to the modifications of the photoionization phase in real time in an excited medium.

Last, we note that our measurement is conceptually close to coherent control experiments in which phase lags due to resonances can be measured through the interference of two paths leading to the same final state [20,21]. The use of combined ir fields and APT opens the possibility to control molecular photoionization processes and to perform attosecond xuv coherent control.

We thank V. Blanchet, R. Cireasa, D. Dowek, A. Huetz, O. Lepelletier, and H. J. Wörner for fruitful discussions. We acknowledge financial support from the EU LASERLAB program and the ATTO-WAVE ANR program.

[1] M. Lebech *et al.*, J. Chem. Phys. **118**, 9653 (2003).
[2] P. M. Paul *et al.*, Science **292**, 1689 (2001).
[3] V. Véniard, R. Taïeb, and A. Maquet, Phys. Rev. A **54**, 721 (1996).
[4] F. Quéré *et al.*, J. Mod. Opt. **52**, 339 (2005).
[5] Y. Mairesse and F. Quéré, Phys. Rev. A **71**, 011401(R) (2005).
[6] K. Varju *et al.*, Laser Phys. **15**, 888 (2005).
[7] J. Mauritsson, M. B. Gaarde, and K. J. Schafer, Phys. Rev. A **72**, 013401 (2005).
[8] A. L. Cavalieri *et al.*, Nature (London) **449**, 1029 (2007).
[9] R. Kienberger *et al.*, Nature (London) **427**, 817 (2004).
[10] M. Raoult *et al.*, J. Phys. B **16**, 4601 (1983).
[11] A. Parr *et al.*, Phys. Rev. Lett. **46**, 22 (1981).
[12] M. Zubek *et al.*, J. Phys. B **21**, 3585 (1988).
[13] P. Dehmer *et al.*, J. Chem. Phys. **80**, 1030 (1984).
[14] E. Toma and H. Muller, J. Phys. B **35**, 3435 (2002).
[15] Y. Mairesse *et al.*, Science **302**, 1540 (2003).
[16] Y. Itikawa *et al.*, J. Phys. Chem. Ref. Data **15**, 985 (1986).
[17] A. Lofthus and P. Krupenie, J. Phys. Chem. Ref. Data **6**, 113 (1977).
[18] S. A. Aseyev, Y. Ni, L. J. Frasinski, H. G. Muller, and M. J. J. Vrakking, Phys. Rev. Lett. **91**, 223902 (2003).
[19] Y. Mairesse *et al.*, Phys. Rev. Lett. **94**, 173903 (2005).
[20] J. Fiss *et al.*, Faraday Discuss. **113**, 61 (1999).
[21] R. Yamazaki and D. S. Elliott, Phys. Rev. Lett. **98**, 053001 (2007).

PAPER VI

Attosecond pulse generation in chromium ablation plasma

L. B. Elouga Bom, S. Haessler, M. Perdrix, F. Lepetit, J.-F. Herrgot, B. Carré, T. Osaki and P. Salières.

in preparation, (2009).

Reconstruction of an attosecond pulse train from harmonics generated from chromium plasma

Luc Bertrand Elouga Bom[1*], Stefan Haessler[2], Michel Perdrix[2], Fabien Lepetit[2], Jean-Francois Herrgott[2], Bertrand Carré[2], Tsuneyuki Ozaki [1] and Pascal Salières[2]

[1] Institut national de la recherche scientifique – Centre Énergie, Matériaux et Télécommunications, 1650 Lionel-Boulet, Varennes, Québec J3X 1S2, Canada

[2] DSM-IRAMIS-Service des Photons, Atomes et Molécules, CEA Saclay, 91191 Gif-sur-Yvette Cedex, France

[*] elouga@emt.inrs.ca

ABSTRACT

We present in this work the first reconstruction of an attosecond pulse train of high-order harmonics generated from lowly ionized plasma produced on solid targets. We demonstrate that plasma can be used to produce extreme ultraviolet pulses with sub-femtosecond durations, similar to that observed using gas medium. We generate high-order harmonics of a femtosecond Ti:sapphire laser from an under-dense chromium plasma plume, comprising five harmonics from the 11^{th} to the 19^{th} order. Using the method of "Reconstruction of Attosecond Beating By Interference of Two-photon Transitions" (RABBITT), we characterize an attosecond pulse train with each pulse having 360 as duration, which is only 1.3 times the theoretical Fourier transform limit. Measurements reveal a very low positive group delay dispersion of 6400 as².

1. INTRODUCTION

High-order harmonics are generated when an intense short laser pulse is focused in to a gas of atoms. It was first shown numerically [1] and then experimentally [2] that the generated harmonic radiation consists of a train of pulses with attosecond duration. This attosecond nature of harmonic radiation, along with its short wavelength, excellent coherence and high brilliance, provide a strong motivation for applications, some of which have already been demonstrated. For example, extreme ultra-violet (XUV) harmonic sources were used in specific atomic [3] and molecular spectroscopy [4], to characterize plasmas [5], and to create and observe XUV nonlinear effects [6-8]. Despite its potentials, many other applications remain unexplored because of the difficulty to handle and manipulate the harmonics, due partially to the quality of XUV optics, as well as the low harmonic intensity.

After several decades of extensive research, a new method for intense harmonic generation is starting to emerge. This method uses lowly ionized laser ablation plasma as the nonlinear medium, instead of the conventional gas of atoms. Contrary to harmonic generation from gas, which results from the interaction between an infrared laser pulse and neutral atoms, plasma harmonics are mainly generated from ions within the laser-produced plasma plume [9]. The first experiments of harmonic generation in ablation plasma were performed in 1992 by Akiyama *et al.* [10] and in 1994 by Wahlström *et al.* [11]. Using an infrared 794 nm laser focused in plasmas of lithium, sodium and potassium, the highest order achieved in these works was the 27^{th} order for lithium plasma [11]. Recently, this method has re-attracted attention, when Ganeev *et al.* demonstrated highly efficient (conversion efficiency of 10^{-5}) harmonic generation from silver plasma [12], which exceeds conversion efficiencies typically obtained with atomic

gases by at least one order of magnitude [19]. However, to show the effectiveness of this new harmonic generation method, it is also very important to demonstrate that plasma harmonics also share the other interesting properties of gas harmonics (such as short wavelength, short pulse duration, focusability and low divergence). We have been concentrating our effort in these directions, and we have generated high-order harmonics from more than 15 different target materials with typical plateau and cutoff features [13], and have generated the highest harmonic order ever obtained from plasma [14]. In this article, we study the temporal duration of the harmonic pulse train generated from plasma. We have measured the harmonics from chromium plasma, and have used the technique of "Reconstruction of Attosecond Beating By Interference of Two-photon Transitions" (RABBITT) [2] to characterize the temporal duration. We show that chromium plasma harmonics have low positive chirp, and that combining the 11^{th} to the 19^{th} harmonics result in attosecond pulses that are only 1.3 times the theoretical Fourier transform limit.

2. EXPERIMENTAL SETUP

In this work, we used the experimental setup installed at the Commissariat à l'Énergie Atomique (CEA) - Saclay, which was developed to characterize harmonic pulses generated from gas. We modified this setup so that it adapted to our experimental needs for harmonic generation from plasma. A schematic diagram of this setup is shown in Fig. 1. First, we separated the uncompressed Ti:sapphire laser beam (800 nm, 300 ps) from the LUCA laser system into two beams, using a beam splitter. One of these beams (pre-pulse) is loosely focused on to a solid target to create the low-ionized plasma. The other uncompressed beam is first sent through an 80 ns delay line, and then through a

compressor. At the exit of the compressor, we have a 50 fs Ti:sapphire laser pulse with a central wavelength of 800 nm. This beam is then further separated into two beams using a mirror (M_H) with a through hole at the center. The external annular part of the beam (the generating beam) is focused in to the plasma to generate the high-order harmonics. The round central part of the beam (dressing beam), which has a two orders of magnitude lower energy than the external part, passes through the hole of the mirror. Alone, it cannot generate harmonics. We add another, very precisely variable delay to this central part of the beam, using a piezoelectric translation stage.

After harmonic generation, an iris blocks the generating beam, while the dressing beam and the harmonics pass. A toroidal mirror then focuses the dressing beam and the harmonics into the detection gas jet, and a magnetic bottle electron spectrometer (MBES) measures the spectrum of the electrons generated by photo-ionization of the target gas argon.

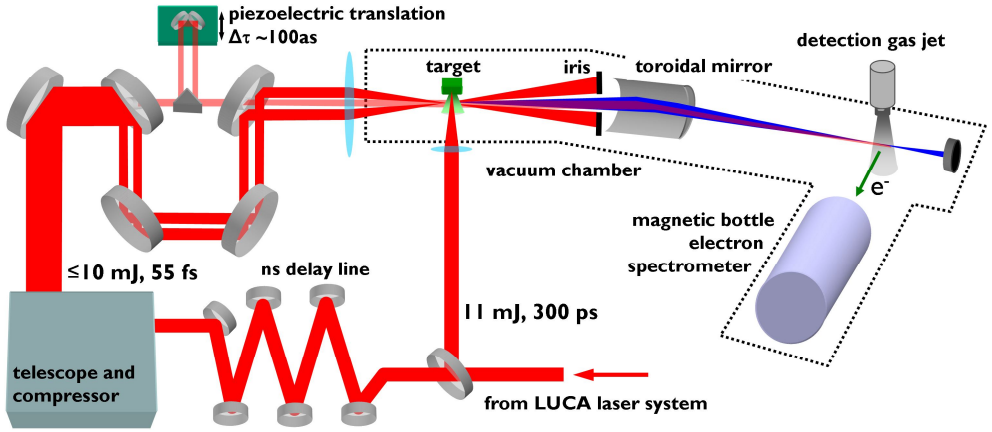

Figure 1: Experimental set up for the reconstruction of the pulse train for high-order harmonics generated from plasma ablation.

3. EXPERIMENTAL RESULTS AND DISCUSSIONS

We chose chromium for this experiment, because it produces a sufficient number of harmonic orders within the measured spectrum range. The harmonics, generated in the chromium plasma, with photon energies higher than the first ionization energy of argon will ionize the gas, thereby generating photo-electrons with spectra as those shown in Fig.2.

We note that the harmonic spectrum in Fig. 2 differs considerably from those observed in other works. Past results using 35 fs Ti:sapphire laser pulses have demonstrated Cr harmonic spectra with cut-off at the 35^{th} order, with strong intensity enhancement of the 29^{th} harmonic [15]. In contrast, the Cr harmonic spectra in the present work have a cut-off at the 19^{th} order. For these experiments, we measured the generating intensity to be 2×10^{14} Wcm^{-2} (opposed to $> 10^{15}$ Wcm^{-2} used in past works) by generating harmonics in argon gas in the same experimental conditions and comparing the measured group delay dispersion to simulations. This lower pump intensity is mainly due to the long nanosecond delay line for the femtosecond pump pulse, which deteriorates the spatial quality of the femtosecond generating beam and thus reduces the pump intensity at focus. An intensity of 2×10^{14} Wcm^{-2} saturates harmonic generation Cr^+ (I_p = 16.5 eV). but should allow efficient HHG in Cr^{2+} (I_p = 31 eV). This is due to the barrier-suppression intensity, $I_{BI}[W\ cm^{-2}] = 4x10^9\ (I_p\ [eV])^4 / Z^2$, being $7x10^{13}$ W cm^{-2} for Cr^+ ions and $4x10^{14}$ W cm^{-2} for Cr^{2+} ions [20]. Here, Z is the effective charge of the screened nuclei, i.e. Z=2 for Cr^+ and Z=3 for Cr^{2+}. The saturation intensity for Cr^+ ions together with their ionization potential give a classical cut-off position [21] at harmonic 19, which is in reasonable agreement to the experimentally observation. For Cr^{2+} ions and an intensity of

of 2×10^{14} Wcm^{-2}, a classical cut-off at harmonic 43 is expected. We thus assume to generate harmonics mainly in the rising flank of the pump pulse in Cr^+ ions and there does not seem to be a significant contribution from Cr^{2+} ions to the signal. The obtained conversion efficiency has not been quantified but we estimate it to be about an order of magnitude lower than what usually is obtained with HHG in noble gases.

Note, that the wavevector mismatch, $\Delta k^e = k^e_q - qk^e_1$, due to free electrons in the plasma cannot explain the observed rapid drop of spectral intensities. Assuming constant absorption for all harmonic orders, the spectral intensity varies as [22]

$$I_q \propto L_{\mathrm{coh}}^2[1-\cos(\pi L_{\mathrm{med}}/L_{\mathrm{coh}})], \tag{1}$$

where L_{med} is the medium length and $L_{coh} = \pi/\Delta k_e$ is the coherence length. For the wavevector of the q^{th} harmonic we can write

$$k^{\mathrm{e}}{}_q = \frac{1}{c}(q^2\omega_0^2 - \omega_{\mathrm{p}}^2)^{1/2}, \qquad \text{with} \quad \omega_{\mathrm{p}}^2 = \frac{n_{\mathrm{e}}e^2}{m_{\mathrm{e}}\epsilon_0}, \tag{2}$$

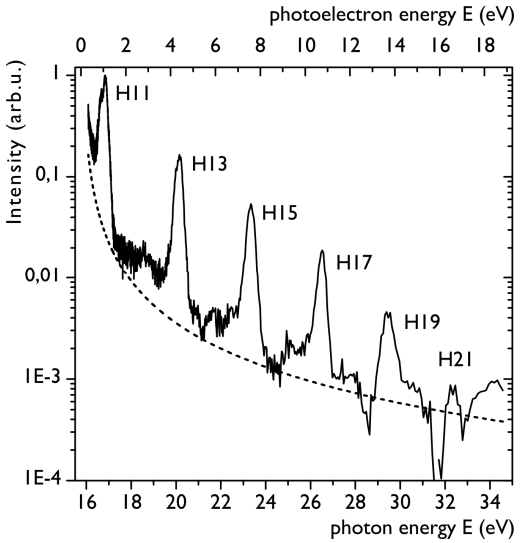

Figure 2: Harmonic spectrum obtained from chromium plasma. The spectrum shows five consecutive harmonic orders, from the 11^{th} to the 19^{th} harmonic. The dashed line marks the noise level of the MBES signal.

where ω_p is is the plasma frequency, ω_0 is the pump laser frequency, m_e and e are the electron mass and charge, respectively, c is the vacuum light velocity, and n_e is the plasma electron density. We estimate the free electron density to be 1×10^{17} cm^{-3} [13], leading to coherence lengths of L_{coh}=1.25 mm for the 11^{th} harmonic, and 0.73 mm for the 19^{th} harmonic. For our observed spectral range, L_{coh} is thus always smaller than the typical length of our plasma medium of 0.6 mm and the phase matching situation should be quite good. Equation 1 then only predicts the spectral intensity to drop by a factor ~2/3 from harmonic 11 to 19, whereas in the experiment (cp. Fig. 2) we observe an exponential drop by more than two orders of magnitude, which can only be attributed to the high harmonic cut-off.

In general, the electromagnetic field of radiation can be represented by its amplitude and phase. Therefore, to reconstruct the electromagnetic field of the harmonic emission, we need to measure its spectral amplitude and phase. The amplitude of each harmonic is given by the harmonic spectrum shown in Fig. 2, which contains five harmonics from the 11^{th} to the 19^{th} order. To determine the harmonic phase, we used the RABBITT method. To this end, we focused into the argon gas the chromium harmonics and the central part of the compressed infrared beam (dressing beam) that passes though the hole of mirror M_H. If an additional laser field with frequency ω_0 is added, two-photon above threshold ionization transitions can occur: absorption of a harmonic photon $(2q+1)\ \omega_0$ accompanied by either absorption or stimulated emission of one photon ω_0. New lines (side-bands) appear in the spectrum, in between the harmonics. Since two coherent quantum paths lead to the same sideband, interferences occur which result in an oscillation of the sideband amplitude as the delay τ between the IR and harmonic field is

scanned with sub-IR-laser-cycle resolution [2,16]. The phase of the oscillation is the phase difference between the two interfering channels. It is determined by the phase difference ϕ_q-ϕ_{q+2} between consecutive harmonics (phase locking) and by the difference of the two-photon transition phases $\Delta\phi^{at}$. For example, if we consider the $(q+1)^{th}$ sideband between the q^{th}- and the $(q+2)^{th}$-harmonic order, the signal intensity is:

$$S_{q+1}(\tau) \propto \cos(2\omega_0\tau + \phi_q - \phi_{q+2} + \Delta\phi^{\mathrm{at}}), \tag{3}$$

The term $\Delta\phi^{at}$, characteristic of the target gas argon, has been calculated [17]. The phase difference $\phi_q - \phi_{q+2}$ between two consecutives harmonics can then be extracted, readily giving the group delay, also called emission time $t_e = \partial\phi/\partial\omega \,|_{q+1} \approx (\varphi_q - \varphi_{q+2}) / 2\omega_0$.

Fig. 3(a) shows the emission times t_e for the sidebands between the harmonics. determined by integrating the emission times from the RABBITT scan. The results show a very low positive group delay dispersion (GDD, also called *attochirp*) of 30 as between two successive harmonics, corresponding to a GDD of 6400 as^2. For the pump intensity used, the GDD should be more than 2 times larger for harmonics in the plateau [18]. Assuming an effective generating intensity equal to the saturation intensity of Cr^+ ions, the GDD should even be 5 times as large. However, it is known that the chirp tends to vanish in the cut-off region, which can explain the low chirp in our Cr harmonics.

Knowing the phases ϕ_q, obtained by integrating the emission times, and the amplitudes A_q and for each harmonic order, we reconstruct the temporal intensity profile I(t) according to

$$I(t) = \left| \sum_{N} A_q \exp(-\mathrm{i}\omega_q t + \mathrm{i}\phi_q) \right|^2 . \qquad (4)$$

The result for the measured five harmonic orders q=11 to 19 is shown in Fig. 3(b). The electromagnetic field reconstructed from the harmonic spectra generated in chromium plasma forms a pulse train, with each pulse of 360 as duration (full width at half maximum). Assuming all 5 harmonics to be in phase, we obtain the shortes possible, i.e. the Fourier transform limited, duration for the measured spectrum. In our case, this amounts to τ_{FL} = 285 as.

The measured duration of 360 as is thus only 1.3 times the Fourier transform limited duration. It is necessary to note that contrary to gas, plasma is a more complex medium, which contains several types of ions, atoms and free electrons. Therefore, plasma is much more dispersive than gas due to its higher free electron density. The effect on the group delay of the harmonic emission, however, remains very small. From eq. 2, we find the group velocity dispersion $\partial^2 k/\partial\omega^2 = c^{-1}[(\omega^2-\omega_p^2)^{-1/2} - \omega^2(\omega^2-\omega_p^2)^{-3/2}]$, added by

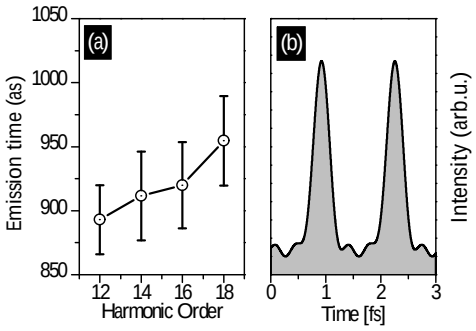

Figure 3: Emission times and reconstructed time profile of the harmonic emission

propagation through a free electron gas with a density of $1\times10^{17}cm^{-3}$. It amounts to -60 as^2 mm^{-1} at harmonic 11 and -12 as^2 mm^{-1} at harmonic 19, which is insignificant compared to the measured GDD with our short medium length. Increasing the electron density or medium length in order to achieve compression of the attosecond pulses down to the Fourier limit would, however, at the same time reduce the coherence length and thus rapidly render impossible efficient high harmonic generation.

4. CONCLUSION

We present in this article the reconstruction of the electromagnetic field of high-order harmonics generated from chromium plasma. For this purpose, we used the RABBITT technique, which has already been used to characterize attosecond pulses generated from gas. We observed that the electromagnetic field generated by five consecutive harmonics from chromium plasma is a train of pulses, with each pulse having an average duration of 360 as. This corresponds to 1.3 times the Fourier transform limit of five harmonics generated by a Ti:sapphire laser. Considering the potentially very high conversion efficiency when using higher pump intensity, these results show that plasma harmonics could become a source for generating intense attosecond pulses.

REFERENCES

[1] P. Antoine, A. L'Huillier and M. Lewenstein, Phys. Rev. Lett. **77**, 1234 (1996).

[2] P. M. Paul, E. S. Toma, P. Breger, G. Mullot, F. Augé, P. Balcou, H. G. Muller and P. Agostini, Science, **292**, 1689 (2001).

[3] J. Larson, E. Mevel, R. Zerne, A. L'Huillier, C.-G. Wahlström and S. Svanberg, J. Phys. B **28**, L53 (1995).

[4] S. L. Sorensen, O. Björneholm, S. Buil, D. Descamps, I. Hjelte, T. Kihlgren, A. L'Huillier, J. Norin, S. Svensson, S. Sundin, C.-G. Wahlström and G. Öhrwall, J. Chem. Phys. **112**, 8038 (2000).

[5] W. Theobald, R. Hässner, C. Wülker and R. Sauerbrey, Phys. Rev. Lett. **77**, 298 (1996).

[6] Y. Kobayashi, T. Sekikawa, Y. Nabekawa and S. Watanabe, Opt. Lett. **23**, 64 (1998).

[7] T. Sekikawa, T. Katsura, S. Miura and S. Watanabe, Phys. Rev. Lett. **88**, 193902 (2002).

[8] D. Descamps, L. Roos, C. Delfin, A. L'Huillier and C.-G. Wahlström, Phys. Rev. A **64**, 031404 (2001).

[9] L.B. Elouga Bom, J.C. Kieffer, R.A. Ganeev, M. Suzuki, H. Kuroda and T. Ozaki, Phys. Rev. A **75**, 033804 (2007).

[10] Y. Akiyama, M. Midorikawa, Y. Matsunawa, Y. Nagata, M. Obara, H. Tashiro and K. Toyoda, Phys.Rev Lett **69**, 2176 (1992).

[11] C.-G. Wahlström, S. Borgström, J. Larsson and S.-G. Pettersson, Phys. Rev. A. **51**, 585 (1995).

[12] R.A. Ganeev, M. Baba, M. Suzuki and H. Kuroda, Phys. Rev. A 339, 103 (2005)

[13] R. A. Ganeev, L. B. Elouga Bom, P. V. Redkin and T. Ozaki, J. Opt. Soc. Am. B **24**, 2770 (2007).

[14] R. A. Ganeev, L. B. Elouga Bom, J.-C. Kieffer and T. Ozaki, Phys. Rev. A **76**, 023831 (2007).

[15] R. A. Ganeev, L. B. Elouga Bom, J.-C. Kieffer and T. Ozaki, Phys. Rev. A **75**, 063806 (2007)

[16] V. Veniard, R. Taieb and A. Maquet, Phys. Rev. A **54**, 721 (1996).

[17] Y. Mairesse, O. Gobert, P. Breger, H. Merdji, P. Meynadier, P. Monchicourt, M. Perdrix, P. Salières and B. Carré, Phys. Rev. Lett. **94**, 173903 (2005).

[18] Y. Mairesse, A. de Bohan, L. J. Frasinski, H. Merdji, L. C. Dinu, P. Monchicourt, P. Breger, M. Kovacev, R. Taieb, B. Carré, H. G. Muller, P. Agostini and P. Salières, Science **302**,1540 (2003).

[19] J.-F. Hergott, M. Kovacev, H. Merdji, C. Hubert, Y. Mairesse, E. Jean, P. Breger, P. Agostini, B. Carré, and P. Salières, Phys. Rev. A **66**, 021801 (2002)

[20] F.A. Ilkov, J.E. Decker, and S.L. Chin, J. Phys. B **25**, 4005 (1992)

[21] K.J. Schafer, B. Yang, L.F. DiMauro, and K.C. Kulander, Phys. Rev. Lett. **70**, 1599 (1993). P. B. Corkum, Phys. Rev. Lett. **71**, 1994 (1993).

[22] E. Constant, D. Garzella, P. Breger, E. Mével, Ch. Dorrer, C. Le Blanc, F. Salin, and P. Agostini, Phys. Rev. Lett. **82**, 1668 (1999)